LOW STRAIN BEHAVIOUR

OF A

PARTICULATE REINFORCED ALUMINUM ALLOY

By

STEPHEN FRANCIS JOSEPH CORBIN, B.Eng, M.A.Sc.

A Thesis

Submitted to the School of Graduate Studies

in Partial Fulfilment of the Requirements

for the Degree

Doctor of Philosophy

(c) Copyright by Stephen Francis Joseph Corbin, 1992

LOW STRAIN BEHAVIOUR OF A PARTICULATE REINFORCED Al ALLOY

DOCTOR OF PHILOSOPHY (1992) McMASTER UNIVERSITY
(Materials Science and Engineering) Hamilton Ontario

TITLE: Low Strain Behaviour in a Particulate Reinforced Aluminum Alloy.

AUTHOR: Stephen Francis Joseph Corbin, B.Eng. (Technical University of Nova Scotia)

M.A.Sc. (Technical University of Nova Scotia)

SUPERVISOR: Professor D.S. Wilkinson

NUMBER OF PAGES: xix, 270

ABSTRACT

The primary purpose of this investigation was to examine the strengthening that arises when reinforcing an aluminum alloy with approximately equiaxed shaped SiC particles. The results indicate that the majority of strengthening that is derived from the particles develops at low strains. For a variety of test conditions explored, about 90% of the total strengthening derived is developed by a plastic strain of about .5%. This is primarily a result of the high strain hardening rate which is exhibit by the composite materials during the onset of plastic flow.

An examination of the Bauschinger effect in the composites indicates that an internal stress, resulting from inhomogeneous plastic flow, develops rapidly in the low strain regime. Microstructural observations suggest that the nature of this inhomogeneous plastic flow is influenced by the distribution of the SiC particles. Initial plasticity appears to be associated with regions of the microstructure which are relatively particle free.

A self-consistent model, based on Eshelby's equivalent inclusion method, has been developed which is capable of calculating the stress partitioning which occurs between the Al matrix and SiC particles during the elastic/plastic transition and beyond. Excellent quantitative agreement between the experimentally measured elastic modulus and that predicted by the model was achieved. When considering a uniform distribution of second phase particles, the model predicts an increase in the initial strain hardening rate. However, it underestimates the actual strain hardening rate which was measured experimentally. The influence of particle distribution was examined by representing the composite microstructure by a bimodal mixture consisting of a particle rich and particle free phase. The model predicts an increase in the initial strain hardening rate as a result of clustering the microstructure in this way. The magnitude of this increased hardening is comparable to that measured experimentally.

ACKNOWLEDGEMENTS

My experience at McMaster has been nothing short of incredible and I have many people to thank for this. Thanks goes to my supervisor Dr. D.S. Wilkinson for his support and guidance over the entire length of this work.

A special note of thanks goes to Dr. J.D. Embury for his guidance, advice, enthusiasm and sense of humour which made my time at McMaster all the more pleasurable.

I am forever in debt to Dr. Z.S. Basinski for the stimulating discussions and the many lessons learned in his presence.

Many thanks to Warren Poole for his help with mechanical testing and all the lengthy and worthwhile discussions which ensued over the past few years.

In addition, thanks goes to Ed McCaffery for his help concerning mechanical testing and computational tasks and to Teresa Castillo for preparing TEM foils.

A sincere appreciation goes to all the students and postdoctoral members of the structural materials group, both past and present, who have made my time at McMaster enjoyable. In particular, I would like to thank the unknown student who initiated the rule that the most senior person gets the best desk in the office. I have certainly enjoyed the privilege of having a window seat.

The financial support of the Natural Science and Engineering Research Council of Canada and McMaster University is gratefully acknowledged. Thanks also to Dr. D.J. Lloyd for his advice and for supplying the materials used in this study.

Most importantly I would like to thank my wife, Sandi, for her love and support, without which this thesis could not have been completed. In addition, her help in preparing the manuscript and in producing the schematic diagrams used throughout this thesis is appreciated.

TABLE OF CONTENTS

(CHAPTER 1 Continued)

(CHAPTER 3 Continued)

LIST OF FIGURES

LIST OF FIGURES (continued)

LIST OF FIGURES (continued)

LIST OF FIGURES (continued)

LIST OF FIGURES (continued)

LIST OF FIGURES (continued)

LIST OF FIGURES (continued)

LIST OF FIGURES (continued)

LIST OF FIGURES (continued)

LIST OF TABLES

CHAPTER 1

INTRODUCTION

1.1 Introduction

In the past 10 to 15 years, new technologies have been developed to incorporate large volume fractions (> 10%) of hard ceramic particles into a metal matrix. At present, there are a number of processes in which this can be achieved (Humphreys et al., 1991) including; 1) molten metal mixing; 2) squeeze casting; 3) spray casting and 4) powder metallurgy.

One of the main advantages of these particulate metal matrix composites (PMMC's) is that they can be manufactured in the form of billets and subsequently thermomechanically processed using methods similar to those used for the monolithic alloys they are based on. Consequently, these composite materials represent a cost effective approach to property enhancement. Among those properties most effected by particle additions are stiffness, strength and wear resistance. In the majority of cases, PMMC materials are based on commercially pure or precipitation hardened alloy matrices reinforced with SiC or Al_2O_3 in either particulate or whisker form.

In attempting to understand the deformation behaviour of PMMC materials it should first be realized that much of the understanding of deformation and strengthening in two phase materials has been derived from theoretical and experimental work on dispersion hardened (DSH) alloys (Brown, 1976). While these materials have some microstructural features in common with PMMC's there are also a number of important differences. These differences primarily pertain to the scale of reinforcement used and the type of matrix being reinforced.

In the area of DSH alloys experimental verification of strengthening models have been

principally accomplished using pure single crystal matrices reinforced with a fine oxide dispersion (Embury, 1985). Conversely the manufacturing routes used for PMMC's presently limits the particle size to greater than 1μm. Therefore, while the volume fraction is higher than DSH alloys, the number of particles per unit volume is generally much smaller. In addition, commercial PMMC's are based on polycrystalline matrices which themselves are often dispersion or precipitation hardened alloys.

The scale of the reinforcement used in PMMC's is such that their microstructures are in a category which traditionally lies between treatments based on continuum mechanics and discrete dislocation or micromechanical models (see Figure 1.1). While the boundary between these two regimes is not well defined, two phase materials with widely spaced, large scale fibres of about .1mm in diameter approximately obey continuum mechanics (Ashby, 1971; pg. 144). In this case the properties of the two phases obey a rule of mixtures and the primary role of the reinforcement is one of bearing a load. Conversely reinforcement of a pure single crystal by a fine oxide dispersion with particle sizes in the range of .01μm is well characterized by dislocation mechanics (Ashby, 1971). In this case, the majority of strengthening is derived by a strong interaction between mobile dislocations and the second phase particles. PMMC's have microstructures which lie between these two bounds and the applicability of continuum or micromechanical models has yet to be fully elucidated.

Two additional complications which are encountered in PMMC materials are the polycrystalline nature of the matrix and the large volume fraction of second phase. The multiplicity of slip which occurs in a polycrystal creates a complex elastic/plastic transition at the onset of plastic flow. This makes it difficult to interpret the strengthening effect of the second phase particles. A high volume fraction of second phase increases the importance of particle-

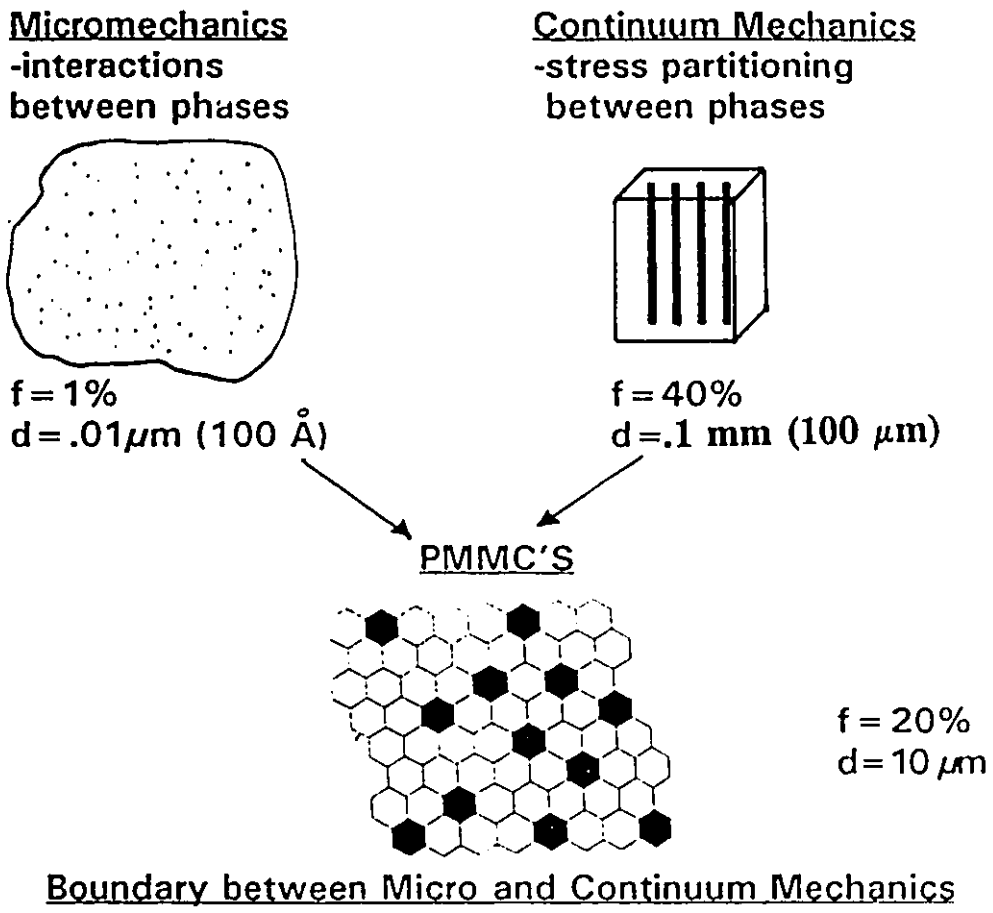

Figure 1.1: Definition of the approximate microstructural boundaries best described by continuum mechanics and micromechanics. (f and d refer to the volume percent and particle size of the second phase)

particle interactions. This is of particular concern when the property mismatches between the two phases (e.g. elastic and thermal expansion mismatch) becomes large and when the particles are non-uniformly distributed throughout the matrix. The latter aspect can create particle rich and particle free regions in the microstructure which occur on a macroscopic scale.

The objective of this thesis is to investigate the role of SiC particles as strengthening agents in a precipitation or age hardenable commercial aluminum alloy. In particular, it will attempt to elucidate the relative importance of scale dependent (micromechanical) mechanisms and scale independent (continuum) mechanisms. The majority of the work will focus on low strain behaviour which incorporates the elastic/plastic transition. Some effort will be made to investigate the role of particle distribution on the strength developed in the low strain regime.

The remainder of this chapter will focus on a brief review of both micromechanical and continuum mechanical models and their applicability to PMMC materials. In addition, some complications that arise due to polycrystalline deformation will be described. Lastly, the Bauschinger effect, which represents a valuable tool in distinguishing different strengthening mechanisms, will be discussed. A description of the experimental procedure (Chapter 2) will be followed by a presentation of the experimental results obtained in this work (Chapter 3).

An extremely important contribution to the theoretical understanding of two phase deformation is Eshelby's equivalent inclusion method (Eshelby, 1957, 1961) which allows one to calculate the level of internal stress developed in a two phase material. This will be presented in Chapter 4 along with a self-consistent formulation based on Eshelby's technique developed to describe the elastic/plastic deformation of PMMC's at low strains. In chapter 5 a discussion of the experimental results will be completed which will make use of the model developed in chapter 4. It will also contain a discussion of the pertinent literature that is presently published in the field

of PMMC's as it relates to the work done during this study. Lastly a summary and some conclusions will be described in chapter 6.

1.2 Critical Microstructural Aspects of Particulate Metal Matrix Composites

The microstructural aspects of interest here are illustrated in Table 1.1 and fall into three primary categories;

1) **Volume Fraction.** While there is some overlap, most PMMC's contain volume fractions which are 10 times that typically found in DSH alloys.

2) **Particle Size.** Particle size is perhaps the most distinguishing feature of PMMC's being typically 100 times larger than that found is DSH alloys.

3) **Particle Spacing.** Clearly the scale of the reinforcement with respect to the microstructural features of the metal matrix (e.g. dislocation line segment and grain size), is quite different for the two classes of material. This scale is best described by referring to the average particle-to-particle spacing. Although there are a number of ways in which to calculate average spacing, we have chosen the method of Ashby (1968) in which the mean planar particle separation S_p is calculated assuming a random distribution of equiaxed particles;

$$S_p = \frac{1}{2}\sqrt{\frac{2\pi}{3f}}\, r \qquad (1.1)$$

where f is the volume fraction of particles and r is the particle radius (assuming a uniform particle size). On this basis the spacing of particles in PMMC's is typically 50 times larger than that found in DSH alloys.

Another important feature of the second phase is its shape. In DSH alloys, particle shapes can range from spherical (Cu-SiO_2) to angular plates (Cu-Al_2O_3) to needle like precipitates (Cu-Al

Table 1.1 Critical Microstructural Features of PMMC and DSH alloys. (Values in parenthesis indicate the range with which the typical value can vary.)

Microstructural Parameter	Dispersion hardened alloys	Particulate Metal Matrix Composite
Volume Fraction	Typical .01 (.001 to .1)	Typical .2 (.05 to .4)
Particle Size (μm)	Typical .05 (.01 to .1)	Typical 10 (2 to 100)
Particle Spacing (μm)	Typical .35 (.05 to 2.5)	Typical 15 (2 to 300)

alloys). For PMMC's, most reinforcements are either angular shaped particles or needle shaped(whiskers). The principal geometric consideration which describes particle shape is their aspect ratio.

One final concern is particle distribution. Since the volume fraction and particle size in PMMC's is quite large, the fact that the particles may not be uniformly distributed throughout the metal can become important. In particular, the formation of particle rich and particle free regions of the microstructure can exists on a relatively macroscopic scale (about 50μm). This can create regions of the microstructure with varying levels of strength and alter the overall stress-strain behaviour of the composite.

The difference in reinforcement scale between DSH and PMMC materials leads to microstructures that are represented schematically in Figure 1.1. In the case of DSH alloys, the second phase is dispersed within a grain of the metal matrix. In the case of PMMC's, the particles are of the same order as the matrix grain size. On this basis it may be expected that the detailed interaction between dislocations and the second phase particles may be quite different in the two cases.

1.3 Micromechanics of Two Phase Materials

A brief review of the micromechanical models which have been developed primarily for DSH alloys will be discussed in this section. Tne applicability of these models to PMMC's will be evaluated particularly in light of the microstructural features described above.

Most models (Brown and Ham, 1971; Ashby, 1971) based on micromechanics focus yielding and work hardening. Emphasis is placed on understanding how the presence of a second phase particle alters the dislocation substructure and work hardening processes which occur in the metal. Little importance is assigned to the load bearing capacity of the particle. However, in

some theories (Brown and Stobbs, 1971a) this aspect is incorporated indirectly through the concept of a back stress acting in the matrix.

1.3.1 Some Factors Which Influence the Yield Strength of Two Phase Materials

A definition of yielding, both in the unreinforced alloy and composite, is difficult because of the very rounded nature of the stress-strain curve in the vicinity of initial plastic flow. This problem will be discussed in more detail later. The following discussion will assume that a proper definition of yielding can be achieved.

1.3.1.1 Changes in the Microstructure of the Metal Matrix

As discussed, MMC's can be fabricated by a variety of routes. During the complex fabrication process it may be expected that the presence of a large volume fraction of particles may alter the resulting matrix microstructure. In particular the grain size and substructure may develop differently in the composite than in the alloy even when the same processing route is followed (Humphreys, 1988; Humphreys et al., 1991). The magnitude of these effects are likely to depend on the particular processing route. Extensive work by Lloyd (1991), indicates that for the composites of interest here, which are processed by a molten metal mixing route, the grain size and substructure of the metal is relatively unaffected by the presence of the SiC particles. Therefore, these factors will be ruled out as major contributors to the value of the yield strength.

Since the composites studied in this work are based on a commercial aluminium alloy which is age hardenable there exists the possibility that the ageing process may be altered by the presence of the reinforcement. Since the state of ageing can have a significant influence on yielding, this may be an important factor. There is evidence in the literature that in some alloy

systems (Christman and Suresh, 1988; Humphreys, 1991) the ageing process is accelerated by the addition of SiC whiskers and particles. In the case of the Al-Si-Mg alloys of interest here, most studies indicate (Dutta and Bourell, 1990; Appendino et al., 1991) that this accelerating effect is much smaller than that observed for other systems such as Al-Cu alloys. In addition, the degree of the effect depends on the ageing sequence. This phenomena has been investigated experimentally and will be described in more detail in section 3.1

1.3.1.2 Internal Stresses of a Thermal Origin

In most cases the metal matrix and ceramic particles have coefficients of thermal expansion (CTE) which are different. In particular, the mismatch is usually such that the CTE of the particle (CTE_p) is less than the CTE of the matrix (CTE_m). Because of the large volume fractions involved in PMMC's, large internal stresses can be created within the composite during a quench from fabrication or heat treatment temperatures.

The fact that internal stresses arise as a result of quenching during a heat treatment step has been well documented experimentally (Withers et al., 1987, 1988) for particulate MMC's. These results of internal strain measurements using neutron diffraction are illustrated in Figure 1.2. (It should be noted that these measurements sample a large volume of the composite material and therefore indicate the average internal strain in the matrix.) The residual strain in the matrix is net tensile which is consistent with the fact that $CTE_p < CTE_m$. Measurements of the internal strain in the particles were also completed. These were found to be compressive. Other work based on neutron diffraction (Allen et al., 1987) and x-ray diffraction (Ledbetter and Austin, 1987; Arsenault and Taya, 1986), confirm these results.

Comparisons of the experimental results with a model developed by Withers et al.

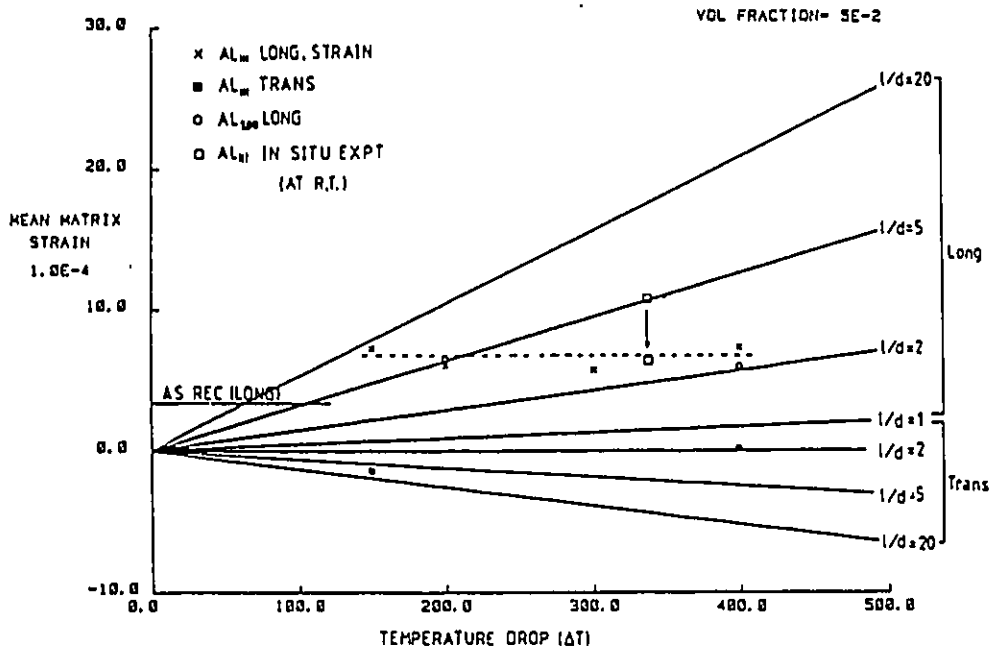

Figure 1.2: Experimental (symbols) and theoretical (solid line) value of the matrix strain due to a temperature drop. The data □ were obtained immediately after cooling and ↓ after a waiting period of 8 hours. (Whithers, 1987)

indicates some interesting results. While the theory predicts that the internal strain (and consequently the internal stress) should rise as the quenching magnitude, ΔT, increases, the experimental results indicate a constant internal strain, which is at a level consistent with a ΔT about of 200° C. The authors suggest that this is evidence of relaxation processes, not included in the model, which reduces the level of internal strain (or stress) developed. They considered the primary processes of relaxation to be diffusion and plastic flow of the matrix.

If one considers that the average internal stress in the matrix as measured by these experiments is uniformly distributed, its influence on stress-strain behaviour can be illustrated by performing tensile and compressive tests. The internal stress will aid the applied stress in tension but resist the applied stress when tested in compression. This should lead to anisotropy in yielding and is one way in which the presence of an internal stress can be evaluated. On this basis an internal stress of thermal origin can not be considered as a strengthening mechanism in the traditional sense, since it will increase the yield strength in one direction but decrease it in the opposite direction.

1.3.1.3 Thermally Induced Dislocation Substructure.

The degree to which diffusional and plastic flow contributes to the relaxation of internal stress is presently not well understood. From the in situ data of Figure 1.2 (□), the level of internal strain measured immediately after a quench and that measured after a waiting period of 8 hours differs significantly. This indicates a relaxation process at room temperature that is time dependent, suggesting a mechanism that is diffusional in nature. Aluminum is at a high enough fraction of its melting point such that diffusion can be considered an important relaxation mechanism at room temperature.

There are a number of TEM studies on PMMC materials in the literature (Vogelsang et al., 1986; Arsenault et al., 1991 and Humphreys, 1988) which report a higher dislocation density in the matrix adjacent to the reinforcing particles. And it is generally considered (Miller and Humphreys, 1991; Arsenault and Shi, 1986; Derby and Walker, 1988; Taya et al., 1991) that this is a result of plastic relaxation of thermal stresses. The contention of some researchers (Arsenault, 1991) is that the increase in the yield strength observed in the composite (as defined by a .2% offset criterion) can be completely accounted for by the dislocation substructure created by plastic relaxation of the thermal stresses. As will be discussed below this ignores the complex nature of flow that develops during the elastic/plastic transition between the proportional limit and the .2% proof stress.

Most of the theories for strengthening based on a dislocation substructure have centred around calculating a dislocation density ρ. This is based on the relief of the shape misfit created by the differences in CTE;

$$\text{misfit} \approx (\alpha_{Al}-\alpha_{SiC})\Delta T \tag{1.2}$$

where α_{Al} and α_{SiC} are the CTE values of the Al matrix and the SiC particle respectively and ΔT is the quenching magnitude. Expressions for strengthening based on CTE mismatch have been derived for dispersion hardened materials (see Ansell, 1968) and more recently for MMC's (Miller and Humphreys, 1991; Arsenault and Shi, 1986; Derby and Walker, 1988; Taya et al., 1991). These models vary in their complexity but all contain one essential feature: The degree of strengthening is proportional to the volume fraction but inversely proportional to the particle size. In other words, these theories are scale dependent. One of the simplest expressions for the strengthening effect is due to Humphreys et al.;

$$\Delta\sigma = \alpha G b \rho^{1/2} \tag{1.3}$$

where $\Delta\sigma$ is the increase in strengthening, α is a constant between .5 and 1, b is the Burger's vector and G is the shear modulus. The dislocation density is expressed as;

$$\rho = 12\Delta T(\alpha_{Al}-\alpha_{SiC})V_p/bd \qquad (1.4)$$

where V_p is the volume fraction of particles and d is the particle size. (The particle shape is assumed to be equiaxed such that only one dimension is needed to define its size). One would expect that a similar relation could be developed that contained aspect ratio. As Humphreys points out, this equation assumes that the dislocations are uniformly distributed such that they represent a forest hardening component and that all the internal stress is relieved by plastic flow. Inputting some typical PMMC values for V_p,d and ΔT of .2, 10μm and 500° C respectively gives an increase in strength of between 10 and 20 MPa. A more complicated model by Taya et al. (1991) gives a value of 30 MPa. This value is not very large considering that it likely represents an upper bound. The previous discussion suggests that, contrary to the assumptions made in the model, a portion of the residual stress is relieved by diffusional processes. In addition neutron and x-ray diffraction experiments indicate that not all of the internal stress is relieved.

The assumption of a uniform distribution of dislocations throughout the matrix also remains problematic. The distribution and density of dislocations are difficult to measure experimentally and there are only a few studies in the literature that have attempted these measurements. Work by Vogelsang et al. (1986) Arsenault et al. (1991) and Humphreys (1988) and Prangnell and Stobbs (1991) using TEM techniques, indicate that in composites with commercial alloys such as 6061, where the yield stress is high, dislocation densities are highest near the reinforcement but decrease at distances further away from the particle. (There is some evidence (Humphreys, 1988) that this dislocation density is more uniform in commercially pure Al matrices.)

The above arguments indicate that a contribution to strengthening from the development of a dislocation substructure upon quenching seems at best suspect. It is important however to point out the importance of scale. For a large volume fraction of fine particles, particularly in a soft matrix, contributions from thermal substructure may become significant.

1.3.1.4 Orowan Bowing

Lastly, the well known theory of the Orowan bowing mechanism can be considered. Humphreys et al. (1991) present this expression in a simple form, assuming equiaxed particles;

$$\sigma_b = 2Gb/L \tag{1.5}$$

where L is the interparticle spacing and is given by;

$$L = 0.6d(2\pi/V_p)^{1/2} \tag{1.6}$$

The contributions from an Orowan bowing process is only significant for spacings below about 1μm. As Table 1.1 indicates, the spacings encountered in PMMC's are much larger than this. For the volume fraction ranges usually of interest in PMMC's particle sizes of .1 to .5μm would have to be incorporated in the metal matrix to give interparticle spacings below 1μm. Therefore the Orowan mechanism is likely negligible as a strengthening mechanism in PMMC's.

Summary. The above discussion points out that predicting the yield strength of PMMC's composite with accuracy is a difficult task. This is primarily due to the various contributions that must be accounted for, some of which may decrease the apparent yield strength (e.g. internal thermal stress), others of which would increase it (e.g. plastic relaxation). Most of the models presented for the yield strength of two phase materials are scale dependent. This indicates that the yield strength increase in PMMC's may be substantially lower than that found in DSH alloys. In particular the Orowan bypassing stress is large for a dispersion of fine particles such as that

found in Cu-BeO alloys (particle sizes $\approx .01\ \mu m$) but minimal for PMMC's with particles sizes 1000 times larger.

1.3.2 Strain Hardening Processes in PMMC's

Most of the understanding of strengthening due to a hard second phase during plastic flow, has been centred on the interpretation of the mechanisms that give rise to an increased strain hardening rate. This has primarily been done using single crystal matrices (see Ashby, 1968 for a review of the experimental work). In this way, the complicating effects of polycrystal deformation can be avoided. Studies using polycrystals have also been successful (Moan and Embury, 1979; Wilson and Konnan, 1964; Bate, Roberts and Wilson, 1981).

As has been pointed out (Brown, 1976), the basic aspects of low temperature work hardening in two phase materials is very well understood at least in outline. The general behaviour in two phase single crystals is characterized by a linear strain hardening rate at low strains followed by a reduced hardening rate that is approximately parabolic in nature. The basic ideas that lead to an understanding of these features will be described below.

1.3.2.1 Back Stress Model-Linear Hardening

There is considerable experimental evidence (Ashby, 1968) that the σ-ϵ behaviour of two phase single crystal materials, such as dispersion hardened and age hardened alloys, is characterized by a high linear hardening rate at low strains up to 2 or 3%. This hardening rate is considerably larger than that of the crystals the second phase is dispersed in, reaching values up to 50 times that of pure single crystals. There is also some evidence of an approximately linear hardening stage in polycrystalline two phase materials such as Cu-W (Kelly and MacMillan,

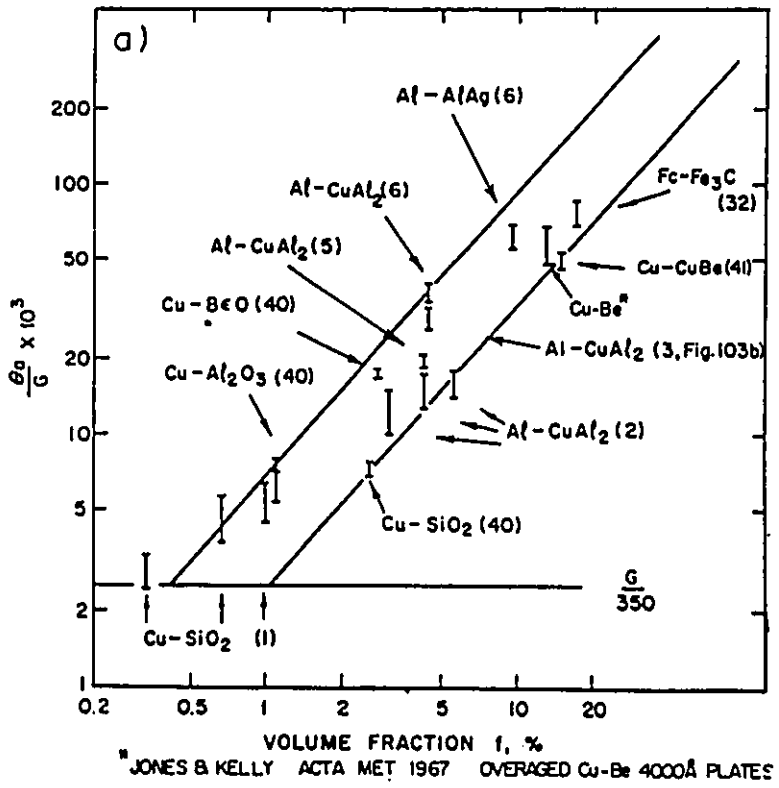

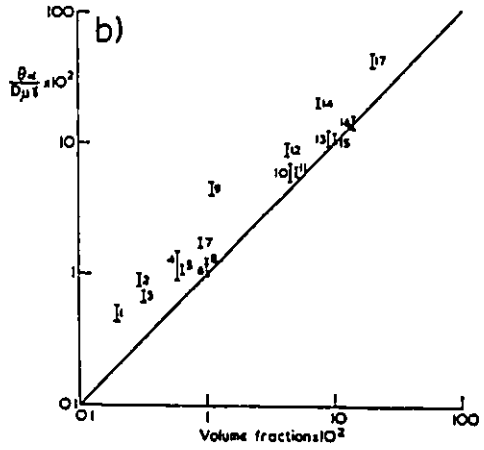

Figure 1.3: Hardening rate versus volume fraction for a variety of two phase materials; a) from Ashby (1968); b) from Brown and Clarke (1975).

1986) and Al-Cu (Moan and Embury, 1979). A survey of hardening by Ashby (1968) and later by Brown and Clarke (1975) reveals that the hardening rate in this region depends only on the volume fraction of second phase and not the particle size. Data according to Ashby is reproduced here as Figure 1.3a. The slope of the line indicated, has a value close to one, suggesting a linear dependence of hardening rate on volume fraction. The scatter in the data is at least partly due to the differences in particle shape and degree of elastic inhomogeneity between the particles and matrix in the various systems. With the exception of reference 32, the data of Figure 1.3a is for single crystal matrices. In addition, the particle size varies by as much as a factor of 100 between the various systems.

The modelling approach used by Brown and Stobbs (1971a) and Brown and Clarke (1975) is based on Eshelby's equivalent inclusion method. The details of this method are described in Chapter 4. The basic principle is based on the stress carried by the reinforcement, which exerts a back stress in the matrix. This resists further forward deformation and is termed the mean matrix stress. The model predicts that the mean matrix stress depends on particle volume fraction and shape and the level of plastic strain. The result due to Brown and Clarke, gives;

$$<\sigma>_m = 2\gamma' D \mu_m f \epsilon_p \qquad (1.7)$$

where γ' is a particle shape factor, μ_m is the shear modulus of the matrix, f is the volume fraction of particles, ϵ_p the plastic strain and D is given by;

$$D = \frac{\mu_p}{\mu_p - \gamma'(\mu_p - \mu_m)} \qquad (1.8)$$

where μ_p is the shear modulus of the particle. If Equation (1.7) was differentiated to obtain the hardening rate, it would contain the linear relationship with f as required, where the slope is determined also by $\gamma' D \mu_m$ which contains the particle shape and elastic inhomogeneity

dependence. The results of this model and its comparison with experiment is shown in Figure 1.3b. Note that the data is normalized by D and μ_m in order to compare the hardening rates for the wide range of particle/matrix systems plotted. This method of comparing the data reduces the scatter and further supports the linear dependence on particle volume fraction.

While this model describes behaviour at low strains, it overestimates the hardening rate at higher strains. It is generally accepted (Brown and Stobbs, 1971b; Humphreys, 1980; Ashby, 1971) that this occurs due to alternative processes which relax the large internal stresses that rapidly develop in the first few % of strain. At low temperatures the possible mechanisms for this range from plastic flow in the matrix to particle flow and/or fracture. For strong elastic particles the primary mechanism of interest is plastic flow in the matrix adjacent to the particles.

1.3.2.2. Plastic Relaxation Model- Parabolic Hardening

While the mechanism of plastic relaxation is generally accepted, there has been some controversy surrounding a quantitative description of the process (Brown, 1976; Humphreys, 1980.). One of the more generally accepted theories is that due to Ashby (1971) which is based on the generation of secondary dislocations around a non-deforming particle. The principal result of this model is that the stress is related to the strain such that;

$$\tau \simeq \sqrt{\frac{fb\gamma}{2r}} \qquad (1.9)$$

where f and 2r are the volume fraction and diameter of the particle, b is the Burgers vector and γ is the shear strain. This particular equation was derived for spherical particles. Similar equations have been derived by Ashby for plate-like shapes. The key feature of this theory is that, in addition to a dependence on volume fraction and particle shape, hardening also depends on the

scale or size of the particles. Comparison between experiment and theory is shown in Figure 1.4 for a Cu-BeO system deformed at liquid nitrogen. The data is taken at a shear strain of 10%.

Ashby has further defined the slip distance λ for equiaxed particles as;

$$\lambda = r/f \tag{1.10}$$

which was derived using an approximate expression for the dislocation density produced by plastic relaxation around the second phase particle. It is therefore an approximate measure of the scale of the second phase microstructure. The degree of dislocation generation as a result of the presence of the second phase, is inversely proportional to the slip distance. The smaller the slip distance, the larger the dislocation density and therefore the larger the contribution to overall hardening. For the Cu-BeO data of Figure 1.4 the volume fraction is low (.02, one tenth that typical for PMMC's). However the particle size is also very small ($\approx .01\mu m$) and the slip distance is, $\lambda = .25\mu m$. Consequently the hardening due to the second phase is large. If it is assumed that the particles in PMMC's are equiaxed and uniformly distributed, the slip distance would be of the order of 50 to 100 μm. As Ashby (1971) states, alloys with spacings of this order should contribute almost nothing to the dislocation density and therefore the hardening rate.

1.3.3 Applicability of the Micromechanics Approach to PMMC's-the Importance of Scale

The above discussion indicates that, with the exception of the back stress model, the primary strengthening mechanisms (i.e. Orowan bowing, thermal dislocation substructure, and secondary dislocation substructure) depends primarily on the scale of the reinforcement as expressed by the spacing. Some approximate calculations have shown that, for the particle sizes and volume fractions typical of PMMC's, it may be expected that these processes do not contribute greatly to the overall strength of the composite. In other words the scale is such that

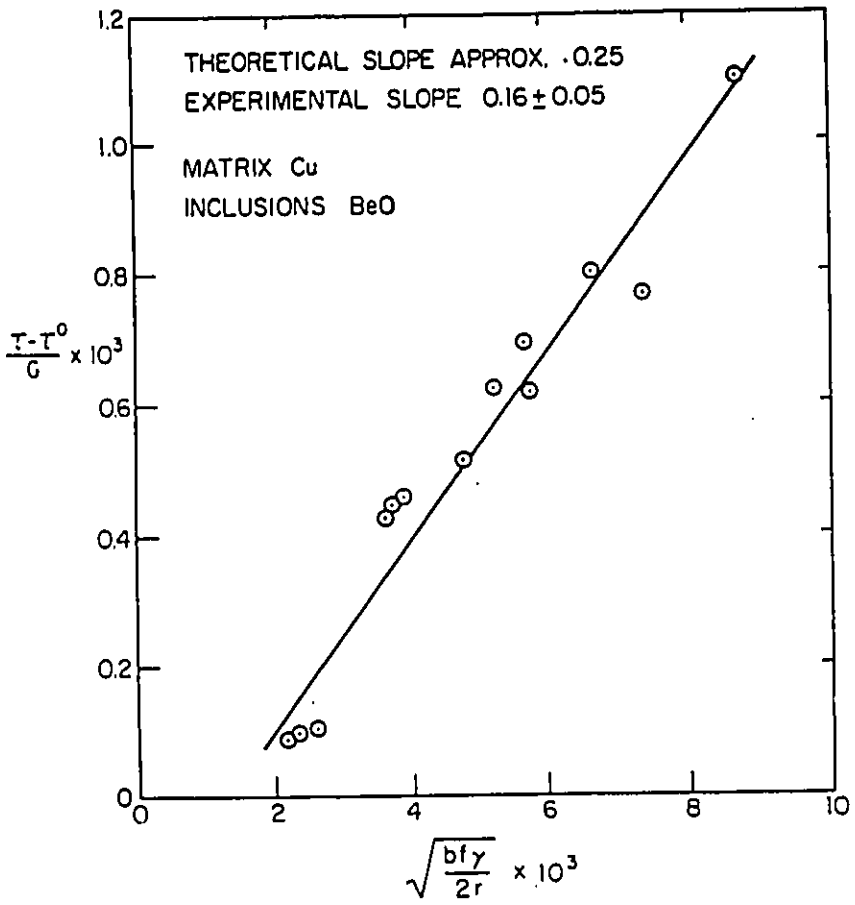

Figure 1.4: Measurement of work hardening at 77 K in Cu single crystals containing roughly equiaxed particles of BeO. (Ashby, 1971)

the composite can be considered on the continuum level and the detailed interaction between the particles and the deformation processes in the metal is rather weak and perhaps negligible.

Chen and Argon (1979) point out that the boundary between micromechanics and continuum mechanics is not clearly defined or agreed upon. However they suggest that deformation around particles of several microns in size can be considered by continuum methods. Goods and Brown (1979) have suggested that the rate of the storage of dislocations in a two phase alloy is dependent on the particle size. In particular, they derive an expression for a critical particle size, below which the interaction between dislocations and the particle is high enough for the substructure that develops to make a major contribution to the local flow stress. Above this size, the strain hardening rate around the particle is approximately equal to that of the matrix and therefore continuum mechanics can be applied. (Their expression was derived for a particle embedded in a single crystal and therefore is not strictly applicable to the case of polycrystals). Their expression is;

$$r_c \simeq \frac{\alpha^2 \mu_m^2 b}{\sigma_y} \left(\frac{d\sigma}{d\epsilon} \right)^{-1} \qquad (1.11)$$

where r_c is the critical particle radius. Values of work hardening ($d\sigma/d\epsilon$) and yield strength (σ_y) typical of single crystals give diameters of about 2 to 4 μm. This is slightly below that typically found in PMMC's. Therefore it may be expected that explanations based on continuum mechanics may be more appropriate. However the particle size is quite close to r_c and, allowing for the range in particle size and volume fraction indicated in Table 1.1, the validity of micromechanics can not be ruled out.

1.4 Complications Due to the Polycrystalline Nature of PMMC's

As described above, most of the understanding of yielding and work hardening in DSH alloys has been achieved by experimental studies in which the second phase particle size and volume fraction have been systematically varied in single crystal matrices. However, as illustrated in Figure 1.1b, the matrix in PMMC's is polycrystalline and the particles are situated adjacent to the matrix grains rather than finely dispersed within them. Because of this characteristic feature of PMMC's it is important to investigate the differences that arise due to polycrystalline deformation. One important characteristic of polycrystalline deformation is the elastic/plastic transition.

1.4.1 Elastic/Plastic Transition

Because of the very rounded nature of the stress-strain curve in the vicinity of yielding, the actual onset of plastic flow is difficult to determine in polycrystals. At this point, it is useful to define some parameters which can best be described by referring to Figure 1.5. This figure schematically represents an experiment in which a material is incrementally loaded to higher and higher strains until plastic deformation is observed. The proportional limit is generally defined as the highest point at which stress is directly proportional to strain (Dieter, 1986) and is equivalent to curve #4. In some materials, upon complete unloading, the non-linearity resulting from loading beyond the proportional limit is recovered (curve #5) and a hysteresis loop is formed. This is generally described as anelastic behaviour. The proportional limit is consequently difficult to measure and may not be representative of the onset of permanent plastic flow.

The elastic limit is usually defined as the greatest stress a material can withstand without any measurable permanent strain remaining on complete unloading. This value will depend on

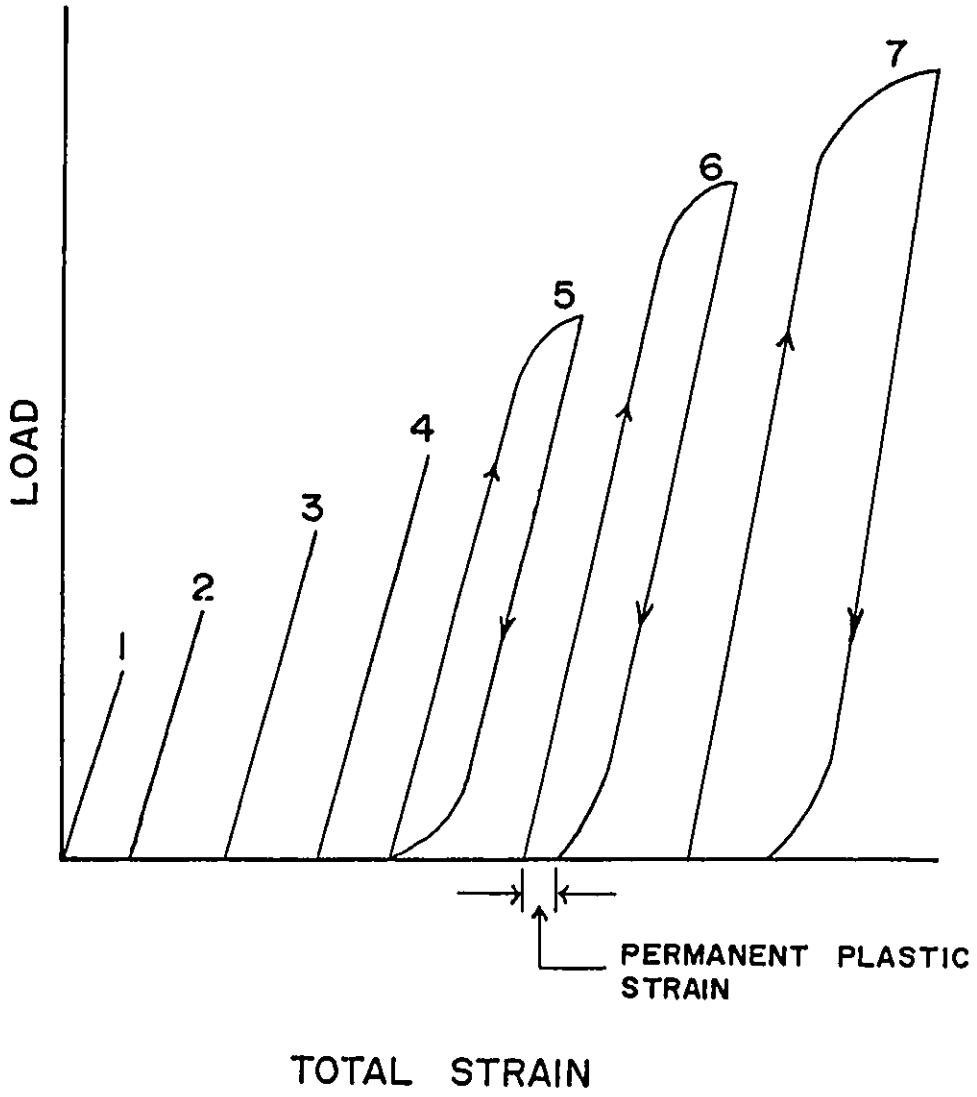

Figure 1.5: Onset of plastic flow in a polycrystalline metal. (Adapted from Dieter (1986)).

the sensitivity of strain measurement used and is represented by curve #5. It will be assumed that the elastic limit can be determined accurately and it will be defined as the yield point.

Once the point of yielding is determined, the stages of strain hardening can be defined. These stages can be described in an idealized way following Mecking (1976) (see Figure 1.6). If the hardening rate (Θ) is plotted versus the stress (σ), the idealized description would indicate that after yielding, the stress-strain curve is linear or that the hardening rate is constant. This is usually referred to as stage II or the pure hardening stage. Both polycrystals and single crystals show deviations from this behaviour at low stresses (low strains) (Mecking, 1976). In the case of polycrystals, the hardening rate is initially very high but decays quickly to the level of stage II. This is primarily thought to occur as a result of an elastic/plastic transition and can be described by referring to Figure 1.7 due to Ashby and Jones (1980). In the case of a polycrystal, individual grains are oriented differently to the applied stress τ. Consequently, slip will be initiated at different points within each grain. This means that some grains will yield first (grain 1). Slip will then progressively spread to other grains (grains 2 and 3) and eventually, the applied stress will be large enough to initiate slip in all grains and the material will begin to deform plastically everywhere.

Many polycrystals of pure metals do not show very distinctive stages of hardening. Figure 1.8 shows Θ versus σ for polycrystals of Cu tested at various temperatures (Mecking, 1976). At all temperatures the elastic/plastic transition is evident. At 77K there appears to be a distinct region of stage II behaviour. (This region is less defined at room temperature). It is clear that all curves show a gradual decrease in hardening rate at larger stresses. This is generally considered to result from softening or recovery processes and is referred to as stage III.

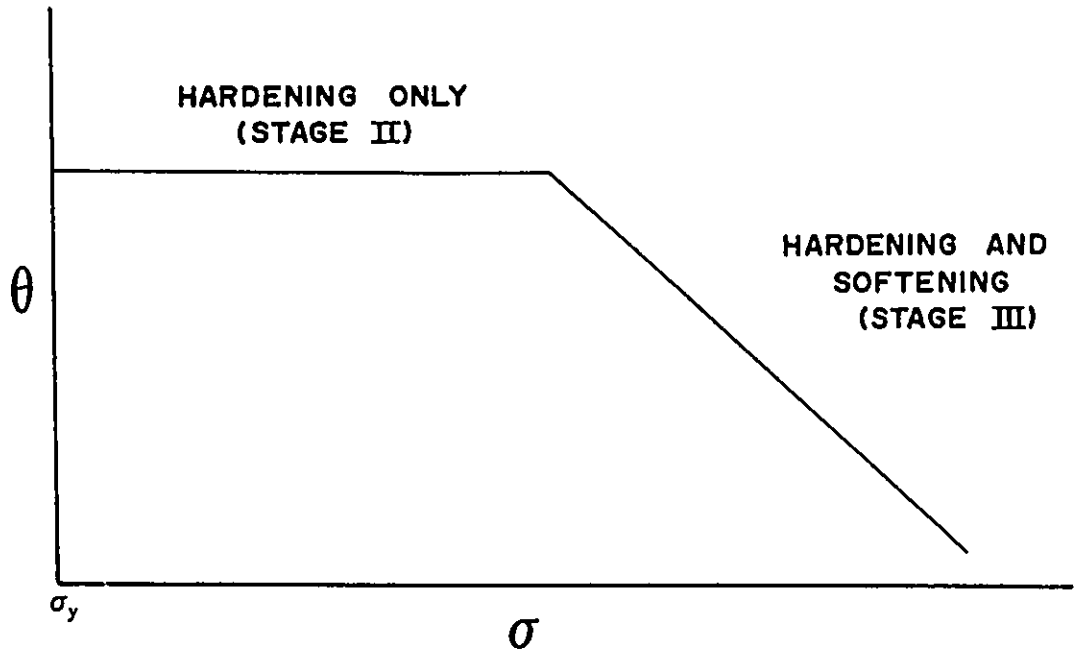

Figure 1.6: Schematic description of the early stages of strain hardening in a polycrystal. (Based on Mecking (1976))

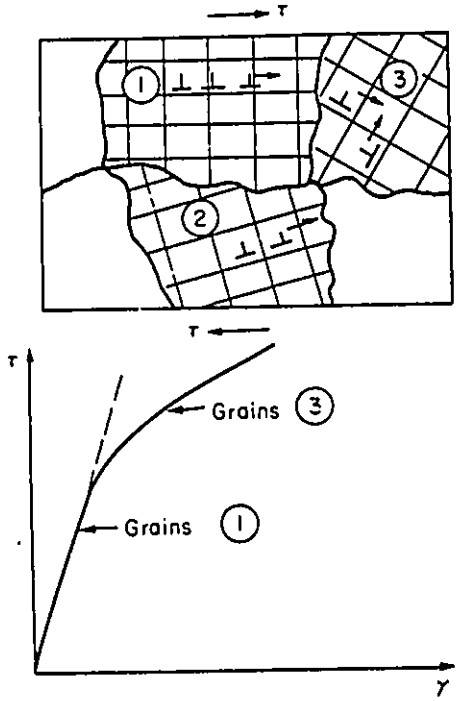

Figure 1.7: The progressive nature of yielding in a polycrystalline material (i.e. the elastic/plastic transition). (Ashby and Jones, 1990)

The region over which the elastic/plastic transition occurs depends on the type of material and temperature. Estimates by Kocks (1987) indicate that at strains of 5 times the elastic strain, the material becomes fully plastic. The relative importance of the elastic/plastic transition depends on the strain regime of interest. If the interest is at larger strains, say above 1 or 2%, then it is often acceptable to incorporate this region into a definition of an offset yield strength.

The difficulty in two phase materials arises due to the strain range over which the hardening effects of the second phase are measurable. If plastic relaxation is difficult, the high hardening rate associated with an unrelaxed back stress will be interpretable in a region beyond the transition. However if relaxation is relatively easy the hardening effects of the particle may be greatly diminished once the elastic/plastic transition is over. This is especially true for largely spaced particles where the plastic relaxation process should not contribute greatly to overall hardening.

Interpretation of hardening on the basis of the back stress model such as that of Brown and Clarke (1975) have been successful for some polyscrystalline materials (Moan and Embury, 1979 (Al-Cu); Kelly and MacMillan, 1986 (Cu-W)). In both cases the geometry of the reinforcement is such that relaxation is relatively difficult. An example of the stress-strain curves in the case of Al-Cu are shown in Figure 1.9. It is clear that both the solid solution and aged material exhibit an elastic/plastic transition. When the material is aged, it forms needle like precipitates (Θ'). Deformation around these particles give rise to the back stress and increases the hardening rate in comparison to the solid solution state. The aspect ratio of these particles is fairly large and relaxation is relatively difficult. The figure indicates that the hardening effect of the particles is evident beyond the transition. Comparisons of the hardening rate in the aged material at strains of 1% reveal good agreement with the theory of Brown and Clarke.

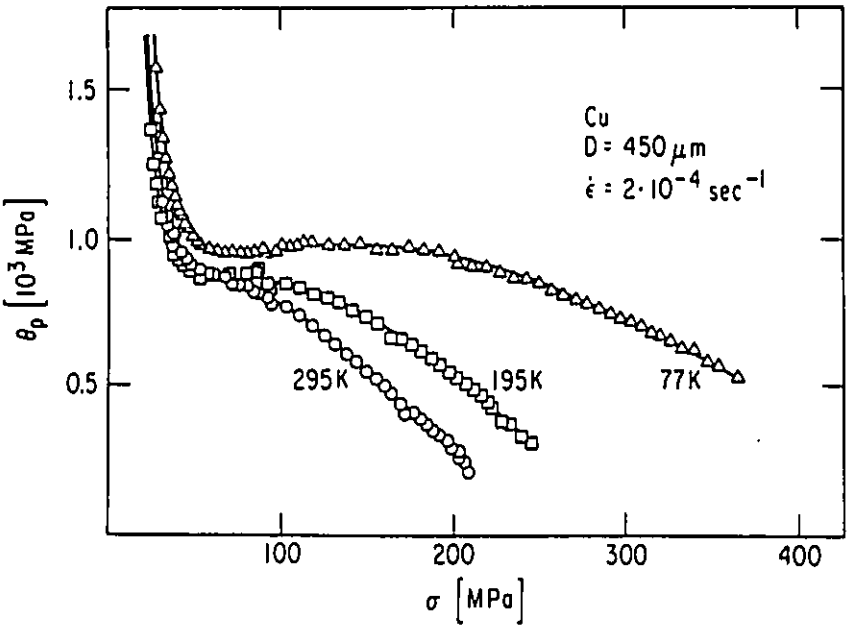

Figure 1.8: Hardening rate versus stress for Cu polycrystals at various test temperatures (Mecking, 1976).

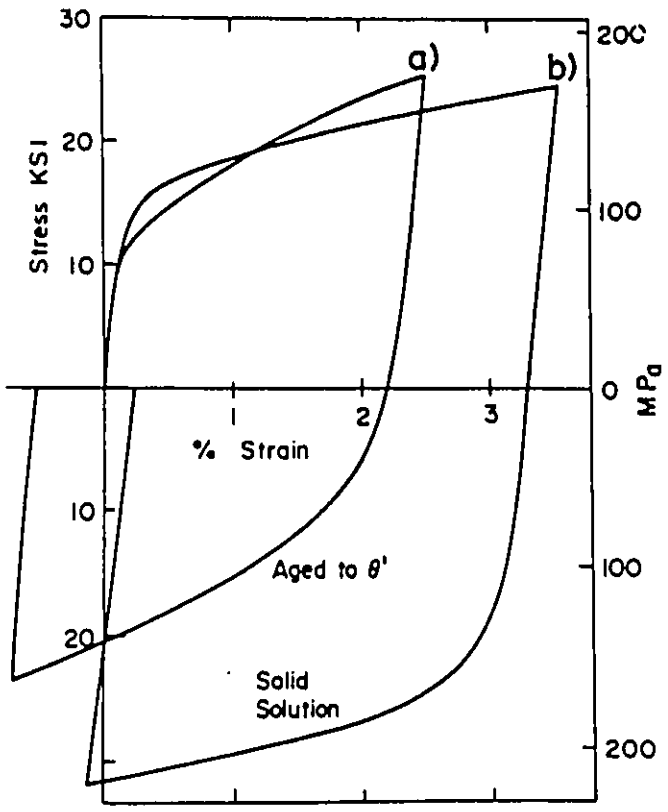

Figure 1.9: Comparison of stress-strain curves for polyscrystalline Al-Cu alloy at 25 C; a) aged to θ' b) solid solution (Moan and Embury, 1979)

1.4.2 The Onset of Plastic Relaxation

It is important to try and understand the issues involved in the relaxation of the back stress in two phase materials and to what degree this process may occur in PMMC's. As stated above, there is some controversy surrounding the mechanisms responsible for plastic relaxation around a particle. Processes that have been proposed are; 1) the formation of primary prismatic loops; 2) nucleation of secondary dislocation arrays and 3) lattice rotations in the matrix surrounding the particles.

It is generally accepted that these processes are dependent both on particle size and the level of plastic strain. These concepts are summarized elegantly by Humphreys (1980) as shown in Figure 1.10. In constructing this picture, it was assumed that the second phase was equiaxed, embedded in a single crystal whose elastic constants are similar to the particle, and does not undergo fracture.

The formation of Orowan loops as a result of a dislocation bowing around the particle (the source of the back stress hardening) can be relaxed by the three processes mentioned above. Which processes occur, depends on the particle size and level of strain. For fine particles ($< .05$ μm) relaxation is rather difficult and may not occur until strains of up to 5 or 10%. For larger equiaxed particles ($> .5$ μm) relaxation is relatively easy, occurring at low strains ($\approx 1\%$) and primarily in the form of secondary dislocations. For the levels of strain of interest here (i.e. below 10%) the mechanisms of interest are the generation of primary loops and secondary dislocations.

Direct applicability of Humphreys description, which has been primarily developed for single crystal DSH alloys, to PMMC's has not been very extensively investigated. One complicating factor arises due to the polycrystalline nature of PMMC's. In this case the particles

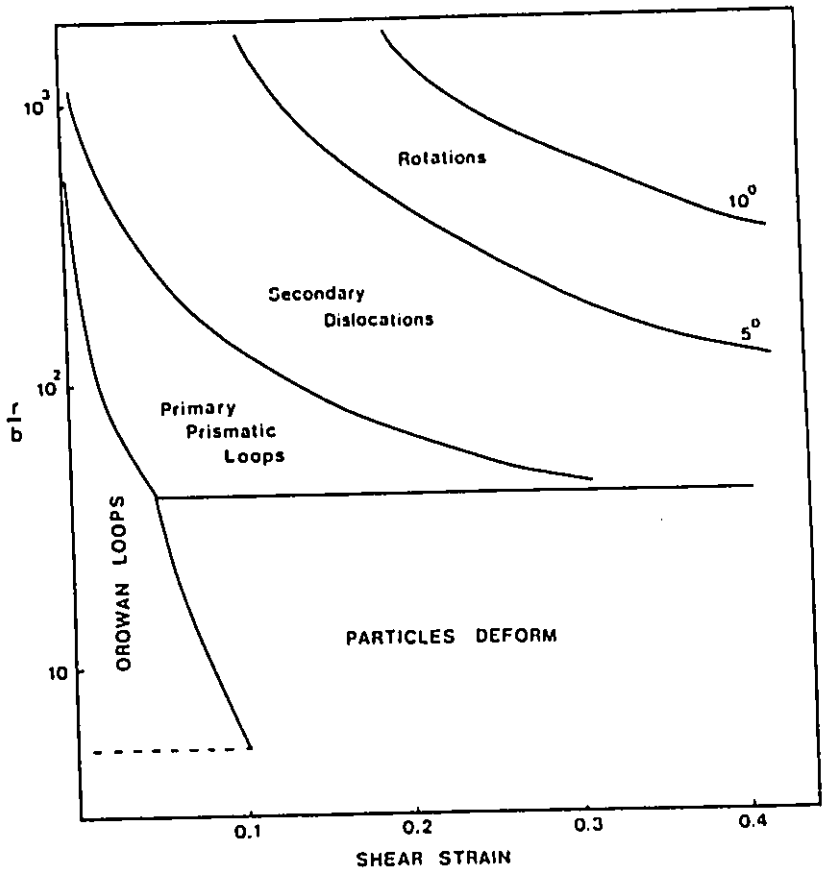

Figure 1.10: Possible relaxation mechanisms in DSH alloys as a function of second phase particle size and level of plastic strain. (Humphreys, 1980)

lie adjacent to the matrix grains rather than in their interior. This, together with the relatively complex multiple slip deformation, makes it difficult to envision a simple array of Orowan loops developing around the particles. Therefore, the formation of primary prismatic loops which are thought to result from cross slip of the Orowan loops (Humphreys, 1980), seems unlikely. Even without this restriction, the description of Figure 1.10 would indicate that for particle sizes encountered in PMMC's, processes involving the nucleation of secondary dislocations should dominate.

In principle, the theory of secondary dislocations derived by Ashby (1971), does not rely directly on an arrangement of Orowan loops around a particle. The density of secondary dislocations can be directly related to any non-homogeneous plastic flow which creates gradients in plastic deformation. In the case of two phase alloys, this results from the incompatibility of the elastic deformation of the particle and the plastic deformation of the matrix. Ashby's development which leads to equation 1.9 considers the particular geometry of a particle embedded in a matrix.

A critical aspect of this theory is the necessity of nucleating a dislocation with a secondary Burgers vector. In the case of an elastic inclusion in a plastic crystal it is thought that this occurs at the particle/matrix interface (Ashby, 1971) (assuming no other sources of dislocation with the proper Burgers vector are available in the matrix near the particle). A number of studies have been initiated to described this process (Weatherly, 1968; Brown et al., 1968; Ashby et al., 1969). For an incoherent interface (which is the case for PMMC's), Ashby estimates that the nucleation process requires the generation of relatively low internal stresses ($\approx \mu/100$) and decreases as the particles become larger.

The assumption that no other source of dislocations exists may be valid for a dispersion

of fine particles in a single crystal. However, for large particles embedded in a polycrystal the presence of grain boundaries and other complicating microstructural features, such as precipitates, may represent possible sources of dislocation motion. In the limit, if this relaxation process is considered on the continuum level it can be stated that plastic relaxation will occur adjacent to the particles when the internal stress reaches the local yield stress, which can be represented by the bulk yield stress of the unreinforced alloy.

By all accounts it can be stated that plastic relaxation of the back stress in PMMC's with approximately equiaxed particles is likely to be easy and occur at relatively low levels of plastic strain. This suggests the possibility that relaxation of a large portion of the back stress may occur during the elastic/plastic transition, making it difficult to interpret hardening on the basis of a back stress model such as that of Brown and Clarke (1975).

1.5 Continuum Mechanics Approach-Stress Partitioning

The discussion of section 1.3, suggests that the scale of reinforcement in PMMC's is such that the elastic/plastic deformation of these materials may be described by the methods of continuum mechanics. It is therefore of value to present a brief description of these methods as they apply to two phase materials.

1.5.1 Elasticity

The principal goal of most models based on continuum composite mechanics is to predict the partitioning of stress and or strain between two macroscopic phases under an applied load;

$$\sigma_c = \sigma_f V_f + \sigma_m V_m \tag{1.12}$$

$$\epsilon_c = \epsilon_f V_f + \epsilon_m V_m \tag{1.13}$$

or

$$\frac{\sigma_c}{\epsilon_c} = E_c = \frac{\sigma_f V_f + \sigma_m V_m}{\epsilon_f V_f + \epsilon_m V_m} \qquad (1.14)$$

The partitioning itself is dependent on the properties of the two phases and their volume fractions, but also on their geometric arrangement within the composite (i.e. aspect ratio of reinforcement). If the stresses and strains in the two phases can be determined, then equation (1.14) can be solved to determine the overall stress-strain relation for the composite.

Traditionally the first step in the process is to determine the upper and lower bound solutions for the elastic modulus. This is normally done using the Voigt (upper) and Reuss (lower) approximations for which the reinforcement geometry is illustrated in Figure 1.11 . In this case it is assumed that the strains are the same in both phases and equal to the applied strain, ϵ_c (i.e. only the stress is partitioned). Thus, equation 1.14 can be simplified to;

$$\sigma_c = (E_f V_f + E_m V_m)\epsilon_c \qquad (1.15)$$

or;

$$E_c = E_f V_f + E_m V_m \qquad (1.16)$$

In the lower bound case (Figure 1.11b) it is assumed that the stresses in the two phases are the same and equal to the applied stress, σ_c (i.e. only strain is partitioned). Thus, equation 1.14 can be solved to give;

$$\sigma_c = (V_f/E_f + V_m/E_m)^{-1}\epsilon_c \qquad (1.17)$$

or;

$$1/E_c = V_f/E_f + V_m/E_m \qquad (1.18)$$

These two bounds lie quite far apart and are not adequate when accurate results are required for reinforcement geometries between those depicted in Figure 1.11. (e.g. short fibres

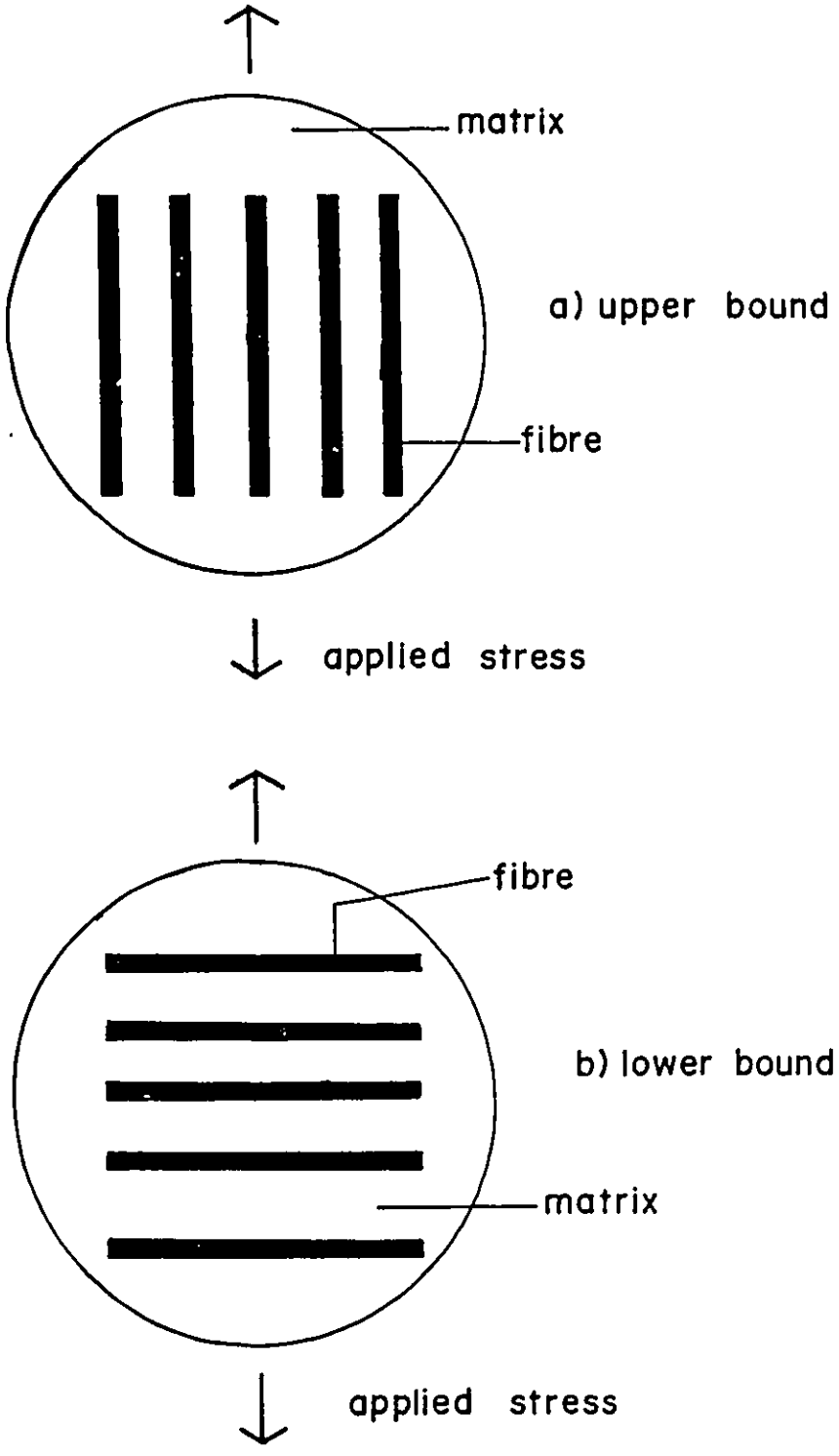

Figure 1.11: Definition of the upper (Voigt) and lower (Reuss) bound geometries for composite materials.

or particles). However some basic ideas can be extracted from the two results.

Considering the case of $E_f > E_m$, the following observations can be made regarding the intermediate state;

1) Neither the stresses or strains in the two phases will be equal (i.e. there will be both stress and strain partitioning).

2) As we move from the lower to upper bound we change from a situation in which $\sigma_f = \sigma_m$ to one in which $\sigma_f >> \sigma_m$.

3) and a situation in which $\epsilon_f << \epsilon_m$ to one in which $\epsilon_m = \epsilon_f$.

Many important two phase materials have geometries which do lie between the Voigt and Reuss bounds and it is important to be able to predict behaviour in this regime. There are a number of both analytical and numerical solutions for the elasticity of composites with these geometries, all of which vary in their complexity. Perhaps one of the simplest is based on the so called shear lag model first proposed by Cox (1952). This analysis centres on the transfer of tensile stress from the matrix to fibre by means of shear stresses operative at the interface between the two phases. A somewhat more complex technique is due to Eshelby's inclusion method, introduced in the last section. The elastic solution using this technique will be developed in chapter 4.

A certain amount of equivalency between the various modelling methods may exist. For example, a recent attempt of modifying the shear lag analysis to include fibre end loading (Clyne, 1989) shows reasonable agreement with Eshelby's method in predicting elastic properties of short fibre composites.

1.5.2 Plasticity

Predicting plastic behaviour is much more complicated and usually involves a number of simplifying assumptions. An understanding of plasticity, especially for composites that have geometries between the upper and lower bounds, is not as well developed as that for elasticity. During this discussion, we will restrict ourselves to the situation in which the reinforcing phase remains elastic while the matrix becomes plastic.

The critical questions are;

1) How does stress or strain partitioning occur? In particular, to what degree is the reinforcement loaded elastically as a result of plastic flow in the matrix.

2) Does the presence of the hard second phase alter the nature of plastic deformation in the matrix? In particular is the work hardening process in the matrix altered? One of the features of continuum mechanics is the assumption that the scale of the reinforcement is such that the deformation of the matrix is unaltered. The validity of this approximation was discussed in section 1.3.

The simplest case to treat is that of the upper bound, in which the rule of mixtures is applied such that;

$$E_{uc}=E_f V_f+\left(\frac{d\sigma}{d\epsilon}\right)_m V_m \qquad (1.19)$$

where E_{uc} is the slope of the composite curve in the plastic regime and E_m is replaced by the strain hardening rate in the matrix $(d\sigma/d\epsilon)_m$. This situation is depicted in Figure 1.12. To simplify the problem the lateral constraints that the fibres can place on the matrix have not been included in this expression (for a treatment of this see Kelly, 1971).

If it is assumed that the matrix is a perfectly plastic material or that $E_f >> (d\sigma/d\epsilon)_m$ then

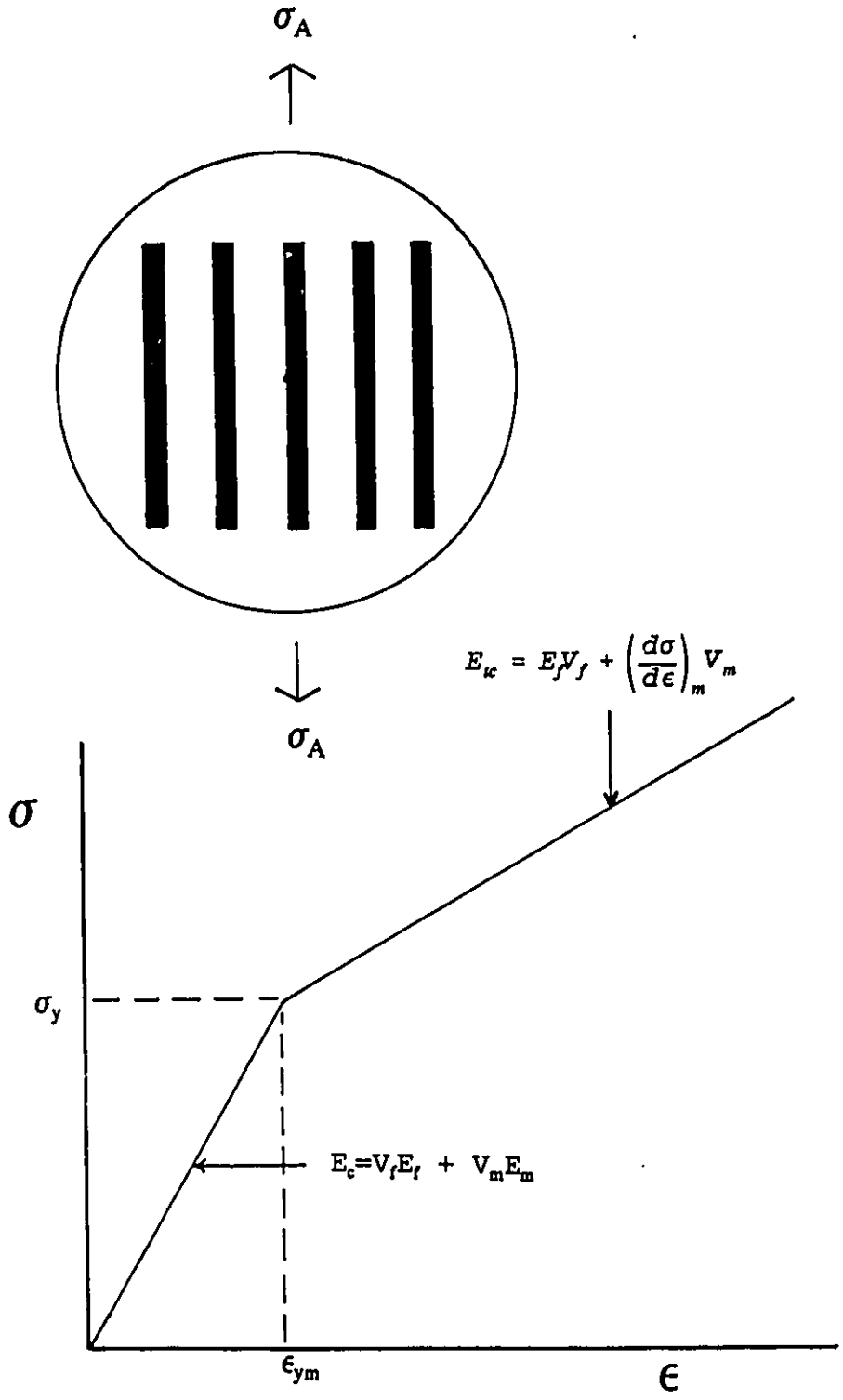

Figure 1.12: Stress-strain curve for upper geometry in Elastic and Plastic regime.

the slope of the composite stress-strain curve is approximately equal to $E_f V_f$ and is entirely due to elastic loading of the fibre during plastic flow of the matrix. Since $\epsilon_c = \epsilon_f$ we can state that the degree of stress partitioned to the fibre during plastic flow, $\Delta\sigma_{fp}$ is equal to;

$$\Delta\sigma_{fp} = E_f \epsilon_p \tag{1.20}$$

and the contribution to the stress of the composite is;

$$\Delta\sigma_{fcp} = E_f V_f \epsilon_p \tag{1.21}$$

In the lower bound case the assumption made is that the stresses in the particle and matrix are equal, i.e. no stress partitioning occurs. Therefore, for composites that lie between the bounds, stress partitioning during plastic flow should occur such that the stress transferred to the particles is between $E_f \epsilon_p$ and zero. A development of stress partitioning for equiaxed particle geometries will be described in chapter 4. It will make use of the ideas of continuum mechanics and incorporate Eshelby's equivalent inclusion method.

1.6 The Bauschinger Effect

The discussion of section 1.4, reveals that a number of contributions to the flow stress of a two phase alloy can exist. If it is assumed that these components add linearly, the flow stress can be expressed in simple terms as;

$$\sigma_f = \sigma_o + \langle\sigma\rangle_m + \sigma_w \tag{1.22}$$

where σ_f is the flow stress, σ_o is the initial yield stress, $\langle\sigma\rangle_m$ is the mean matrix stress and σ_w is the contribution from the work hardening processes in the matrix. Delineating the relative contributions from each mechanism would be of great value, but a difficult task based on the information available from a tensile test only. This delineation can be done qualitatively and in some case quantitatively by performing Bauschinger experiments.

The Bauschinger effect is simply the observation that, after forward deformation, reversing the strain path results in a decreased flow stress. The ways in which the Bauschinger effect can be characterized is best done by referring to the schematic representation of Figure 1.13. A material is stressed in the forward direction (which may be either tensile or compressive) beyond the point of yielding σ_o, to a flow stress of σ_f. If the material were unloaded to the point A and immediately reloaded in the forward direction it should follow the path indicated by the line segment ATS. If no Bauschinger effect was present, unloading and then reloading in the reverse direction would result in the curve indicated by points A, B and C where σ_r' would be equal in magnitude to σ_f. In the presence of a Bauschinger effect the reverse yield stress $\sigma_r < \sigma_f$ (point D). In general the subsequent deformation is rounded in nature but may reach a stage in which the flow curve is parallel to that in the forward direction. The permanent offset ($\Delta\sigma$) is generally termed "permanent softening". The flow stress difference during the rounded portion is often termed "transient softening". Many materials exhibit varying degrees of both permanent and transient softening. Consequently, complete descriptions of the Bauschinger effect have been based on both concepts. Two common parameters which characterize the transient softening regime are the Bauschinger strain (ϵ_B) and the back stress (σ_b) (Abel, 1987). The Bauschinger strain ϵ_B, is the amount of reverse plastic strain at which the reverse stress is equal to some fraction (usually between .5 and .75) of the forward stress, σ_f (see Figure 1.13). The Bauschinger stress σ_b (also referred to as the back stress) is equal to $(\sigma_f-\sigma_r)/2$, where σ_r is the reverse yield strength determined at some offset strain value (usually between 0 and .1% reverse strain).

1.6.1 Permanent Softening

One approach to a physical understanding of permanent softening for two phase materials

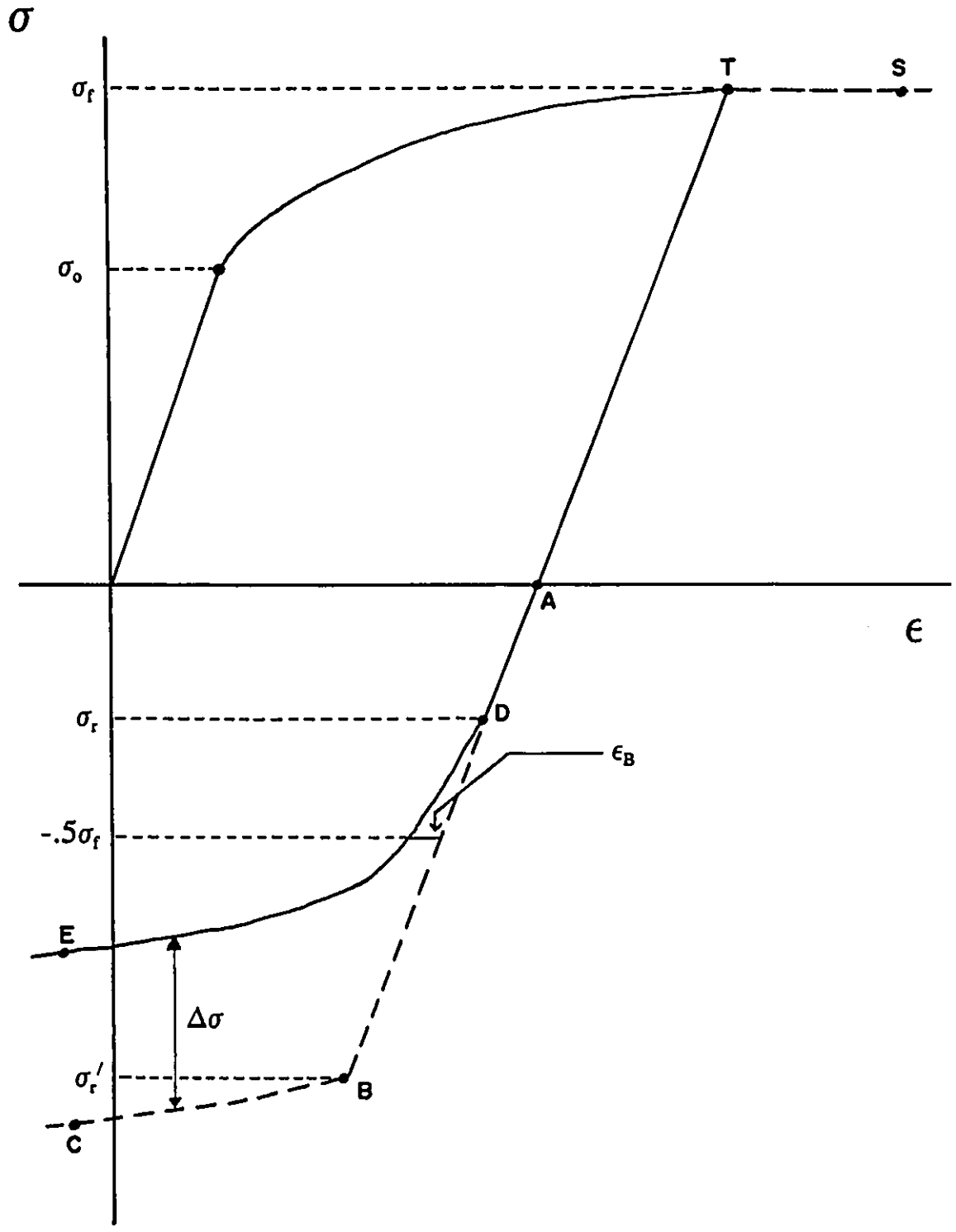

Figure 1.13: Schematic representation of the Bauschinger effect.

has been described by Kelly and Macmillan (1986). They consider a model system consisting of continuous, elastic fibres all aligned parallel to the load direction, situated in an elastic/perfectly plastic matrix. The matrix is assumed to have no Bauschinger effect associated with it. The stress-strain behaviour of this material has been described in Section 1.5.2. Permanent softening can be explained by considering what happens if this material is unloaded after a certain amount of plastic strain ϵ_p (Figure 1.14). When the matrix strain (which in this case is equal to the macroscopic strain) is reduced by 2 ϵ_{ym} the matrix will yield in compression. With continued load reversal the stress-strain curve then becomes parallel to the forward flow curve. Consequently, if the reverse curve is transformed into the forward quadrant a permanent offset of $\Delta\sigma$ is obtained. The value of this offset can be calculated by determining the difference between the forward stress σ_f and the reverse yield strength, σ_r.

The forward stress σ_f is equal to;

$$\sigma_f = (E_f V_f + E_m V_m)^* \epsilon_{ym} + E_f V_f \epsilon_p$$

$$= E_c \epsilon_{ym} + E_f V_f \epsilon_p \qquad (1.23)$$

where ϵ_p is the plastic strain. The reverse yield stress σ_r is:

$$\sigma_r = \sigma_f - 2(E_c)\epsilon_{ym}$$

$$= E_f V_f \epsilon_p - E_c \epsilon_{ym} \qquad (1.24)$$

Therefore the value of permanent softening is the difference between (1.23) and the negative of (1.24) or:

$$\Delta\sigma = 2E_f V_f \epsilon_p \qquad (1.25)$$

Comparing this equation with equation (1.21), it can be stated that the permanent softening is twice the elastic stress carried by the fibre as a result of plastic flow. This stress is equivalent to the internal stress in the material and therefore permanent softening in this simple case should be

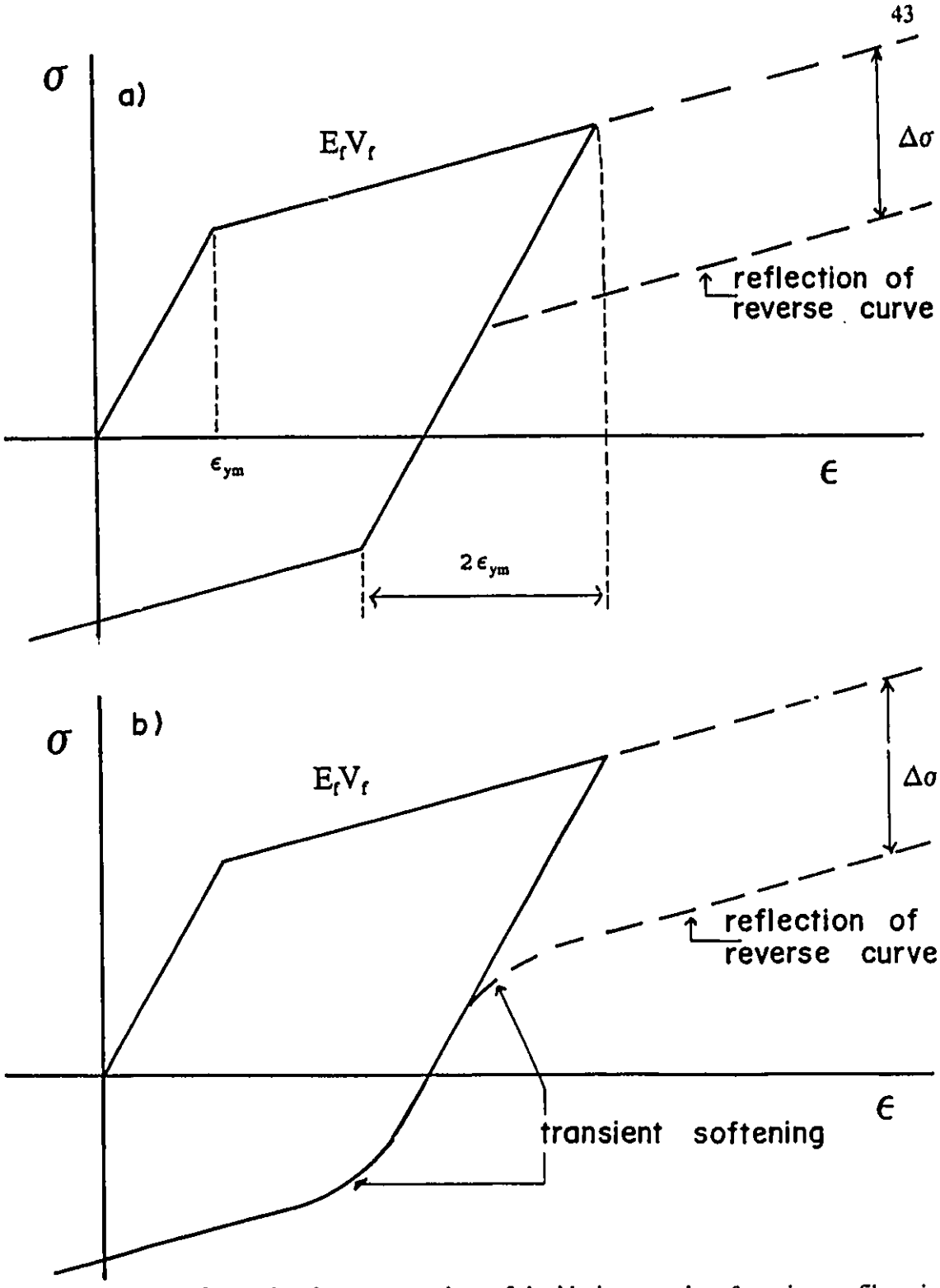

Figure 1.14: a) Forward and reverse portions of the ideal composite of continuous fibres in an elastic/perfectly plastic matrix, b) Including the effects of transient softening.

twice the mean internal stress or mean matrix stress, $<\sigma>_m$ given in equation (1.22).

In principle, this description of permanent softening can apply to any reinforcement geometry including short fibres and spheres. In these cases, the mean internal stress can be calculated using Eshelby's Equivalent Inclusion method (Brown & Stobbs, 1971a; Brown & Clarke, 1975, Withers et al., 1989).

This description of the Bauschinger effect makes three important assumptions;

(1) no transient softening is present,

(2) no relaxation of the mean matrix stress occurs during forward flow, and

(3) the plastic structure around the second phase is stable upon unloading.

This description works well for materials like pure Cu reinforced with continuous fibres of W. In this material, the geometry of the fibres is such that permanent softening is very large and the degree of transient softening that does occur is proportionally much smaller. In addition, plastic relaxation of the mean stress is also relatively difficult, especially at low temperatures and low strains. In other systems, transient softening cannot be neglected.

1.6.2. Transient Softening

One of the earliest descriptions of transient softening is that due to Orowan (1959) who considered an array of second phase obstacles which were inhomogeneously distributed throughout the matrix. In this case, the transient softening arises purely from a statistical sampling of obstacles by dislocations and is not the result of a long range internal stress. A situation can be envisioned where this effect is also accompanied by the presence of a mean matrix stress. Prangnell et al. (1992) point out that, in this case, a determination of permanent softening and therefore the mean matrix stress, can still be achieved by extrapolation from beyond

the transient softening region (Figure 1.14b). This method was used successfully to explain the work hardening behaviour of Cu-SiO_2 (Atkinson et al., 1974). In this case, the transient softening regime was very short and much smaller in magnitude than the observed permanent softening.

An alternative description of transient softening is related to long range internal stress. In particular, it is based on the concept that the internal stress is not uniformly distributed throughout the matrix as assumed by the description of Kelly & Macmillan (1986). The approach was first proposed by Masing (1927) to describe polycrystalline deformation and has been developed more recently by Asaro (1975) and Sowerby et al. (1979).

In this model, the grains of a polycrystal are represented by a number of elastic-perfectly plastic elements (of the same elastic modulus, E) having various yield strengths, σ_1,σ_2...etc. (Figure 1.15a). In the simplest case, these elements are assumed to be connected in parallel, therefore strain is homogeneous throughout the material. Each element is also assumed to have no Bauschinger effect associated with it. The essential features of this model can be related by treating the situation of only two elements, each occupying 50% of the total volume. To further simplify the description the yield strength of element 1, σ_1 has been chosen to be half the yield strength of element 2, σ_2. At a strain of $\epsilon_1=\sigma_1/E$ (point A, Figure 1.15b), element 1 will yield at an overall applied stress of σ_1. The slope of the curve beyond this point is then 1/2E until at an overall stress of $(\sigma_1 + \sigma_2)/2$ and at a strain of $\epsilon_2=\sigma_2/E$ (point B), the second element yields. Since both elements are perfectly plastic, the stress-strain curve will then exhibit no hardening with continued straining. If the material is then unloaded at point C and the strain is reduced elastically by a value of $2\epsilon_1$, element one will then yield in compression (point D). Since both elements remain elastic from point C to point D, the stress is reduced by $\sigma = 2\epsilon_2 E$ or $2\sigma_1$. Therefore at this point, the stress on the second element is σ_2-$2\sigma_1$ and since $\sigma_1=1/2\sigma_2$ the stress

a)

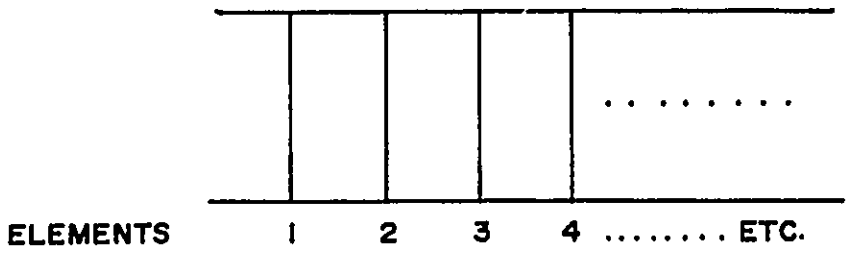

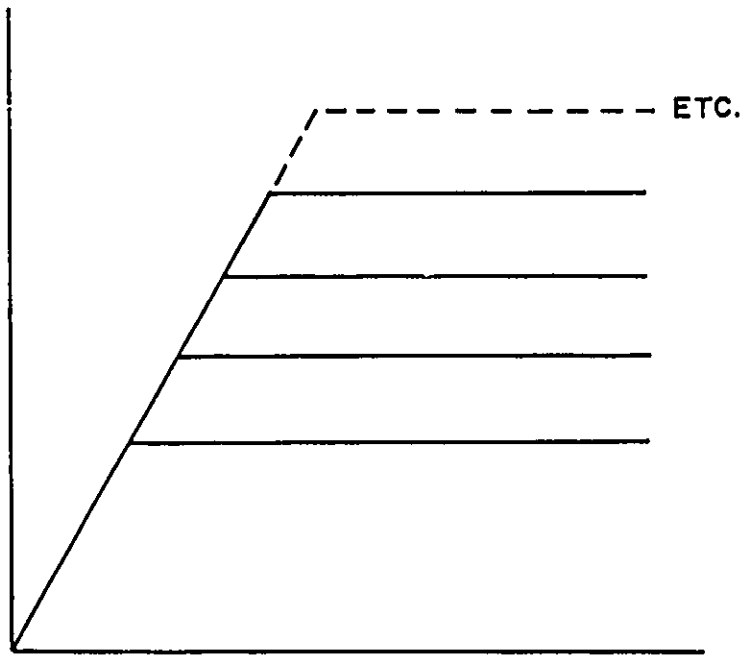

FIG. 1.15 a

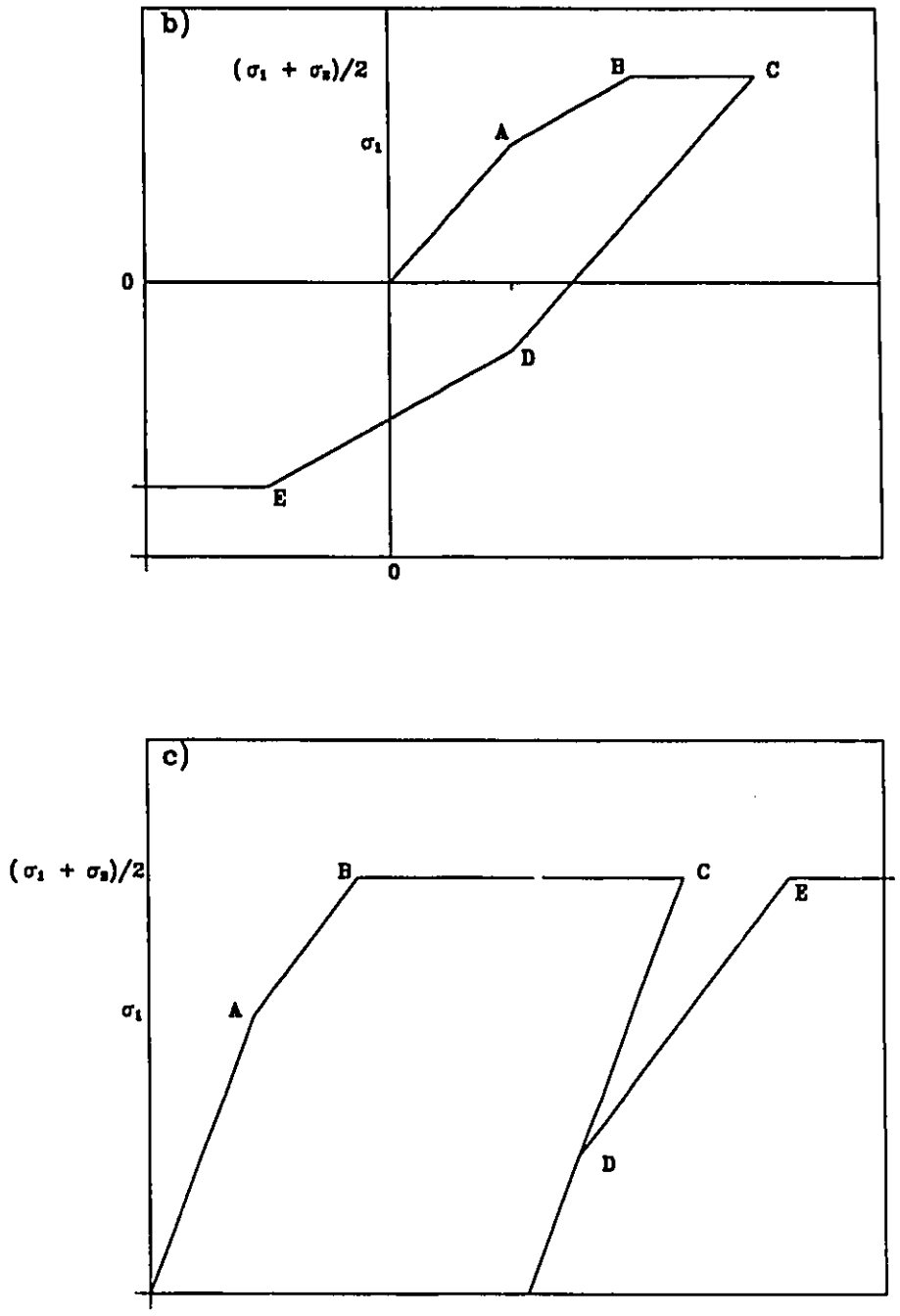

Figure 1.15: Description of the Masing model; a) the elements of the model and their strength; b) the forward and reverse σ-ϵ curves; c) reflection of the reverse curve into the forward quadrant.

on the second element is zero. Therefore an additional reverse strain of ϵ_2 (where $\epsilon_2=\sigma_2/E$) must be applied before element 2 will yield (point E). Further straining will of course show no hardening. If the reverse portion of this curve is transformed into the forward quadrant (Figure 1.15c) then it is clear that a model of this type predicts transient softening but no permanent softening. As pointed out by Sowerby et al. (1979), regardless of the number of elements chosen, two important observations can be made.

(1) The Bauschinger stress $(\sigma_f - \sigma_r)/2$ will always be equal to $(\sigma_f-\sigma_o)$ where σ_o is the yield strength of the first element (in the case above $\sigma_o=\sigma_1$).

(2) Permanent softening is not predicted providing all elements are elastic/perfectly plastic. Therefore the Masing model is widely applicable to any material which exhibits inhomogeneous plastic flow and consequently is not exclusive to two phase materials. The model can be extended to the type of composite materials of interest here by assuming that one element always remains elastic. In this case the possibility of predicting permanent softening exists.

The Masing solid does exhibit strain hardening even though the individual elements themselves do not. This strain hardening is entirely due to elastic loading of the elements that have not yielded during plastic flow of the elements that have yielded. This represents the internal stress and is the origin of the Bauschinger effect. The average stress on the solid at point C is $(\sigma_1 + \sigma_2)/2$ and since $\sigma_1=1/2\sigma_2$ (and therefore $\epsilon_1=1/2\epsilon_2$) the stress in the material will be unloaded to zero after the strain is reduced by $3/2\epsilon_1$. Therefore the internal stress on element 1 is equal to $-\sigma_1/2$ and that on element 2 is equal to $+\sigma_2/4$. In the case of more than two elements, each element would have a different internal stress, the value of which would depend on the number of elements that have yielded and their yield strengths. Therefore the Masing model describes a solid in which the internal stress varies throughout the microstructure and

consequently is non-uniform in nature.

The Masing model and that of Kelly and Macmillan clearly represent two extreme cases. Nevertheless, they provide a useful framework in which the behaviour of real materials may expect to range. While some materials may predominantly exhibit one type of behaviour, both aspects of the Bauschinger effect may be present to one degree or another.

1.6.3. Complications Arising in PMMC's.

The particulate reinforced alloy studied here has a number of features which differ from the simple materials described above. Firstly, the reinforcement is not continuous but is approximately equiaxed in shape. As discussed in Section 1.5.1, this leads to both stress and strain partitioning. Consequently the simplification that the strain is equal in both phases is not valid. Secondly, the matrix is a rather complex alloy which not only exhibits strain hardening (i.e. it cannot be characterized as elastic/perfectly plastic) but is also expected to exhibit a Bauschinger effect as a consequence of its polycrystalline nature and second phase microstructure. The PMMC is then perhaps better described by a Masing solid (unreinforced alloy) reinforced with elastic spheres. However, this also oversimplifies the problem. While the matrix would possess the inhomogeneity of plastic flow described by the Masing model, the grains are not arranged in parallel. Consequently, an accurate quantitative description of the matrix material using the Masing model is not possible.

Because of this dual nature of the composite materials under study here it is expected that they would be characterized both by transient and permanent softening.

1.7 Summary and Conclusions

The scale and arrangement (with respect to matrix grain structure) of second phase particles in PMMC's is very different than that of DSH alloys. Consequently, mechanisms based on dislocation/particle interactions, which give rise to a large degree of strengthening in dispersion hardened alloys, may play only a small role in the strengthening of metal matrix composites.

One mechanism proposed for strengthening in DSH alloys which is important for PMMC materials is the development of an internal stress (mean matrix stress). In this case, strengthening is dependent on volume fraction and particle shape only, and not on particle size. The theory for the mean matrix stress as developed by Brown and Stobbs (1971a) and Brown and Clarke (1975) has a strong connection with continuum mechanics methods. Kelly and Macmillan (1986) (see pages 212-214 and 247-249) have pointed out that the methods of Brown and Stobbs, when applied to an upper bound situation like Cu reinforced with continuous fibres of W, gives very similar results to a simple rule of mixtures based on continuum mechanics (described in section 1.5.2). However, because of the scale and equiaxed shape of particulate MMC's, relaxation processes are relatively easy to initiate. This may limit the applicability of a model based on an unrelaxed internal stress to very low strains and also limit the degree of stress partitioned to the particles during plastic flow. In addition the low strain regime is complicated by the elastic/plastic transition that results due to the complex polycrystalline matrix which the particles reinforce. This further complicates the interpretation of the strengthening that develops at low strains, due to the presence of SiC particles.

The presence of an internal stress as a result of a mismatch in CTE between the particles and matrix also necessitates an investigation of the low strain regime. This internal stress is

present before mechanical testing and therefore will have the greatest influence at the onset of yielding.

In this study, a series of mechanical tests were designed and performed to investigate the low strain behaviour of an aluminium alloy reinforced with various volume fractions of SiC particles. These included;

1) load/unload experiments of the kind described in section 1.4.1 to obtain a definition of yielding;

2) tensile tests in which measurements of the strain hardening rate were made at low plastic strains;

3) comparisons of tensile and compressive behaviour at low strains (up to .01 strain) to characterize the yield asymmetry that may result from the presence of a internal stress of thermal origin and;

4) measurements of the Bauschinger effect to provide qualitative information concerning the development of internal stress (or stress partitioning) at low plastic strains.

Within the context of these experiments the overall magnitude of stress borne by the SiC particles was varied by changing the level of matrix strength. This was accomplished by performing heat treatments which produced various ageing conditions in the matrix.

In addition to these experiments, estimates of the influence of damage accumulation on the flow strength of the composite was performed by measuring the change in elastic modulus of the materials as a function of plastic strain. Finally some conclusions regarding the overall strengthening effect of the particles were made by observing stress-strain behaviour at higher strains (up to 7% strain) and as a function of test temperature.

A model, which is largely based on a continuum mechanics approach, is developed to

describe the elastic/plastic behaviour observed in the composite at low strains. In particular, it estimates the degree of stress partitioned to the SiC particles during the elastic/plastic transition. The model is also used to investigate the role that particle distribution may have on the strain hardening rate of the composite.

CHAPTER 2

EXPERIMENTAL PROCEDURE

2.1 Introduction

The majority of the experimental work performed in this study involved a variety of mechanical tests which were performed to investigate the deformation behaviour of an age hardenable aluminum alloy reinforced with SiC particles. They include, load/unload experiments, tensile and compression tests, Bauschinger experiments, measurements of the elastic modulus as a function of plastic strain and high temperature tensile tests. All these experiments were performed using a servo-hydraulic mechanical test system (MTS) equipped with a high temperature furnace and extensometer.

The characteristics of the reinforcement (i.e. particle size, volume fraction and aspect ratio) were determined by image analysis which was performed by Lloyd (1990). In addition, the precipitate structure produced in the matrix by a variety of ageing steps was characterized for both the unreinforced alloy and composite materials using Transmission Electron Microscopy (TEM).

2.2 Mechanical testing

A schematic of the gripping geometry and furnace set-up for the MTS machine is shown in Figure 2.1. The high temperature extensometer used had a gauge length of 25.4 mm. The extensometer was calibrated using a Mitutoyo dial gauge with a 0-50.8 mm range and a .00508 mm step size (Figure 2.2). For the range setting chosen, an extension of +/- 1 mm corresponds to a voltage of +/- 10 volts.

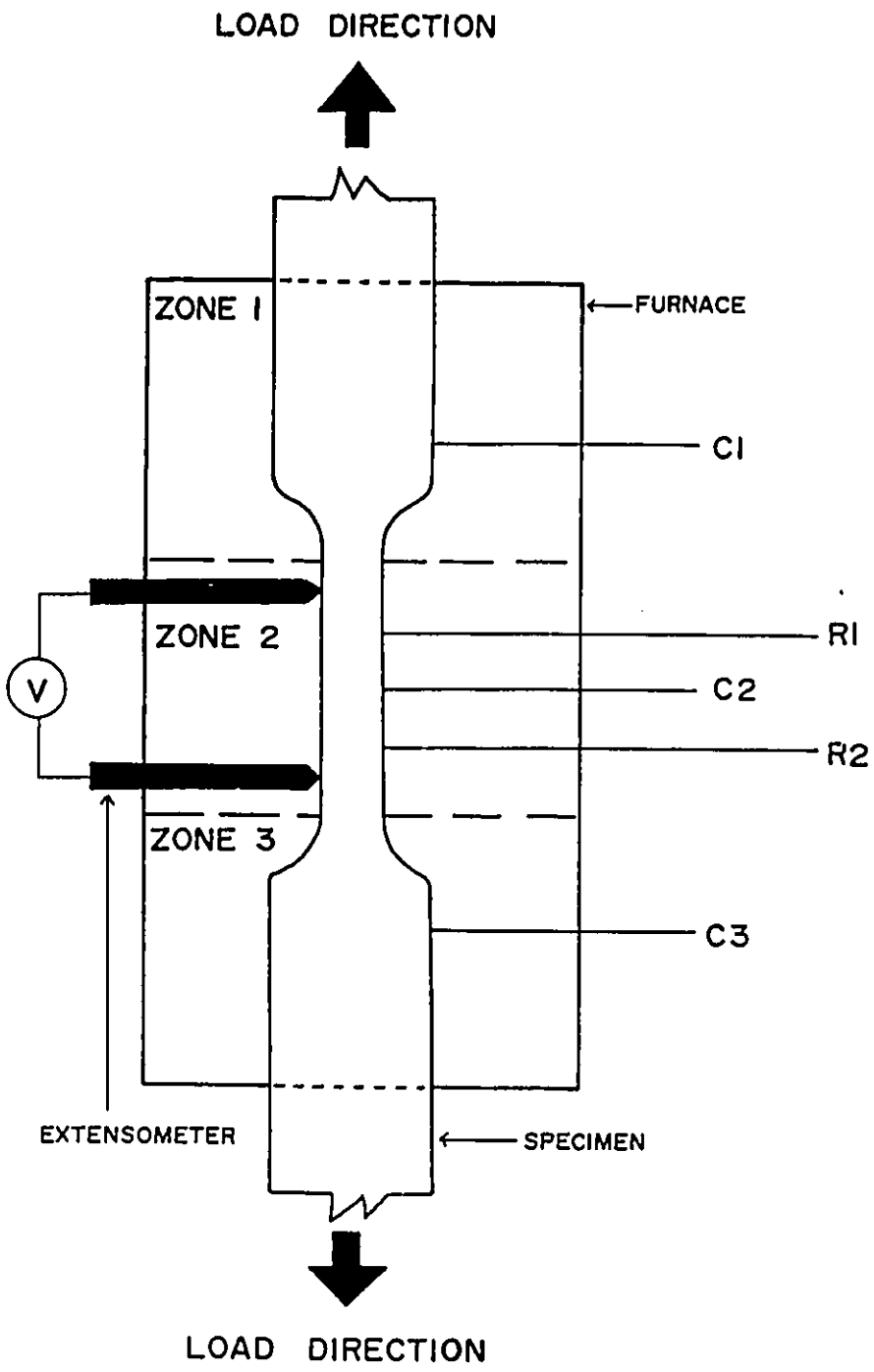

Figure 2.1: Mechanical test system gripping geometry and furnace set-up. (C1, C2 and C3 refer to control thermocouples; R1 and R2 refer to reading thermocouples.)

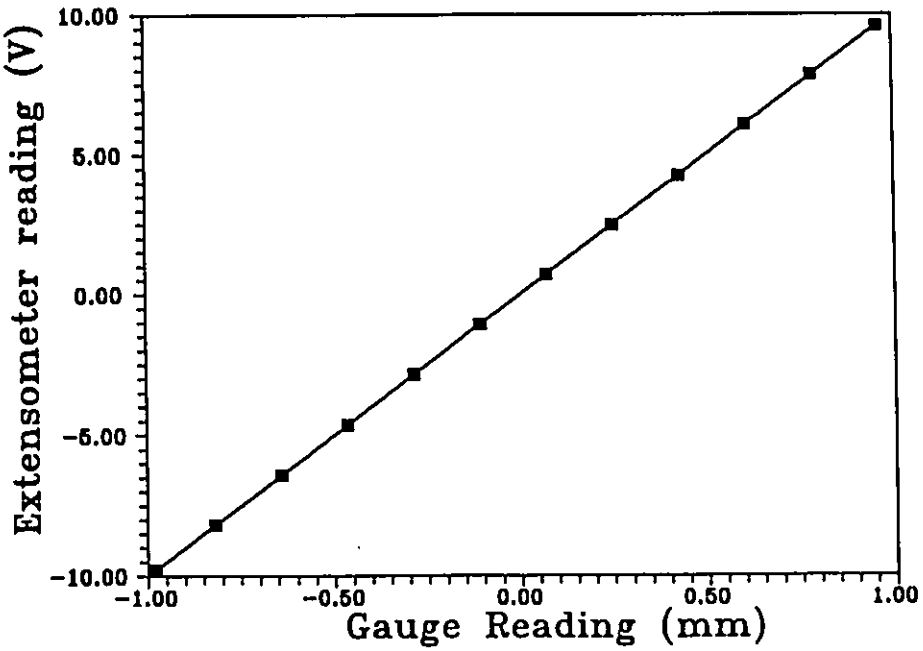

Figure 2.2: Extensometer calibration using dial gauge.

In performing load reversal tests, such as Bauschinger experiments, it is important to minimize any hysteresis that may originate from the extensometer or backlash (slack) in the load frame. The load frame was equipped with fatigue grips that could be hydraulically pressurized to minimize any slack that may occur in going from tension to compression or vice-versa. To measure the magnitude of any hysteresis that may be present in the system, a specimen made from tool steel was cycled in tension and compression (Figure 2.3). No measurable hysteresis was observed.

2.2.1 Specimen Geometry

Restrictions in the specimen geometry are related to compressive testing (or the compressive cycle of a Bauschinger experiment). The most critical geometrical aspect is the length (l) to diameter (d) ratio of the gauge region (l/d). The gripping of the specimen creates lateral end constraints that can cause barrelling instabilities (Prangnell et al. ,1992). The magnitude of this effect increases as the l/d ratio decreases. In addition, non-uniform stress concentrations can exist near the blended radius of the tensile sample. If the specimen is very stout (i.e. l/d is small) this region of non-uniform stress could represent a significant portion of the deforming region. Both these arguments suggest that l/d should be maximized.

Conversely, the possibility of buckling instabilities increases as l/d increases, and therefore places limits on the upper bound of l/d. The conditions for buckling in the plastic regime depend primarily on the flow stress (applied load) and strain hardening characteristics of the material being tested. Estimates of the maximum amount of compressive loading (assuming perfect alignment) can be made using the Euler-Engesser buckling equation (Shigley, 1986);

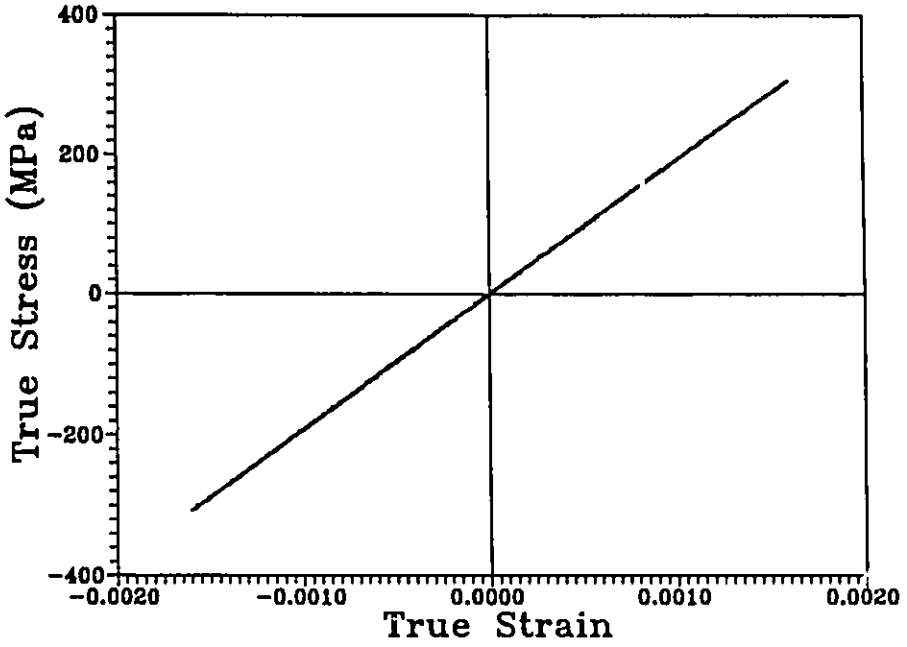

Figure 2.3: Cyclic loading of a tool steel in tension and compression to check for any hysteresis present in the testing system.

$$P_{cr} = \frac{4\pi^2 \left(\frac{d\sigma}{d\epsilon}\right) I}{l^2} \qquad (2.1)$$

where P_{cr} is the critical load above which buckling is predicted, $d\sigma/d\epsilon$ is the strain hardening rate of the material, I is the second moment of area ($\pi d^4/64$ for a circular cross-section) and l is the length of the column (gauge region). This equation assumes that both ends of the column are fixed. Dividing both sides of Equation (2.1) by the cross-sectional area of the sample gives;

$$\frac{P_{cr}}{A} = \sigma_{cr} = \frac{\pi^2}{4}\left(\frac{d\sigma}{d\epsilon}\right)\left(\frac{d}{l}\right)^2 \qquad (2.2)$$

where σ_{cr} is the critical stress for buckling. Rearranging this expression gives;

$$\frac{\left(\frac{d\sigma}{d\epsilon}\right)}{\sigma_{cr}} = R_{cr} = \frac{4}{\pi^2}\left(\frac{l}{d}\right)^2 \qquad (2.3)$$

The value of l/d which would prevent buckling depends on the ratio of the strain hardening rate to the flow stress, R. This ratio, in turn is dependent on the level of compressive strain imposed. During this work the primary focus was on the low strain regime. Consequently the compressive tests and the compressive cycle of the Bauschinger experiments were limited to plastic strains of about .01. At this level of strain the value of R for the materials studied here ranged between 15 and 20 depending on the ageing condition. According to equation (2.3) this would limit the upper value of l/d to between 6 and 7. The value of l/d of the specimen geometry chosen (Figure 2.4) was 4. This geometry would accommodate the 25.4 mm gauge length extensometer, and is well below the critical value necessary to prevent buckling.

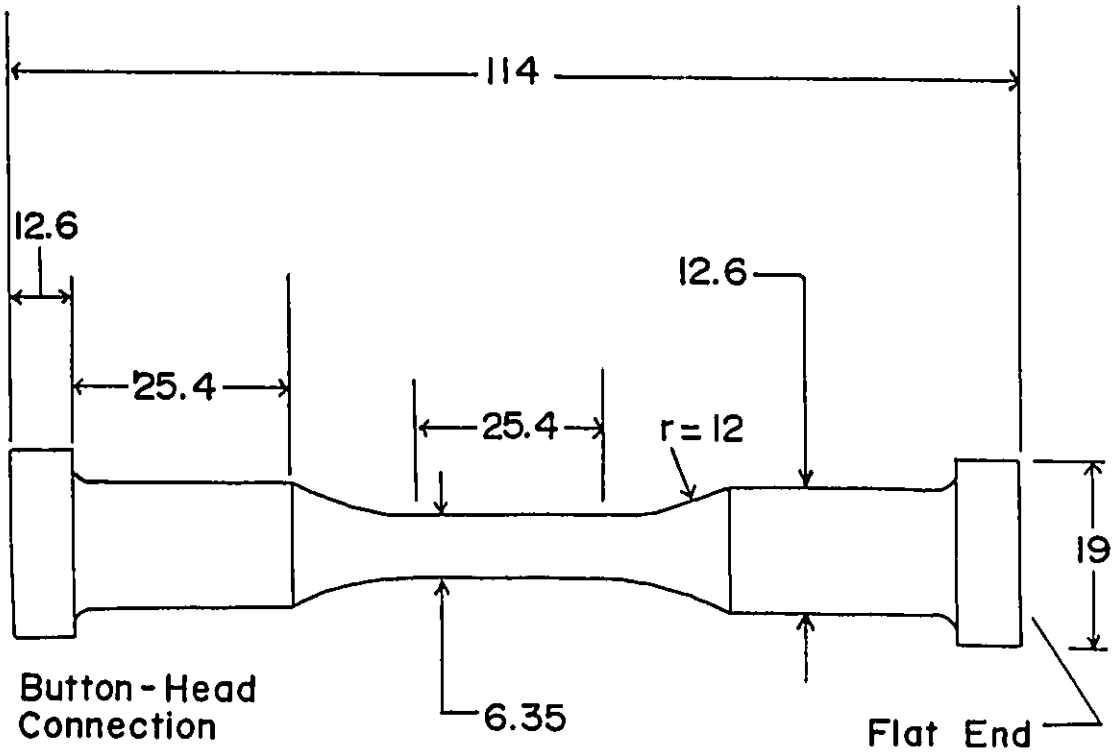

Figure 2.4: Geometry of specimen used for mechanical testing.

2.2.2 Specimen Alignment

Good alignment of the specimen in the load frame is important for both the monotonic tests and Bauschinger experiments. In the monotonic tests it was desired to measure plastic strains of the order of 10^{-5}. To do this it was important that the stress-strain curve have a high degree of linearity in the elastic range. Misalignment can create stress concentrations large enough to cause plastic flow at very low applied stresses which may give rise to initially non-linear behaviour. In the Bauschinger experiments good alignment is necessary to reduce the possibility of buckling during the compressive cycle.

Alignment was achieved using a tool steel specimen with the same geometry as that in Figure 2.4, The specimen was sectioned into two halves and the faces machine parallel. Each half was placed in the grips and pressurized in the same manner as that used for the mechanical testing. The bottom grip attached to the load cell was then adjusted until the two halves were judged to be aligned by visual inspection. The degree of alignment achieved by this technique was checked using two extensometers which were positioned diametrically opposite to one another on a specimen. The specimen was then deformed in tension to about 1% strain and then deformed in compression by a similar amount (Figure 2.5). Some small differences exist between the two extensometers concerning the measurement of the elastic modulus. However, the flow curve that is measured is nearly identical, both in the forward and reverse directions. This indicates that the degree of buckling during compressive loading was maintained at an acceptable level.

2.2.2 Temperature Control

The furnace used for the high temperature tests was equipped with three zones (see Figure 2.1), each with its own controls. Control thermocouple C2 was spot welded to the mid-section

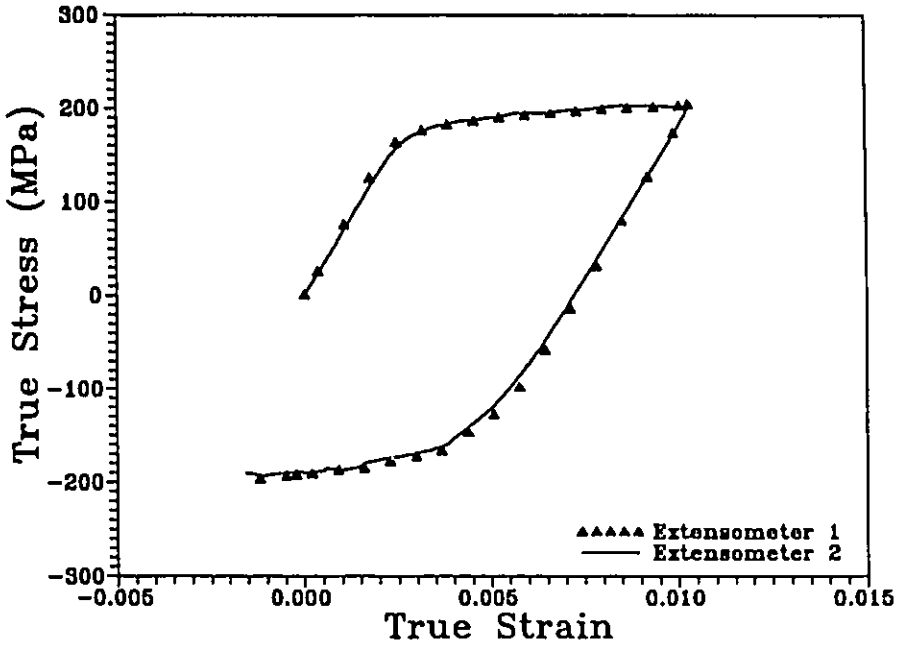

Figure 2.5: Bauschinger experiment using two extensometers, diametrically opposite to one another, to measure strain.

of the specimen gauge length. Control couples C1 and C3 were inserted in small ports in the top and bottom grips. The actual temperature of the specimen was determined by two reading thermocouples, R1 and R2 which were spot welded to the gauge length of the specimen as indicated in the figure. In this way, any temperature gradient in the specimen could be measured. After a stabilization period of about 1 hour, readings from the top and bottom thermocouples, R1 and R2, differed by no more than 1°C.

All the mechanical tests performed in this study were performed using the same experimental set-up described above. Tests were performed in stroke control at a strain rate of $2x10^{-3}$ s^{-1}. Because of the sequential nature of these experiments, it will be clearer to described the details of each test as their results are described in chapter 3.

2.3 Ageing Heat Treatments

Table 2.1 describes the various heat treatments used in this study. All materials were solution treated, quenched and naturally aged at room temperature for 16 hours (T4). This was followed by artificial ageing at 155°C for 9 hours followed by quenching (T61). Overaged structures were created by further ageing the T61 material at either 200°C (OA200) or 300°C (OA300). The hardness profile versus ageing time at both of these temperatures is illustrated for the unreinforced alloy in Figure 2.6. After 200 hours at 200°C and 30 hours at 300°C, the hardness values reach a constant value, indicating the development of a stable microstructure. A time of 216 hours and 48 hours were chosen for the OA200 and OA300 conditions respectively.

2.4 Transmission Electron Microscopy

The primary goal of the Transmission Electron Microscopy (TEM) work was to

Table 2.1 Description of the various ageing treatments used in this study.

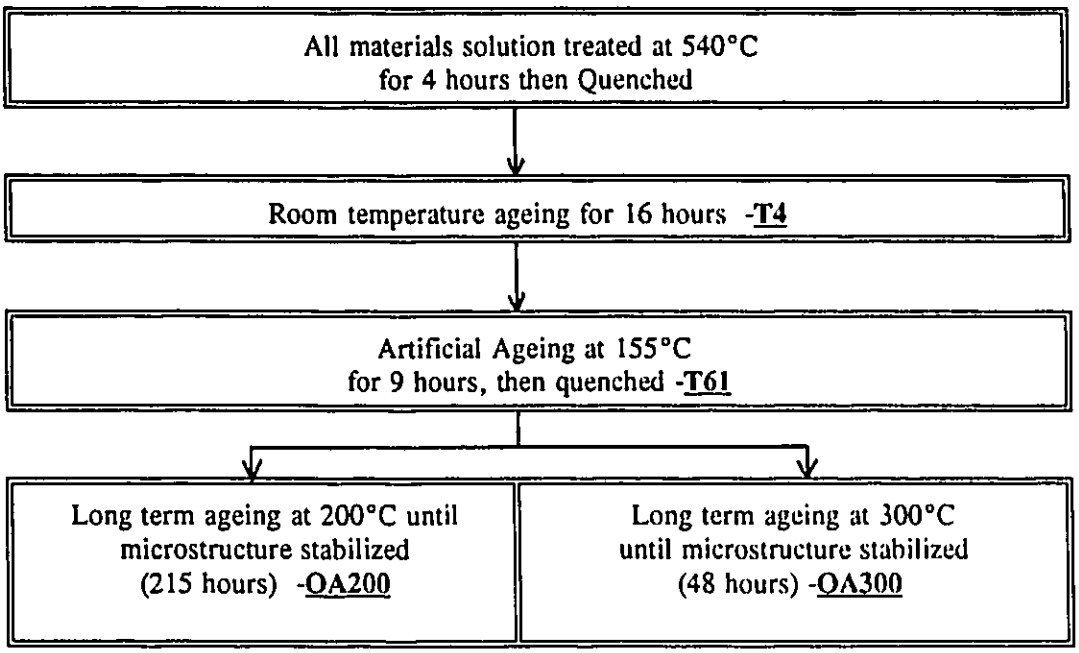

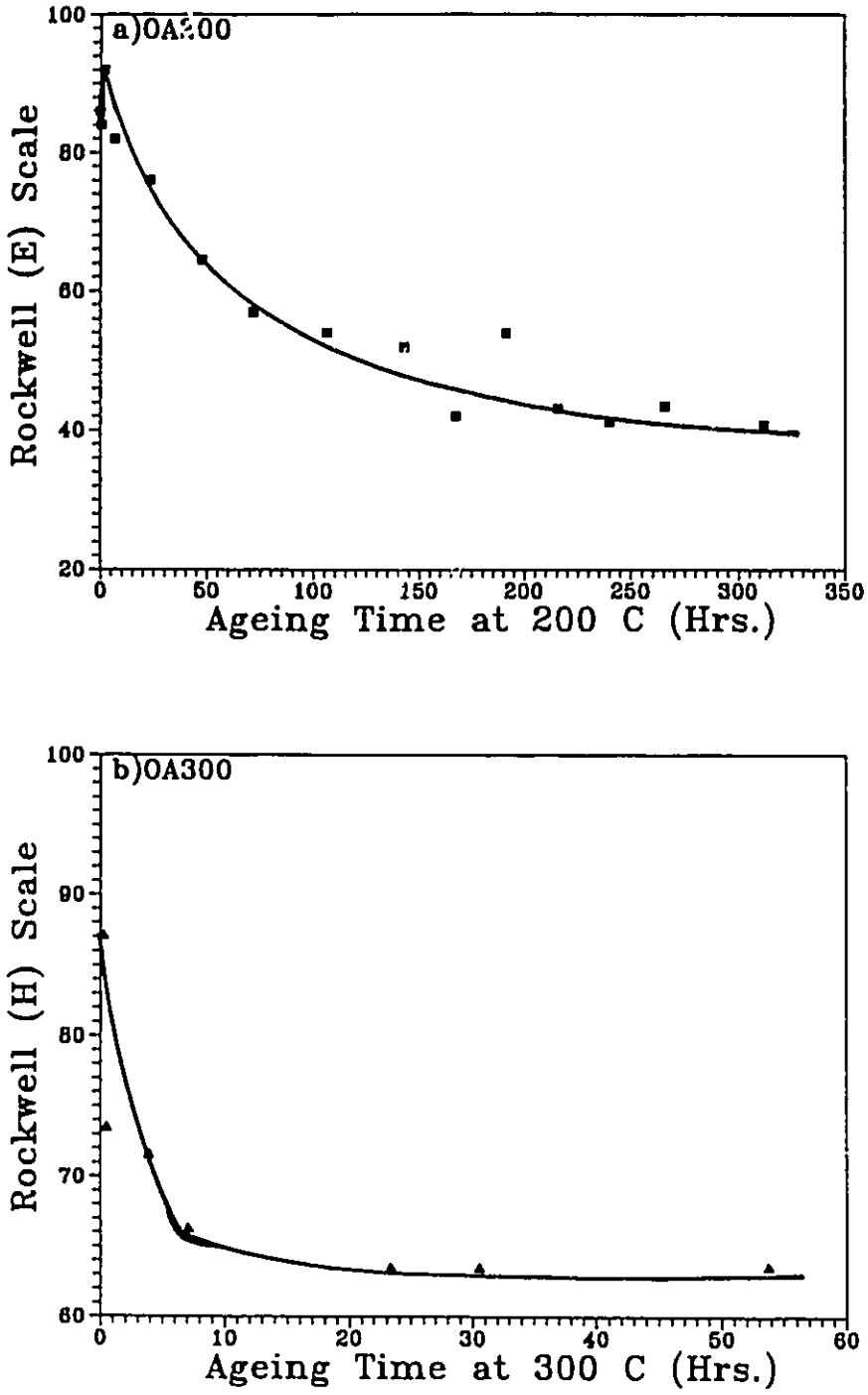

Figure 2.6: Ageing profiles for long term high temperature exposure; a) ageing at 200°C; b) ageing at 300°C.

determine the type of precipitates that were produced in the metal matrix during the various ageing treatments performed. A TEM Philips CM12 was used at 100 kV using a double tilt specimen holder. Preparation of the thin foils involved the following steps:

1) Slices 1.1 to 1.5 mm thick were cut from a heat treated specimen using a diamond blade at low speeds. Discs 3 mm in diameter were then cut from this using a spark cutting machine.
2) These discs were then mechanically polished to a thickness of about 100 μm using 600 grit SiC paper.
3) Further thinning to about 20 μm was achieved using a dimple grinding technique.
4a) In the case of the unreinforced alloy, samples were then electro-polished to perforation in a Tenpol (an automated jet electro-polishing unit) using Methanol-30% nitric as electrolytes. The electrolyte was cooled to around -40 C and the voltage kept at 35 V.
4b) In the case of the composites, following dimple grinding, samples were ion milled to perforation at -196 C.

The precipitate structure produced by the various ageing conditions was then examined using bright and dark field imaging techniques.

CHAPTER 3:

EXPERIMENTAL RESULTS

3.1 Material Characterization

The materials investigated in this work were provided by Alcan International. The base alloy and composite materials, containing various volume fractions of SiC particles were manufactured via a molten metal mixing route (Duralcan process). After incorporation of the SiC particles into the melt, the materials were cast into 171 mm diameter billets, homogenized at 480°C for 4 hours and then extruded into 20 mm diameter rods using an extrusion ratio of 70:1. The base alloy used is A356 Aluminium which has a chemical composition of 6.8% Si and .41% Mg. The alloy is age hardenable with the formation of Mg_2Si precipitates. The composite materials investigated in this work have nominal volume fractions of 10 and 20 %.

The choice of this alloy system is primarily based on the stability of SiC in Aluminum. In a liquid metal mixing process, there is a potential for Al to react with SiC. It has been shown (Lloyd and Dewing, 1988) that the following reaction can occur;

$$4Al + 3SiC \leftrightarrow Al_4C_3 + 3Si$$

In alloy systems such as 7075 and 6061, significant reaction between SiC and the melt can occur with holding times less than 1 hour. This reaction is undesirable because it can degrade the reinforcement.

Calculations by Lloyd (1989) reveal that the formation of Al_4C_3 can be greatly reduced and even prevented if the Si level in the matrix alloy is increased. The Si levels in A356 are sufficient to significantly reduce reactivity between the particles and the melt for the processing

times used in practice. Consequently in this system the interface between the SiC particles and matrix should be relatively clean.

3.1.1 Image Analysis

Examples of the microstructures for the 10 and 20 vol% composites are shown in Figure 3.1. The dark angular shaped particles are SiC, the finer grey phase is a Si rich phase characteristic of the unreinforced alloy. Polished sections for the 20 vol.% composite are shown parallel and perpendicular to the extrusion direction (Figures 3.1a and b). The extrusion process does not create any significant anisotropy in particle distribution with respect to direction. Image analysis of the composite materials was performed by Lloyd (1990). The mean volume fraction, particle size and aspect ratio of the particles is given in Table 3.1. In both cases, the measured volume fraction is slightly higher than the nominal compositions. (During this work, these materials will be referred to by their nominal values). The mean particle size and aspect ratio of both volume fractions are similar and are about 8 μm and 2 respectively. All these parameters had a distribution in value. An example of the particle size distribution is shown in the inset below Table 3.1. The particle size ranges from about 2μm to 20 μm.

Figure 3.1 indicates that the SiC particle distribution is somewhat inhomogeneous. An experimental study of particle distribution using image analysis techniques has recently been completed by Lloyd (1991) on both as cast and extruded composites made by the Duralcan process. Results for a 10 vol% SiC composite in the extruded state are illustrated in Figure 3.2. One characteristic feature of the distribution is that there are a large number of particles whose interparticle spacing is less than about 3 μm. According to Lloyd this corresponds to a volume fraction of about 35%. (Long time sedimentation experiments of SiC particles in water, have achieved particle volume fractions of 40 vol%. This may suggest an upper limit for the degree

Table 3.1 Morphological parameters for the SiC reinfrocement in the 10 and 20 vol% composites. (Lloyd, 1990).

Parameter	Volume Fraction V_p	Particle Size (μm)	Aspect Ratio (S)
10% SiC /A356	11.08 +/- 1.48	7.85 +/- 4.03	1.96 +/- .67
20% SiC /A356	21.15 +/- 1.87	8.32 +/- 4.17	2.00 +/- .69

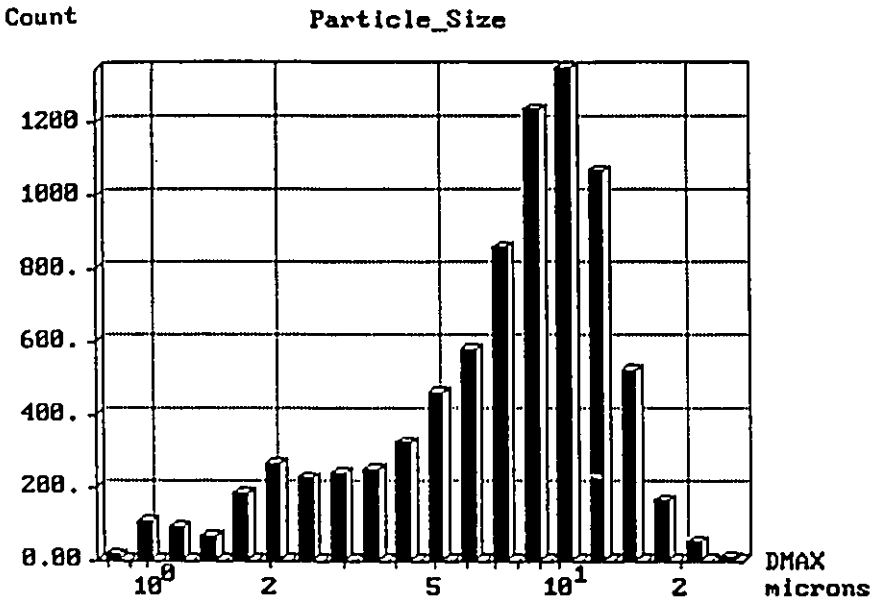

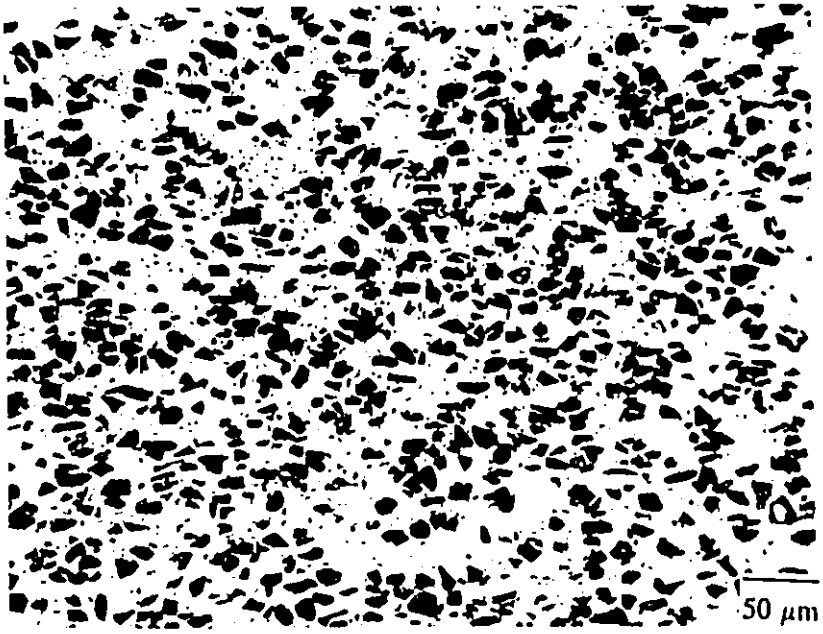

3.1 a

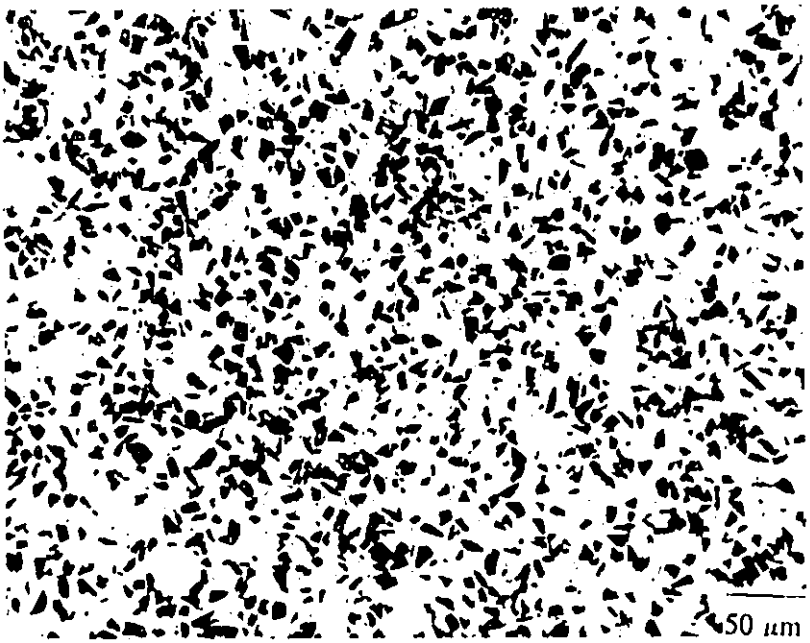

3.1 b

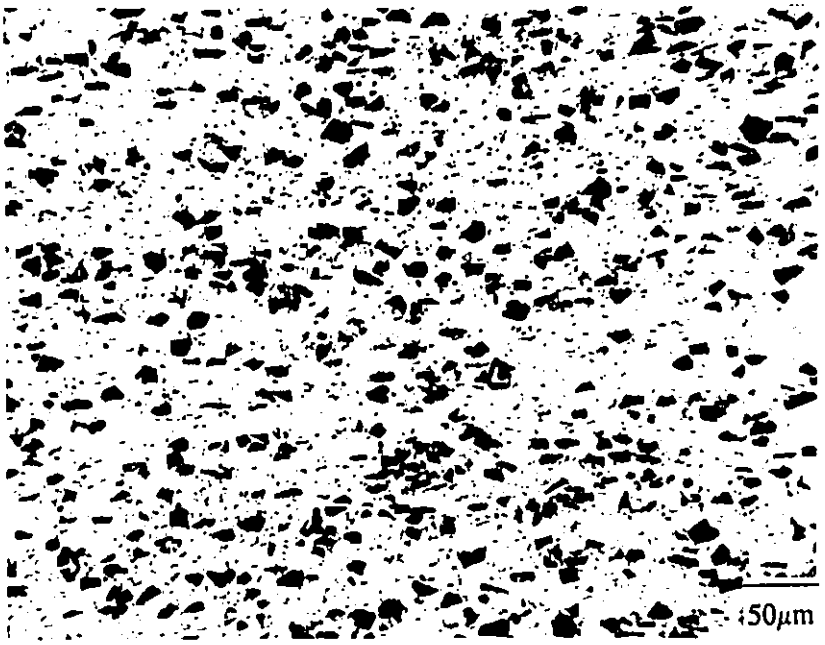

3.1 c

Figure 3.1: Microstructure of the SiC/A356 composites; a) 20 vol% SiC composite polished parallel and; b) perpendicular to the extrusion direction; c) 10 vol% SiC composite polished parallel to the extrusion direction.

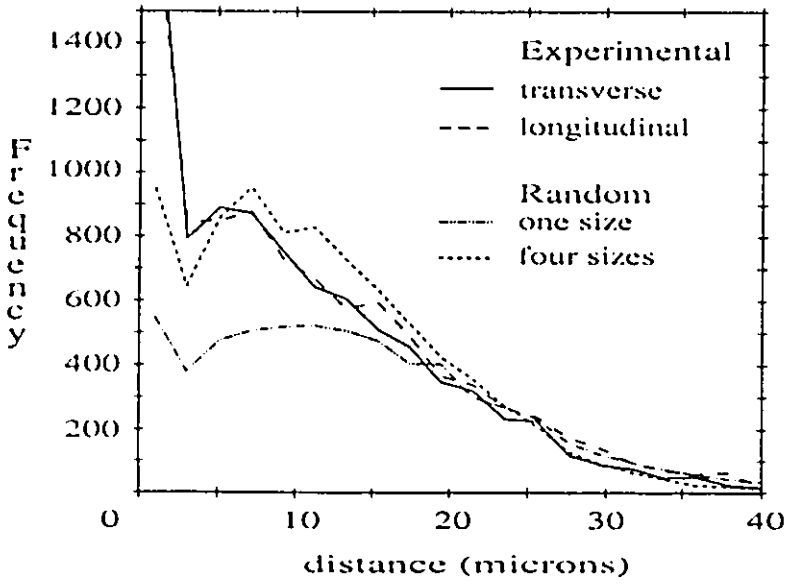

Figure 3.2: Distribution of minimum particle separation in a 10 vol% SiC Al composite. Included are those expected for random distributions. (Lloyd, 1991)

to which the particles can cluster into particle rich areas). Lloyd has also compared the experimentally measured distribution with that expected for a random distribution. A random distribution based on four sizes of particles fits the experimental data reasonably well for particle separations above about 5 μm. However it is unable to predict the large number of particles with spacings below this value.

3.1.2 Ageing Characteristics

The primary objectives of the heat treatments described in section 2.3 were to;

1) vary the matrix flow strength and investigate its influence on composite properties;

2) investigate a wide range of matrix precipitate morphology, from underaged to overaged structures;

3) simulate long term high temperature exposures by overageing the materials for long periods of time at temperatures above that used for artificial ageing.

3.1.2.1 Ageing Sequence

Several studies (Thomas, 1961; Lutts, 1961; Jacobs, 1972; Smith, 1973) using transmission electron microscopy (TEM) and x-ray diffraction, indicate the following precipitation sequence in Al-Si-Mg alloy systems;

$$supersaturated\ solid\ solution \rightarrow G.P.zones \rightarrow \beta' \rightarrow \beta(Mg_2Si)$$

The β' phase is needle shaped, metastable and semi-coherent while the β phase is platelet shaped, stable and incoherent. (If an excess of Si exists in the alloy (as in A356), Si precipitation may also accompany this sequence). Work by Lutts (1961) and Jacobs (1972) indicates that the G.P. zone precipitates are relatively stable and are the only precipitate structures present even after

long ageing times at temperatures at or below 160°C. This is confirmed by more recent studies (Dutta and Bourell, 1990; Appendino et al., 1991) using differential scanning calorimetry (DSC) and TEM techniques.

All of the above studies indicate that artificial ageing temperatures above about 175°C begin to precipitate β' after relatively short ageing times. Prolonged ageing at temperatures above 200°C coarsens the β' phase and also begins to precipitate the β phase. Few studies have observed the structure developed at 300°C after long ageing times. It would be expected however (Thomas, 1961), that the equilibrium β (Mg_2Si) precipitate would be the primary precipitate structure present under these conditions.

3.1.2.2 Influence of SiC Particles

A number of investigators have reported that the presence of SiC particles accelerates the ageing response in the matrix metal when compared to the unreinforced alloy (Nieh and Karlak, 1984; Christman and Suresh, 1988; Dutta and Bourell, 1990; Humphreys et al., 1991; Appendino et al., 1991). This effect is particularly pronounced in Al-Cu alloys where the time to peak ageing in the composite can be roughly half the time required for the unreinforced alloy (see Figure 3.3; Christman and Suresh, 1988). Many researchers have attributed this acceleration to enhanced nucleation and growth of precipitates caused by a greater dislocation density in the matrix (Christman and Suresh; Dutta and Bourell). The origins of this dislocation density result from differences in thermal contraction during a quench (see section 1.3.1.3).

Detailed work by Dutta and Bourell, and Appendino et al. on an Al-Si-Mg alloy (6061) reinforced with SiC particles has been recently carried out using hardness measurements, TEM studies and DSC. This work indicates that the room temperature ageing response (T4) of the alloy and composite are essentially identical. During this ageing sequence, only G.P. zones were

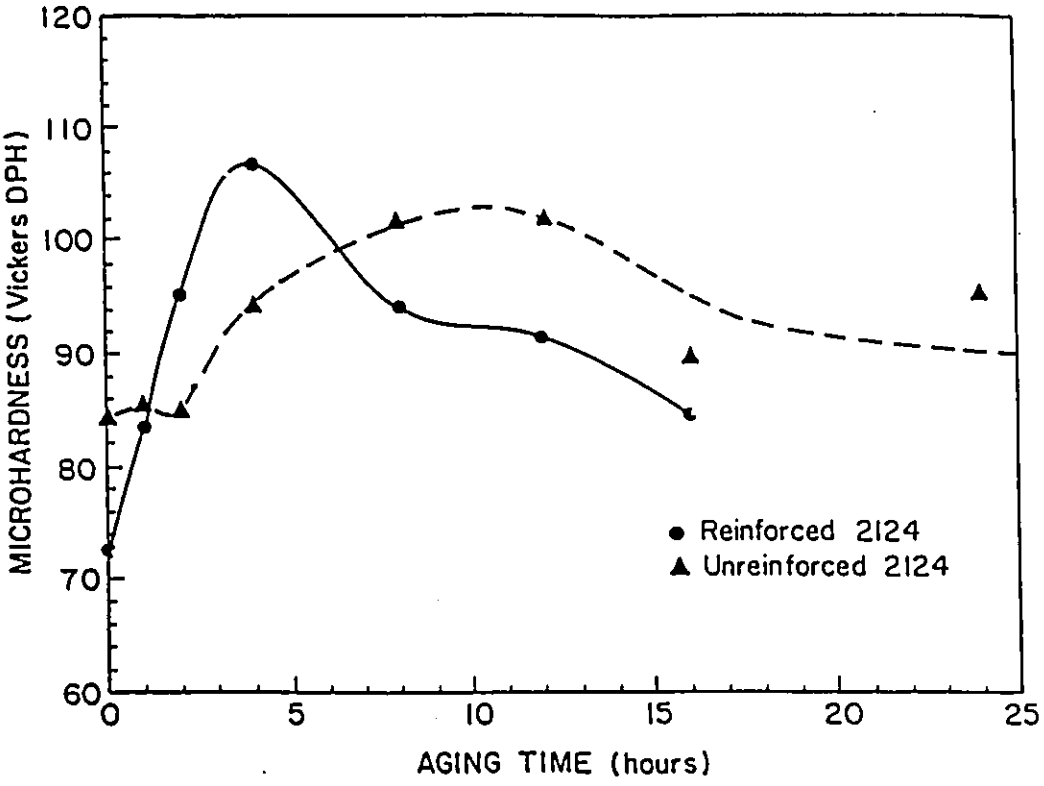

Figure 3.3: Ageing characteristics in a 2124 Al alloy and SiC composite (Christman and Suresh, 1988)

formed. Artificial ageing at 180 degree C indicated some accelerated ageing in the composite material. Work by Dutta and Bourell indicates that ageing at this temperature nucleates β' precipitates. These results suggest that the accelerated ageing effect in this alloy system is primarily associated with the sequence in which the β' phase forms.

3.1.2.3 Transmission Electron Microscopy Observations.

From the above discussion the most critical ageing steps used in this study are the T61 and OA200 treatments. From the work of Lutts (1961) and Jacobs (1972) it would be expected that ageing at 155 °C (T61) should produce only G.P. zones. However the accelerating effect of the SiC particles may prematurely nucleate the β' phase during this stage. In the OA200 condition, the nucleation and growth of β' is expected and therefore the accelerating influence of the particles may create a different precipitate morphology in this ageing condition. Consequently, TEM observations of the unreinforced alloy and 20 vol% composite were made in the T61 and the OA200 states. In addition, the precipitate morphology in the unreinforced alloy was observed in the OA300 state.

Figure 3.4a illustrates the microstructure typically found in the 20 vol% composite when aged to the T61 condition. The contrast in the Al matrix suggests the presence of G.P. zones. Faint streaks in the electron diffraction pattern (Figure 3.4b) obtained from an area in the aluminium matrix similar to that illustrated in Figure 3.4a where observed. It was determined that these streaks were parallel to the $<100>$ directions in Al. These results agree with that of Thomas (1961) and are characteristic of the presences of G.P. zones having $<100>$ growth directions. The presence of needle shaped precipitates (β') were not observed in this ageing condition. Similar results were obtained for the unreinforced alloy. These observations agree with those obtained by Wang et al. (1990) using as cast SiC/A356 composites aged at 205°C for short

3.4 a

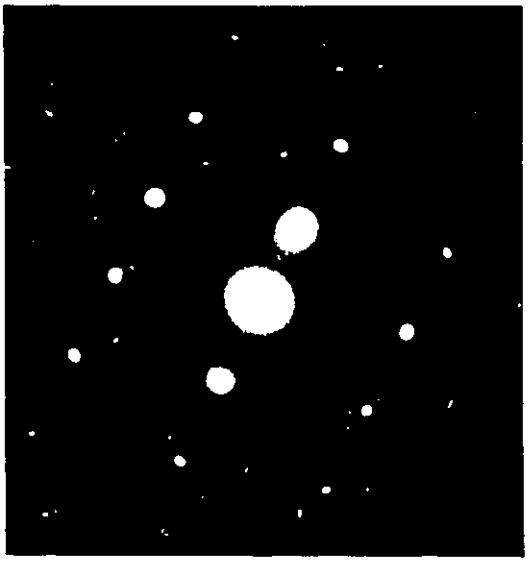

3.4 b

Figure 3.4: a) Microstructure of Al matrix adjacent to a SiC particle illustrating the presence of presence of G.P. zones. (Courtesy I. Hassan); b) electron diffraction pattern from Al grain within 20 vol% composite. Beam direction is [013].

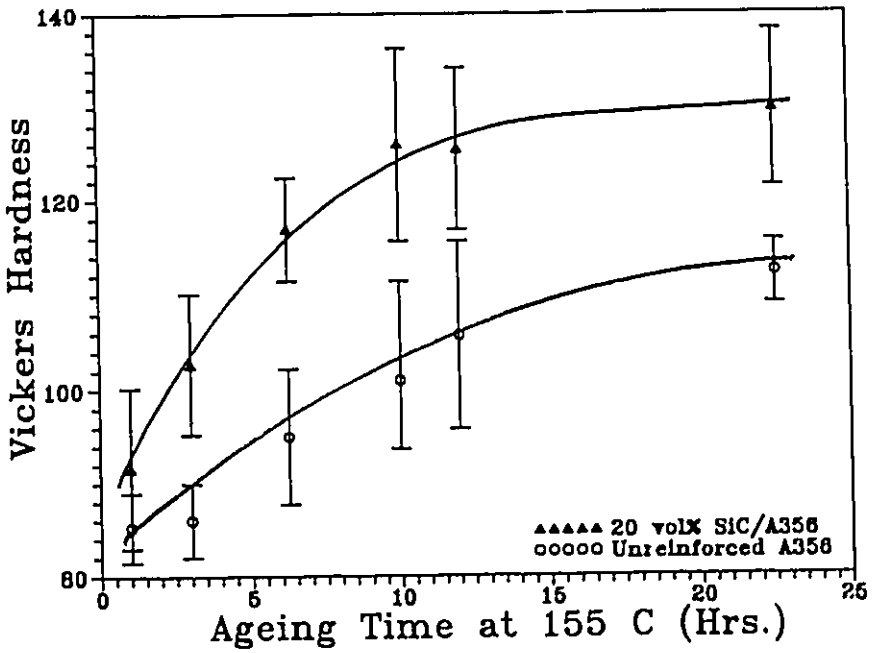

Figure 3.5: Ageing profile for the A356 alloy and 20 vol% composite at 155°C

times.

The interface between the SiC particles and Al matrix shown in Figure 3.4a is typical of that observed during this study. There was no evidence of reaction between the particles and matrix and no preferential precipitation occurred at the interface. This is consistent with TEM observations made by Wang et al. (1990) and Bardal and Hφier (1990) who found no evidence of Al_4C_3 formation at the interface in a SiC/A356 composite. However both these studies, which involved as cast materials, reported the formation of some magnesium spinels ($MgAl_2O_4$) at the particle/matrix interface. This phase was not observed in the material studied here.

The variation in hardness with ageing time at 155°C was measured for the alloy and 20 vol% composite (Figure 3.5). At a given ageing time, the higher hardness reading in the composite results from the presence of the SiC particles. There is some evidence of a small acceleration in the ageing kinetics of the composite. However, considering the error in the readings, this is not a large effect. This evidence, together with the TEM results, indicates that the SiC particles do not significantly alter the ageing process during the T61 treatment used for the materials studied here.

Figure 3.6a shows the precipitate morphology found in the unreinforced alloy after overaging the T61 material for 9 days at 200°C (OA200). The formation of a needle shaped precipitate is clearly indicated. In addition, a platelet shaped precipitate is also present. (Figure 3.6b illustrates this plate-like precipitate in more detail). These observations are consistent with those of Thomas (1961), Jacobs (1972) and Smith (1973) and indicate the presence of the intermediate β' phase and stable β phase. Because of the excess Si that is present in A356, its precipitation may also occur during this stage. Figure 3.6a indicates a large number of plate-like precipitates, some of which could be Si rather than Mg_2Si. A quantitative determination which would distinguish between these two precipitates was not attempted.

3.6 a

b)

.08 μm

c)

Figure 3.6: a) Bright field image of unreinforced microstructure in OA200 condition; b) bright field and c) dark field image of the platelet β precipitate.

Figure 3.7 illustrates the precipitate morphology observed in the composite material when aged to the OA200 state. (As the micron bars indicate, the magnification in Figure 3.7 is about three times that of Figure 3.6). Qualitatively, the same precipitate structures (i.e. β' and β) as that observed for the unreinforced alloy are present in the composite. The size of the precipitates appear to be approximately of the same order in the two materials. There is some evidence of a lower volume fraction of β phase in the composite material. However this may partly be due to the smaller field of view at the higher magnification. In addition, for the composite material, some difficulty was encountered in obtaining large regions of the foil that were thin enough to reveal the precipitate structure. Consequently, the data was limited, making a quantitative comparison concerning precipitate size and volume fraction extremely difficult.

Figure 3.8 indicates the precipitate structure observed in the unreinforced alloy after ageing at 300°C for 48 hours (OA300). This ageing condition would appear to correspond with a disappearance of the needle shaped β' precipitate. However the plate like β phase is present. Although they were not positively identified, Si particles are also expected to be present in this ageing condition.

3.2 Monotonic Stress-Strain Behaviour

3.2.1 Introduction

This section will describe the results of experiments carried out on the tensile and compressive behaviour of the unreinforced A356 alloy and composites containing 10 and 20 vol% of SiC particles. The tensile tests were performed to fracture so that observations at higher strains could be made. With the range used for the extensometer, strains up to 7% could be measured accurately. The stroke was also recorded so that the entire load-elongation curve to fracture could

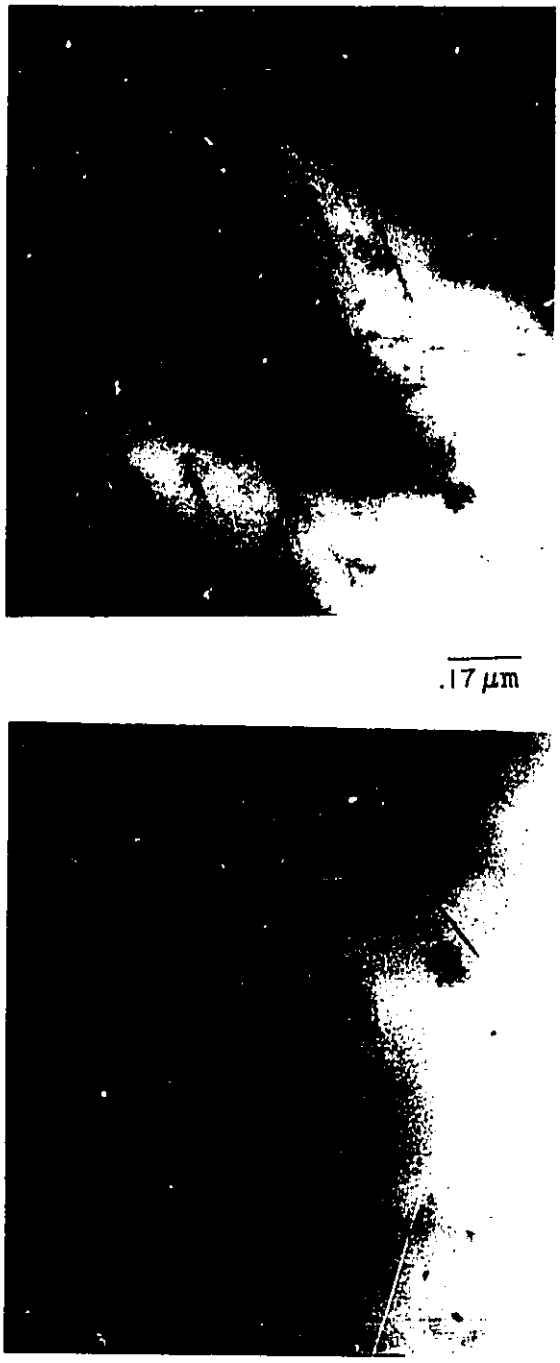

Figure 3.7: Bright field images of the precipitate structure found in the 20 vol% composite in the OA200 condition.

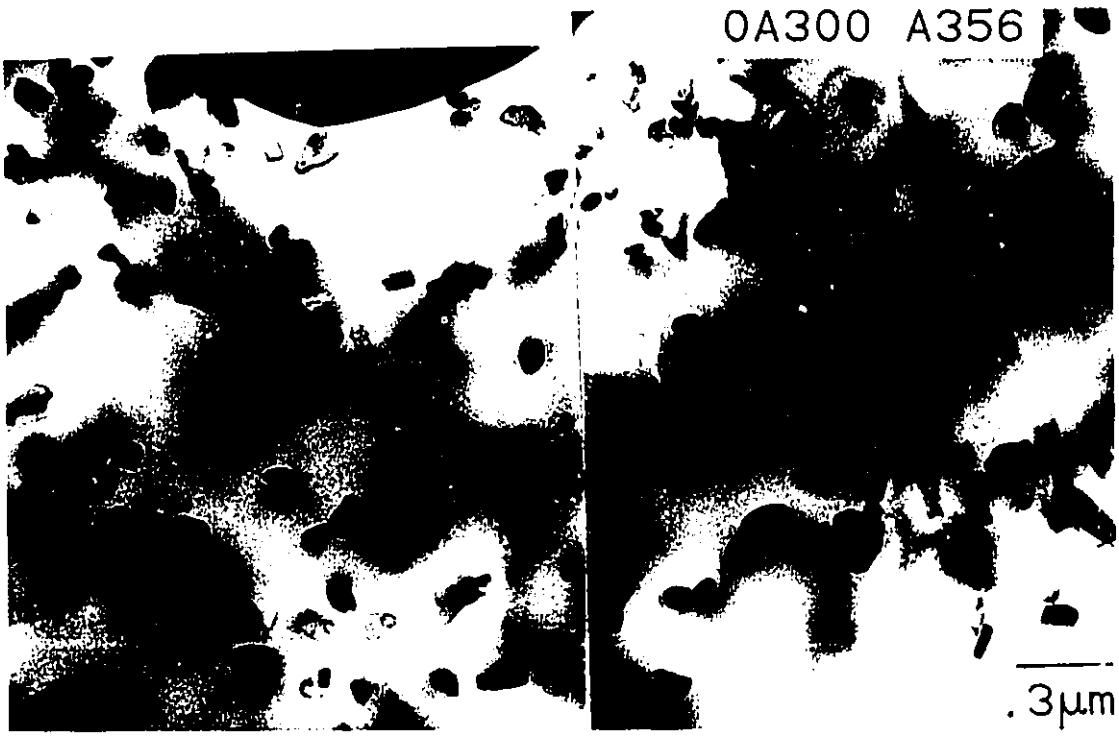

Figure 3.8: Bright field image of precipitate structure for the unreinforced alloy in the OA300 condition.

be obtained. The compression tests were performed to a strain of about 1% after which the sample was reversed into tension. Therefore they also represent Bauschinger experiments in which the initial deformation was compressive. (The Bauschinger experiments will be discussed in more detail in section 3.3). The discussion in this section can be separated into two areas; 1) observations at low strains (up to .02), 2) observations at higher strains (up to the about .07). At low strains the results of load/unload experiments will be reviewed and a definition of yielding will be determined. In addition differences between tension and compression will be discussed. In both strain regimes the influence of matrix ageing condition has been investigated.

Comparisons of tensile behaviour have been made using the true stress-true plastic strain curves. This was adopted for the following reasons;

1) The primary goal is to investigate the influence of SiC particles on plastic deformation,

2) In observing the effects of ageing condition, the yield strength varies considerably. Consequently the degree of elastic strain also varies. Subtracting this out makes comparisons based on plastic strain more direct,

3) The unreinforced, 10 and 20 volume % composites all have different elastic moduli. Therefore direct comparison is best done by subtracting out the elastic portion of the curve.

The tension and compression behaviour have been compared using the same material. In this case the elastic modulus is the same and comparisons are best made based on the total true stress-true strain curves.

During the deformation of the composite, the particles remain elastic. Consequently the amount of material which can contribute to plastic flow is reduced. For more direct comparison this effect has been accounted for by calculating the matrix plastic strain as;

$$\epsilon^e_p = \epsilon_p/(1-f)$$

where f is the SiC particle volume fraction, ϵ_p is the experimentally measured plastic strain and ϵ^c_p is the corrected plastic strain. In all figures the plastic strain is reported as e^c_p.

Strain hardening rates, were calculated from the true stress-true plastic strain curves, corrected as described above. According to this definition of strain hardening all the materials will exhibit rates that tend toward infinity as zero plastic strain is approached. For comparison purposes it is best to concentrate on finite values of plastic strain. Therefore most of these plots begin at plastic strains that are higher than $5x10^{-5}$, (typically $2x10^{-4}$).

Strain hardening is often interpreted by plotting it versus true stress. In this section however the primary interest is in comparing the strain hardening rate achieved in the composites with that in the alloy at the same level of plastic strain. Consequently strain hardening rate is plotted versus true plastic strain.

3.2.2 Low Strain Behaviour

The elastic modulus obtained from the stress-strain curves of the materials is given in Table 3.2 along with the number of specimens and the sample standard deviation. An increase in modulus of 20 and 50% results from the addition of 10 and 20 vol% respectively of SiC particles.

3.2.2.1 Onset of plastic flow

A description of the onset of yielding in the context of load/unload tests has been previously discussed in section 1.5. The results of a load/unload test performed on the 20 vol% composite studied here is illustrated in Figure 3.9. With the sensitivity of strain measurement used, the first loop for which permanent deformation was detected exhibited a plastic strain of about $5x10^{-5}$. Loop #6 shows a very small amount of hysteresis, opening to a strain of $2x10^{-5}$ but

TABLE 3.2 Elastic Modulus and sample standard deviation S for the various materials tested

Material	# of specimens	E(GPa)	S(GPa)
A356	10	70.5	2.7
10%/A356	13	85.4	3.8
20%/A356	18	106.7	4.9

$$S=\sqrt{\frac{\sum_{i=1}^{n}(x_i-\mu)^2}{n-1}}$$

where n is the number of samples and μ is the sample mean

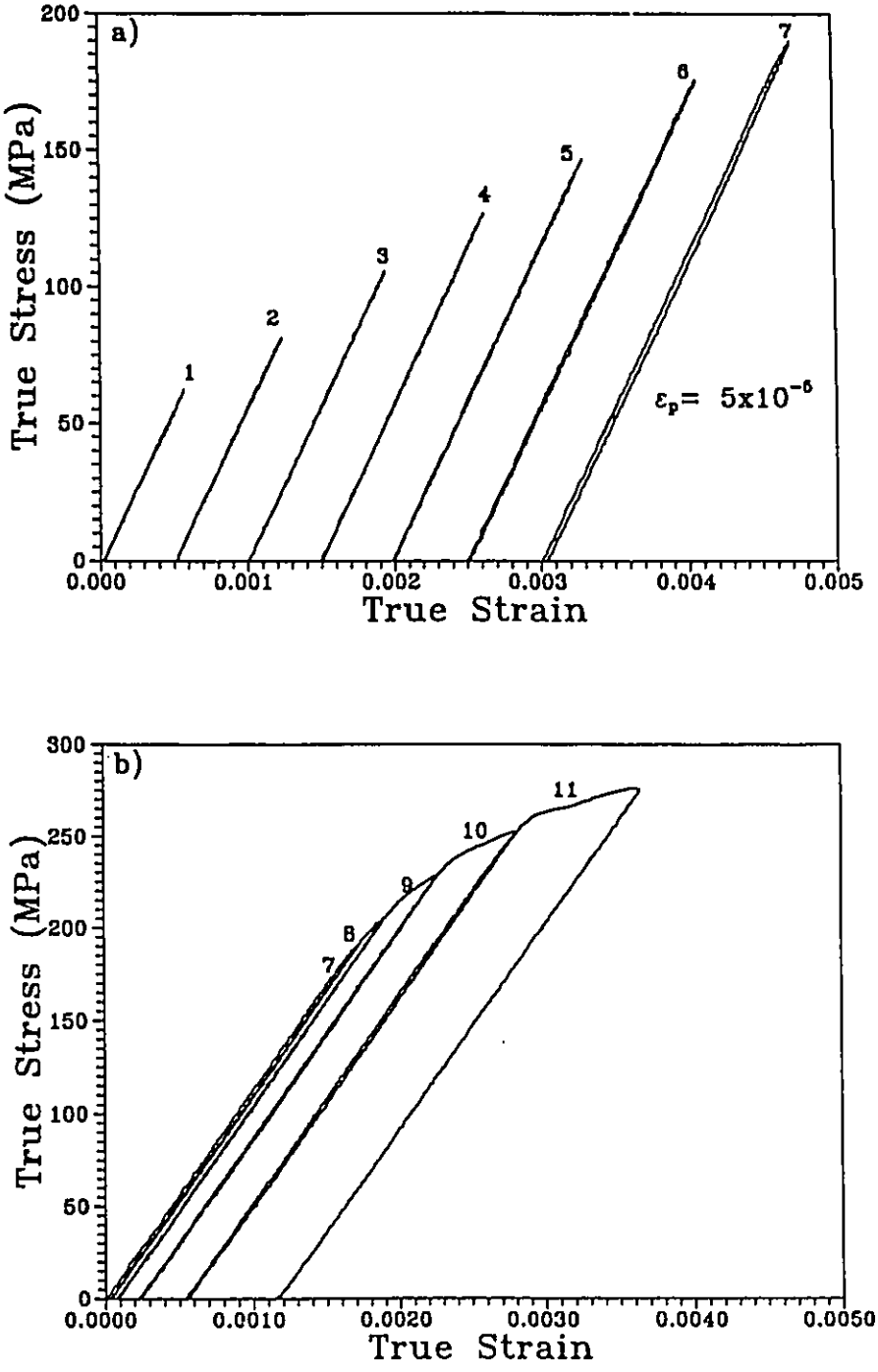

Figure 3.9: Load/unload experiments for 20 vol% composite; a) up to the point of plastic flow; b) loaded to further plastic deformation.

appearing to close when unloaded. At higher strains (Figure 3.9b, loop #10), some hysteresis occurred when unloading and then reloading was performed. This effect will be discussed in Section 3.3. The elastic limit determined in this manner can be derived from curve #6 as 175 MPa.

Determining the elastic limit using this incremental loading is very tedious and time consuming. Consequently it was desired to get a similar measurement from the monotonic stress-strain curves. Comparison of a monotonic curve and a load/unload curve is shown in Figure 3.10. for the 10 vol% composite. This comparison shows that using offset constructions (represented by the unloading line) on the monotonic curve at various plastic strains down to at least $5x10^{-5}$ is a valid way in which to measure the flow stress of the material. Consequently, we have defined the yield strength as the stress at which a permanent plastic strain of $5x10^{-5}$ has been accumulated and have measured it using the offset construction technique on monotonic curves.

3.2.2.2 Tension Tests

The total true stress-true strain curves for the unreinforced alloy up to .01 are plotted in Figure 3.11a for the four ageing conditions studied. The highest strength is achieved by artificial ageing (T61), followed by natural ageing (T4) and the overaged treatments. Note that the T4 and OA200 states have very similar strengths but represent underaged and overaged structures. The plastic strain hardening rates versus true plastic strain are illustrated in Figure 3.11b. Although the strength is influenced by ageing it would appear that strain hardening rates, up to the plastic strains plotted (.005), are relatively insensitive to heat treatment. However, there is some evidence that the strain hardening rates are somewhat higher in the underaged (T4) and peakaged (T61) structures when compared to the overaged structures, especially in the strain range up to .002.

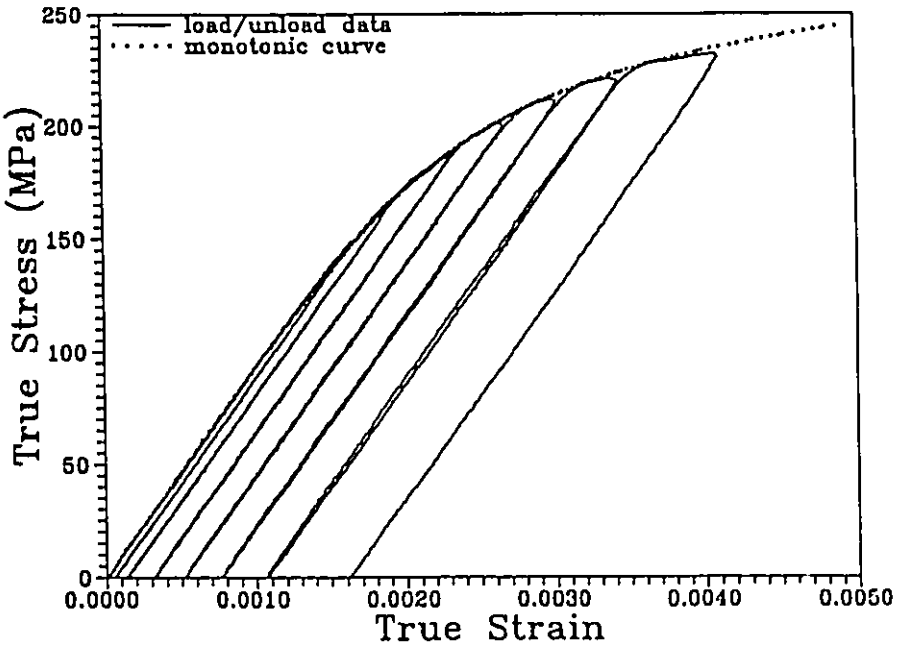

Figure 3.10: Comparisons between load/unload and monotonic stress-strain curves for the 10 vol% composite.

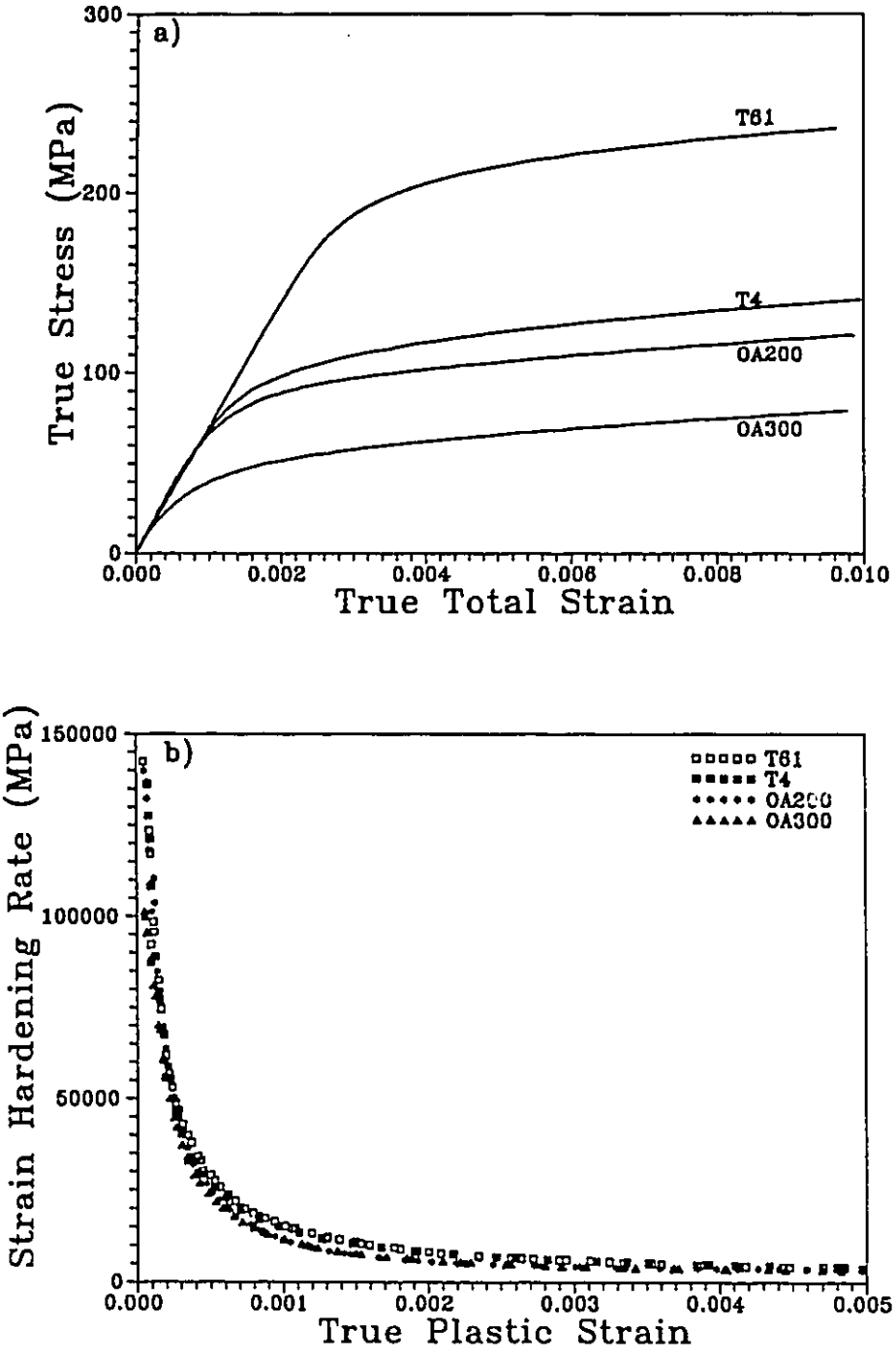

Figure 3.11: Unreinforced A356 in various ageing condition; a) true stress-strain curve; b) strain hardening rate versus true plastic strain (ϵ^c_p)

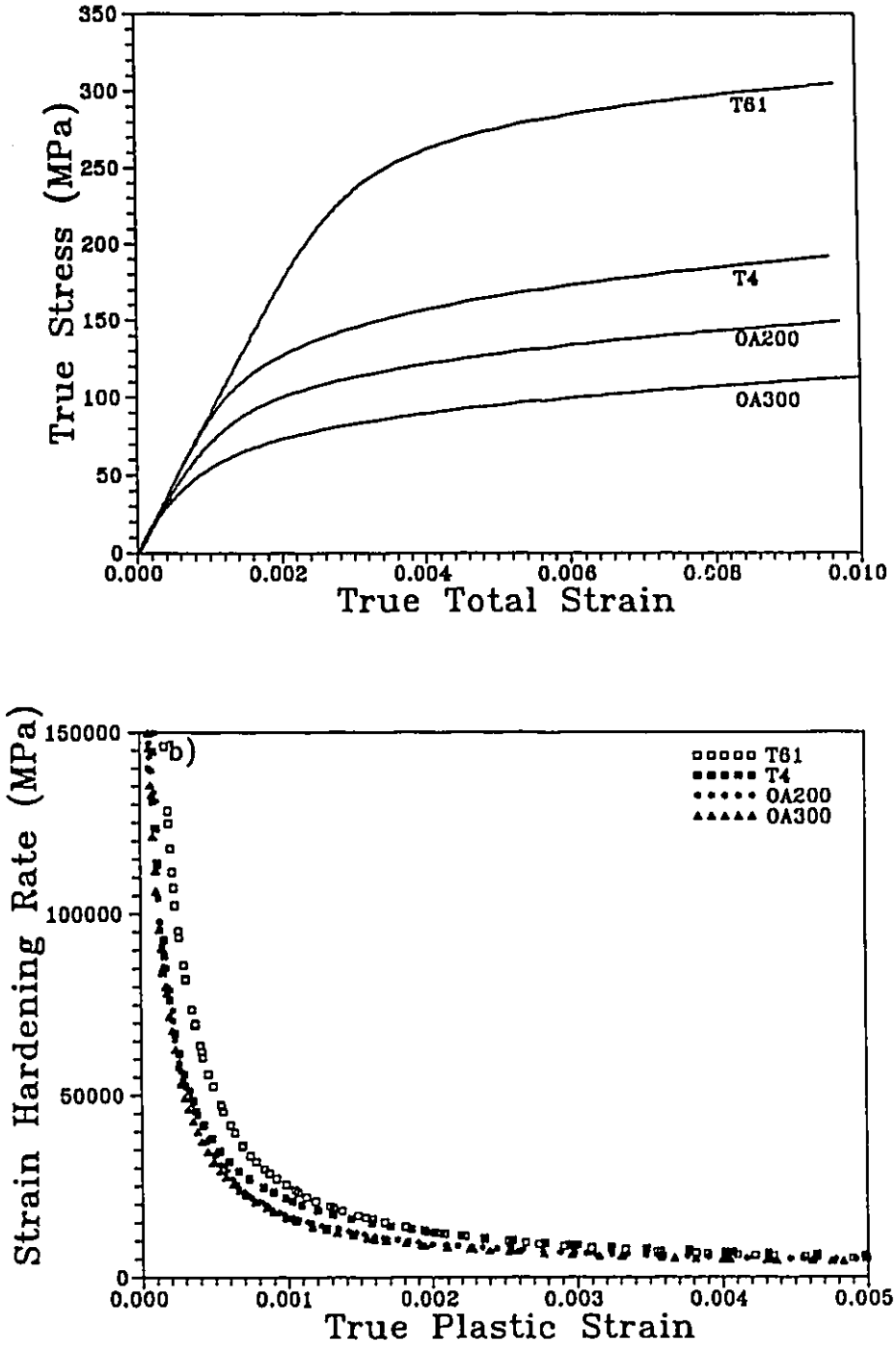

Figure 3.12: 10 vol% SiC/ A356 composite in various ageing condition; a) true stress-strain curve; b) strain hardening rate versus true plastic strain (ϵ^c_p)

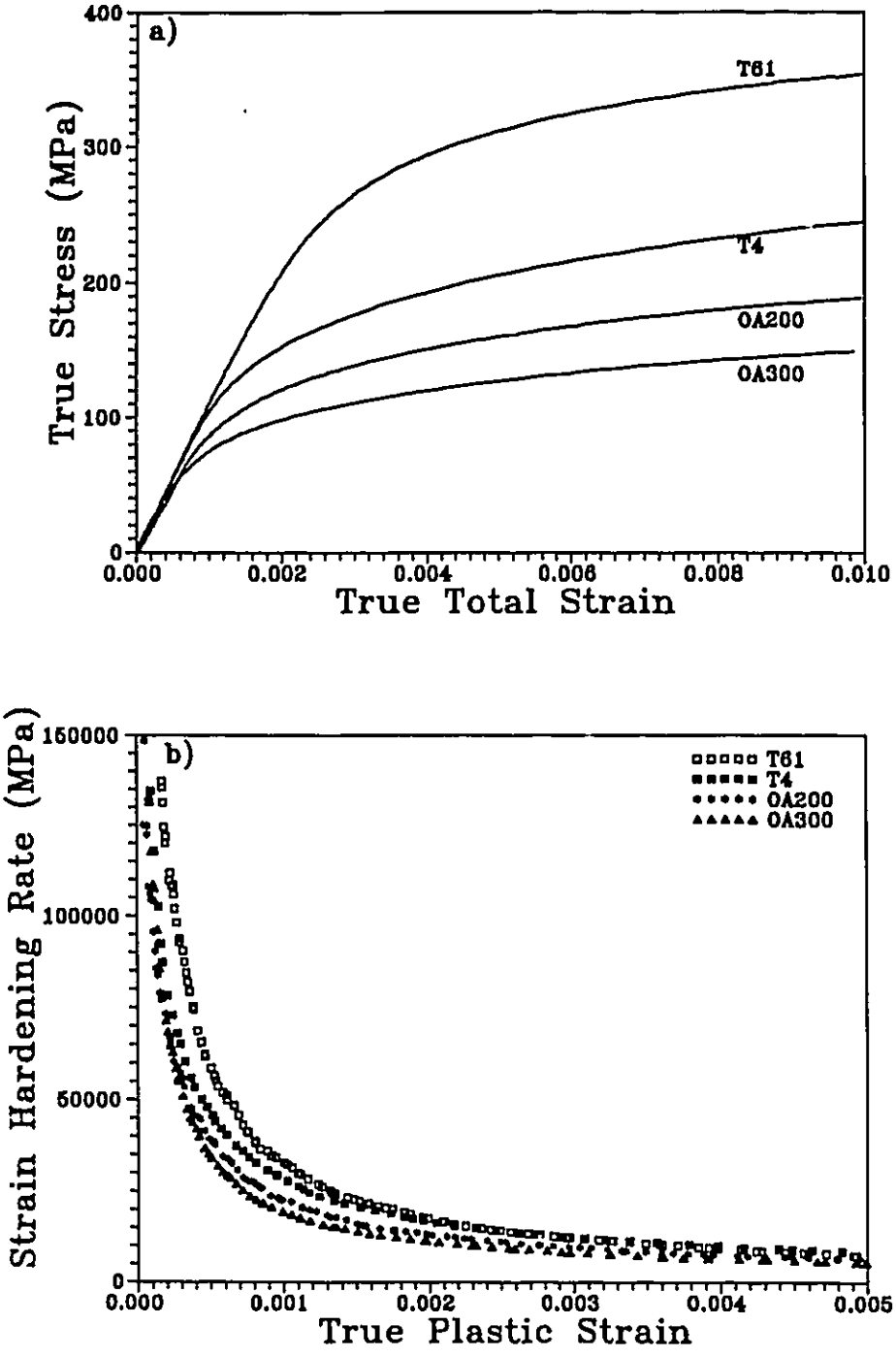

Figure 3.13: 20 vol% SiC/A356 composite in various ageing condition; a) true stress-strain curve; b) strain hardening rate versus true plastic strain (ϵ^c_p)

Figures 3.12a and 3.13a show the stress-strain behaviour for the 10 an 20 vol% composites respectively, as a function of ageing. The same trends seen for the alloy are reflected for the composite data. The trends in strain hardening rates (Figures 3.12b and 3.13b) are somewhat different. In the case of the composites, ageing influences strain hardening behaviour to a larger degree. The T61 condition exhibits higher hardening rates, particularly for the 20 volume% composite at low strains. The lowest hardening rate again occurs in the overaged structures.

Figure 3.14 allows a direct comparison of the true stress-true plastic strain curves for the alloy with that of the composites in the various ageing conditions. It is evident that there is a modest increase in the yield strength which increases with the volume fraction of SiC added. This difference ranges between 10 to 35 MPa depending on the ageing condition. Once the materials begin to deform plastically the difference in strength increases, reaching values of 60 to 110 MPa by strains of .01. This is a result of a higher strain hardening rate in the composite material which is clearly shown in Figure 3.15.

The strain hardening rate is initially a factor of 2 higher in the 20 volume percent composite when compared to the unreinforced alloy at the same level of plastic strain. This difference decreases with plastic strain and appears to be largest for the materials in the hardest ageing condition. The magnitude of the difference increases with an increase in volume fraction of SiC particles.

To summarize the above results, the difference between the flow curve of the composite and alloy is illustrated in Figure 3.16 for the various ageing conditions. Clearly there is a rapid rise in strengthening at low strains up to .002 followed by a more modest rise in strength after strains of .005. This corresponds to the same strain regime in Figure 3.15 where the difference in strain hardening rate is most significant. The rise is largest in the 20 vol% composite and in

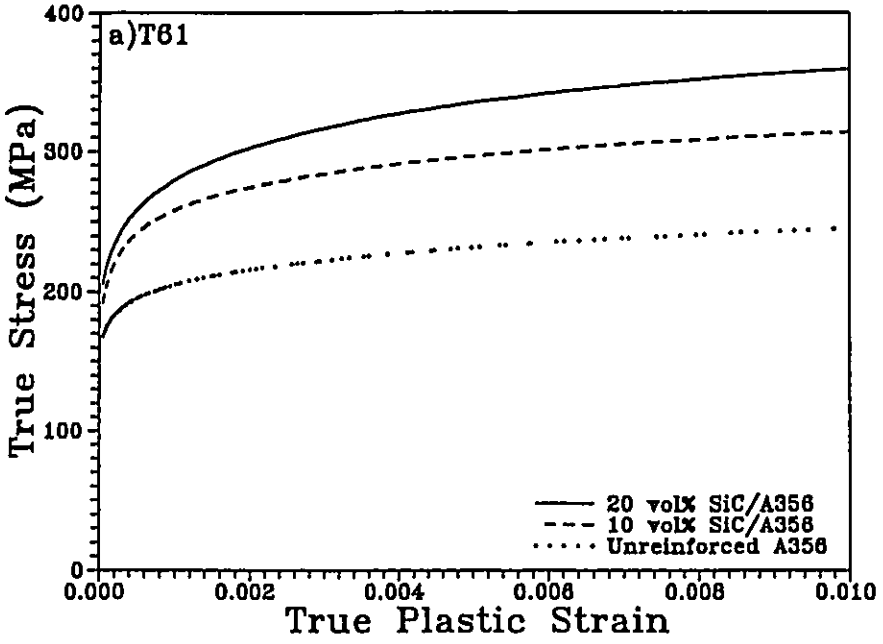
a)T61
True Stress (MPa)
True Plastic Strain
0
100
200
300
400
0.000
0.002
0.004
0.006
0.008
0.010
20 vol% SiC/A356
10 vol% SiC/A356
Unreinforced A356

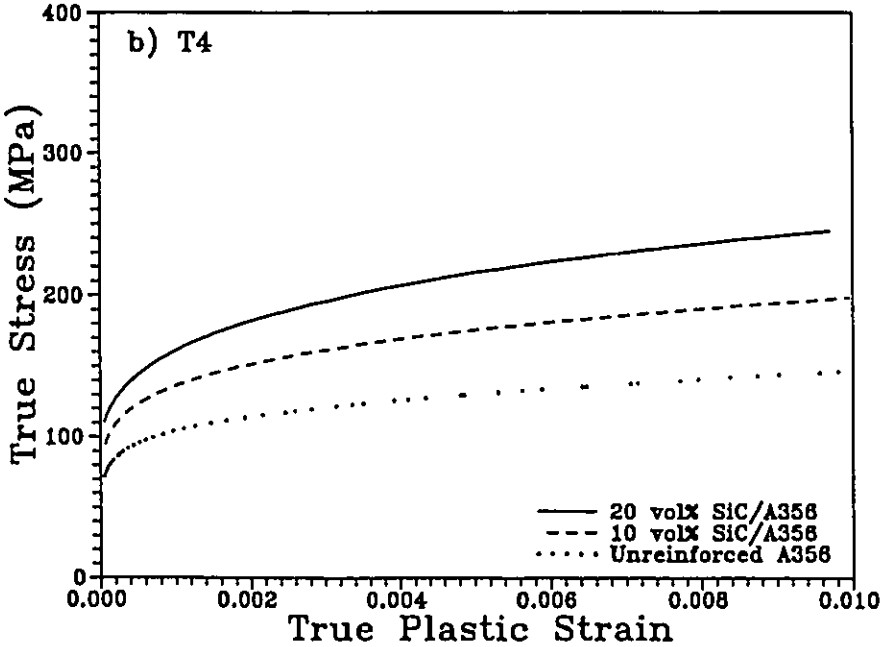
b) T4
True Stress (MPa)
True Plastic Strain
0
100
200
300
400
0.000
0.002
0.004
0.006
0.008
0.010
20 vol% SiC/A356
10 vol% SiC/A356
Unreinforced A356

FIG. 3.14 a,b

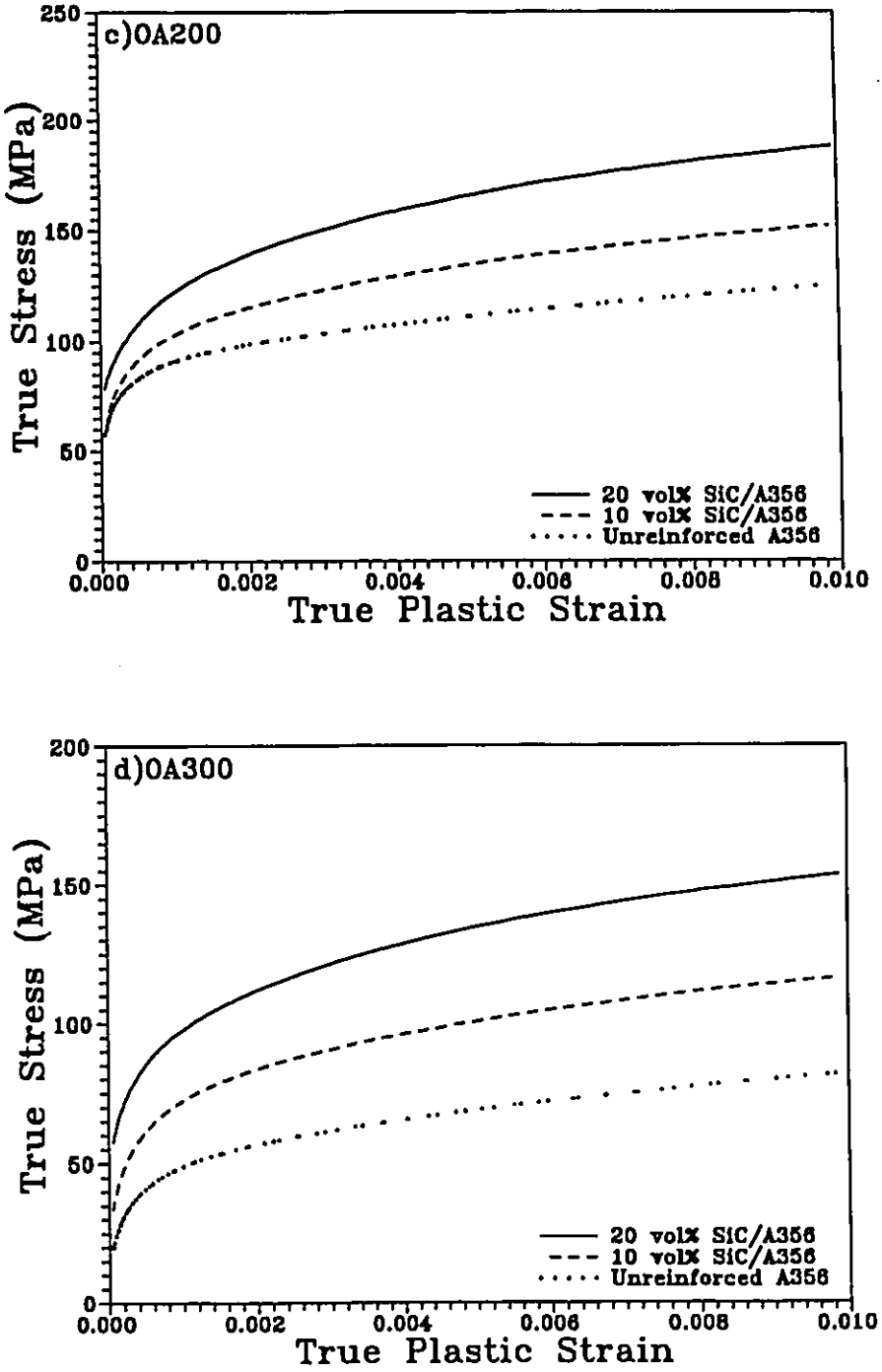

Figure 3.14: Plastic stress-strain curves comparing unreinforced alloy and 10 and 20 vol% SiC composites in; a) T61; b) T4; c) OA200; and d) OA300 ageing conditions

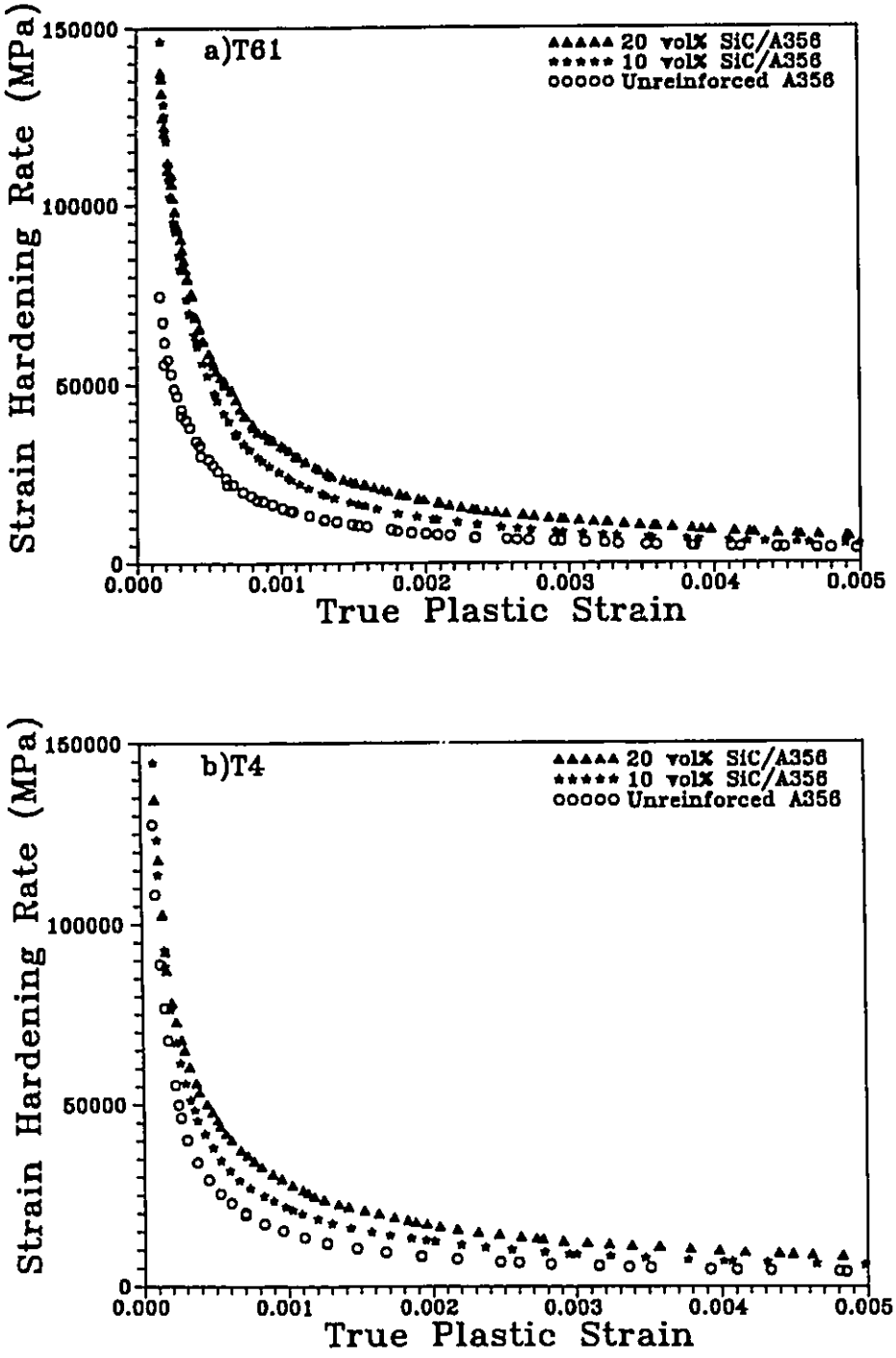
a)T61
▲▲▲▲▲ 20 vol% SiC/A356
★★★★★ 10 vol% SiC/A356
ooooo Unreinforced A356
Strain Hardening Rate (MPa)
150000
100000
50000
0
0.000
0.001
0.002
0.003
0.004
0.005
True Plastic Strain
b)T4
▲▲▲▲▲ 20 vol% SiC/A356
★★★★★ 10 vol% SiC/A356
ooooo Unreinforced A356
Strain Hardening Rate (MPa)
150000
100000
50000
0
0.000
0.001
0.002
0.003
0.004
0.005
True Plastic Strain

FIG. 3.15 a, b

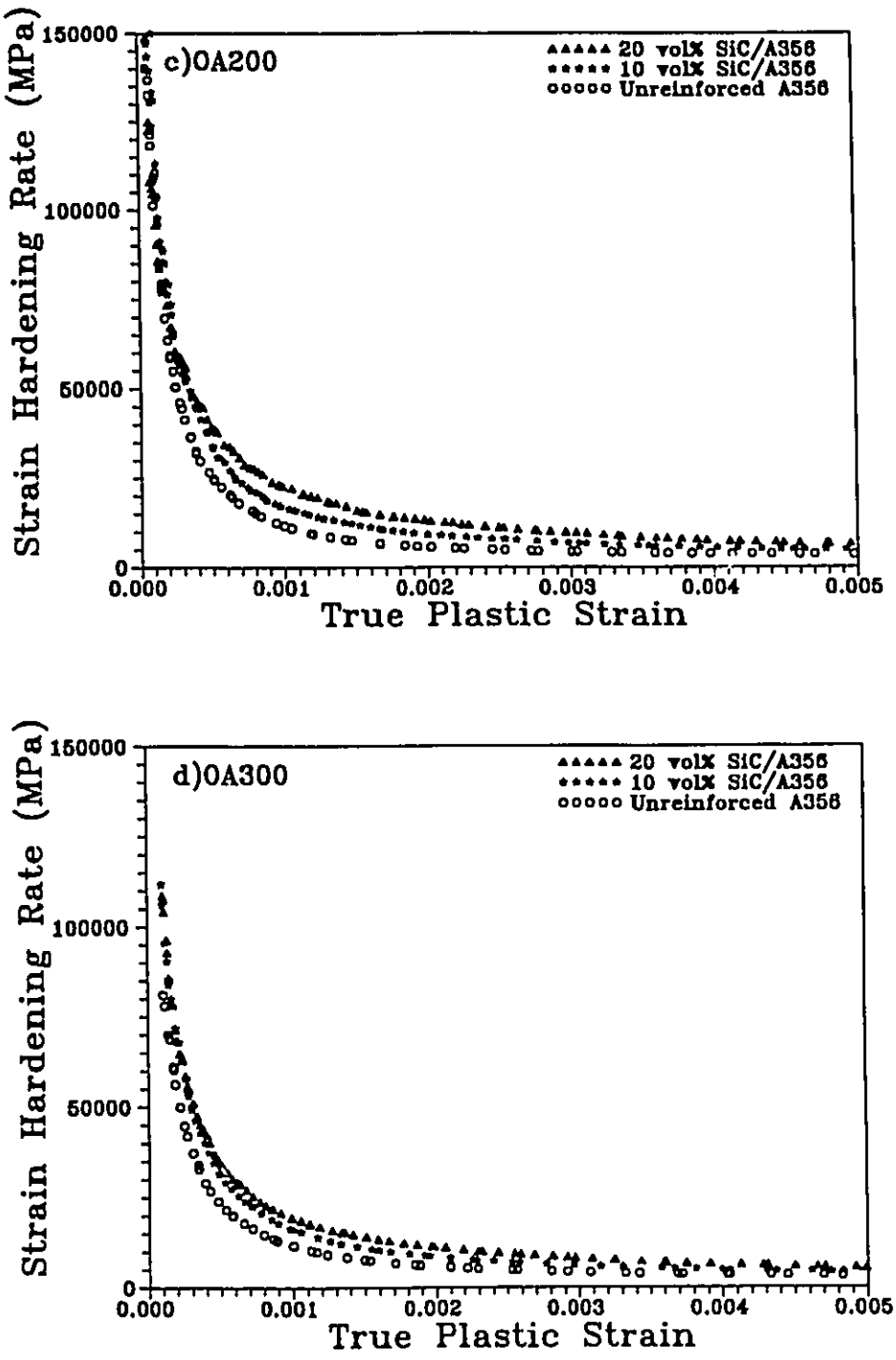

Figure 3.15: Strain hardening rate versus plastic strain (ϵ^c_p) for unreinforced alloy and 10 and 20 vol% SiC composites in; a) T61; b) T4; c) OA200; and d) OA300 ageing conditions

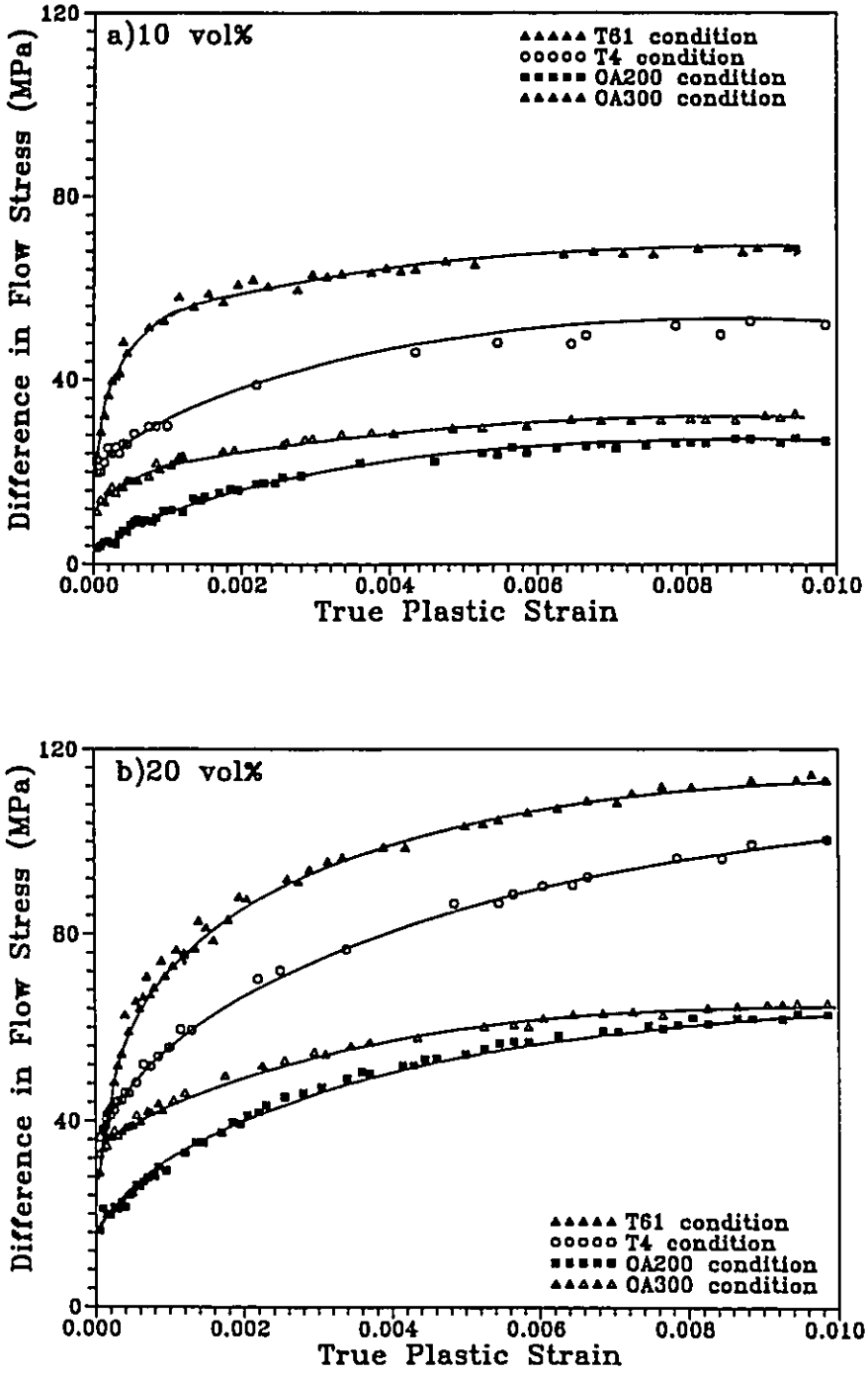

Figure 3.16: Difference in flow stress between composite and alloy versus plastic strain (ϵ^c_p); a) 10 vol% composite; b) 20 vol% composite.

the T61 and T4 conditions.

Reproducibility in stress-strain behaviour. Reproducibility in stress-strain behaviour was very good within the same heat treated batch. Figure 3.17a illustrates an example of 3 tensile samples machined from the 20 vol% SiC composite and heat treated together to the T61 condition. The reproducibility of the heat treatment itself was more difficult as indicated by the five samples of Figure 3.17b all of which were given nominally the same heat treatment but performed on a different date. The T61 condition was the most difficult condition to reproduce. Figure 3.17c shows the variation between specimens heat treated to the OA200 condition on four different occasions. To avoid problems with variability all comparisons between alloy and composite and between tension and compression were made with materials from the same heat treated batch.

3.2.2.3 Compression Tests

Compression tests up to a strain of .01 were performed on the same materials discussed in the previous section in order to compare with tensile behaviour. The total true stress-true strain curves for the unreinforced alloy are plotted in Figure 3.18 for the various ageing conditions. The alloy exhibits a strength differential effect such that the compression curve is slightly higher than the tensile curve. After plastic strains of about .001 this difference remains essentially constant with continued straining.

The true stress - true strain curves for the composite materials are show in Figure 3.19. This shows significantly different behaviour than that of the unreinforced alloy. The composite materials yield at lower stresses in compression when compared to tension, particularly in the harder aged conditions. Figure 3.20 illustrates the strain hardening rates in the 20 vol% composite. Results for the 10 vol% composite are similar. The higher rates in compression results

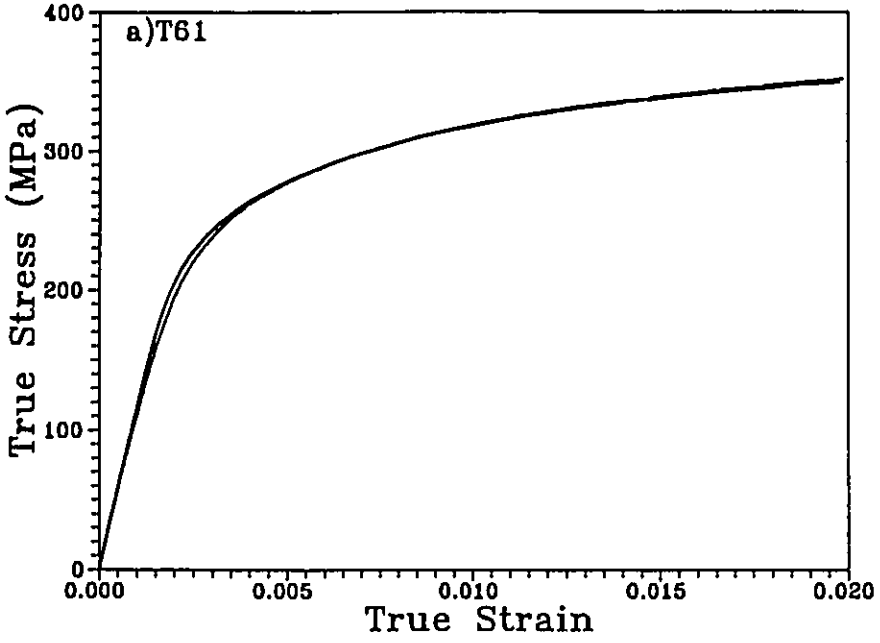
a)T61
True Stress (MPa)
400
300
200
100
0
0.000
0.005
0.010
0.015
0.020
True Strain

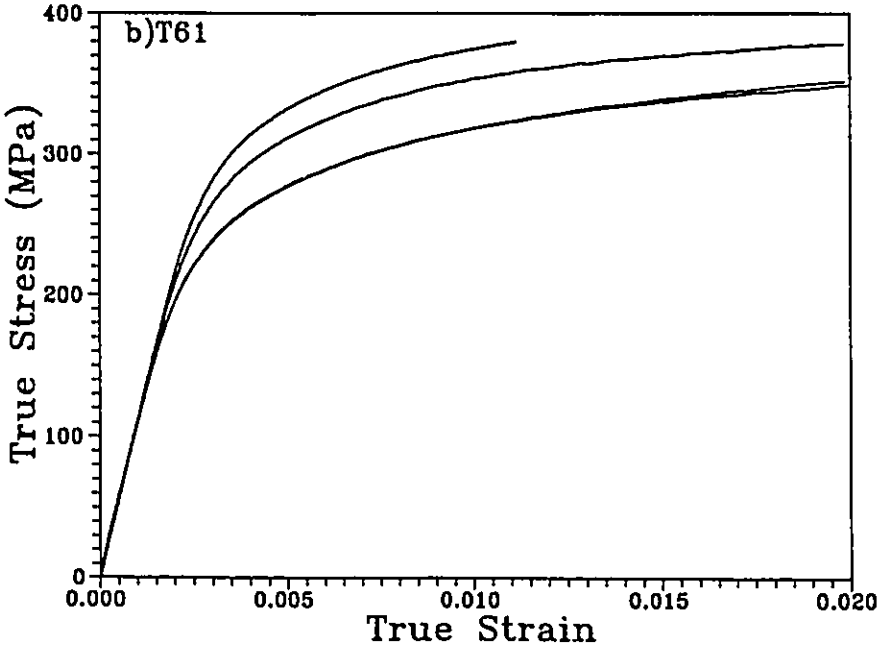
b)T61
True Stress (MPa)
400
300
200
100
0
0.000
0.005
0.010
0.015
0.020
True Strain

FIG. 3.17 a, b

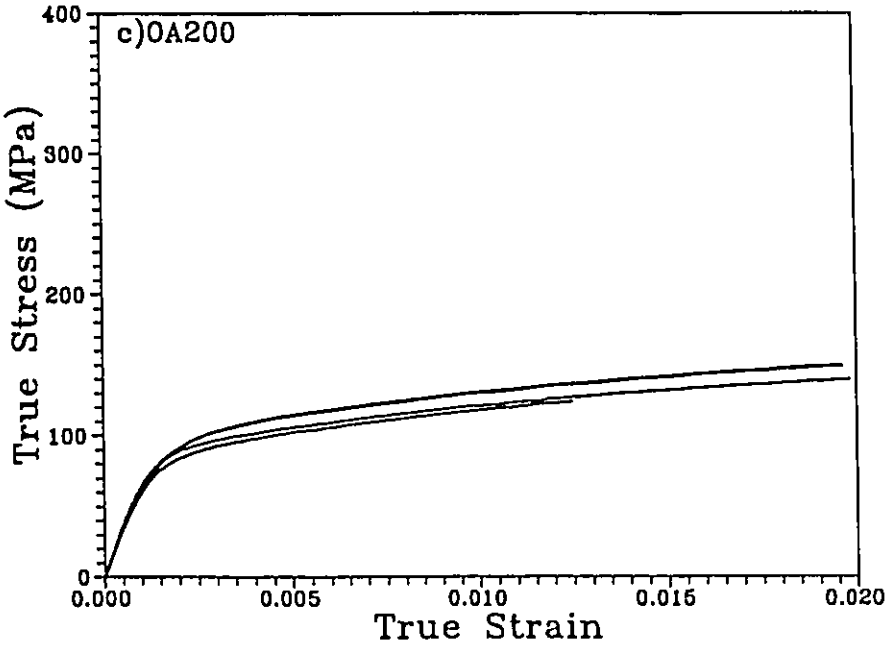

Figure 3.17: Variability between; a) 3 specimens within the same heat treatment batch (T61 condition); b) specimens in 3 different heat treatment batches (T61 condition); c) specimens in 4 different heat treatment batches (OA200 condition).

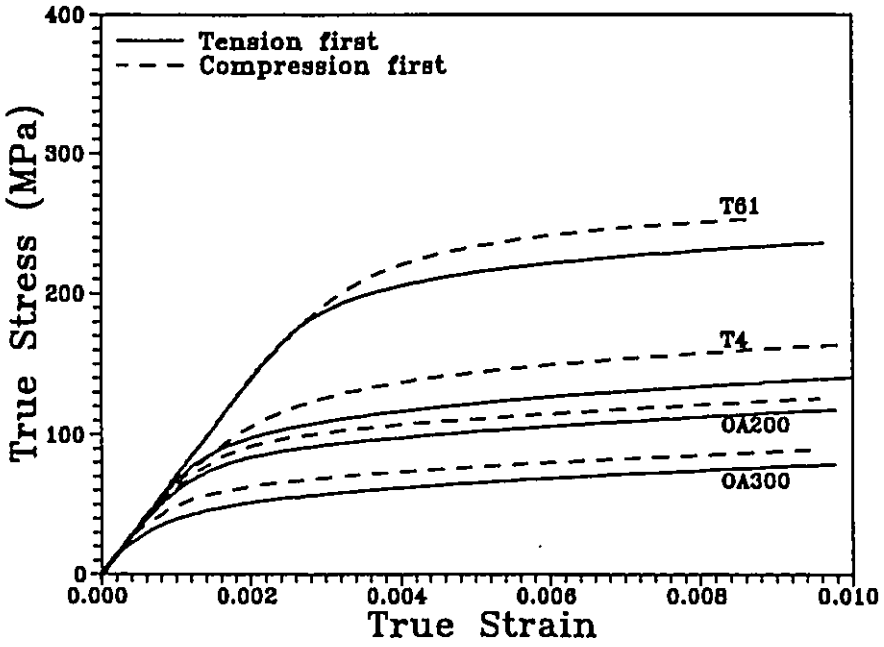

Figure 3.18: Differences between the flow behaviour in tension and compression for the unreinforced A356 alloy.

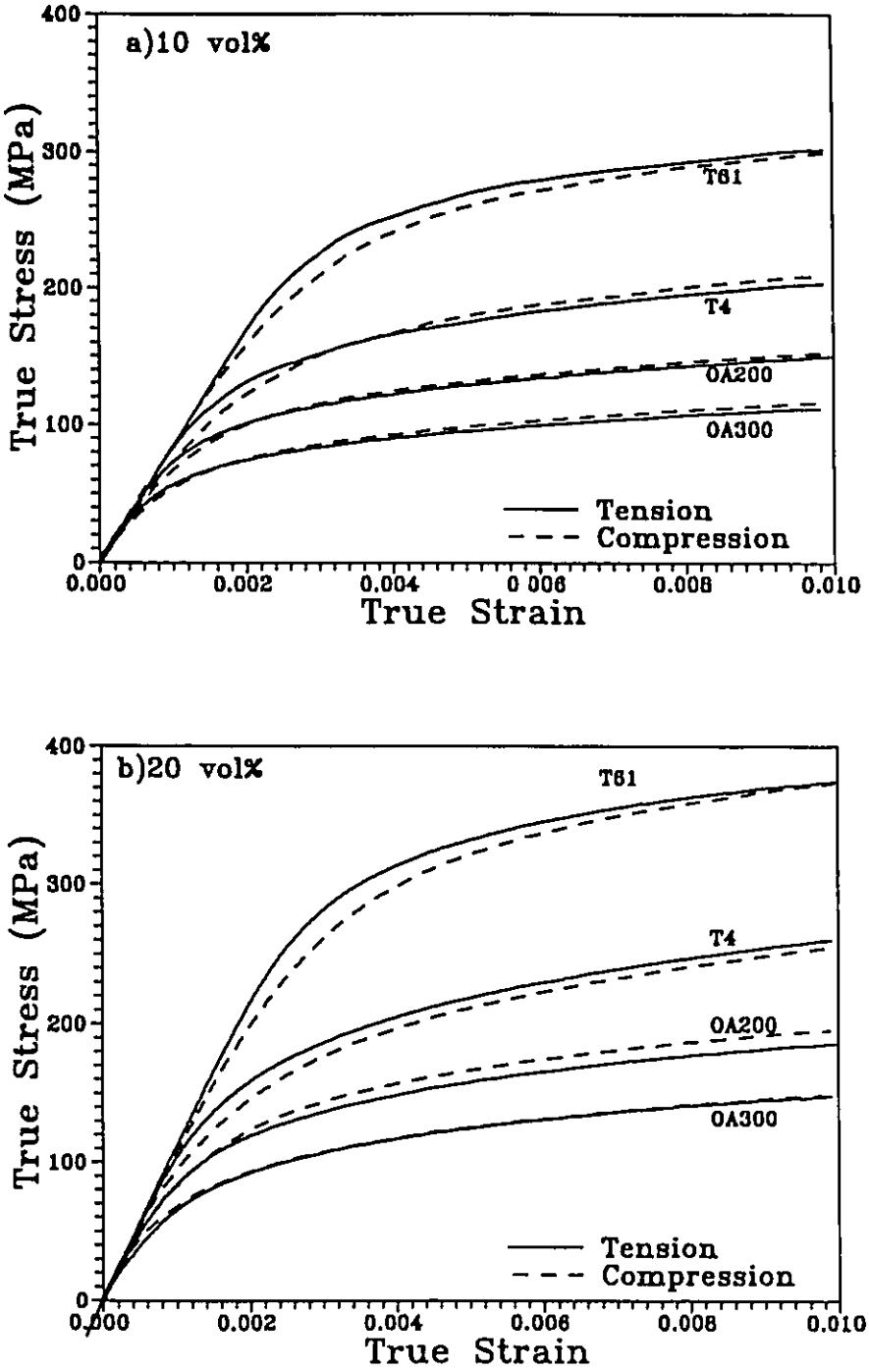

Figure 3.19: Differences in tension and compression for the composite materials; a) 10 vol% SiC/A356; b) 20 vol% SiC/A356.

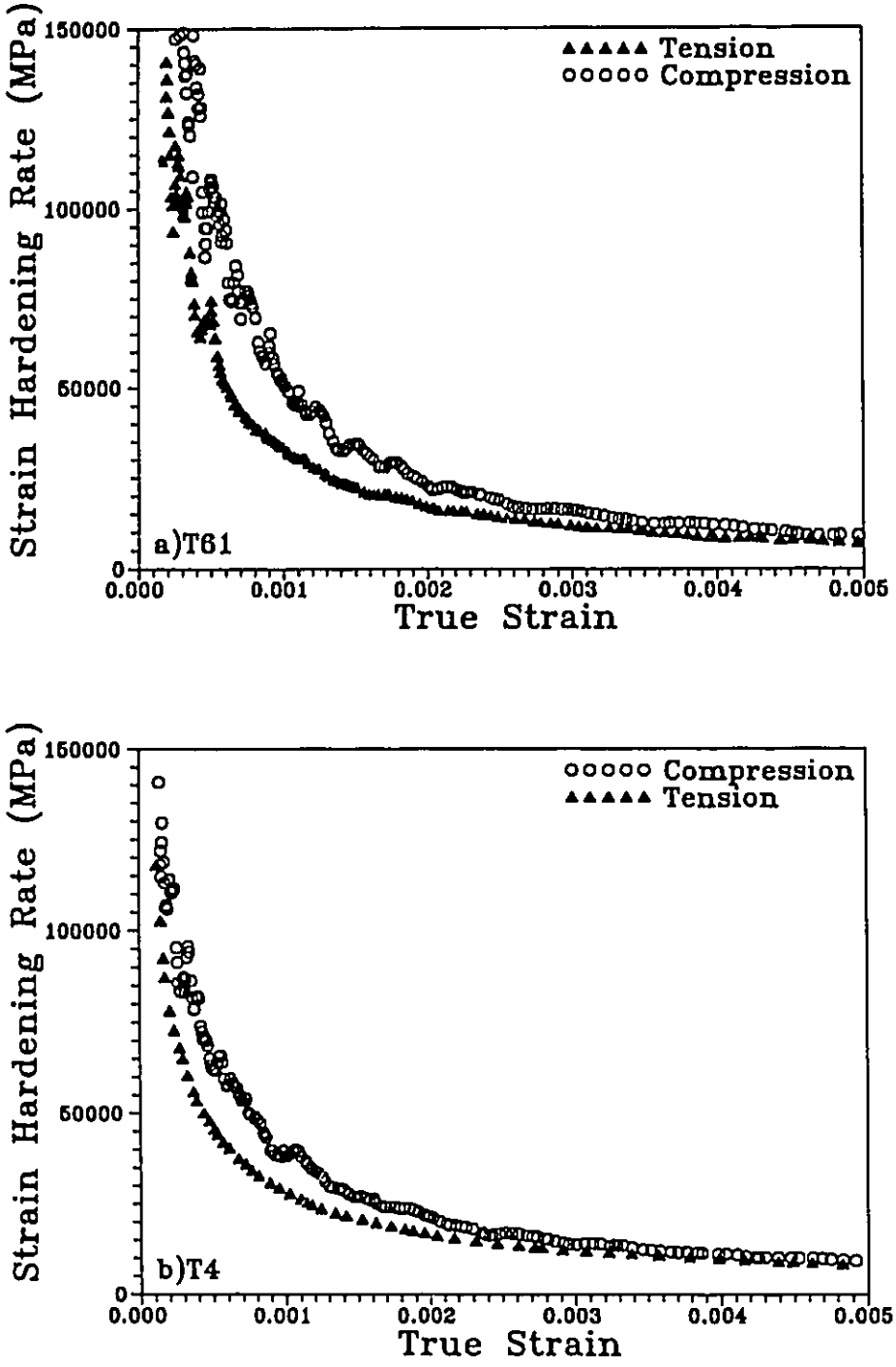
Strain Hardening Rate (MPa)
150000
100000
50000
0
▲▲▲▲▲ Tension
ooooo Compression
a)T61
0.000
0.001
0.002
0.003
0.004
0.005
True Strain
Strain Hardening Rate (MPa)
150000
100000
50000
0
ooooo Compression
▲▲▲▲▲ Tension
b)T4
0.000
0.001
0.002
0.003
0.004
0.005
True Strain

FIG. 3.20 a, b

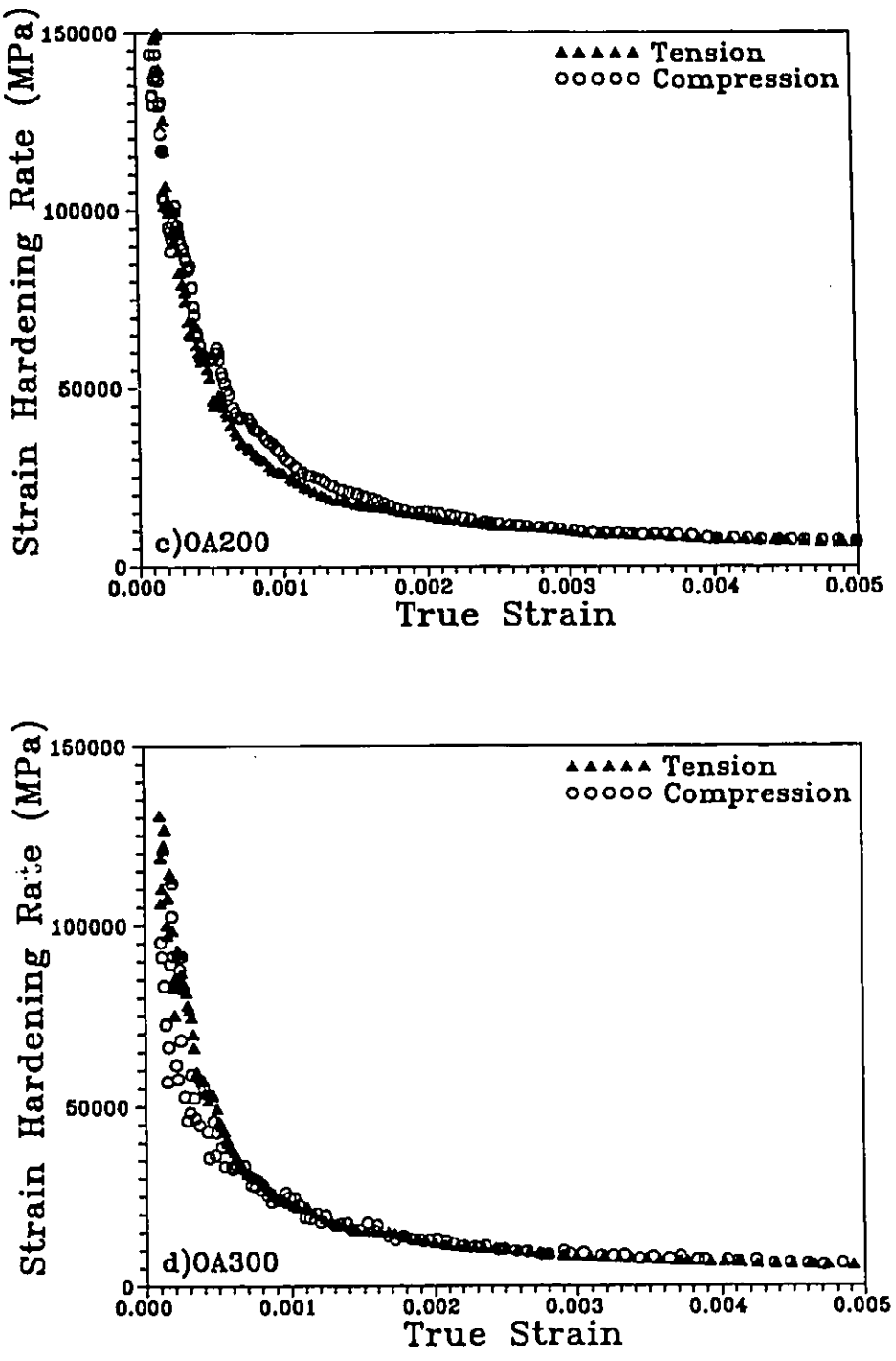

Figure 3.20: Strain hardening rate, in tension and compression, versus plastic strain (ϵ^c_p) for 20 vol% composite in; a) T61; b) T4; c) OA200 and d) OA300 ageing condition

in a "cross over" effect such that the compression flow curve is equal to or higher than the tension curve at higher strains. Figure 3.21 shows stress-strain behaviour over a larger range of strain for the composite materials. (These curves are derived from the forward portions of load reversal tests such as that depicted in Figure 3.37. The details of these experiments will be described in section 3.3). The cross over effect in the composites is more clearly shown over this strain range.

From the results of Figures 3.19 and 3.21 it is evident that the cross over effect is largest in the T4 and T61 conditions. In the overaged conditions the effect is much smaller, the compression curves generally cross over at lower strains and begin to display a strength differential effect similar to the unreinforced alloy at lower strains than that seen for the T4 and T61 conditions.

With such a subtle difference between tension and compression, it is important to establish how reproducible the cross over effect is. Figure 3.22 presents a third heat treatment for the 20 vol% composite in the T61 condition. Comparing this result with that of Figure 3.19b and 3.21c, which represent two separate heat treatments, a consistent trend is established. Although some quantitative differences exist (i.e. the level of strain for cross over is different form batch to batch) the same general characteristic is seen.

3.2.3 Stress-Strain Behaviour at Larger Strains

In this section, the stress-strain behaviour of the alloy and composite will be compared up to strains of .07. In many cases, if the composite does not fracture first, it begins to neck at strains beyond .07. Consequently, comparisons with the alloy, which does deform uniformly beyond this strain, become complicated.

A summary of the plastic stress-strain curves for all the materials is illustrated in Figure

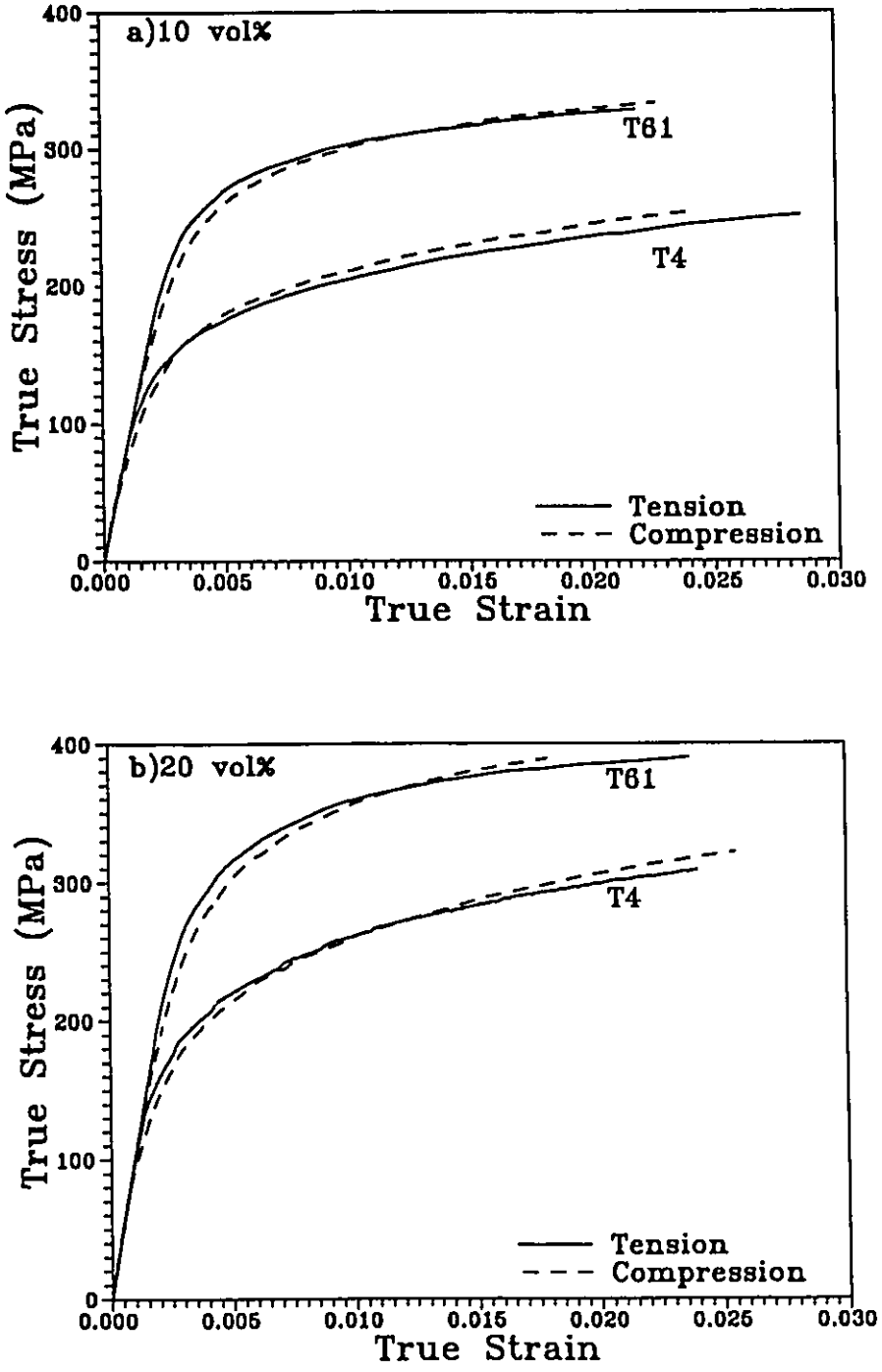

Figure 3.21: Difference between tension and compression over a larger strain range for; a) 10 vol% and; b) 20 vol% composite. Curves were derived from multi-loop tests (see section 3.3.3).

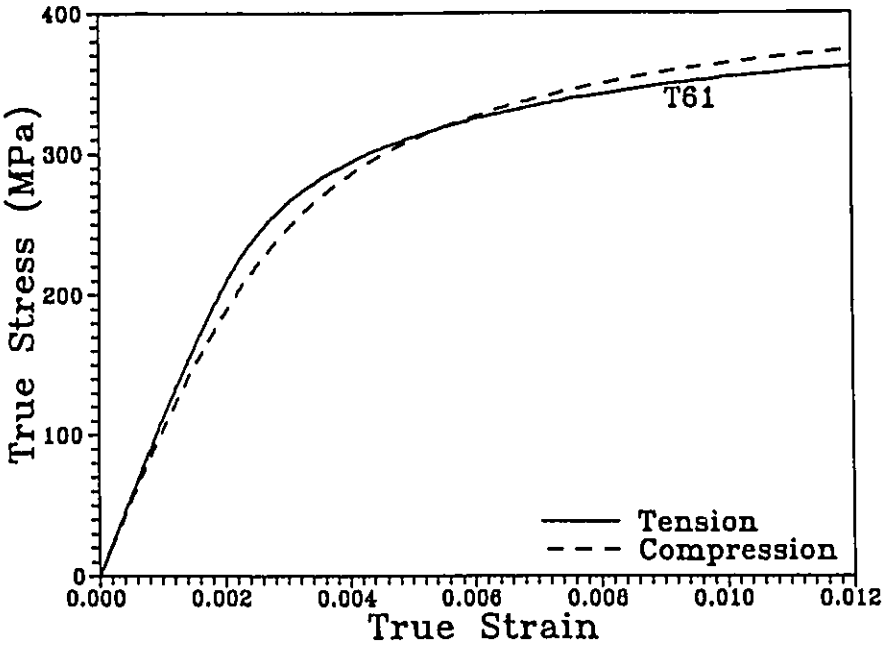

Figure 3.22: Third heat treatment batch for the 20 vol% Composite in the T61 condition.

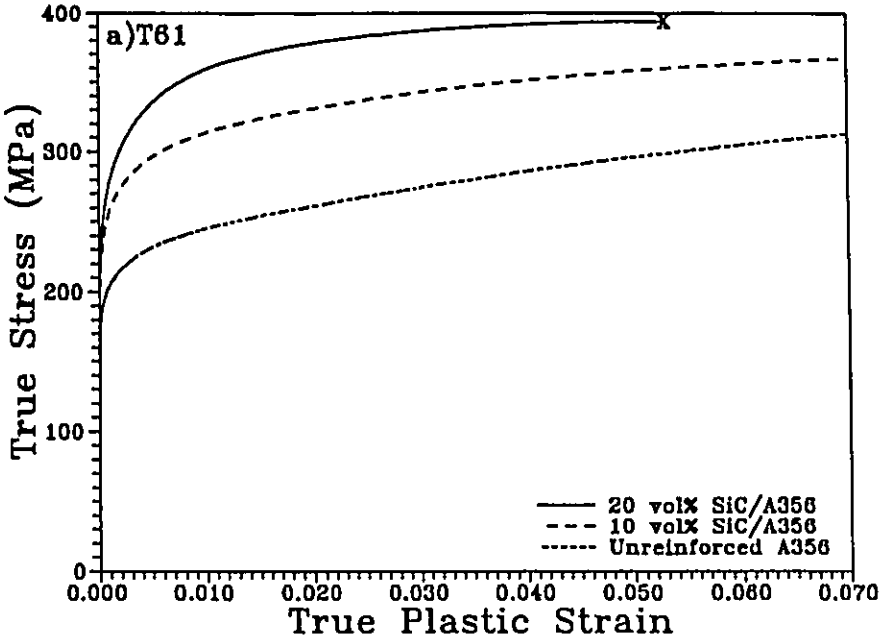
a)T61
True Stress (MPa)
True Plastic Strain
0
100
200
300
400
0.000
0.010
0.020
0.030
0.040
0.050
0.060
0.070
20 vol% SiC/A356
10 vol% SiC/A356
Unreinforced A356

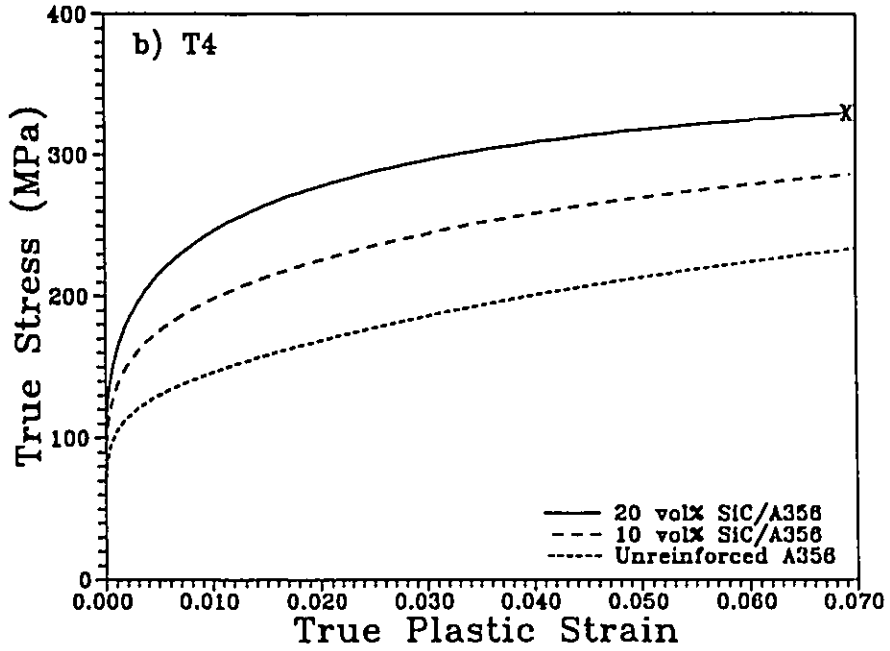
b) T4
True Stress (MPa)
True Plastic Strain
0
100
200
300
400
0.000
0.010
0.020
0.030
0.040
0.050
0.060
0.070
20 vol% SiC/A356
10 vol% SiC/A356
Unreinforced A356

FIG. 3.23 a, b

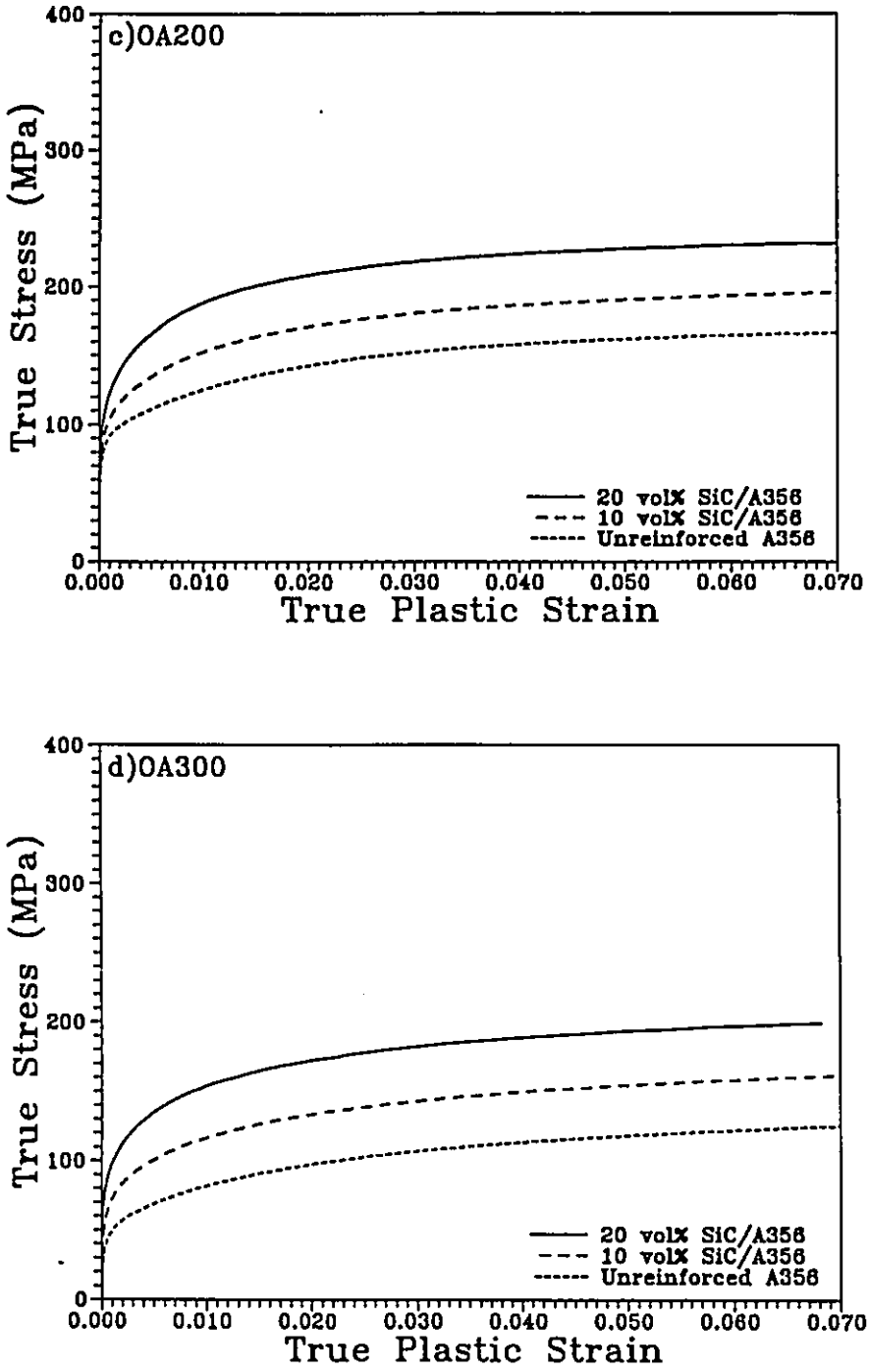

Figure 3.23: True plastic stress-strain curves comparing the alloy and composites at larger strains in; a) T61; b) T4; c) OA200 and d) OA300 ageing states.

3.23. The small difference in yield strength between the alloy and composite is much more evident in these figures. It is also clearer that much of the strengthening developed in the composite occurs at low plastic strains (up to .005 to .01). After this , the curves become somewhat parallel.

Figure 3.24. plots the strain hardening rates of the materials in the different ageing conditions. In all the materials, the strain hardening rate continually decreases with strain. However after strains of about 2-3%, the decrease is more gradual and in some cases hardening rates become nominally constant with strain.

In the unreinforced alloy the hardening rates are influenced by ageing conditions at these higher strain. This is in contrast to that previously observed at low strains (Figure 3.11b.). At the highest strains the hardening rate in the T4 and T61 conditions are approximately equal. The overaged structures have lower hardening rates.

The composites show similar trends with ageing condition. However the hardening rate in the T61 state is lower than that in the T4 state and is equal to or below the rates for the overaged structures.

Figure 3.25. compares the alloy and composite strain hardening rates in a given ageing condition. As previously described, at low strains the hardening rate is higher in the composites and increases with volume fraction. However in the T4 and T61 states, the hardening rates in the composite drop below that of the alloy at strains of about 0.018 and 0.026 respectively. In the overaged structures the hardening rates of all the materials become equal at roughly the same levels of strain.

To summarize the effects this strain hardening behaviour has on strengthening, the difference in the flow strength of the alloy and composites is plotted in Figure 3.26. Again we see a very rapid increase in strengthening for all ageing conditions in the first .005 to .01 of

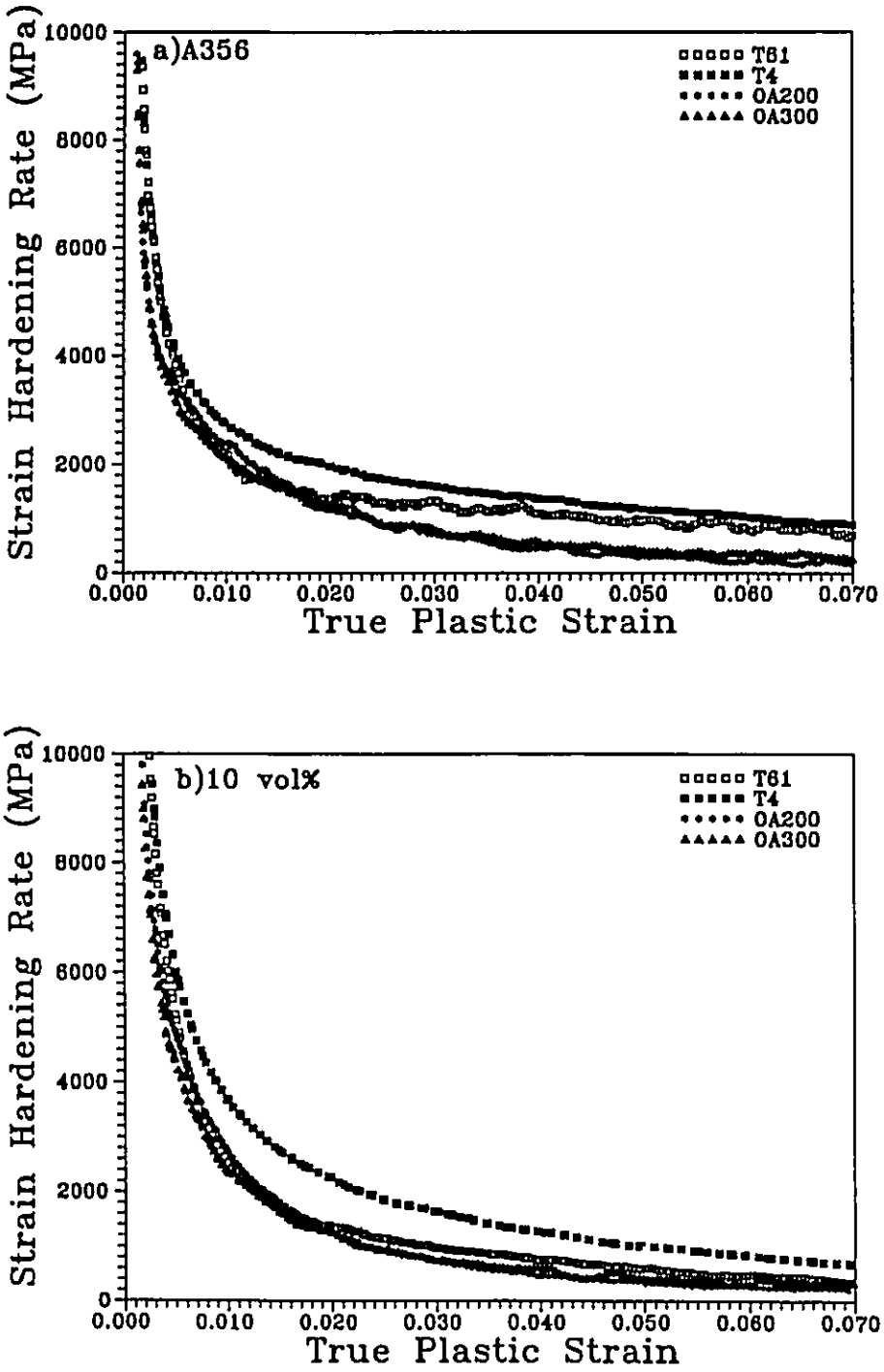
a)A356
T61
T4
OA200
OA300
Strain Hardening Rate (MPa)
True Plastic Strain
0
2000
4000
6000
8000
10000
0.000
0.010
0.020
0.030
0.040
0.050
0.060
0.070
b)10 vol%
T61
T4
OA200
OA300
Strain Hardening Rate (MPa)
True Plastic Strain

FIG. 3.24 a,b

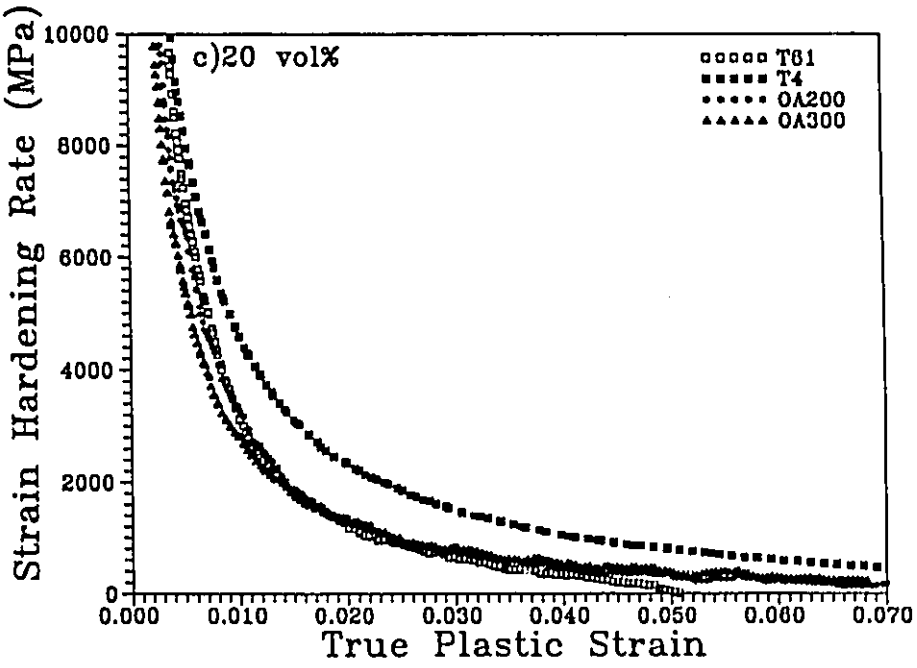

Figure 3.24: Strain hardening rate versus plastic strain (ϵ^c_p) for different ageing conditions; a) unreinforced A356; b) 10 vol%/SiC composite; c) 20 vol%/SiC composite.

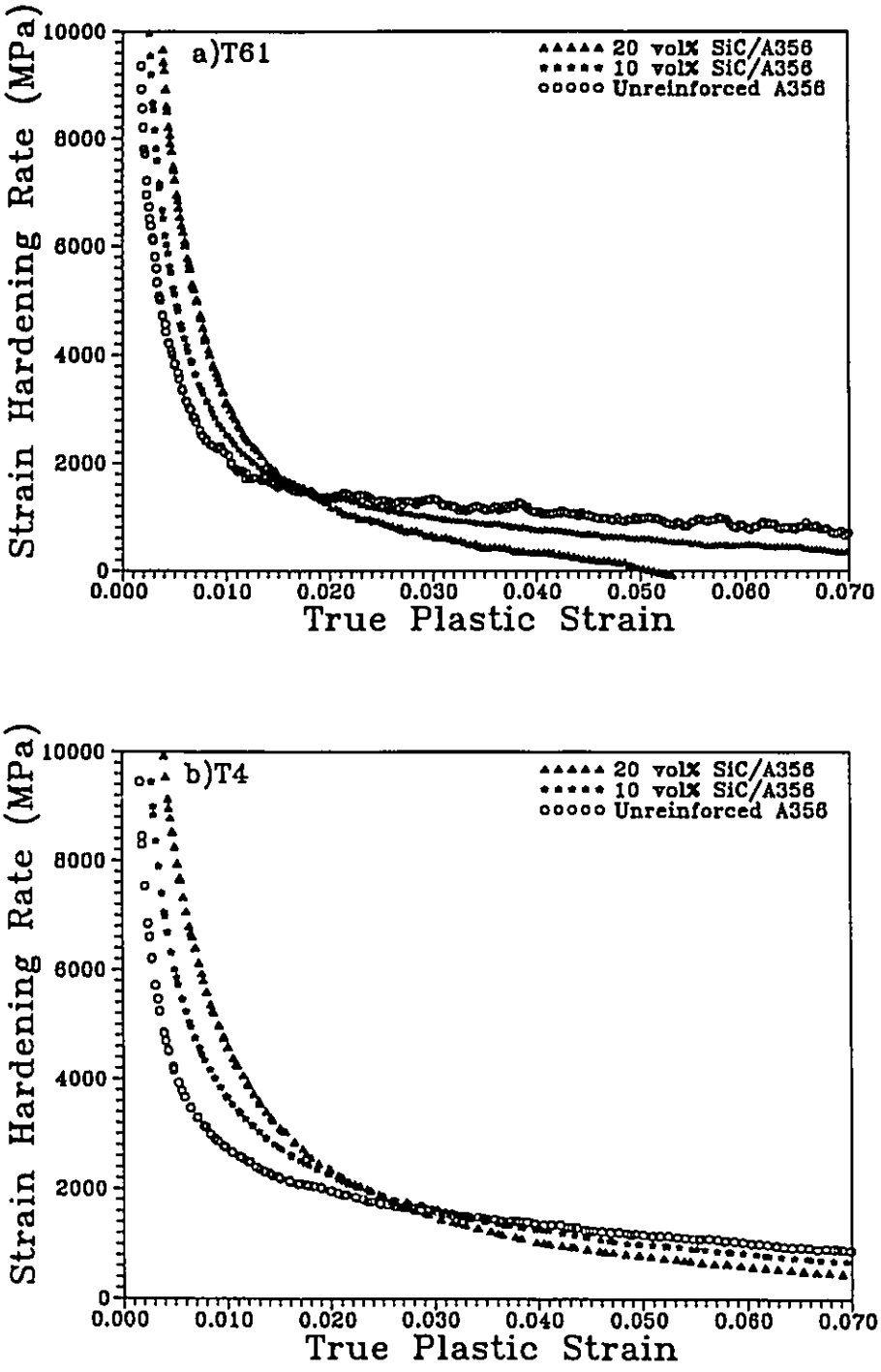
a)T61
20 vol% SiC/A356
10 vol% SiC/A356
Unreinforced A356
Strain Hardening Rate (MPa)
True Plastic Strain
0
2000
4000
6000
8000
10000
0.000
0.010
0.020
0.030
0.040
0.050
0.060
0.070
b)T4
20 vol% SiC/A356
10 vol% SiC/A356
Unreinforced A356
Strain Hardening Rate (MPa)
True Plastic Strain

FIG. 3.25 a, b

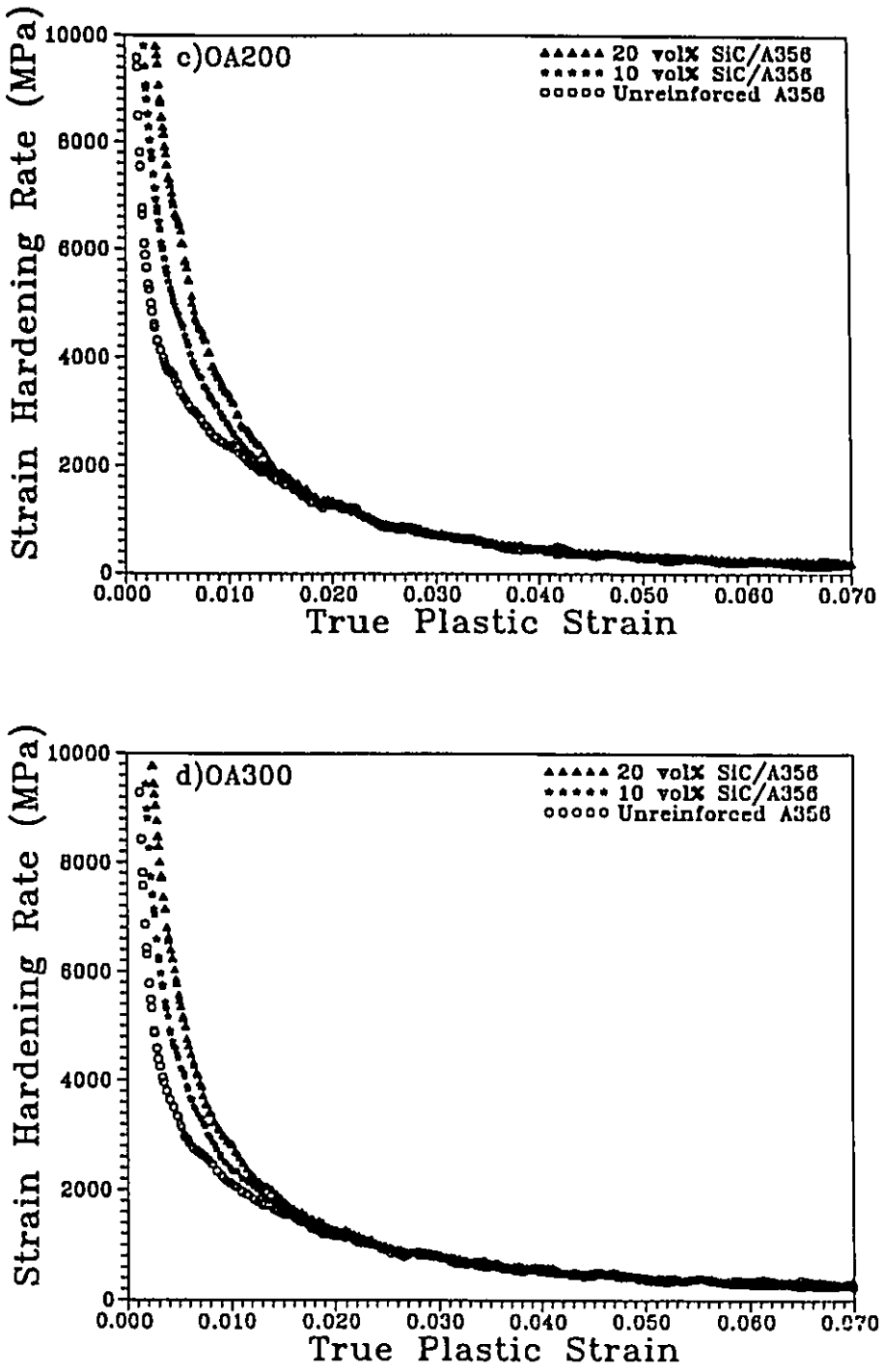

Figure 3.25: Comparison of the strain hardening rate in the alloy and composites when aged to the; a) T61; b) T4; c) OA200 and d) OA300 states.

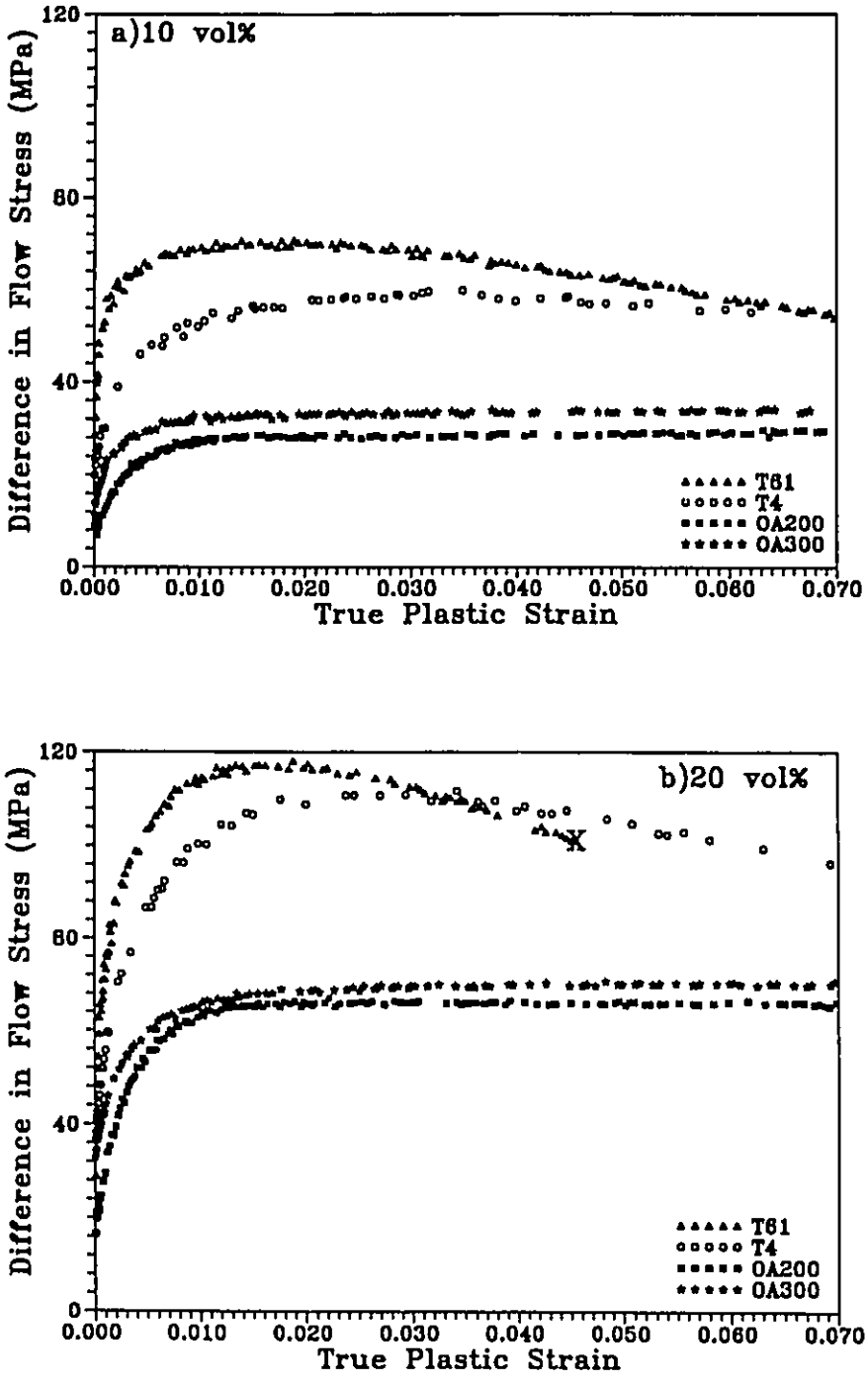

Figure 3.26: Difference between the flow stress of the composite and alloy in the various ageing conditions; a) 10 vol% SiC/A356; b) 20 vol% SiC/A356.

plastic strain. This increase drops off earlier in the overaged conditions and is approximately constant after a strain of .02. This results in stress-strain curves which are parallel as indicated in Figure 3.23c and d. In the T4 and T61 conditions, maximum strengthening occurs at strains which correspond to the point at which the hardening rate in the composites drop below that of the alloy in Figure 3.25.

Figure 3.26 indicates that the strengthening increment obtained increases with an increase in particle volume fraction. Strengthening is nominally the same for T4 and T61 conditions and is roughly twice that obtained with the overaged structures which are also nominally equal. However the actual stress levels achieved in these materials differ considerably. It is useful to compare strengthening on a normalized basis by plotting the ratio of the composite to alloy flow stress versus strain (Figure 3.27). On this basis the degree of strengthening achieved at large strains is similar in all ageing conditions for a given volume fraction. The T4 and T61 curves show a continual decrease in strengthening ratio after strains of about .015. The overaged curves show signs of saturating after strains of .03. Similar trends are seen for both 10 and 20 vol% composites although the value of the ratio is smaller in the 10 vol% composite. For both volume fractions, the strengthening ratio is somewhat higher in the OA300 ageing condition.

3.2.4 Plastic Flow on a Polished Surface

The results of sections 3.2.2 and 3.2.3 clearly indicates that the majority of strengthening afforded by the SiC particles develops during the initial stages of plastic flow. In particular, very high strain hardening rates are exhibited by the composite materials at plastic strains below .5%. This strain regime is in the range of the elastic/plastic transition which was described in the introduction. Because of the importance of this region, it would be helpful to obtain direct evidence of how plastic flow is initiated in the composite materials.

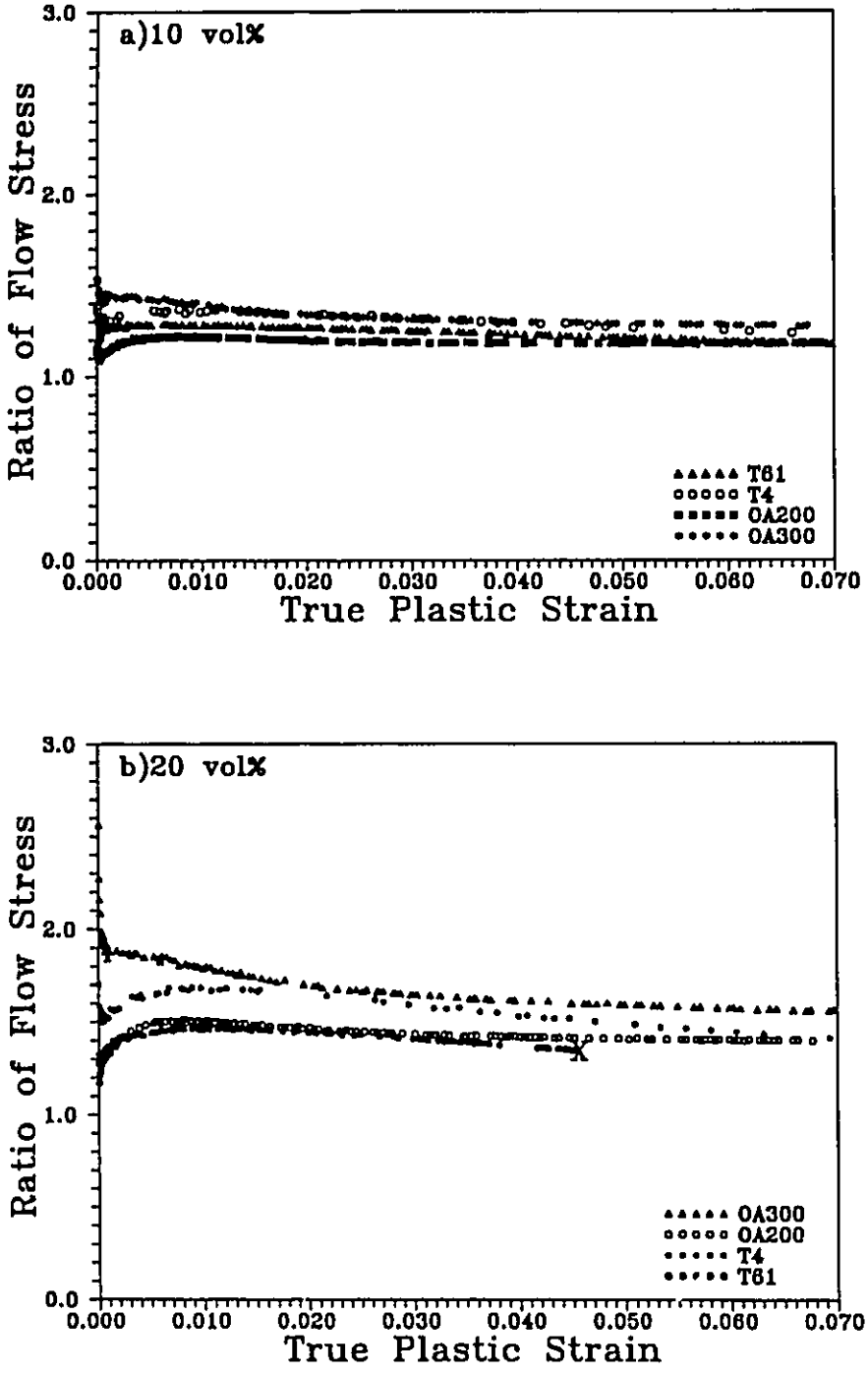

Figure 3.27: Ratio between composite and alloy flow stress versus plastic strain (ϵ^{c}_{p}) for the; a) 10 vol% and b) 20 vol% composite.

To accomplish this a cylindrical shape, with the dimensions of the gauge section of a tensile sample, was machined from the 20 vol% composite. A surface along the axis of the cylinder was then polished so that observations of plastic flow could be made. The sample was then deformed in compression to induce a small amount of plastic flow, after which its polished surface was observed under an optical microscope using Nomarski contrast. In this way slip lines on the surface could be resolved.

After a plastic strain of .05%, no slip was resolvable on the surface. After a further plastic strain of .1% (i.e. a total of .15%), the majority of the sample still did not indicate any resolvable slip. However some regions of the microstructure did reveal some slip lines. Micrographs which represent the slip morphology in these regions are presented in Figure 3.28.

The evidence of these micrographs suggests that the initial plastic flow is associated with regions of the matrix that are relatively particle free (regions marked A,B,C.) This indicates that the complex pattern of flow that occurs in the elastic/plastic transition, is further complicated by the non-uniform distribution of the SiC particles.

3.3 The Bauschinger Effect

3.3.1 Introduction

The principal goal of the experiments in this section was to obtain qualitative information concerning the development of internal stress (mean matrix stress) as a function of SiC content, variation in the flow strength of the matrix due to heat treatment and the level of plastic prestrain. The primary focus was on the low strain regime, therefore the data obtained here was limited to plastic prestrains below about 3% in tension and 1.5% in compression.

As discussed in the introduction, there are a number of ways in which the Bauschinger

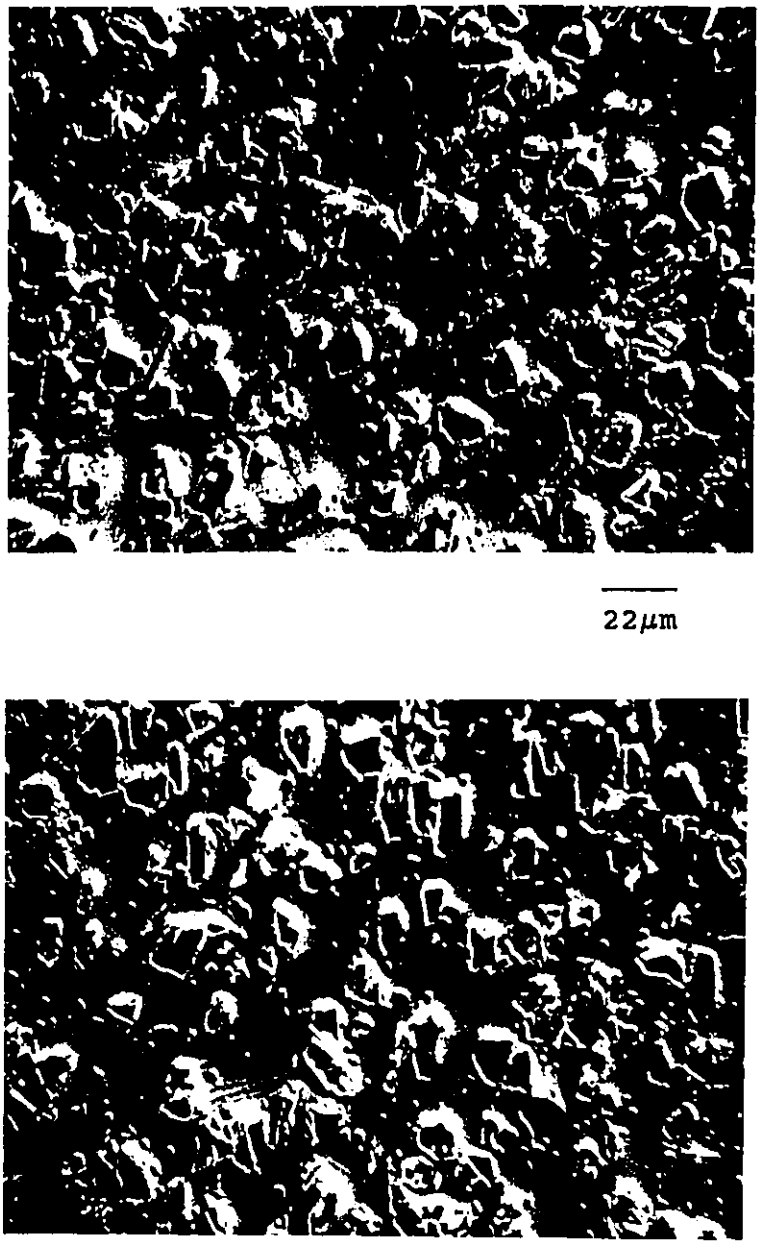

Figure 3.28: Slip lines on the polished surface of a 20 vol% composite deformed in compression by .15% plastic strain.

effect in a material may be characterized. These include a measurement of permanent softening, $\Delta\sigma$, the Bauschinger stress, σ_b and the Bauschinger strain, ϵ_B. A choice of which measurements to use depends, in part on the type of reverse behaviour exhibited by the material. Therefore the first section of this work (section 3.3.2), investigated the general characteristics of the Bauschinger effect in the unreinforced alloy and composite materials. Single loop experiments were performed to a prestrain of about .01. Only the unreinforced and 20 vol% composite were tested in this way. In addition, the influence that a variation of matrix flow strength, as a result of heat treatment, had on the Bauschinger effect was also investigated.

In section 3.3.3 the development of the Bauschinger effect with plastic strain was investigated. Tests on the alloy and both the 10 and 20 vol% composites were performed to investigate the effect of increasing SiC content. The form of the experiments of section 3.3.3 were largely developed on the basis of observations made on the single loop experiments and will be described in more detail in section 3.3.3.

3.3.2 Single Loop Experiments

The general characteristics of the Bauschinger effect in the alloy and composite are illustrated in Figure 3.29. All the materials have very rounded reverse flow curves after a forward plastic strain of about .01. The forward flow stress and reverse yield strength (measured with offsets of .0001, .001 and .002) are plotted in Figure 3.30. All the specimens, regardless of heat treatment or SiC content exhibit yield stresses in the reverse direction in the range of +/- 20 MPa. This small amount of plastic flow during unloading appears to be a general characteristic of most materials and has been observed to occur in a variety of both pure FCC and BCC metal polycrystals (Woolley, 1954).

By reflecting the reverse curve into the forward quadrant, more detailed observations can

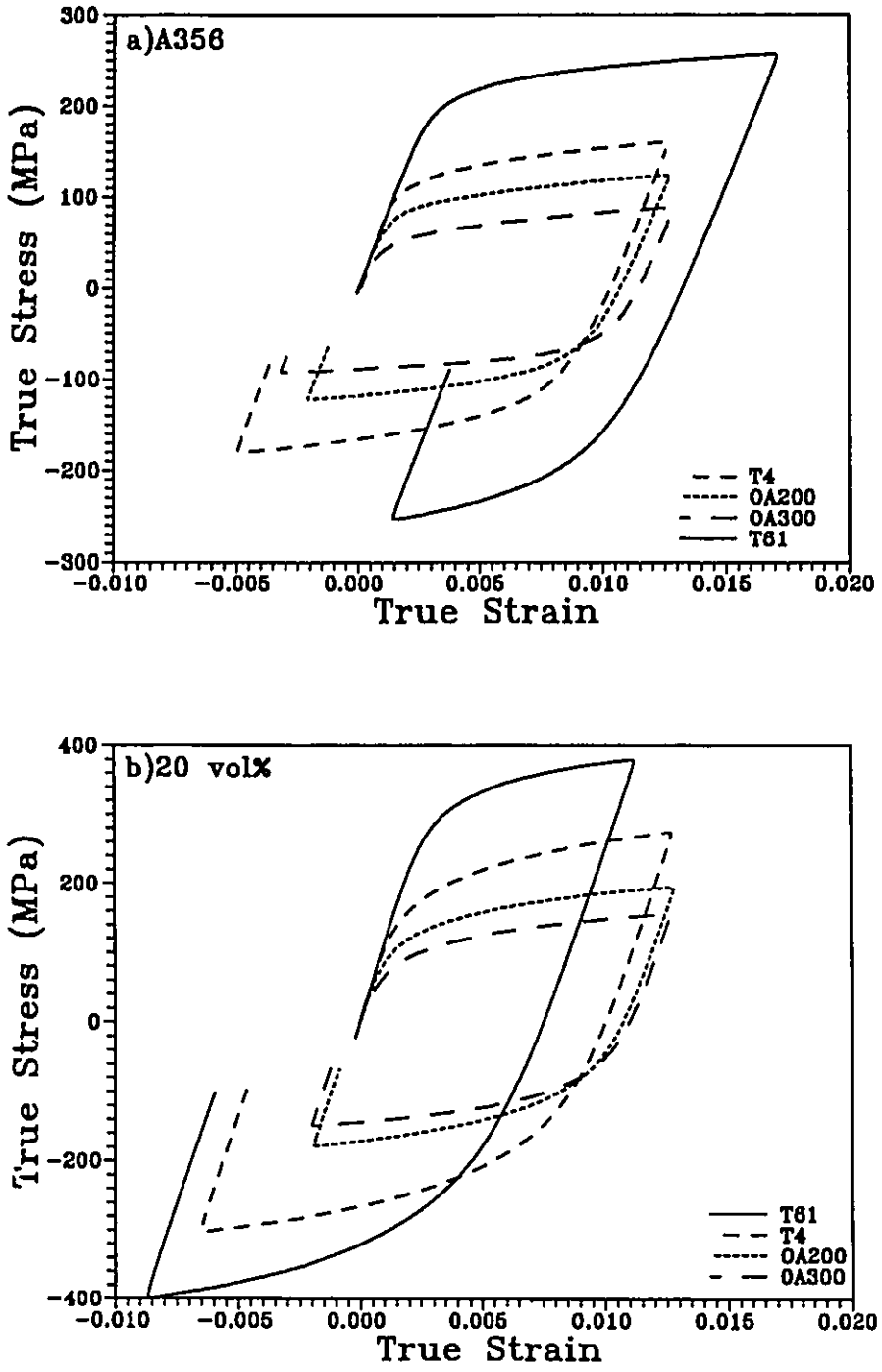

Figure 3.29: Bauschinger loops for the materials in various ageing conditions; a) unreinforced A356; b) 20 vol% composite. Forward deformation was in tension.

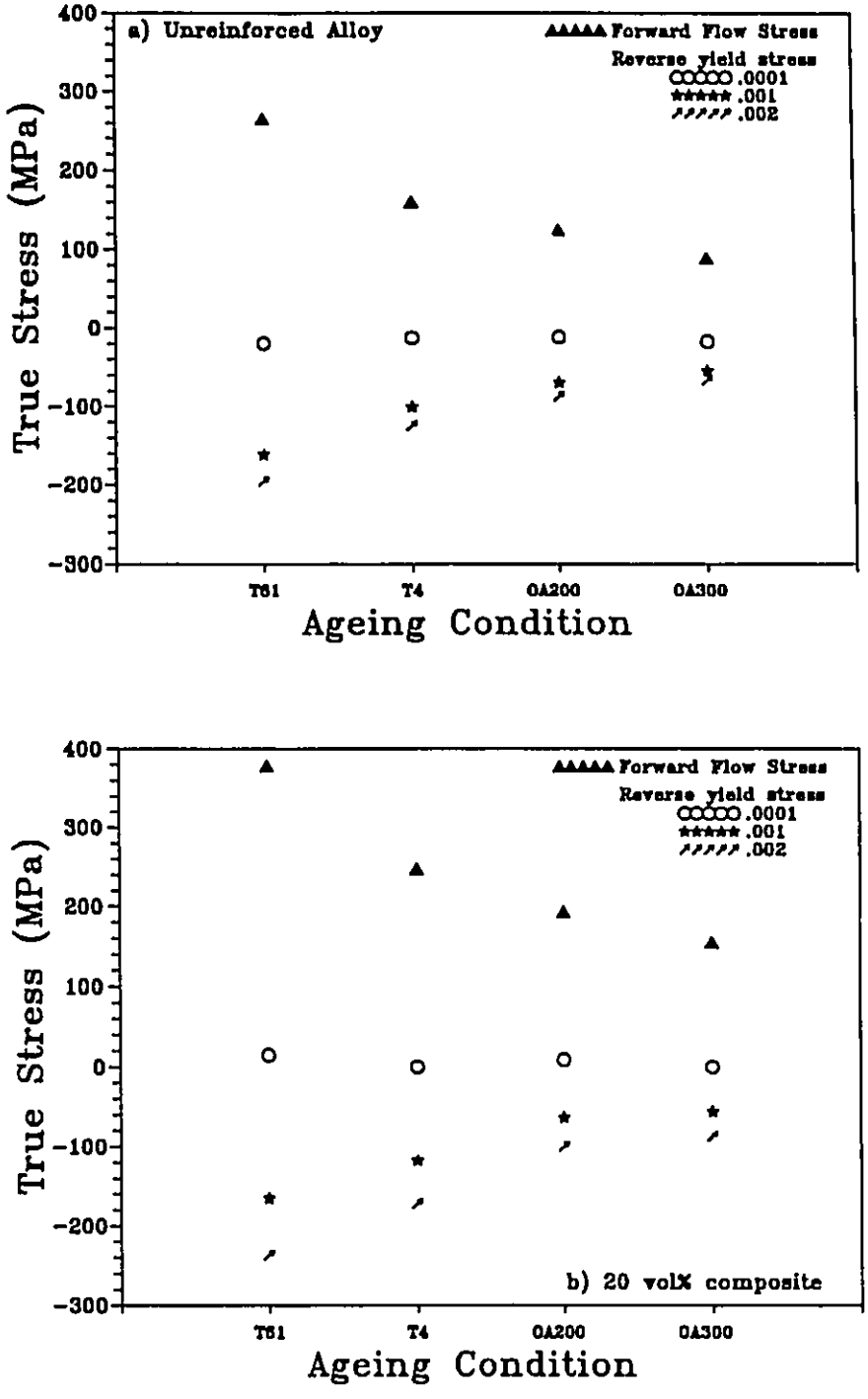

Figure 3.30: The forward flow stress σ_f, and reverse yield strength σ_r determined at offset strains of .0001, .001 and .002 for; a) unreinforced A356; b) 20 vol% composite.

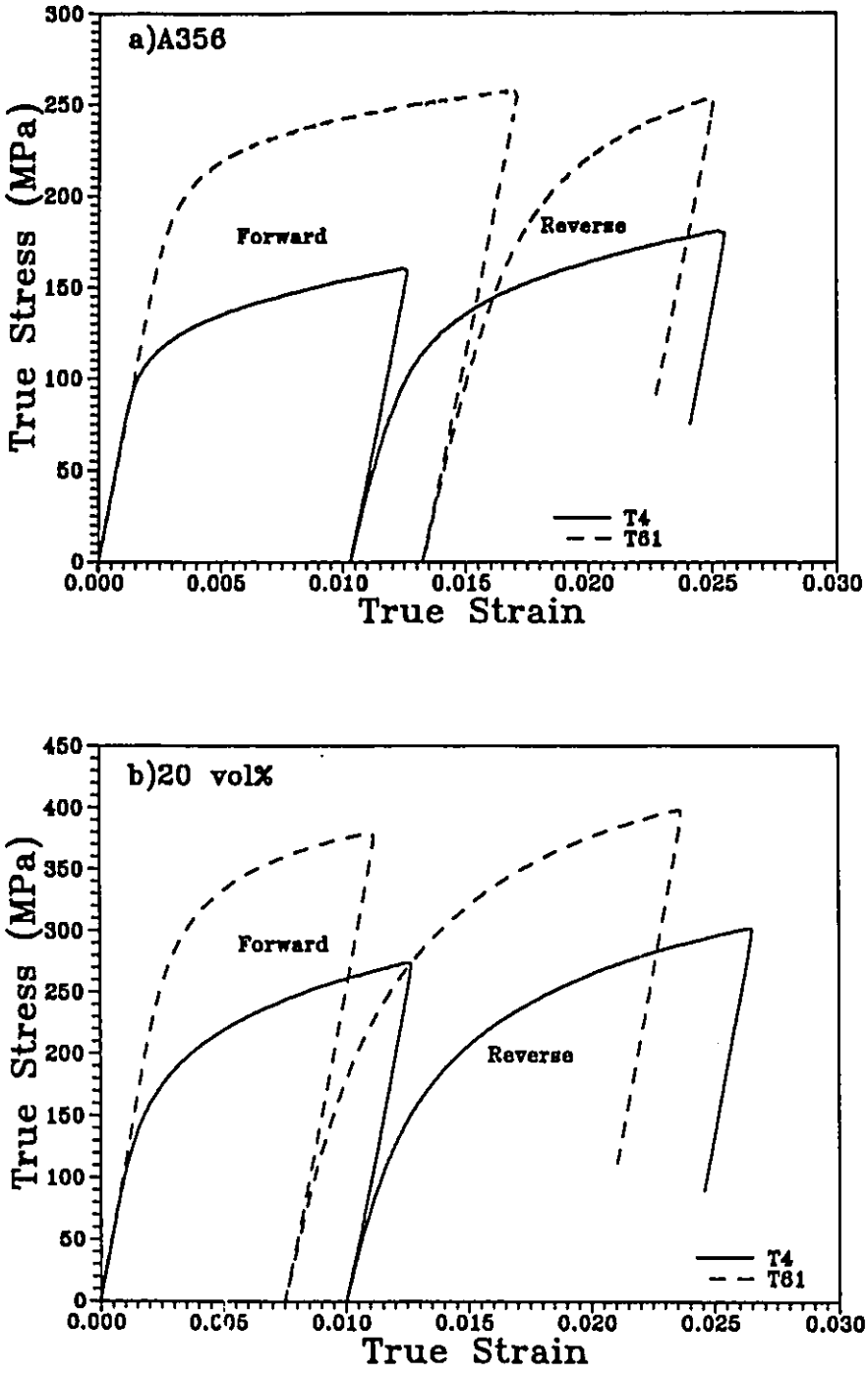

Figure 3.31: Reflection of the reverse portion of the Bauschinger loop for the materials aged to the T4 and T61; a) unreinforced alloy; b) 20 vol% composite.

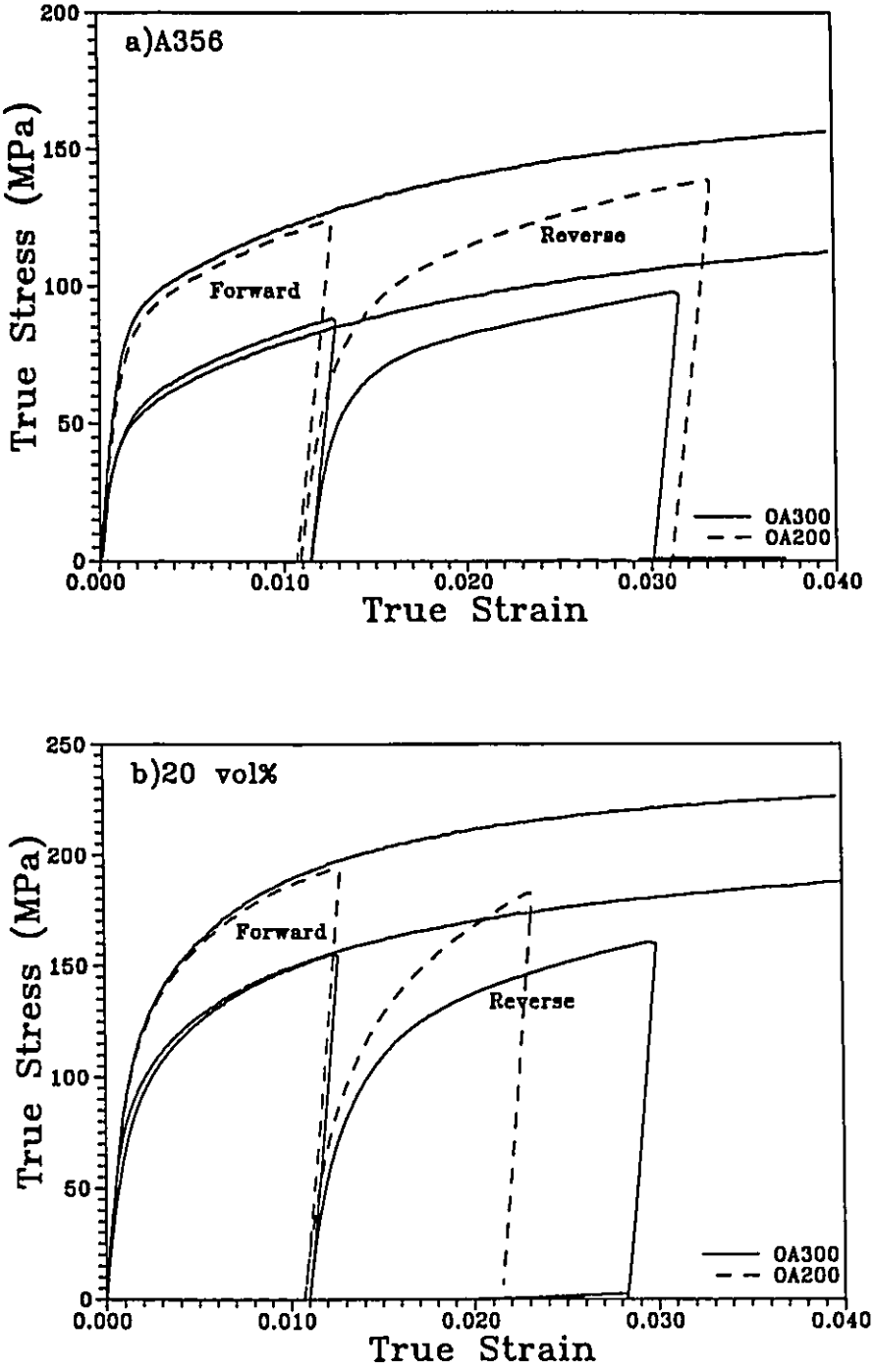

Figure 3.32: Reflection of the reverse portion of the Bauschinger loop for the materials aged to the OA200 and OA300; a) unreinforced alloy; b) 20 vol% composite.

be made (Figure 3.31 and 3.32). Included in Figure 3.32 for comparison is a monotonic stress-strain curve for the materials tested in tension. In both the composite and alloy, and for all ageing conditions, the reverse portion of the stress-strain curves are very rounded and deviate significantly from the elastic reloading line. The level of reverse strain in these experiments was limited because of the specimen dimensions (see Chapter 2). However the results do suggest that the level of permanent softening, regardless of matrix ageing condition is very small. This is emphasised by the work of Beulieu (1991) presented in Figure 3.33a. In this case the composite (in the T61 condition) was tested in tension to a higher prestrain ($\approx .015$) than that used here. No permanent softening is observed, in fact it is evident that the reverse curve attains a stress level higher than that expected if the forward curve was extrapolated to the same cumulative strain. This observation is dependent on the initial testing direction. In Figure 3.33b the composite was tested first in compression and then reversed in tension. In this case, the strain hardening rate exhibited in the reverse curve is lower than in the previous case. One possible explanation for this behaviour relates to the larger degree of damage accumulation that may occur when the material is deformed in tension. This points out a further complication in interpreting permanent softening in these materials.

3.3.2.1 Difference Between Tension and Compression

Bauschinger loops for the unreinforced alloy in which the initial deformation was either tension or compression are illustrated in Figure 3.34a. (Curves for the T61 state are not included because the level of plastic strain was different in tension and compression and are therefore not directly comparable). As discussed in section 3.2, the forward curves are characterized by a strength differential. This differential is not evident in reverse flow, where the curves are essentially identical regardless of the direction of the forward deformation. In the composite

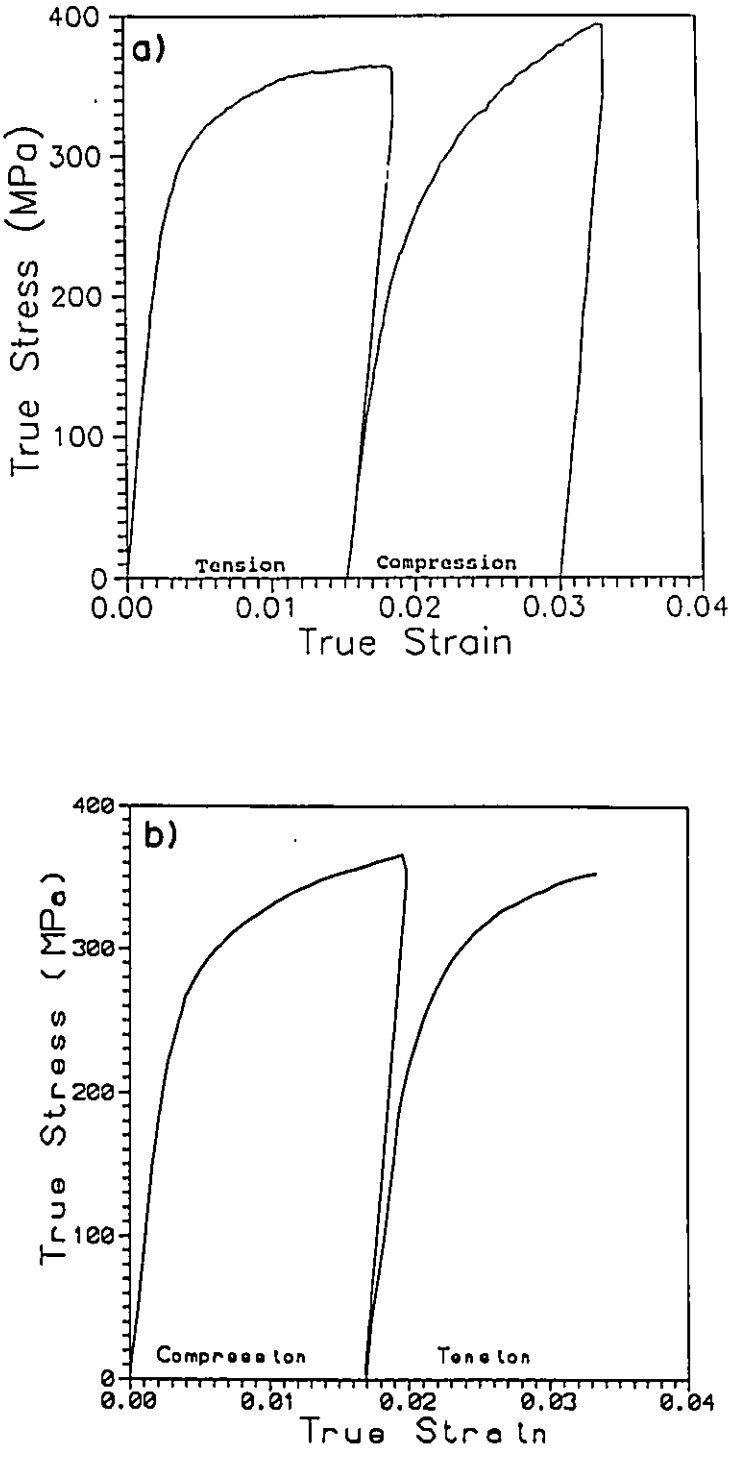

Figure 3.33: Reflected Bauschinger loops for the 20 vol% composite in the T61 condition; a) deformed initially in tension; b) deformed initially in compression (Beulieu, 1991).

materials (Figure 3.34b), the forward curves are nearly identical except for the cross over effect discussed in section 3.2. (The OA200 and T61 conditions were not included for the same reasons given above for the alloy in the T61 state). The reverse portion of the curves are again essentially identical regardless of the initial testing direction.

3.3.2.2. Influence of Matrix Ageing Condition.

The above results indicate that the Bauschinger effect in the materials studied here is characterized by a large transient softening effect, with little or no permanent softening. Therefore qualitative interpretations concerning ageing condition are best done using a measurement such as the Bauschinger strain, ϵ_B (defined in section 1.6). The Bauschinger strain, at load reversals of 50% 60% and 70% was measured (see Figure 3.35). It is clear that, at the level of prestrain chosen ($\approx .01$), the Bauschinger strain is always larger in the 20 vol% composite compared to the alloy. The trends with ageing condition are similar for both materials. The Bauschinger strain is roughly the same in the T4 and T61 conditions, is largest in the OA200 condition and, in the case of the alloy, attains a level similar to the T4 and T61 conditions in the OA300 state. In the composite material, ϵ_B in the OA300 state, while smaller than that measured in the OA200 condition, remains at a higher level than that observed for the T4 and T61 states. Comparisons of behaviour at 50%, 60% and 70% reverse loading reveal qualitative agreement. In particular the trends concerning ageing condition and SiC addition are the same no matter what level of load reversal is chosen. As would be expected the Bauschinger strain increases as the value of load reversal chosen increases.

3.3.3 Multi-loop Experiments.

Characterization of the Bauschinger effect using Bauschinger strain, require only a small

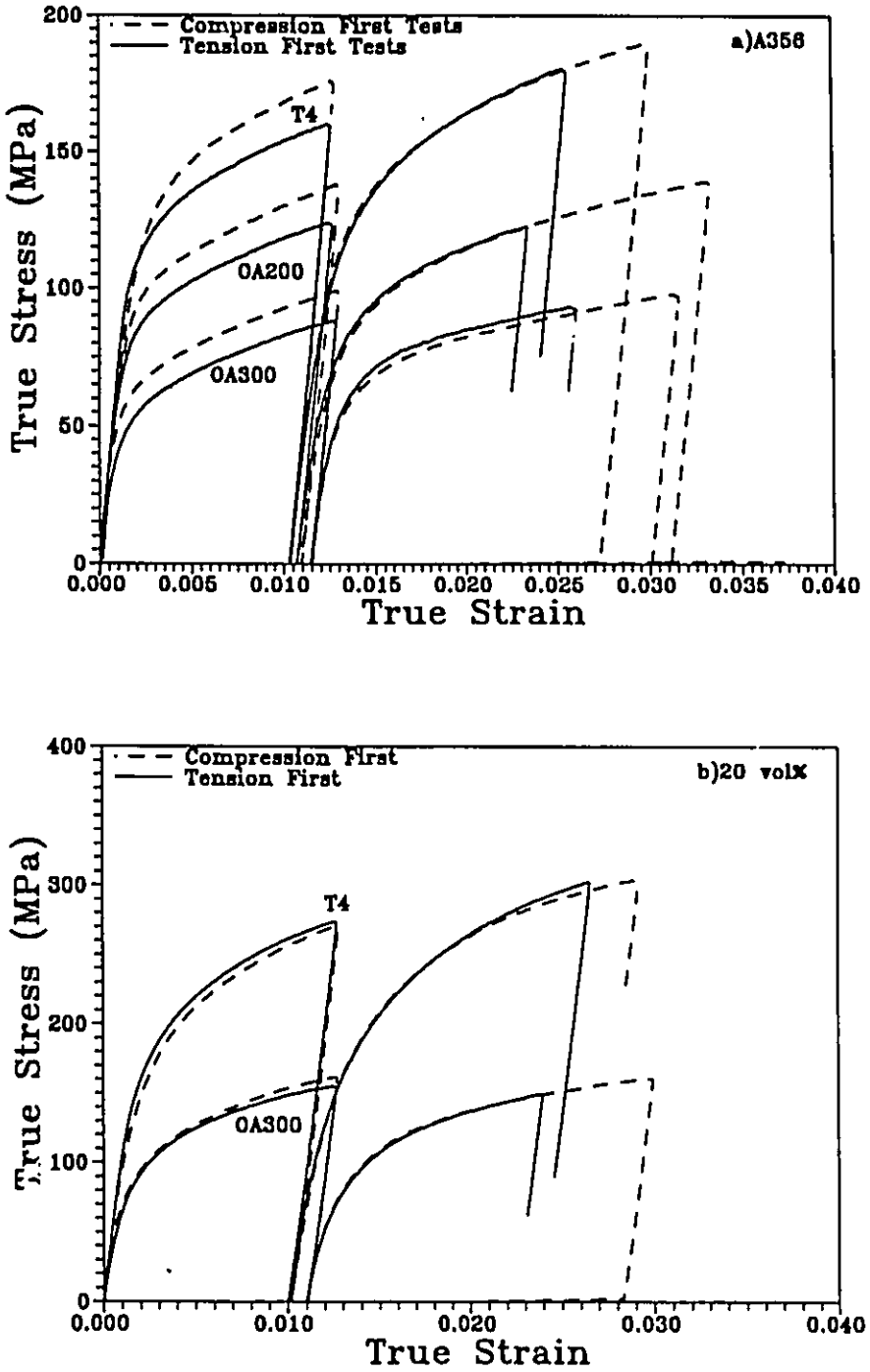

Figure 3.34: Reflected Bauschinger loops for tension first and compression first tests; a) A356 alloy in T4, OA200 and OA300 states; b) 20 vol% composite in T4 and OA300 states.

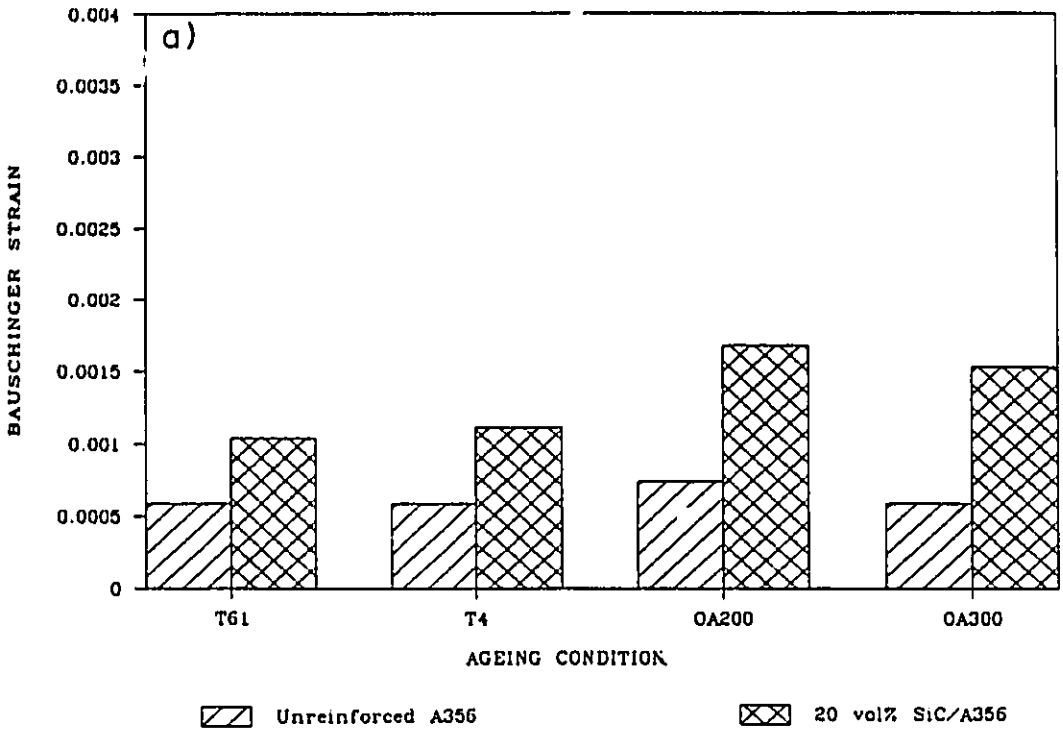
a)
BAUSCHINGER STRAIN
0.004
0.0035
0.003
0.0025
0.002
0.0015
0.001
0.0005
0
T61
T4
OA200
OA300
AGEING CONDITION
Unreinforced A356
20 vol% SiC/A356

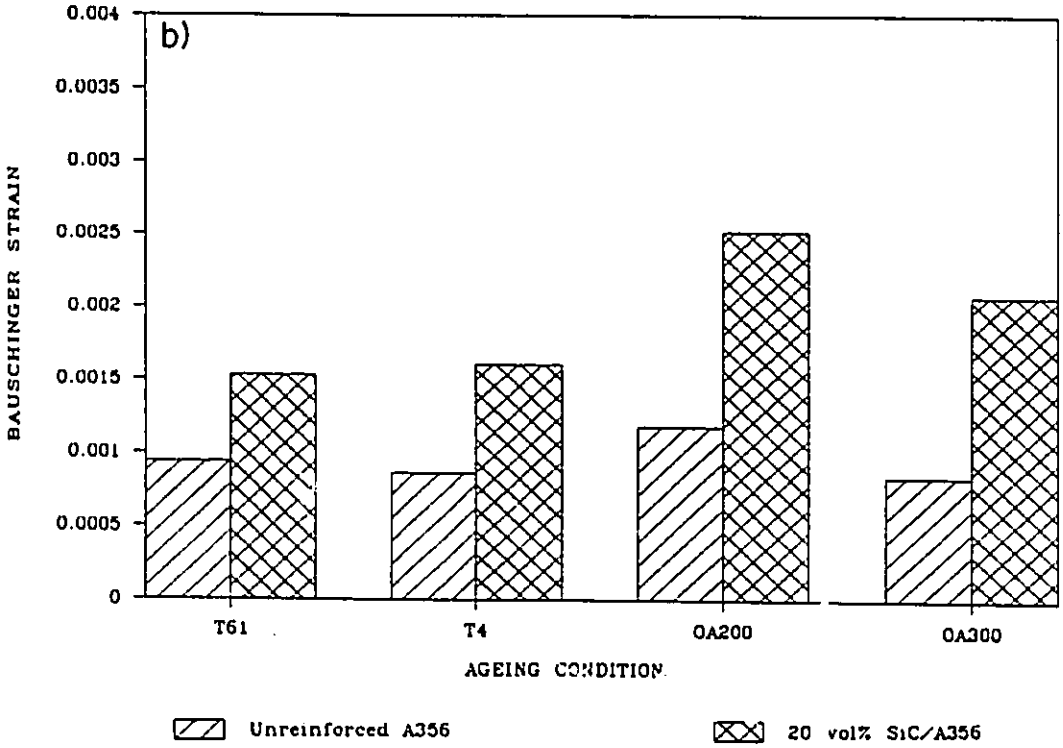
b)
BAUSCHINGER STRAIN
0.004
0.0035
0.003
0.0025
0.002
0.0015
0.001
0.0005
0
T61
T4
OA200
OA300
AGEING CONDITION
Unreinforced A356
20 vol% SiC/A356

FIG. 3.35 a,b

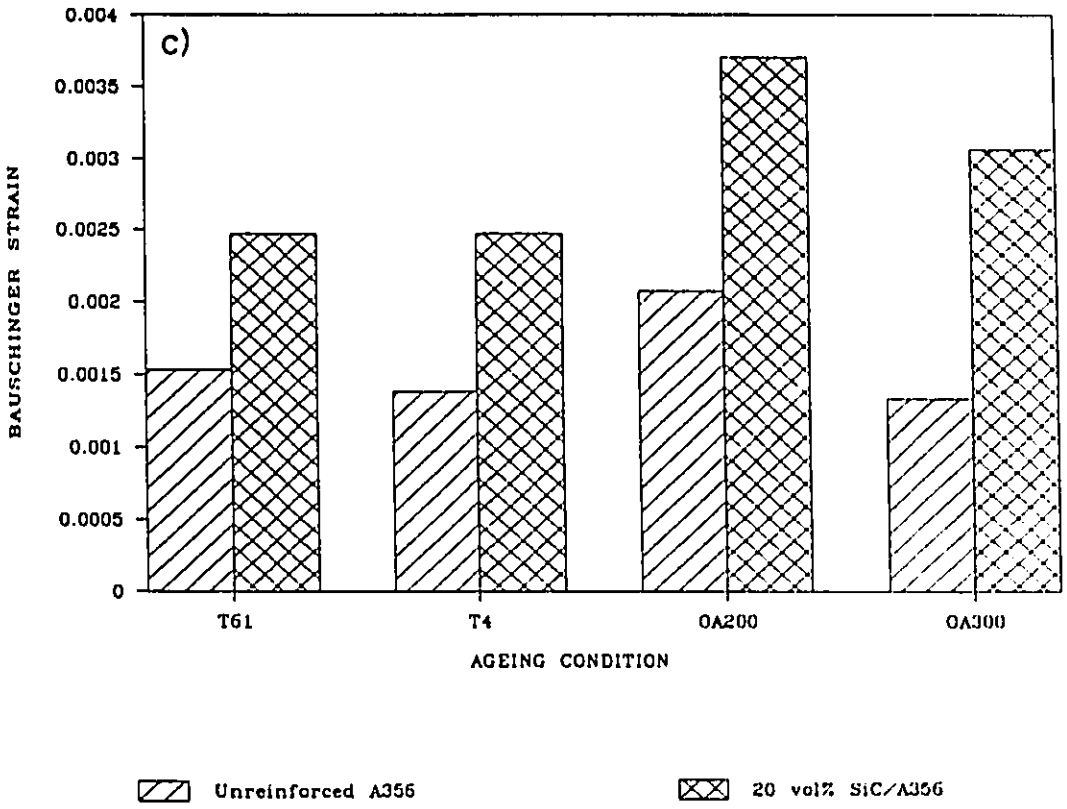

Figure 3.35: The Bauschinger strain measured at various levels of reverse loading for the A356 alloy and 20 vol% composite; a) 50%; b) 60%; and c) 70% reverse loading.

degree of reverse loading (i.e. perhaps only 50% of the forward stress). Consequently the possibility of investigating the influence of the degree of plastic deformation using a single specimen was considered. The procedure for performing these experiments can be described by referring to Figure 3.36.

If a material exhibits no Bauschinger effect, then the reverse stress-strain curve (after a forward prestrain to σ_f) will remain elastic until a stress of $-\sigma_f$ is reached (point B in Figure 3.36a). If the material is then reloaded from this point in the forward direction it will again remain elastic until σ_f (point A) is reached and continued plastic deformation will commence.

In the presence of a Bauschinger effect, upon reversing the strain path after a forward prestrain the material will deform plastically before a stress of $-\sigma_f$ is reached (point B′ in Figure 3.36b). If the sample is then reloaded from this point in the forward direction, a hysteresis loop will form. This procedure can be repeated as a function of plastic strain by further straining in the forward direction (point C) and then reverse loading again to point D, thus producing multiple hysteresis loops at various strain levels. A number of measurements can be made from these loops. The Bauschinger strain, can be measured as well as the reverse yield stress at some offset strain (from which the Bauschinger stress can be calculated). However, both these measurements require that a linear elastic portion in the unloading curve be defined. Typically the unloading curve is somewhat rounded immediately upon load reversal making it difficult to distinguish a linear portion with which to measure an offset strain. This difficulty can be avoided by simply measuring the width of the hysteresis loop formed in such a test (This will be termed the Bauschinger loop width). Using this technique a Bauschinger loop width of zero would of course indicate no Bauschinger effect. As the loop width increases the Bauschinger effect increases. Providing the degree of unloading is always the same percentage of the forward stress, this technique can be used to make qualitative comparisons describing the effects of SiC content,

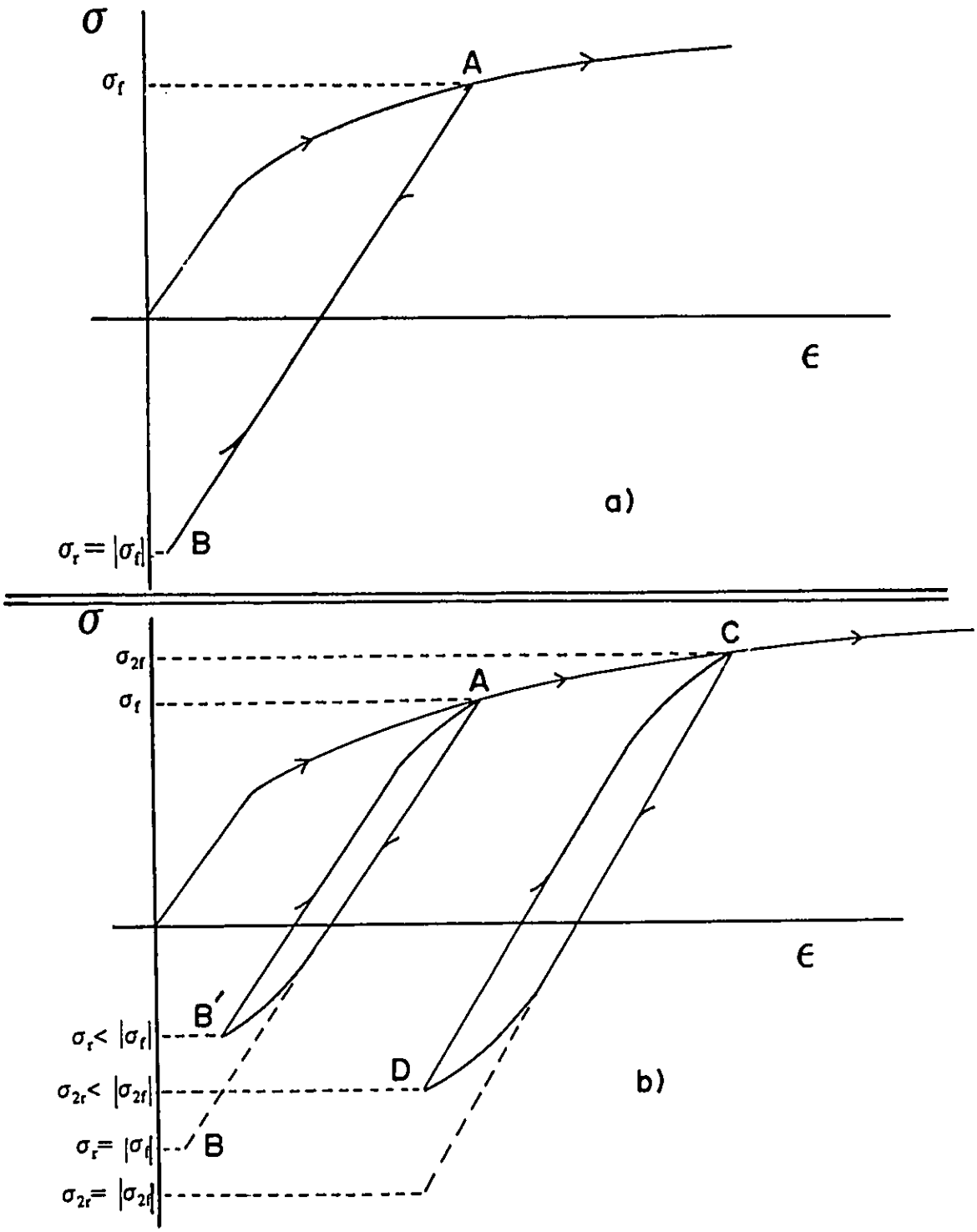

Figure 3.36: Schematic representation of; a) forward and reverse loading in a materials with no Bauschinger effect; b) multiple forward and reverse loading for a material which exhibits a Bauschinger effect.

matrix ageing condition and plastic strain on the development of the level of internal stress in materials.

From the previous section it is clear that the information obtained for the single loop work shows similar trends wether looking at load reversals of 50, 60 or 70% of the forward stress. Previous work by Buckley and Entwistle (1956) on pure polycrystalline Al, also indicates the general conclusions that the qualitative trends concerning the Bauschinger effect (as measured by the Bauschinger strain) did not depend on the value of reverse loading between 50 and 100%. The degree of reverse loading chosen in the multi-loop tests was 50% in order to minimize the disturbance of reverse flow on the state of the material developed in the forward direction.

To verify the validity of the multi-loop tests, comparisons of the stress-strain curves for monotonic, single and multi-loop tests were made. An example of such a comparison is illustrated in Figure 3.37a for the unreinforced alloy in the T61 condition. It is evident that the unloading procedure does not disturb the shape of the forward stress-strain curve. This is further illustrated in Figure 3.37b where the stress-strain curve was reconstructed from the forward portions of the multi-loop experiments and compared to the monotonic curve. (This was the procedure used to obtain the curves Figure 3.22 of section 3.2).

Figure 3.38 illustrates the tensile portion of a series of multi-loop tests performed on the 20 vol% composite in three different ageing conditions. In the T4 and T61 conditions reloading from reverse deformation is followed by a return of the stress-strain curve to it previous level. This was the case for all the materials in these ageing conditions. A somewhat different effect was evident for the OA300 condition (Figure 3.38c). In this case a small softening effect occurs as a result of reverse flow such that, upon reloading, the level of the flow stress does not immediately recover to the previous level. There may be some concern that this softening effect results in a disturbance of the structure that was previously developed in the forward direction.

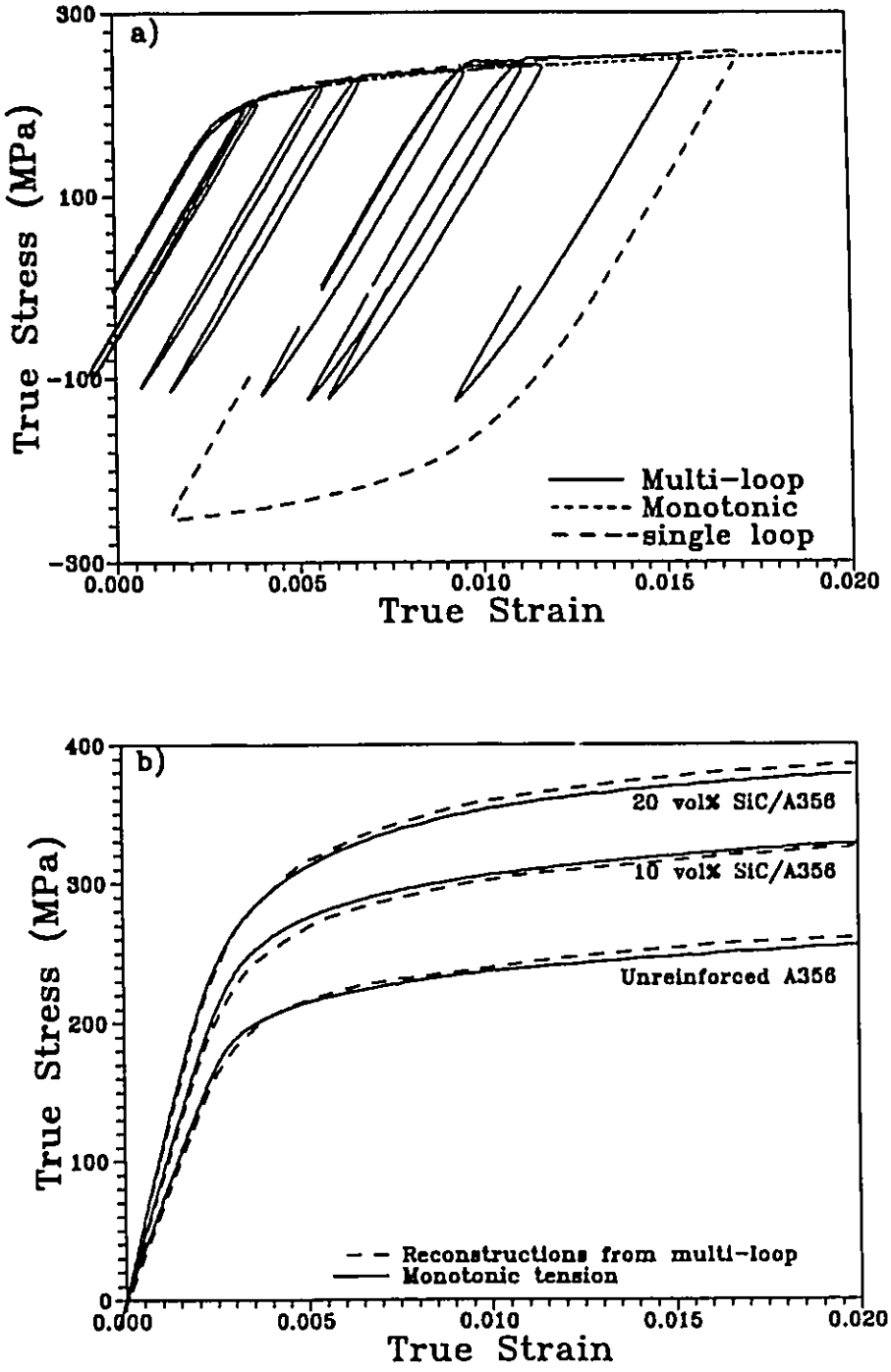

Figure 3.37: a) Comparisons of single, multi loop and monotonic σ-ϵ curves for the A356 alloy in the T61 condition. b) Comparisons of the monotonic curves with those reconstructed from the multi loop experiments.

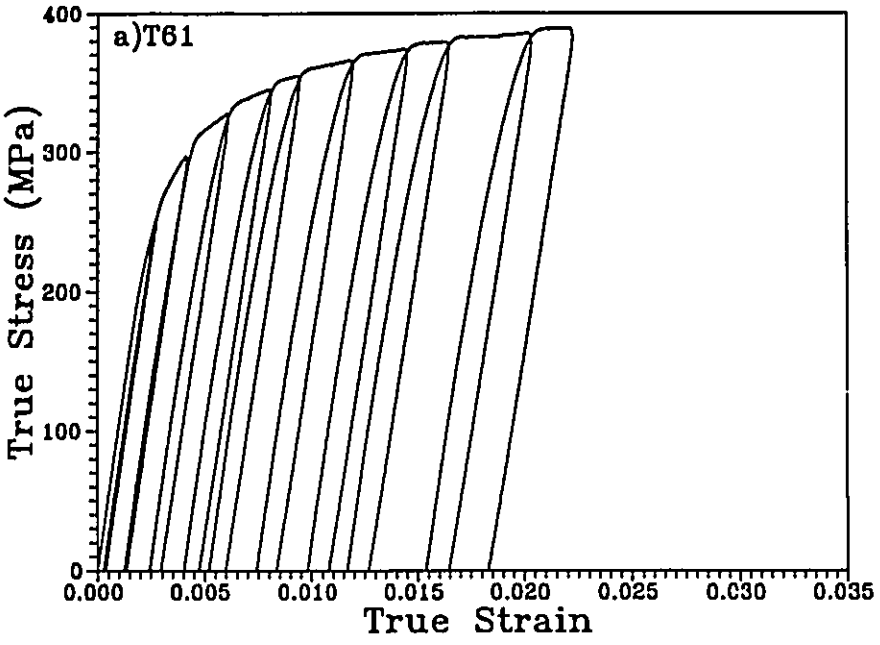
a)T61
True Stress (MPa)
400
300
200
100
0
0.000
0.005
0.010
0.015
0.020
0.025
0.030
0.035
True Strain

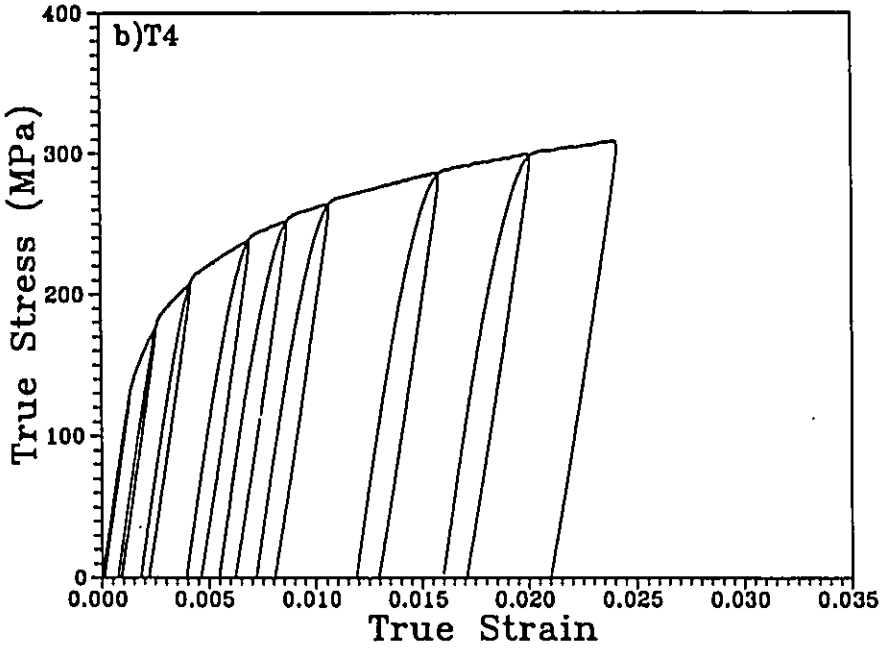
b)T4
True Stress (MPa)
400
300
200
100
0
0.000
0.005
0.010
0.015
0.020
0.025
0.030
0.035
True Strain

FIG. 3.38 a, b

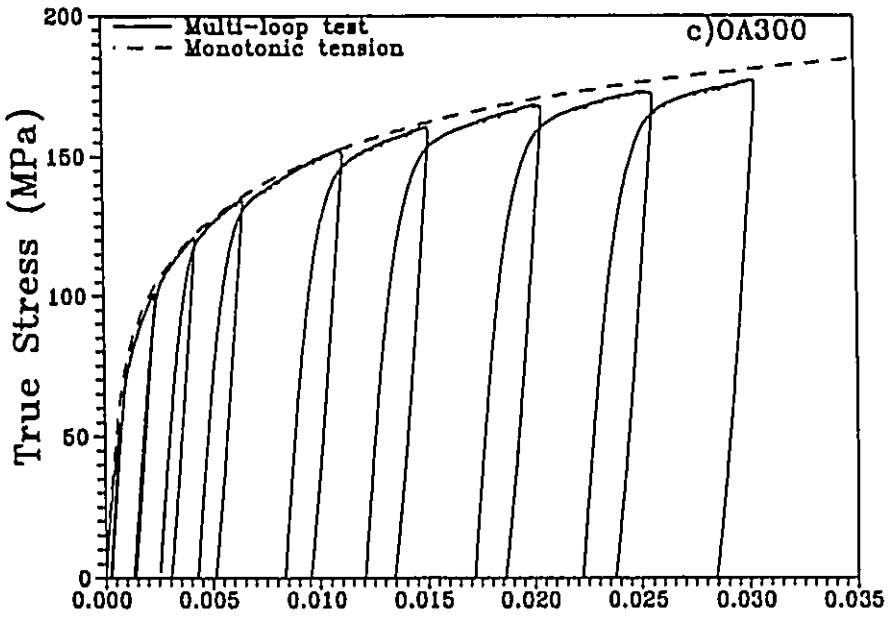

Figure 3.38: Tensile portion of the multi-loop experiments for the 20 vol% composite in the; a) T61; b) T4 and c) OA300 ageing states.

However, by comparing the multi-loop curves to a monotonic curve, it appears that after further forward strains of .005 the curves recover close to the level expected without reverse loading.

Figure 3.39 plots the Bauschinger loop width versus plastic strain for all the materials. It is evident from these results that the Bauschinger effect (as measured from the Bauschinger loop width) rises very rapidly in all the materials during the first .005 of plastic strain. This rise is more rapid as the SiC content is increased. All materials also show a more gradual rise in the Bauschinger effect after strains of .01.

The data of Figure 3.39 is replotted in Figure 3.40. so that some observations concerning the influence of ageing condition can be made. For the alloy and composites, the initial rise in the Bauschinger loop width is very similar up to strains of about .005. At plastic strains above this level, the Bauschinger loop width in the composites becomes larger in the OA300 state. These results are consistent with the observations concerning ageing condition made from the Bauschinger strain measurements on single loop tests (Figure 3.35). Also consistent with these observations is that the Bauschinger loop width in the unreinforced alloy (Figure 3.40c.) is nominally the same in the T4, T61 and OA300 states over the entire prestrain range investigated.

An alternative method for measuring the Bauschinger effect is the Bauschinger stress σ_b (as defined in Section 1.6.). The value of σ_b was measured from two separate multi-loop experiments for the 20 vol % composite in the T61 condition (Figure 3.41). Also included is a measurement made from the single loop test which was deformed to a prestrain ϵ_p, of .0095. All three specimens give very consistent results. This data indicates the same trends as the Bauschinger loop data, namely that the Bauschinger effect rises very rapidly during the first .005 of plastic strain.

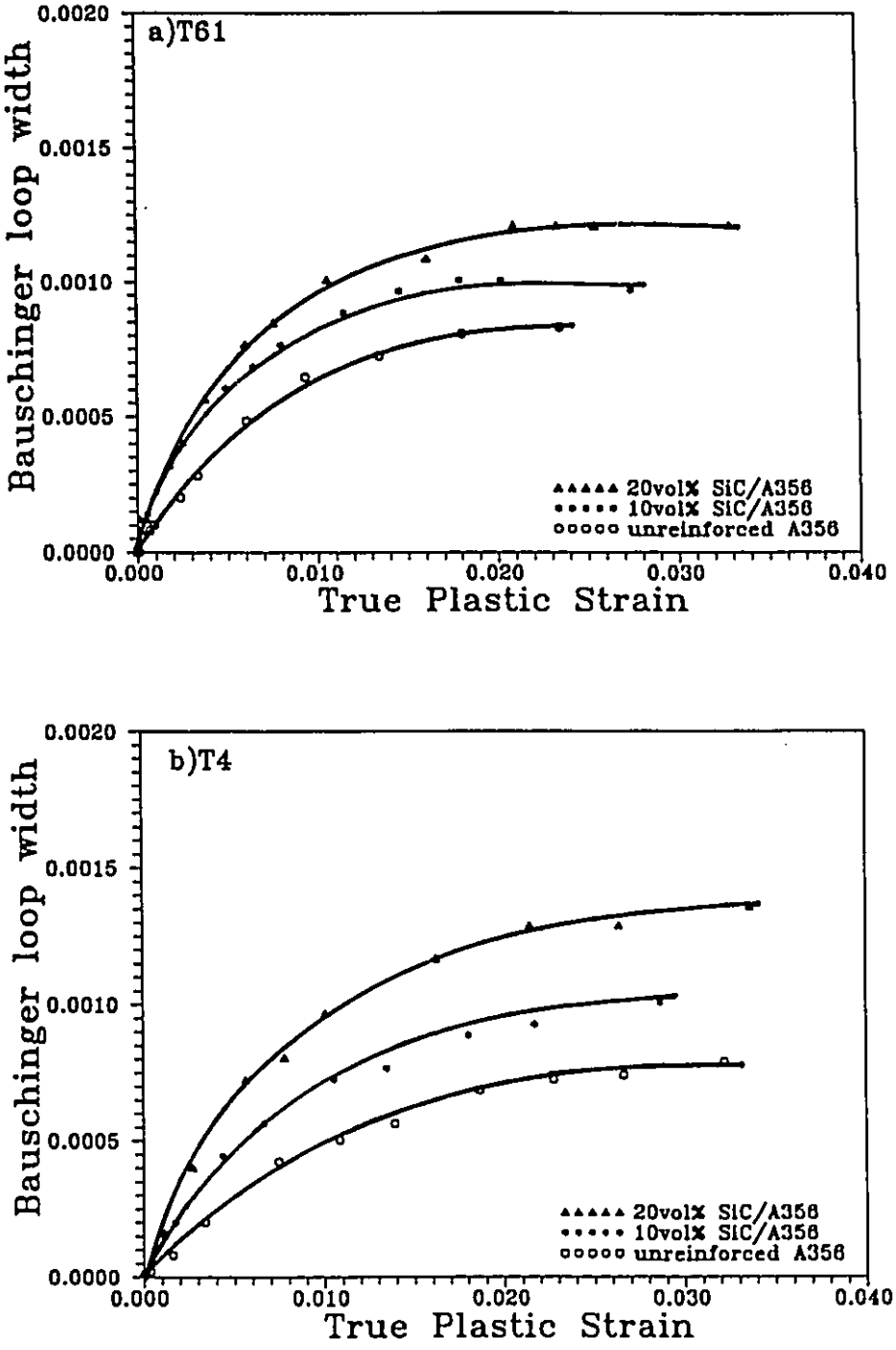
a)T61
Bauschinger loop width
0.0020
0.0015
0.0010
0.0005
0.0000
0.000
0.010
0.020
0.030
0.040
True Plastic Strain
▲▲▲▲▲ 20vol% SiC/A356
••••• 10vol% SiC/A356
ooooo unreinforced A356
b)T4
Bauschinger loop width
0.0020
0.0015
0.0010
0.0005
0.0000
0.000
0.010
0.020
0.030
0.040
True Plastic Strain
▲▲▲▲▲ 20vol% SiC/A356
••••• 10vol% SiC/A356
ooooo unreinforced A356

FIG. 3.39 a,b

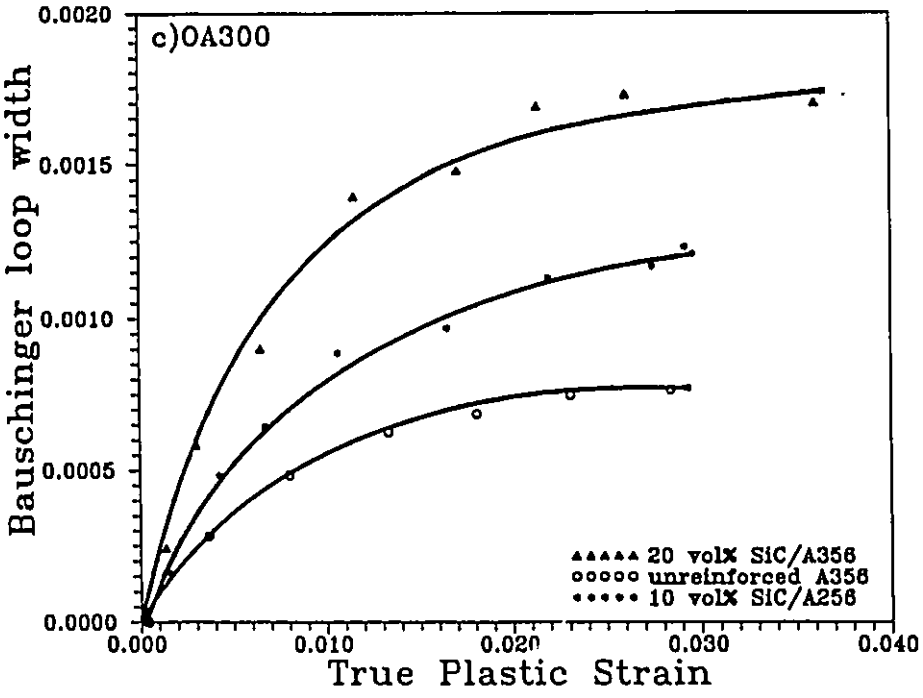

Figure 3.39: Bauschinger loop width versus plastic strain (ϵ^c_p) for the alloy and composites aged to the; a) T61; b) T4 and OA300 states.

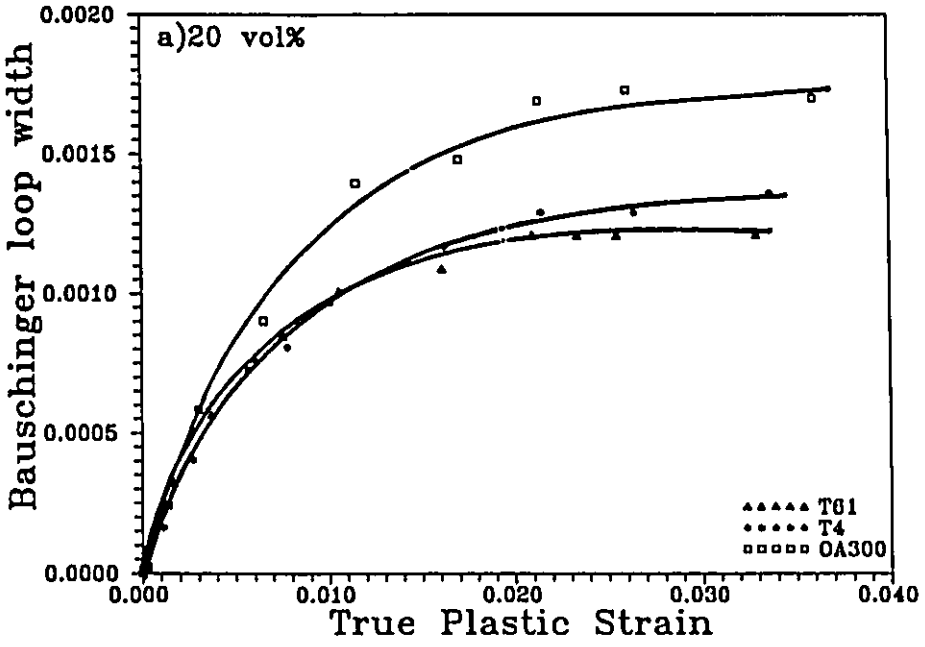
a)20 vol%
Bauschinger loop width
0.0020
0.0015
0.0010
0.0005
0.0000
0.000
0.010
0.020
0.030
0.040
True Plastic Strain
T61
T4
OA300

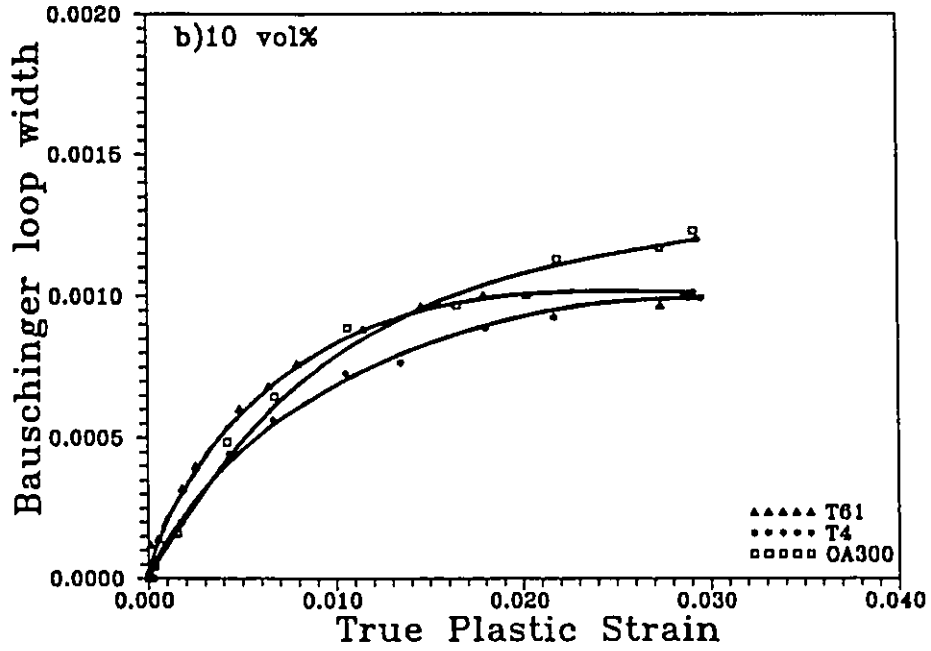
b)10 vol%
Bauschinger loop width
0.0020
0.0015
0.0010
0.0005
0.0000
0.000
0.010
0.020
0.030
0.040
True Plastic Strain
T61
T4
OA300

FIG. 3.40 a, b

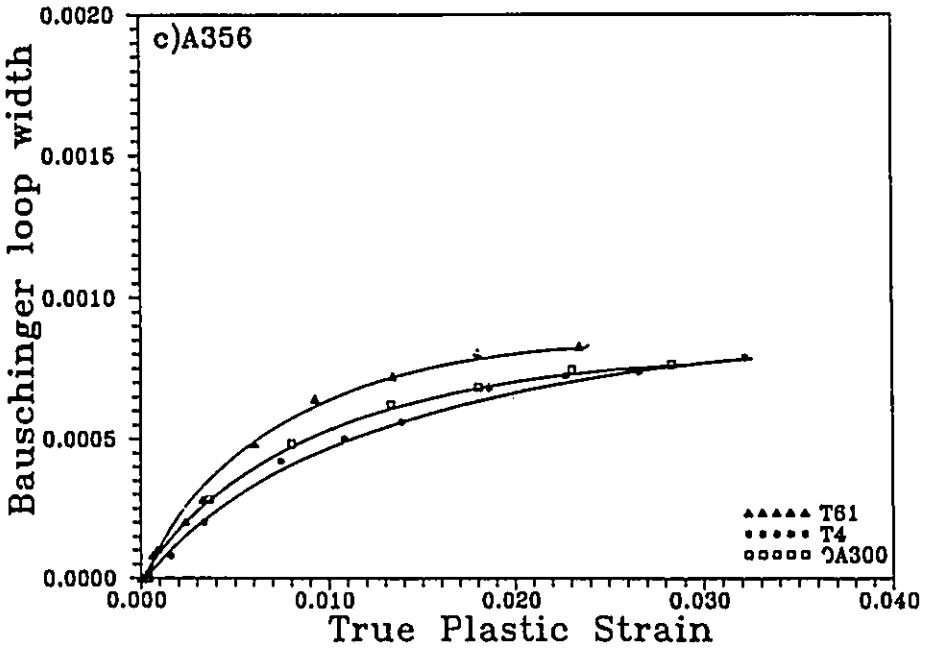

Figure 3.40: Comparison of the Bauschinger loop width in three ageing conditions as a function of plastic strain (ϵ^c_p) for; a) 20 vol% composite; b) 10 vol% composite and c) A356 alloy.

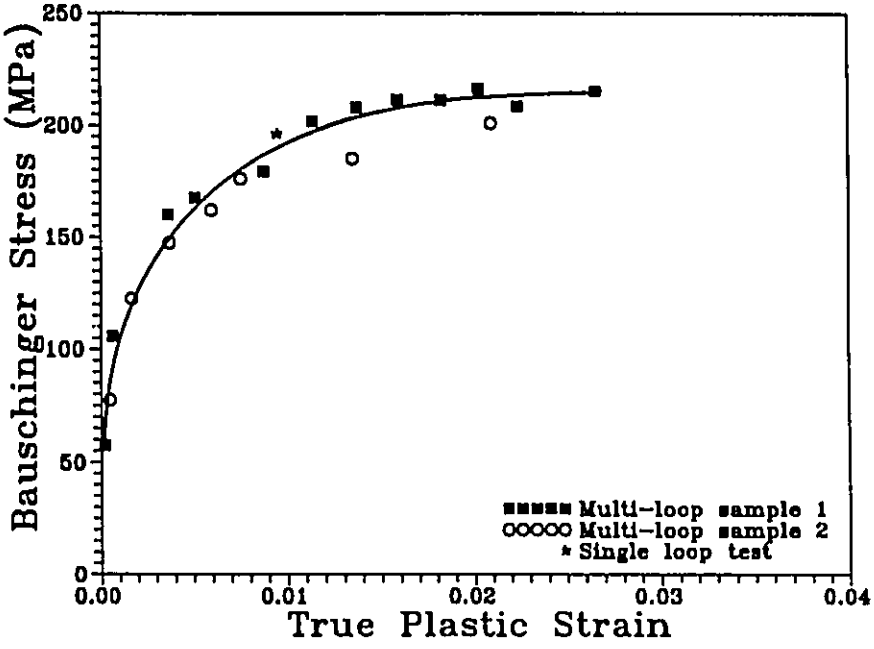

Figure 3.41: The Bauschinger stress as a function of plastic strain (ϵ^c_p) for the 20 vol% composite in the T61 condition. Included are measurements from two separate multi-loop tests and a single loop test.

3.4 Influence of Temperature on Strengthening

The focus of this section is to investigate the influence of test temperature on the overall strengthening effect of the SiC particles. The discussion can be separated into two sections; 1) investigations of long term temperature exposure (including effects due to microstructural coarsening and test temperature); and 2) investigation of test temperature effects only. For this purpose, only the alloy and 20 vol% composite were investigated.

An example of the influence of temperature on stress-strain behaviour up to a strain of .07 are plotted in Figure 3.42 for the alloy and 20 vol% composite in the OA300 condition. Similar trends are seen for both materials. It should be noted that at 200 and 300°C the flow stress saturates after strains of .02. In fact most of the high temperature data meet the conditions for necking (based on the Considere criterion) at about .05 strain. This is in contrast to the room temperature data which still shows some degree of strain hardening and reaches the criterion for necking at about .1 strain. Similar results were observed for the OA200 materials tested at 150 and 200°C.

3.4.1 Long Term Temperature Exposure

As discussed in section 3.1, long term temperature exposures of the T61 materials at temperatures above that used for ageing, causes microstructural coarsening. The development of stable microstructures at 200°C and 300°C were obtained with the OA200 and OA300 ageing treatments. Simulation of long term temperature testing was performed on overaged materials at 200°C and 300°C respectively. This procedure is not identical to a long term test, since it involves a cool down and re-heating step. As discussed in the introduction, this cool down and re-heating step likely induces some plastic flow that would otherwise not occur, as a result of

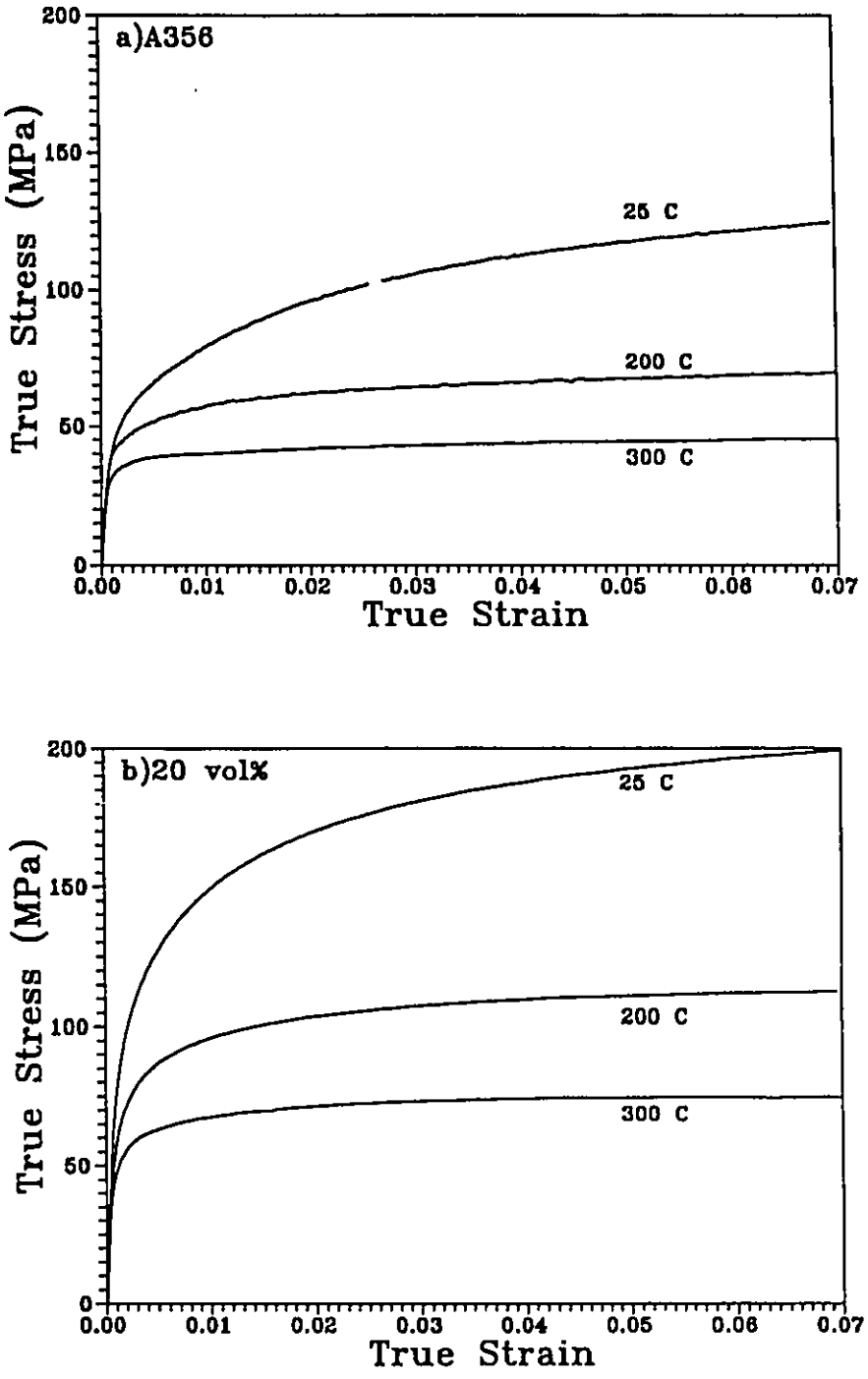

Figure 3.42: Material aged to the OA300 state and tested at 25°C, 200°C and 300°C; a) unreinforced alloy; b) 20 vol% composite.

CTE mismatch. This would complicate interpretations of the onset of plastic flow in the materials. However the focus here is on the overall strengthening effect when the composite and alloy curve becomes parallel. Consequently it is assumed that the microplastic effects do not greatly influence the overall strengthening attained.

Figure 3.43 shows the difference between the 20 vol% composite and the alloy as a function of strain, for the T61 (25°C), OA200 (200°C) and OA300 (300°C) cases. Clearly the level of strengthening is greatly reduced by long term exposure and reaches a value of about 30 MPa at 300°C (reduced from 120 MPa at 25°C).

Figure 3.44a illustrates the limit stress for the alloy and composite as a function of test temperature. The limit stress at 200°C and 300°C was defined as the level of stress reached when the stress-strain curves saturated in stress (Figure 3.42). In the T61 case saturation was not reached. In this case the stress at which maximum strengthening was observed was chosen as the limit stress. The strength of both alloy and composite (as well as the strengthening increment) is greatly reduced as a result of long term exposure and high temperature testing. This data naturally includes influences of both test temperature and microstructural coarsening. In Figure 3.44b data for the composite material for the overaged conditions tested at 25°C is included. It is evident that a large portion of the loss in strength (over half the total loss) is due to microstructural change during heat treatment. The presence of the SiC particles does not greatly alter the microstructural change (see section 3.1) occurring in the matrix. Consequently this limits the effectiveness of the particles as high temperature strengthening agents.

3.4.2 Influence of Test Temperature Only

In order to evaluate the effects of test temperature only, the materials were tested at 200°C and 300°C in the OA300 condition and 150°C and 200°C in the OA200 condition. The

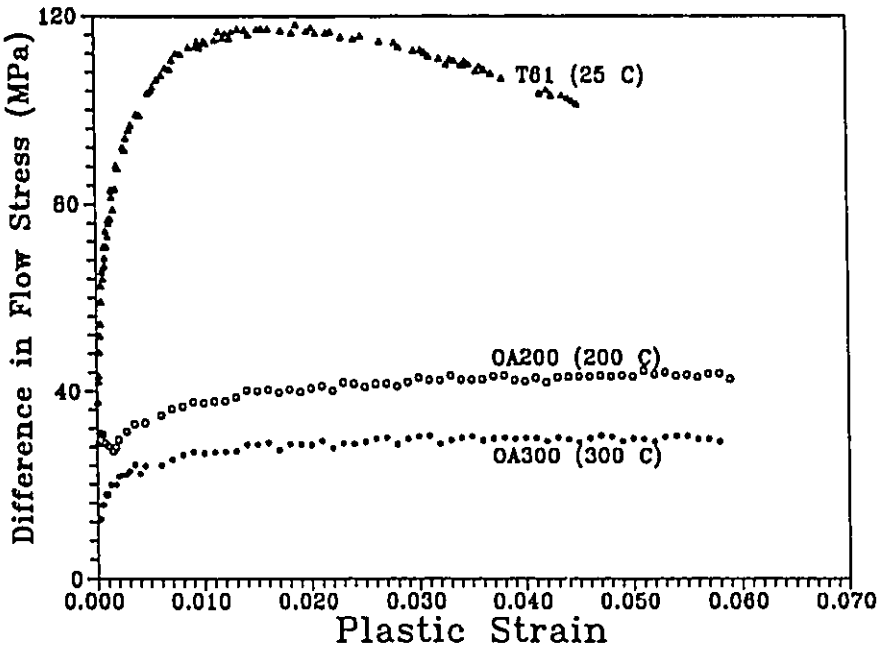

Figure 3.43: Difference in the flow stress of the alloy and 20 vol% composite when tested at 25°C, 200°C and 300°C. Samples tested at 200°C and 300°C were first aged to the OA200 and OA300 states respectively

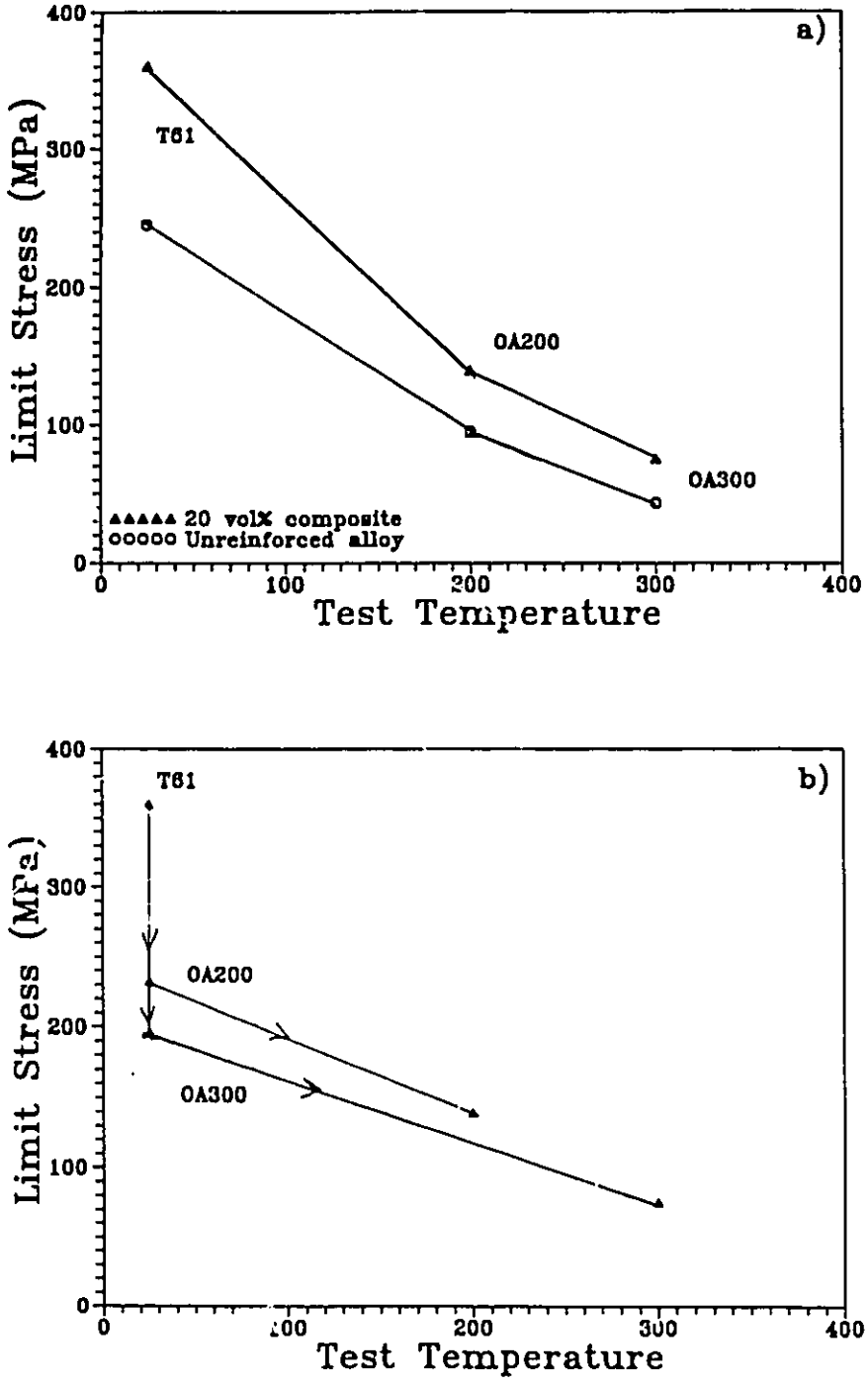

Figure 3.44: a) Limit stress versus test temperature. Specimens tested at 200°C and 300°C were first aged to the OA200 and OA300 states respectively. b) Includes room temperature data for the overaged states.

differences between the flow curves of the composite and alloy (as obtained for example, from the curves of Figure 3.42a and b) for each condition is shown in Figure 3.45 as a function of plastic strain. Room temperature results for OA300 and OA200 are included for comparisons. Figure 3.46 plots the limit stress versus temperature. Without microstructural coarsening there is still a loss in strength for both the alloy and composite and a reduction in the strengthening increment with an increase in test temperature. Nevertheless, the degree of strengthening that does remain, still represents a substantial proportion of the matrix flow strength. To illustrate this, the ratio of the composite to matrix flow stress, versus plastic strain, is plotted for the OA300 (a) and OA200 (b) conditions as a function of temperature in Figure 3.47. Clearly the normalized strengthening increment is relatively unaffected by test temperature. At larger strains ($> .03$) normalized strengthening is slightly larger at temperatures above 25°C.

It should be noted that at the higher temperature the effects of strain rate become more significant. All tests done during this study were performed at a strain rate of 2×10^{-3} s^{-1}. Testing at lower strain rates may yield results which differ significantly from those obtained here.

3.5 Damage Accumulation

The results of section of section 3.2.3 suggest that, at least in the T4 and T61 conditions, damage accumulation may play an important role in the large strain behaviour of the composite materials studied. This is primarily due to the observation that the hardening rate in the composite falls below that of the unreinforced alloy at strains above .02 to .03. It would be of great value to measure the degree of damage accumulation as a function of plastic strain in order to evaluate its influence of the flow stress of the composite.

One way in which this may be done is to measure the modulus of the material as a

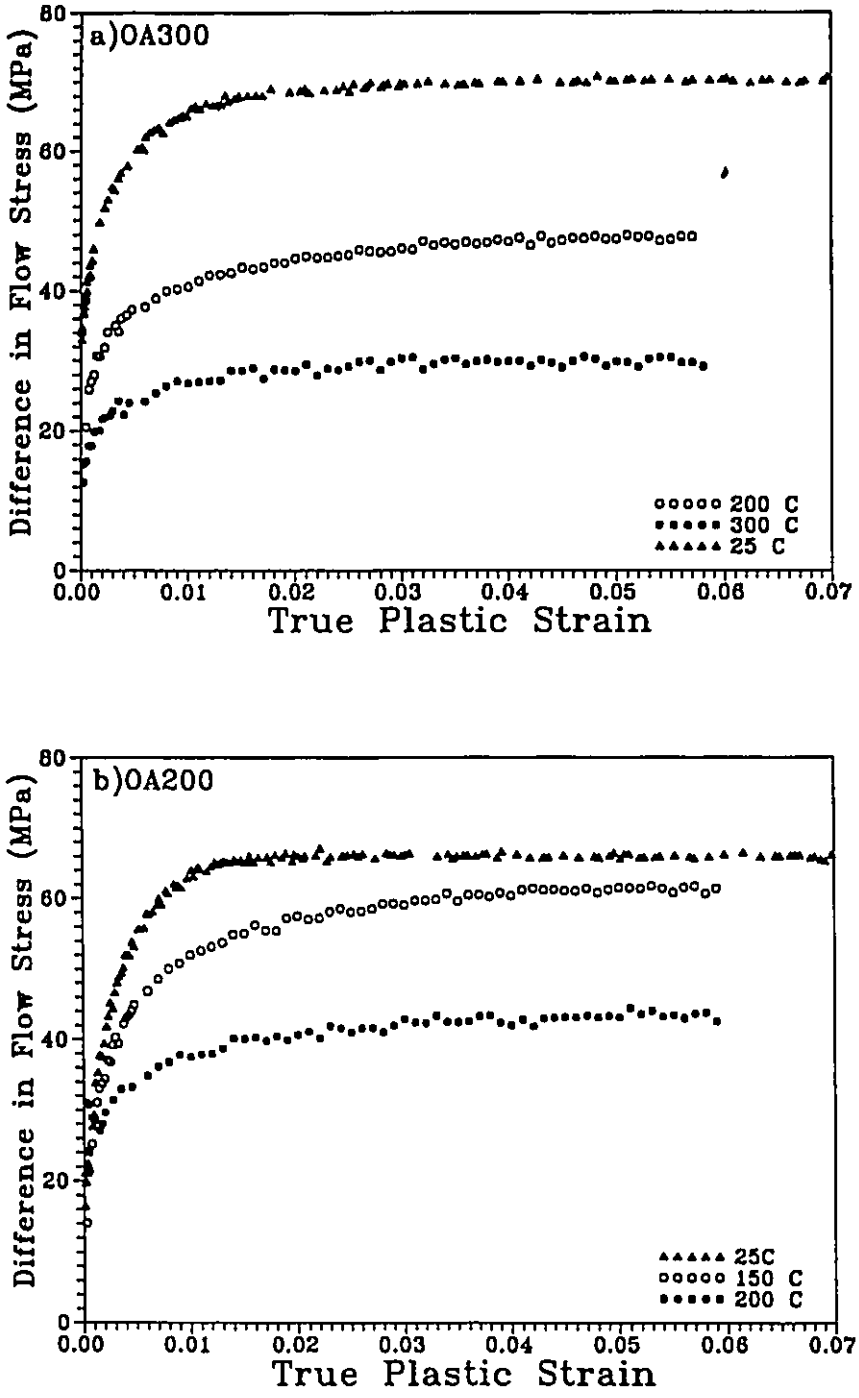

Figure 3.45: Difference between composite and alloy flow stress at various test temperatures. All materials were overaged prior to tensile testing; a) overaged to OA300 state; b) overaged to OA200 state.

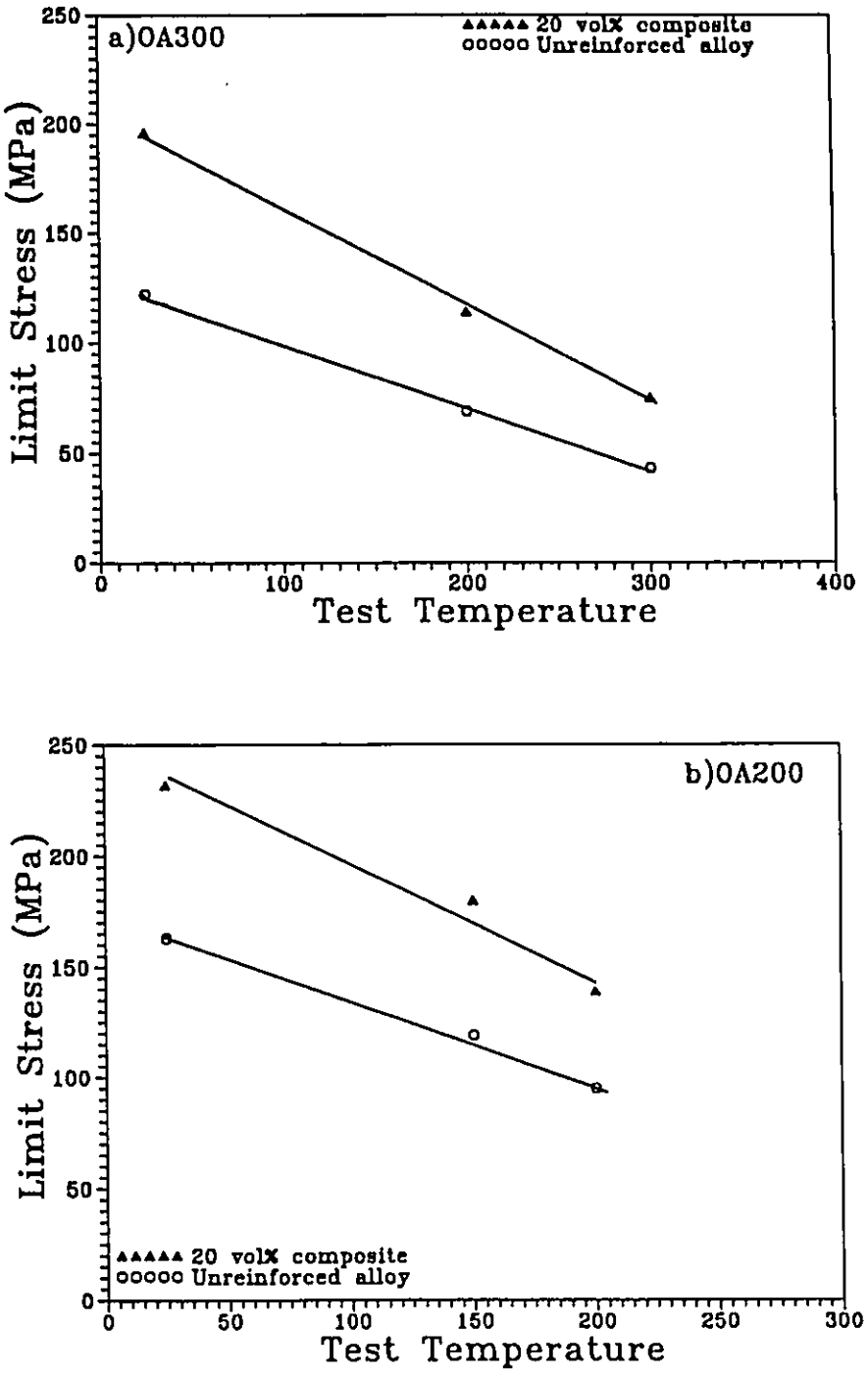

Figure 3.46: Limit stress for alloy and 20 vol% composite versus test temperature; a) overaged to OA300 state; b) overaged to OA200 state, prior to testing.

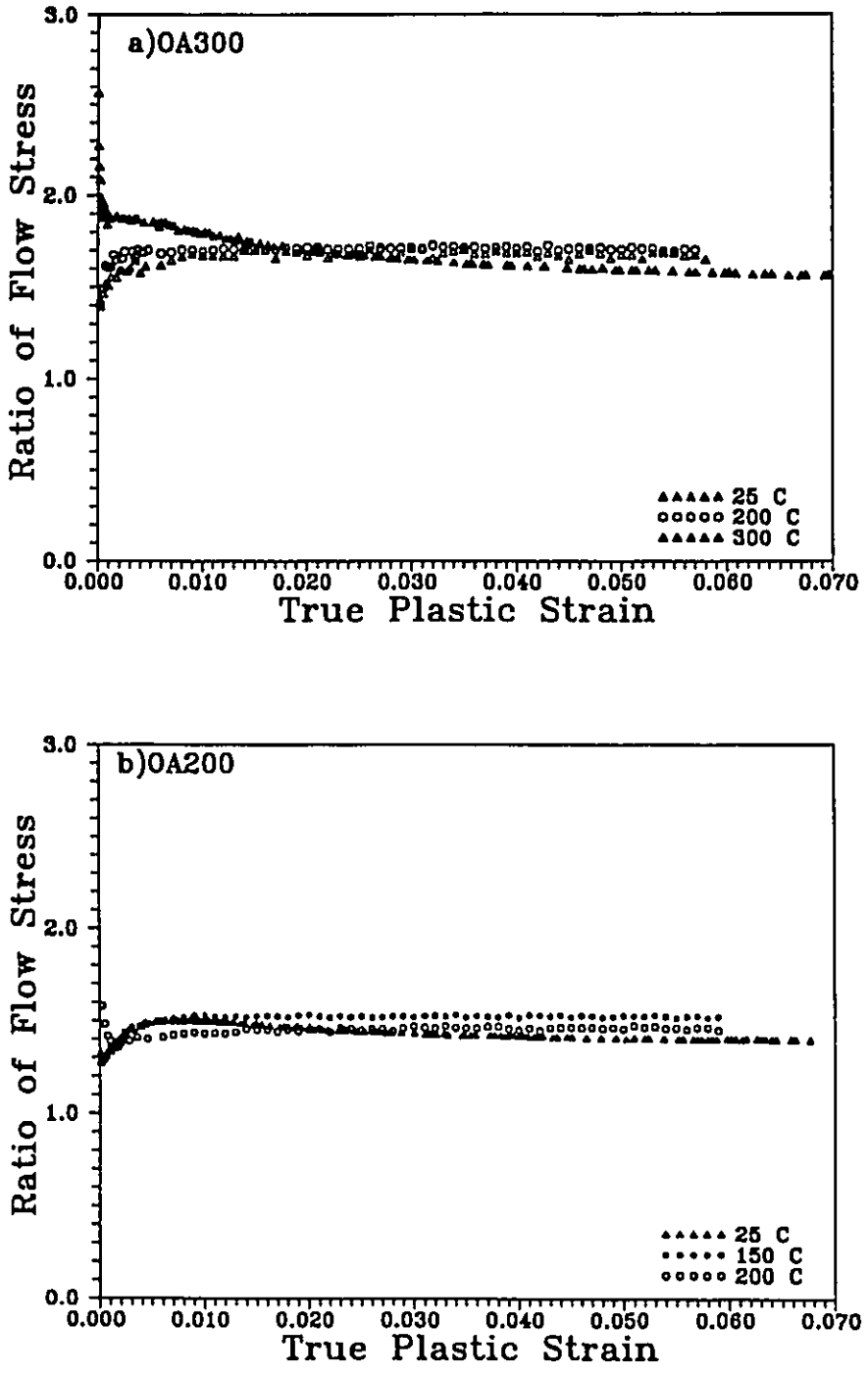

Figure 3.47: Ratio of flow stress between the unreinforced alloy and 20 vol% composite versus test temperature; a) overaged to OA300 state; b) overaged to OA200 state, prior to testing.

function of plastic strain. Studies suggest (Zok et al., 1988; Vasudevan et al., 1989; Lloyd, 1991) that at room temperature and in the age hardened state, damage and fracture in MMC's is primarily associated with particle fracture. It is clear from the modulus measurements presented in section 3.2.2 that the effective modulus is increased as a result of reinforcing the alloy with SiC. This is due to elastic stress partitioning to the SiC particles. If damage is associated with particle cracking, then in principle this should be measurable by a decrease in the elastic modulus. Difficulties in making these measurements arise experimentally for a number of reasons;

1) the unreinforced alloy may also exhibit some degree of damage accumulation (e.g. fracture of the Si particles or void formation at the Si/Al interface), resulting in a drop in modulus or;

2) the magnitude of the drop in modulus may not be large enough to distinguish from experimental scatter.

The first problem was dealt with by measuring the modulus of the unreinforced alloy as a function of plastic strain. The second problem was alleviated by measuring the modulus of the sample several times it the elastic regime to determine the scatter in the modulus readings.

Figure 3.48a illustrates an experiment performed on the unreinforced alloy. The dashed line indicates a monotonic test for comparison. The sample was first cycled in the elastic region several times to obtain an accurate reading of the initial modulus and to measure the scatter in experimental readings. After a certain amount of plastic strain, the sample was unloaded to zero applied load. The current modulus was measured by cycling the sample in the elastic region two or three times. The sample was then reloaded to a larger level of plastic strain and the procedure repeated.

The results of such an experiment for the unreinforced alloy in the T61 condition are shown in Figure 3.48b. (The data symbol indicates the sample mean value and the bars indicate

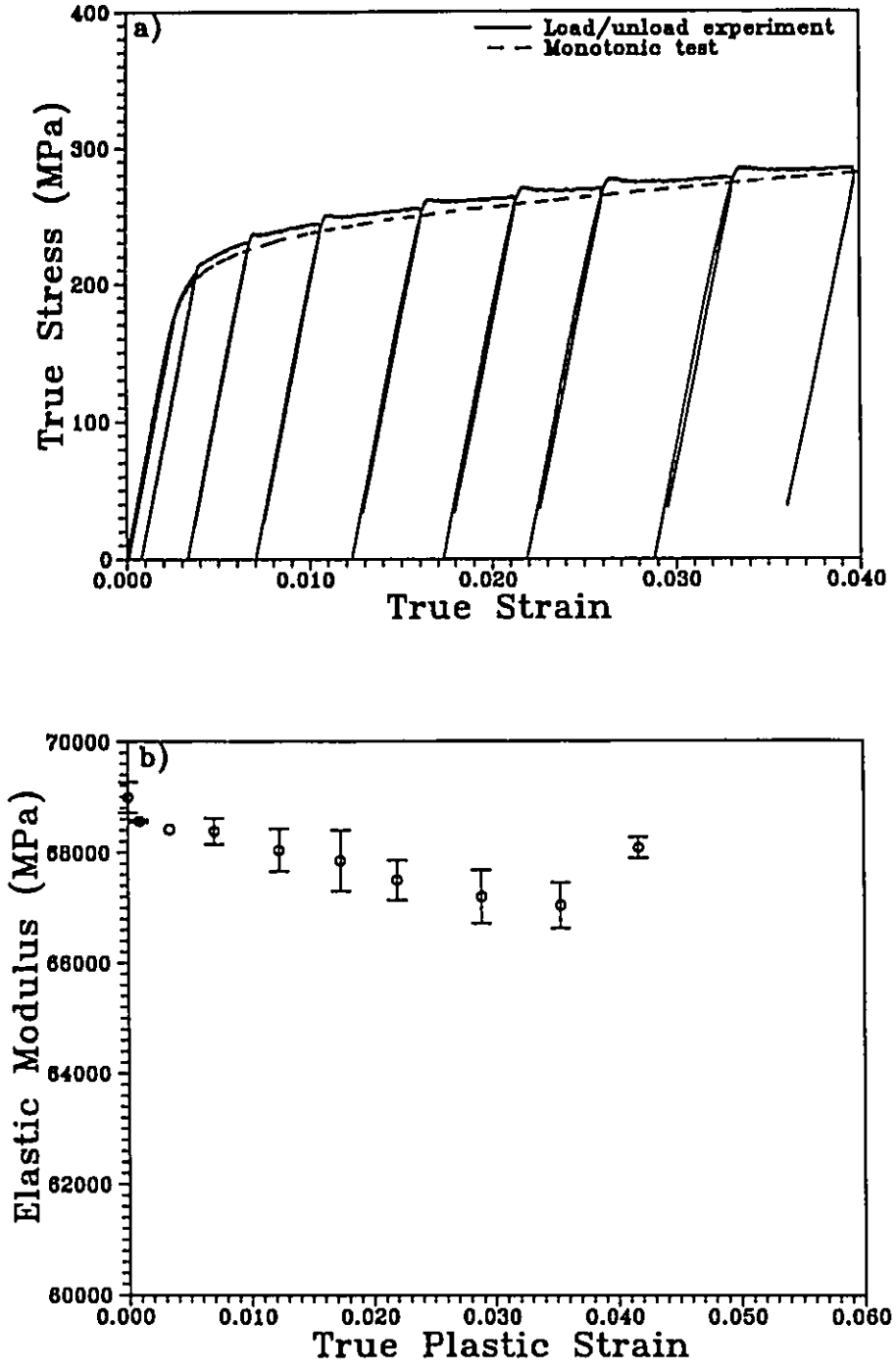

Figure 3.48: a) Unloading experiment used to measure the modulus of a sample versus plastic strain. b) Elastic modulus versus plastic strain (ϵ^c_p) for the A356 alloy in the T61 condition.

the sample standard deviation). There is a measurable loss in modulus in the material which reaches a level of about 3% by a plastic strain of .035. This is above the scatter in the measurement represented by a sample standard deviation of about +/- .5%.

The results of an identical experiment on the 20 vol% composite in the T61 condition are illustrated in Figure 3.49a. The drop in modulus in this case is much larger, reaching a level of 8% by a plastic strain of .05. The same experiment was performed on the 20 vol% composite material in the OA300 state (see Figure 3.49b). Again there is a drop in modulus which reaches a level of about 3.5% by a strain of .05.

The current modulus is divided by the initial modulus in Figure 3.50 to obtain a normalized modulus that allows a comparison between the materials. Clearly the rate of modulus loss is much larger in the 20 vol% composite in the T61 condition. The rate of loss in the 20 vol% composite in the OA300 state is about the same as that measured in the unreinforced alloy in the T61 condition.

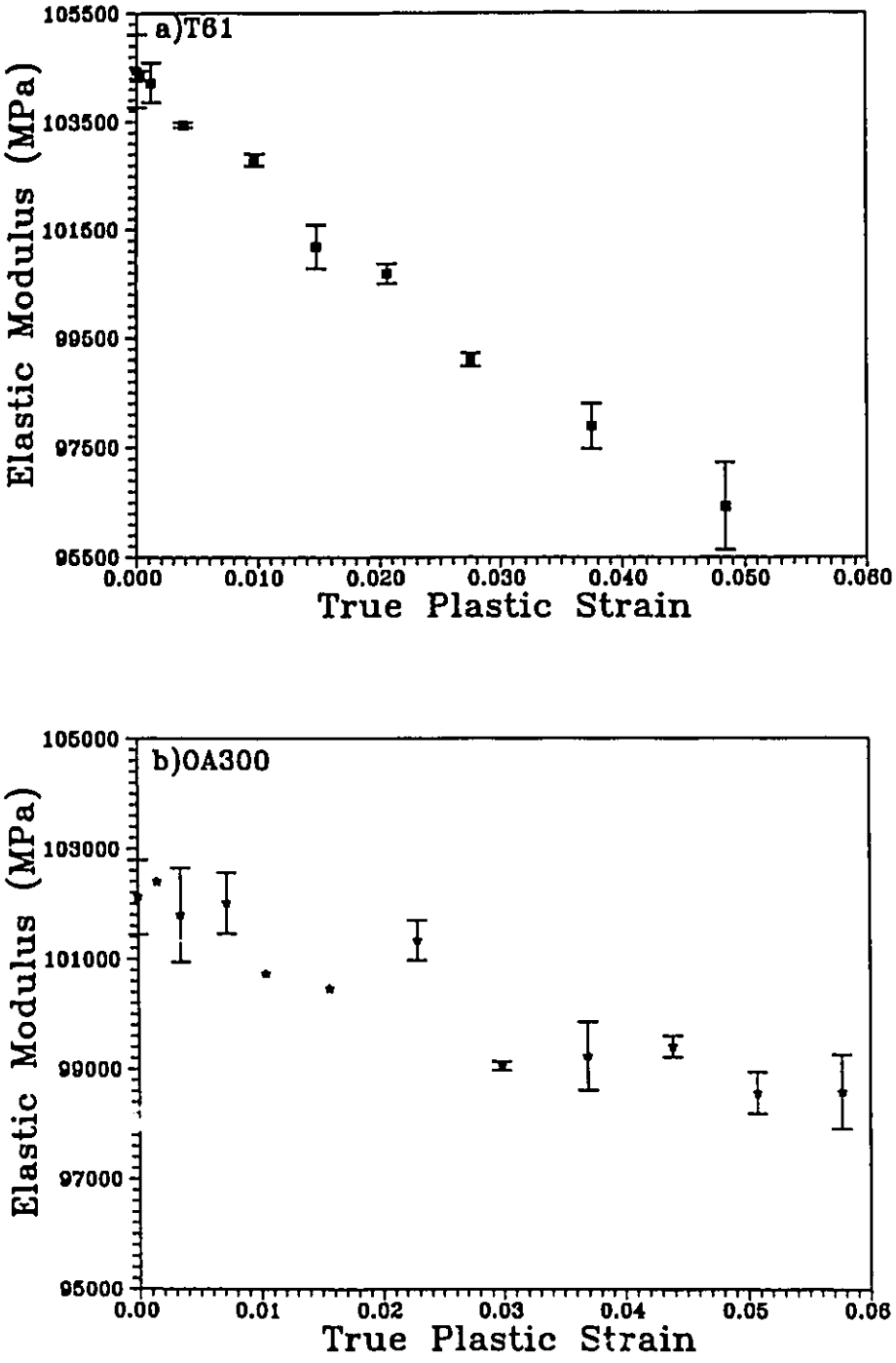

Figure 3.49: Elastic modulus as a function of plastic strain (ϵ^c_p) for 20 vol% composite in; a) T61; b) OA300 ageing states.

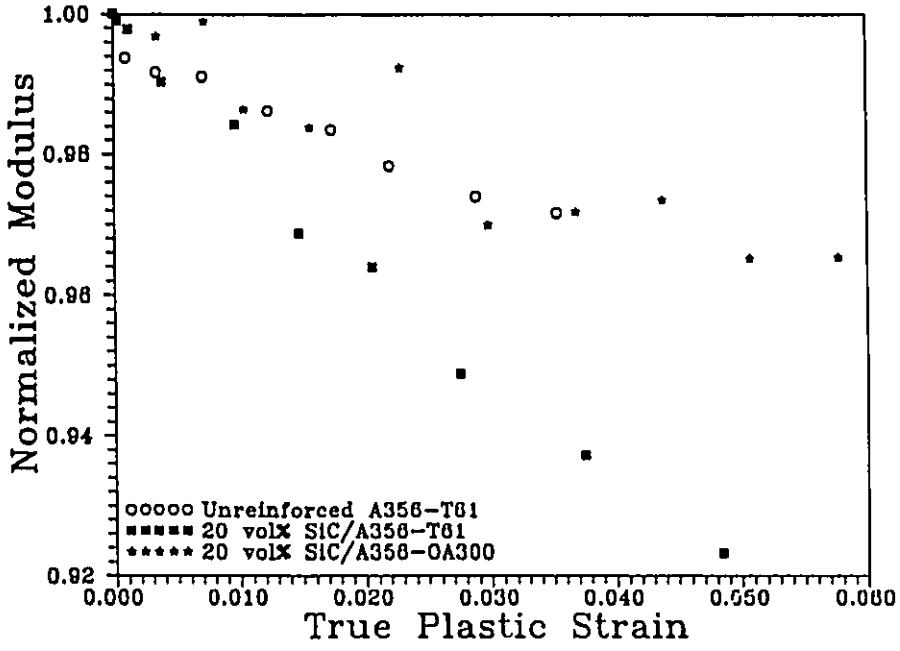

Figure 3.50: Comparison of the normalized modulus versus plastic strain (ϵ^c_p) for the various materials studied.

CHAPTER 4:

ESHELBY'S EQUIVALENT INCLUSION METHOD AND THE SELF-CONSISTENT FORMULATION

4.1 Introduction

Eshelby's Equivalent Inclusion method (Eshelby, 1957) has been used by a number of authors (Brown and Stobbs, 1971a; Brown and Clarke 1977; Pedersen, 1983) to solve for the internal stress developed in a two phase system. An excellent review of this method and its application to metal matrix composites has recently been completed (Withers et al., 1989). In this chapter we will present Eshelby's method for the case of a particle embedded in both the infinite and finite matrix. The solution for the finite matrix was first suggested by Brown and Stobbs and later extended by Pedersen using the so called Mean Field Approximation. This approximation was designed to deal with the problem of composites containing a high volume fraction of second phase. The Mean Field theory slightly underestimates composite properties (Withers et al., 1989).

An alternative method for dealing with the high volume fraction problem is based on a Self-consistent method (Hill, 1965) and incorporates the Equivalent Inclusion method. This model will be developed and compared with the infinite and finite Eshelby methods when applied to composite elasticity. The self-consistent method will then be extended to model the plastic behaviour of the composite and the influence of particle distribution on plastic flow will be investigated.

During the development, it will become clear that the Eshelby formulation is based on a prediction of the average stress and strain developed in the two phases. In its present form it can say very little about local fluctuations in the stress or strain level. This constitutes a limitation

of the method and must be kept in mind when applying the model to experimental results. In situations where local stress or strain level deviate significantly from the average values it would be expected that the Eshelby solution will not provide a fully detailed account of the behaviour.

4.2 The Infinite Eshelby Solution

The problem that we wish to solve is depicted in Figure 4.1. A particle with elastic properties represented by the stiffness tensor C_p, is embedded in an infinite matrix with elastic properties C_m. We are interested in the case in which the system is initially stress free (e.g. no volume or thermal misfit exists between the particle and matrix). A tensile stress σ_A is applied as shown. If $C_p > C_m$ a shape misfit will result due to the different strain response in the particle and matrix and the two will reach an equilibrium or constrained state. This disturbance due to the presence of the particle, and the resulting stress concentrations, can be dealt with using Eshelby's Equivalent inclusion method providing that the shape of the particle can be represented by an ellipse.

Eshelby first considers the elastic field around a misfitting ellipsoidal particle embedded within a infinite isotropic matrix with the same elastic constants as the particle. This will be referred to as the homogeneous case. Through a series of cutting and welding operations the particle is removed from the matrix and imagined to undergo a stress free shape change or transformation strain (strain e^T). Surface tractions are then applied to the particle to return it to its original shape and it is replaced back in the hole of the matrix. On removal of these surface tractions the matrix will constrain the particle such that it cannot attain its transformed shape. This constrained state is represented by a strain of e^C. According to Hooke's law the resulting stress in the particle is;

$$\sigma^P_{ij} = \sigma^C_{ij} - \sigma^T_{ij} \qquad (4.1)$$

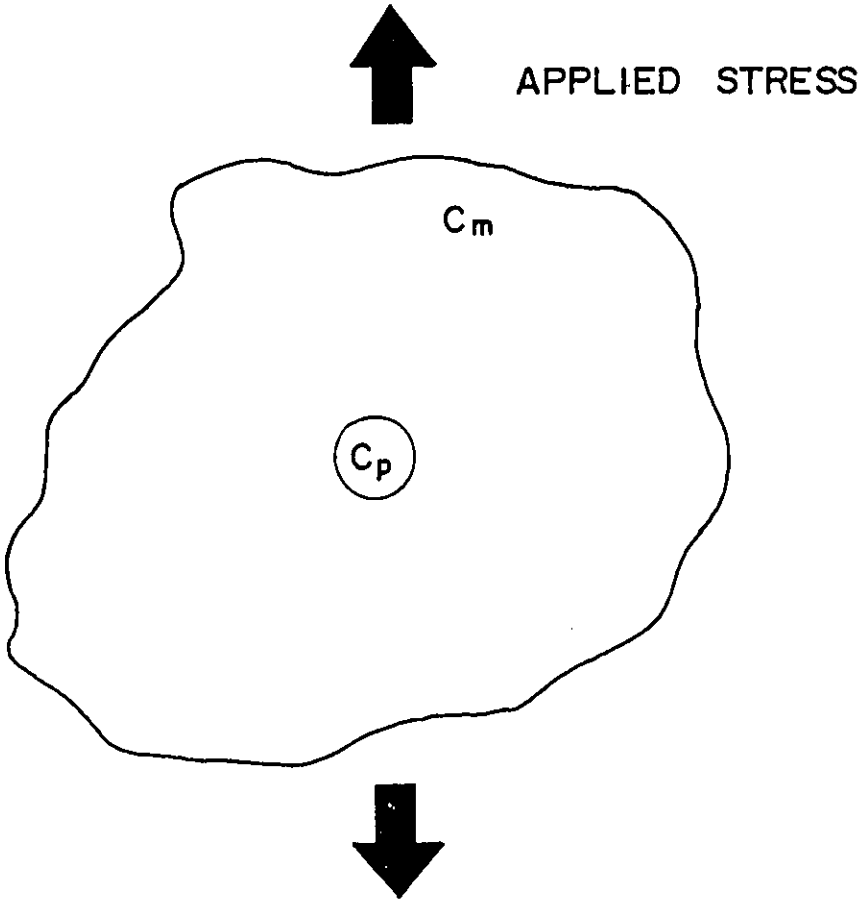

Figure 4.1: A particle with elastic properties C_p embedded in an infinite matrix with properties C_m under an applied stress.

or

$$\sigma^{p}_{ij(hom)} = C_m(e^{C}_{ij} - e^{T}_{ij}) \tag{4.2}$$

where $\sigma^{p}_{ij(hom)}$ is the stress in the particle for the homogeneous case, e^{C}_{ij} are the components of the constrained strain and e^{T}_{ij} are components of the transformation strain. One of the principle results of Eshelby's work is the development of the so called Eshelby tensor, S_{ijkl} (which will be represented by the symbol $\underline{S}$) which relates the constrained strain to the transformation strain as follows;

$$e^{C}_{ij} = \underline{S} e^{T}_{kl} \tag{4.3}$$

The derivation of the $\underline{S}$ tensor is complicated. However its value depends only on the inclusion shape and the poisson's ratio of the matrix. Brown and Clarke (1977) have calculated $\underline{S}$ for a number of inclusion geometries ranging from long fibres to spheres. Substituting the expression for e^{C}_{ij} in equation (4.2) indicates that the stress in the particle can be obtained from a knowledge of $\underline{S}$ and e^{T}_{ij}.

4.2.1 Elastic Inhomogeneity

The above solution is general for an elastically homogeneous system (i.e. $C_m = C_p$ etc.) with a defined transformation strain. However the solution of interest here is as defined in Figure 4.1 where a load is applied to an elastically inhomogeneous system (i.e. $C_m \neq C_p$). The stress in the particle in this situation is;

$$\sigma^{p}_{ij} = \sigma^{C}_{ij} + \sigma^{\wedge}_{ij} \tag{4.4}$$

or

$$\sigma^{p}_{ij(inh)} = C_p(e^{C}_{ij} + e^{\wedge}_{ij}) \tag{4.5}$$

where $\sigma^{p}_{ij(inh)}$ is the stress in the particle for the inhomogeneous case $\sigma^{\wedge}_{ij}$ is the applied stress and $e^{\wedge}_{ij}$ is the associated applied strain. In this case there is no way in which e^{C} can be expressed in

terms of $e^{\wedge}$. Eshelby overcomes this problem by stating that an equivalent homogeneous system can be chosen with a transformation strain defined in such a way to be identical to the loaded heterogeneous system (see Withers et al. (1989) for a detailed description of this process). This can be explained by considering that a shape misfit arises between the particle and matrix because of their different strain responses to an applied load (resulting from their different elastic properties). This shape misfit can be represented by a transformation strain e^{T} such that;

$$\sigma'_{ij(in)} = \sigma'_{ij(hom)} \tag{4.6}$$

or

$$C_p(e^{C}_{ij}+e^{\wedge}_{ij}) = C_m(e^{C}_{ij}+e^{\wedge}_{ij}-e^{T}_{ij}) \tag{4.7}$$

As in the previous homogeneous case we can define e^{C} in terms of e^{T} using $\underline{S}$. The remainder of the problem involves obtaining an expression which relates e^{T} to $e^{\wedge}$. This can be done by solving a set of simultaneous equations which are created from equation 4.7 using values of ij = 11,22,33. The details of this step are described in Appendix A.1. The important result of this solution for a spherical inclusion is that;

$$e^{T}_{ij} = Be^{\wedge}_{ij} \tag{4.8}$$

where;

$$B = \frac{C_m - C_p}{(C_p - C_m)\underline{S} - C_m} \tag{4.9}$$

where $\underline{S}$ is calculated for a sphere. Since e^{C} can be expressed in terms of e^{T}, which in turn can be expressed in terms of $e^{\wedge}$, the stress in the particle can be calculated knowing only $e^{\wedge}$, the applied strain. From this, composite properties can be calculated.

This is a rigorous analytical solution for composites with low volume fractions since it is based on an infinite matrix. However for larger volume fractions of second phase this solution begins to break down.

4.3 The Finite Eshelby Solution.

Efforts to extend the above solution to a finite case have been developed progressively by a number of authors over the last 30 years. (Eshelby, 1957; Brown and Stobbs, 1971; Tanaka and Mori, 1972; Brown and Clarke, 1977; Pedersen, 1983). The most recent results of these developments are described by Withers et al. (1989). It is useful to briefly review the principal results of these studies.

One important result of the infinite solution is that the stress in the particle is uniform and can be expressed in terms of the applied stress. Conversely the local stresses that are generated in the matrix adjacent to the particle as a result of the shape misfit are complicated and non-uniform. Upon calculating these local stresses in the matrix for the case of a spherical particle, Brown and Stobbs (1971a) determined that they averaged to zero throughout a spherical region surrounding the particle. Work by Tanaka and Mori (1972) revealed that this was the case for any ellipsoidal shape. The finite solution can then be described (following Withers et al., 1989) by referring to Figure 4.2.

Imagine a spherical boundary around a portion of the infinite matrix which includes the particle. According to equilibrium conditions the stresses across this boundary must be equal and opposite. If this region is cut out of the infinite solid the constraining effect of the infinite matrix will be removed and this finite solid will respond by changing its overall shape. To satisfy the boundary conditions at the external surface, Eshelby (1954; 1957) introduced the concept of an image stress. An imaginary stress field is assumed to exist on the opposite side of the boundary, such that it satisfies the boundary conditions at the free surface (Hull and Bacon, 1984; pg.88-90). This additional stress field is consequently often termed an image stress or image source. The form of this stress was later defined more precisely by Brown and Stobbs (1971a) who realized that the image stress must balance the stress in the particles in order to satisfy the

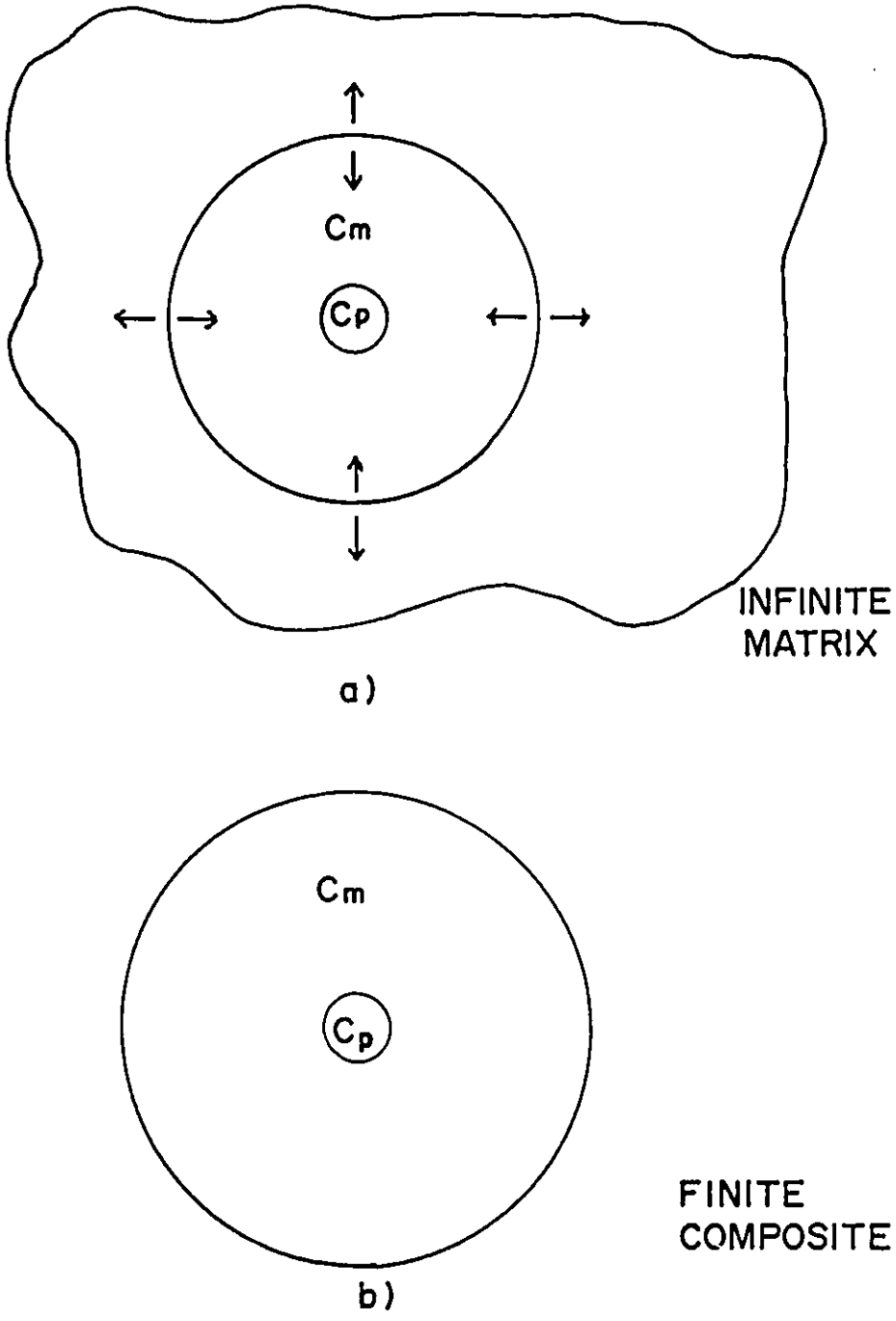

Figure 4.2: a) the infinite matrix as described in Figure 4.1; b) a section of the matrix containing the particle cut from the infinite matrix

boundary conditions at the surface;

$$<\sigma>_{im} + V_p\sigma_p = 0 \qquad (4.10a)$$

where $<\sigma>_{im}$ is the image stress, V_p is the volume fraction of the particles and σ_p is the stress in the particle. The fluctuating stresses in the matrix do not contribute to the image stress because their average value is zero. For a homogeneous composite the shape change should be uniform. One way of thinking of this is to consider that the element in Figure 4.2 is acted upon by a stress equivalent to $<\sigma>_{im}$ which causes a uniform distortion of $<e>_{im}$ in both the matrix and particle. This image stress is now commonly known as the mean stress or mean matrix stress $<\sigma>_m$, after Brown and Stobbs (1971a) and Brown and Clarke (1977). This stress is shared in such a way that equation (4.10a) becomes;

$$V_m<\sigma>_m + V_p<\sigma>_p = 0 \qquad (4.10b)$$

For a more detailed discussion of this equation see appendix A.2

How the mean stress is distributed in the case of the inhomogeneous composite is less clear. It would be expected that the strain created in the two phases as a result of the mean stress would be different because of the differences in stiffness. However Pedersen (1983) proposed the mean field approximation which assumes that even in the inhomogeneous case the mean stress is sampled equally by the two phases. As Withers et al. points out, this approximation leads to underestimates of composite behaviour.

In the context of the calculations, we can now state that the stress in the particle for the finite solid is;

$$\sigma^{P}_{ij(fin)} = C_p(e^{C}_{ij} + e^{\wedge}_{ij} + <e>_{mij}) \qquad (4.11)$$

which is equivalent to equation (4.5) except for the additional term $<e>_m$ due to the image stress. Using the method of the equivalent inclusion (equation (4.7), see Appendix A.2) a new expression for e^T can be derived;

$$e^{T}_{ij} = B^{f} e^{\wedge}_{ij} \tag{4.12}$$

where;

$$B^{f} = \frac{C_m - C_p}{[\,(C_p - C_m)\,(\underline{S} - V_p(\underline{S} - I)) - C_m\,]} \tag{4.13}$$

where V_p is the volume fraction of particles and I is the identity tensor. Note that B^f is equivalent to B except for the additional term $V_p(\underline{S}\text{-}I)$ in the denominator.

Having an expression for the stress in the particle, the elastic modulus of the composite for an applied tensile stress can be calculated (for details see Appendix A.3). The results of this for the infinite and finite cases are respectively;

$$\frac{1}{E_c} = \frac{1}{E_m} + \frac{V_p}{E_m}\left[\frac{E_m - E_p}{(E_p - E_m)\,\underline{S} + E_m}\right] \tag{4.14}$$

and

$$\frac{1}{E_c} = \frac{1}{E_m} + \frac{V_p}{E_m}\left[\frac{E_m - E_p}{(E_p - E_m)\,[\underline{S} - V_p(\underline{S} - I)\,] + E_m}\right] \tag{4.15}$$

The results of these calculations are illustrated in Figure 4.3. The modulus of the composite has been normalized by the modulus of the matrix in order to make comparisons with experiments. Included are experiments obtained from the present work on the A356 alloy as well as those reported in the literature for other alloy systems (ASM Handbook 1990). Good agreement between experiment and the infinite solution is obtained with volume fractions below about 25 volume %. At higher volume fractions this solution is no longer applicable. The finite solution also gives good results but to higher volume fractions. However, as mentioned, this solution underestimates the experimental data over the entire volume fraction range reported in the figure.

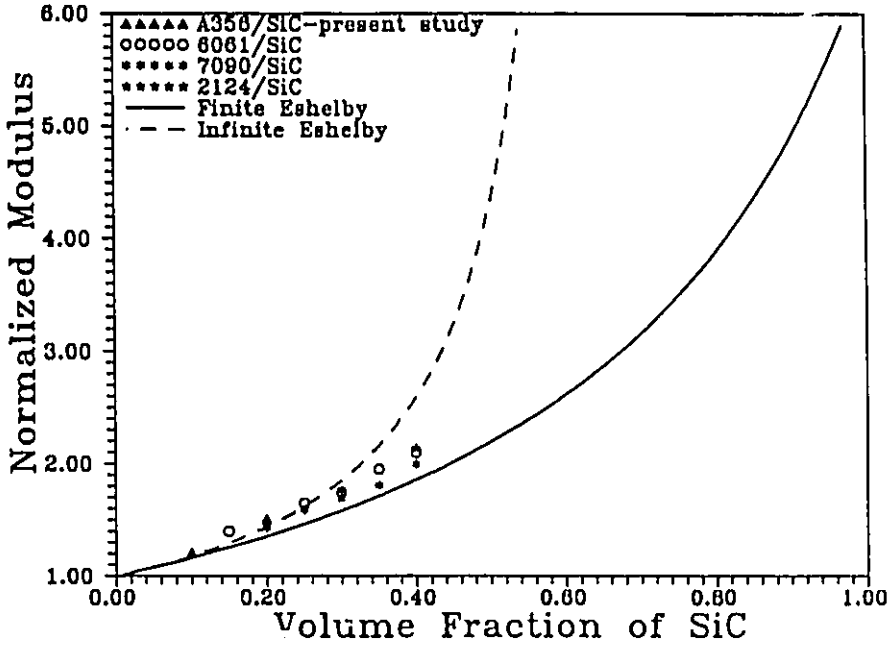

Figure 4.3: Comparisons of the infinite and finite Eshelby solutions for elastic modulus. Included are experimental data from this study and that reported in the ASM Handbook. The ratio of $E_{SiC}/E_{Al} \approx 7$

4.4 The Self-Consistent Analysis

4.4.1 Elastic Behaviour

An alternative method for determining the elastic modulus of high volume fraction particulate composites, can be developed using the self-consistent method. This was first proposed by Hershey (1954) and Kroner (1958) to solve the problem of the elasticity of polycrystalline materials. It was later developed by Hill (1965) to predict the elastic properties of composite materials. The basic concept behind the analysis can be described by referring to Figure 4.4. Assume we have a infinite composite made up of a random distribution of roughly spherical SiC particles (aspect ratio unity) embedded in an interconnecting phase consisting of approximately equiaxed grains of Al matrix. If we isolate a single particle, we can determine the stress on it due to an applied load on the infinite body as discussed in section 4.2. However, in this case we make the approximation that the particle samples the average properties of the infinite body in which it is embedded. Thus we require the properties of the composite itself which remain to be determined. Following the procedure of the infinite Eshelby solution (see Appendix A.4) it can be determined that the stress in the particle (in the direction of loading) is related to the applied stress by;

$$\sigma^{P}_{11} = \left[\frac{E_p}{\underline{S}E_p + (1-\underline{S})E_c}\right]\sigma^{A}_{11} \qquad (4.16)$$

where σ^{P}_{11} is the stress in the particle in the direction of loading, σ^{A}_{11} is the applied stress, E_p and E_c are the elastic constants of the particle and composite respectively. This solution is identical to the infinite Eshelby solution with the exception that the elastic constants of the infinite matrix E_m are replaced by the elastic constants of the composite E_c. In order to complete the self-consistent analysis, an expression for the stress in the matrix must be found. It is proposed that

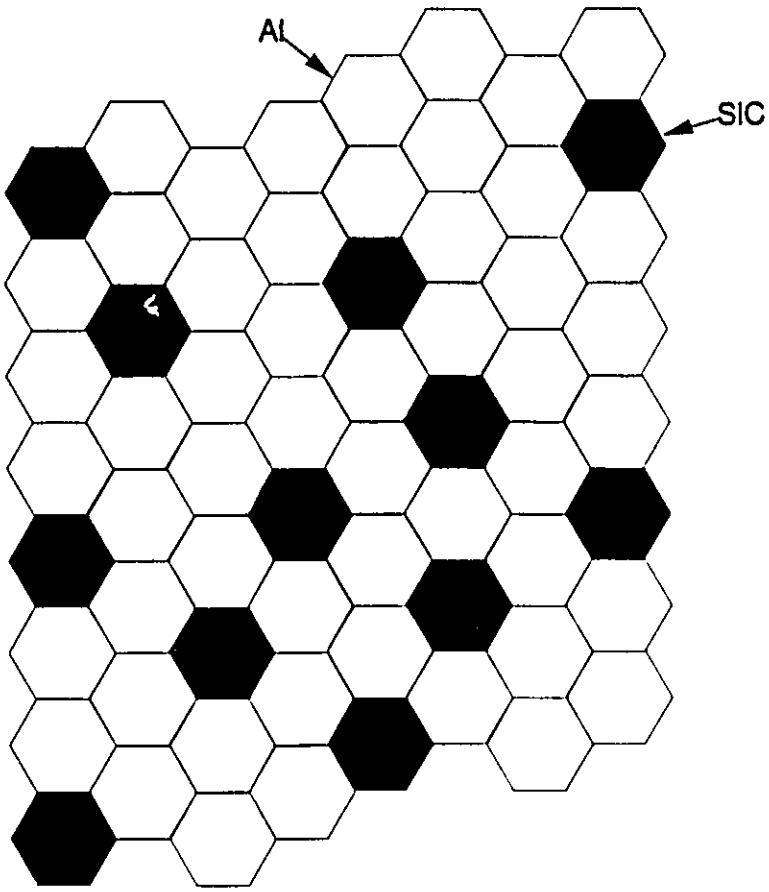

Figure 4.4: A random distribution of SiC particles in a polycrystalline matrix of Al. Both particles and Al grains have an aspect ratio of unity and are approximately spherical.

this can be done by treating the matrix on the same footing as the particle. It is then assumed that the calculated stress represents the average stress in the matrix within the composite. The validity of this approach can be discussed in the following way.

As the Eshelby method makes clear, although the stress in the particle is uniform, there is a complicated stress state in the matrix adjacent to the particle which is not uniform. However, as discussed by Brown and Stobbs (1971a) these stresses average to zero and can be neglected when considering the overall or average stress in the matrix. Consequently, the average stress in the matrix is uniform and can be calculated in the same way as that for the particle. Thus the stress in the matrix is;

$$\sigma_{11}^{m} = \left[\frac{E_m}{\underline{S}E_m + (1-\underline{S})E_c}\right]\sigma_{11}^{A} \qquad (4.17)$$

where σ^m_{11} is the stress in the matrix in the direction of loading, σ^A_{11} is the applied stress, E_m and E_c are the elastic constants of the matrix and composite respectively.

The basic concept of self-consistency can be described by referring to Equation (A3) which was derived in Appendix section A.2. This equation describes the basic connections between the two phases in the composite;

$$V_m(<\sigma>_m + \sigma^A) + V_p(<\sigma>_p + \sigma^A) = \sigma^A \qquad (4.18)$$

By inspection;

$$\sigma^p = <\sigma>_p + \sigma^A \; ; \quad \text{and} \quad \sigma_m = <\sigma>_m + \sigma^A \qquad (4.19)$$

When a load is applied to the elastically heterogeneous system, the particle and matrix constrain each others strain response. The constraint is equal and opposite in the two phases and results in the development of an internal stress such as that described by equation (4.10b). This constraint is superimposed upon the applied stress as described by equation (4.18). Consequently, the properties of the overall composite can be calculated from a knowledge of the internal constraint

between the two phases only. In this way the solution is self-consistent.

If we substitute the stresses calculated, (4.16) and (4.17), into equation (4.18) we get the following;

$$V_m\left[\frac{E_m}{\underline{S}E_m+(1-\underline{S})E_c}\right]+V_p\left[\frac{E_p}{\underline{S}E_p+(1-\underline{S})E_c}\right]=1 \qquad (4.20)$$

For a spherical particle and a poisson ratio of 1/3, $\underline{S}$ is equal to 7/15. Therefore equation (4.20) reduces to;

$$V_m\left[\frac{15E_m}{7E_m+8E_c}\right]+V_p\left[\frac{15E_p}{7E_p+8E_c}\right]=1 \qquad (4.21)$$

Consequently the elasticity of the composite can be expressed using only the volume fraction and elastic constants of the two phases. Rearrangement of equation (4.21) leads to the following expression;

$$8E_c^2 + [(7-15V_p)E_p + (7-15V_m)E_m]E_c - 7E_pE_m = 0 \qquad (4.22)$$

Inspection of equation (4.22) reveals that it is a quadratic equation for E_c where;

$$a=8; \quad b=[(7-15V_p)E_p + (7-15V_m)E_m]; \quad c=-7E_pE_m \qquad (4.23)$$

We can now solve for the modulus of the composite using the self-consistent model and compare it to the infinite and finite Eshelby models. Figure 4.5a shows such a comparison using moduli values of 70 GPa for the matrix (Al) and 450 GPa for the particle (SiC). Included are moduli values using the upper bound (Voigt) and lower bound(Reuss) solutions for the composite modulus. The three solutions discussed here give essentially identical results up to about 10 vol% of particles. As expected, both the self-consistent and finite Eshelby solutions lie between the Voigt and Reuss bounds over the whole volume fraction range. Figure 4.5b shows the normalized modulus results in order to compare theory with experiment. Although all three methods show good agreement up to about 25 vol.%, the self-consistent method exhibits better agreement in the

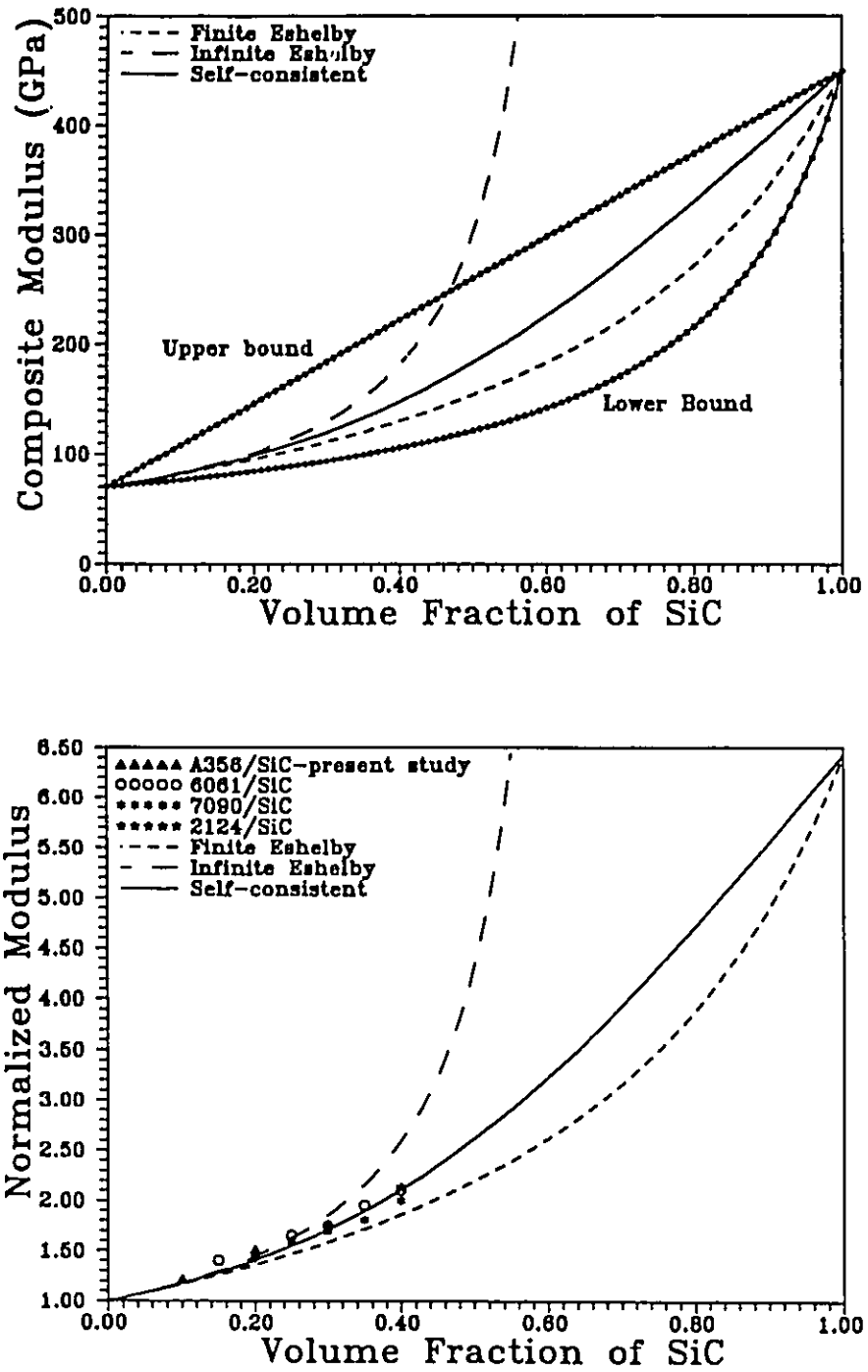

Figure 4.5: Comparison of the self-consistent method with Eshelby solutions for elastic modulus; a) including upper and lower bound solutions; b) including experimental data

range of 25 to 40 vol%. Modulus values for volume fractions above 40% could not be found in the literature.

4.4.2 Plastic Behaviour

Predicting plastic behaviour is a much more complicated problem and usually involves a number of simplifying assumptions. The approach taken in this section is similar in spirit to that described in the introduction (section 1.5) for the upper and lower bound cases. We treat the problem on the continuum level and consider the matrix and particles to be discrete macroscopic phases. We also assume that the stress-strain behaviour of the matrix within the composite can be represented by that of the unreinforced alloy. This assumes that the presence of the particles does not alter the properties of the matrix. (This has been discusses in more detail in the introduction (section 1.3) and in the section on microstructural characterization (section 3.1)). We consider that the particles remain elastic with a modulus representative of SiC and do not fracture during straining.

It is realized that, in the real material, plastic deformation will be inhomogeneous and will create strain gradients within the material. However it is assumed that these variations in strain level within the matrix can be adequately described by an average strain which can be calculated using the self-consistent formulation.

We will follow an approach similar to that taken by Chen and Argon (1979) and choose to represent plastic behaviour as a incrementally linear elastic problem. At each increment of applied stress the self-consistent formulation will be used to calculate the average stress and strain in each phase, using the slope of the matrix stress-strain curve at a given strain level, to represent the incremental elastic modulus of that phase. Knowing the stress and strain partitioning, the overall properties of the composite can then be calculated by the averaging

process provided by the self-consistent method.

4.4.3 Critical features of the self-consistent formulation

Particle Shape. One of the critical features of calculations based on Eshelby's method is that the particle must be represented by an ellipse with an assigned aspect ratio. Most commercial MMC's however are reinforced by particles or whiskers which have sharp corners and it has been proposed (Christman et al., 1989; Bao et al., 1991) that they are better represented by cylindrical shapes. The major difference between these two shapes is the arrangement of stress concentrations that can be generated at the particle ends and, in the case of the cylindrical shapes, at sharp corners.

Recent photoelastic experiments (Withers et al., 1991) have been performed to directly observe and compare the stress fields around ellipsoidal and cylindrical particles embedded in a matrix. The aspect ratio of both particles was about 3 and the stiffness ratios of the photoelastic materials used for the matrix and particle were stated to be typical of that found in MMC's. Their results indicate that the stress field around the end of the two types of particles show a high degree of similarity when the composite was loaded elastically. The exception to this being very close to the sharp corner of the cylinder. Estimates of the stress distribution using photoelastic measurements also indicated that the mean particle stress was essentially identical for the two shapes of particles. In addition, the value of this mean stress was well predicted, although slightly underestimated, by the Finite Eshelby method. Overall these results indicate that, at least for properties that depend primarily on volume averaged stresses such as elastic modulus, the composite is well represented by ellipsoidal shaped particles.

The situation is admittedly more complicated for plastic flow, where the local stress concentrations near particle corners can create plastic strain gradients in the material. However,

the volume of material experiencing this larger strain level may be relatively small especially for low volume fractions of reinforcement. Consequently it is difficult to asses the influence sharp corners exert on overall plastic flow. However, finite element studies on plastic deformation in MMC's (Bao et al., 1991; Christman et al., 1989) suggest that reinforcement by cylindrical particles offers larger degrees of strengthening than ellipsoidal particles. Calculations by Bao et al. (1991) indicate that the most significant difference is at an aspect ratio of unity, where unit cylinders give strengthening increments that are approximately twice as large as those calculated for spheres.

In summary, although the effects of reinforcement shape appears to be qualitatively well characterized, the magnitude of the effect has yet to be fully elucidated both experimentally and theoretically with respect to plastic deformation. However it is reasonable to suggest that representing reinforcements be elliptical shapes will result in an underestimation of composite flow strength.

Aspect ratio. The measured average aspect ratio of the SiC particles used in the composites of this study is 2 (see section 3.1). Results from Bao et al. indicate that for both elliptical and cylindrical shapes increasing the aspect ratio from 1 to 2 results in only a small increase in the predicted level of strengthening. Consequently, the simplification in the self consistent model of representing the reinforcement by spheres is justified, but will likely result in a slight underestimation of flow strength.

Averaging effects. The averaging processes for the incremental elastic approach described above necessitates that the particles sample "smooth out" moduli of the surrounding matrix material. Such smoothing artificially inhibits local deformation which invariably would occur to relieve local stress concentrations. As pointed out by Chen and Argon (1979) this aspect of the self-consistent theory likely results in an overestimate of composite flow strength,

especially at larger strains. This overestimation may be partly compensated for by the underestimates of strength due to the choice of a spherical particle to represent particle shape.

4.4.4 Description of the numerical procedure.

In the elastic region calculations using $\nu = 1/3$ and $\nu = 1/2$ differ only by 2 to 3% in the volume fraction range of interest. Since $\nu = 1/2$ is more appropriate for plastic flow, calculations for overall stress-strain behaviour were performed using this value.

In this case, $\underline{S}$ is equal to 2/5 and the stress connectors of equations (4.16) and (4.17) become;

$$\sigma^p = \left[\frac{5E_p}{2E_p+3E_c}\right]\sigma^A ; \sigma^m = \left[\frac{5E_m}{2E_m+3E_c}\right]\sigma^A \qquad (4.24)$$

and equation 4.22 becomes;

$$3E_c^2 + [(2-5V_p)E_p + (2-5V_m)E_m]E_c - 2E_pE_m = 0 \qquad (4.25)$$

Equation (4.25) corresponds to the equation for the modulus of a composite containing an isotropic dispersion of spheres given by Hill (1965).

The overall stress-strain behaviour of the composite is then numerically determined using the following steps (the procedure is described in Table 4.1);

1) The initial elastic values of E_p and E_m are used to calculate E_c using equation (4.25).

2) Starting with an initially unstressed body an applied stress increment of $\Delta\sigma^{\wedge}$ is imposed. The stresses resulting in the two phases are then calculated using the equations of (4.24).

3) the resulting increments in strain are then calculated using;

$$\Delta\epsilon = \Delta\sigma/E \qquad (4.26)$$

where $\Delta\epsilon$ is the increment in strain, $\Delta\sigma$ is the increment in stress and E is the elastic constant of the individual phase or that of the overall composite. The overall stresses and strains are then calculated by summation. This process is then repeated using the current values of E_p, E_m and

the calculated value of E_c.

Choice of a Constitutive Equation. The calculation of a stress-strain curve for the composite requires a knowledge of the individual constitutive equations of the particle and matrix. The stress-strain curve of the particle can be represented by an elastic curve with a modulus equal to that of SiC. In the case of the unreinforced alloy, the constitutive equation chosen must offer a realistic description of the stress-strain response of the matrix during the elastic/plastic transition (i.e. the low strain regime). A number of equations were explored but it was found that an equation based on the Ramberg-Osgood relationship (Bao et al., 1991) gave the best results. This equation is described by;

$$\epsilon = \frac{\sigma}{E} + \alpha \frac{\sigma_o}{E} \left(\frac{\sigma}{\sigma_o} \right)^{1/N} \qquad (4.27)$$

where σ_o is the yield strength of the material, N is the strain hardening exponent and E is the elastic modulus. This equation has advantages over those based on the Holloman model ($\sigma = k\epsilon^N$) because it only depends on the parameters σ_o and N and not the strength coefficient k. The value of α will be taken to be 3/7 following Bao et al.. Values for σ_o and N were chosen to be that typical of the aluminum alloy studied here (i.e. $\sigma_o = 200$ and $N = .1$). We first wish to explore the stress-strain behaviour of the composite assuming a random distribution of particles all of equal size and of spherical shape (see Figure 4.4). This can be represented by a single volume fraction, equal to the average volume fraction of particles. The stress-strain curves based on this distribution for composites ranging in volume fraction from .10 to .35 are illustrated in Figure 4.6a. As expected, as the volume fraction of particles increases the degree of strengthening increases. Perhaps the most interesting feature of the theoretical curves is the "saturation" effect in which the composite curve becomes nearly parallel with that of the alloy. This is more easily seen in Figure 4.6b where the ratio of the composite to alloy flow stress, at the same strain level,

Table 4.1: Numerical procedure used to calculate the elastic/plastic stress-strain curve of the composite. (D and D′ represent the constants of equation (4.24)).

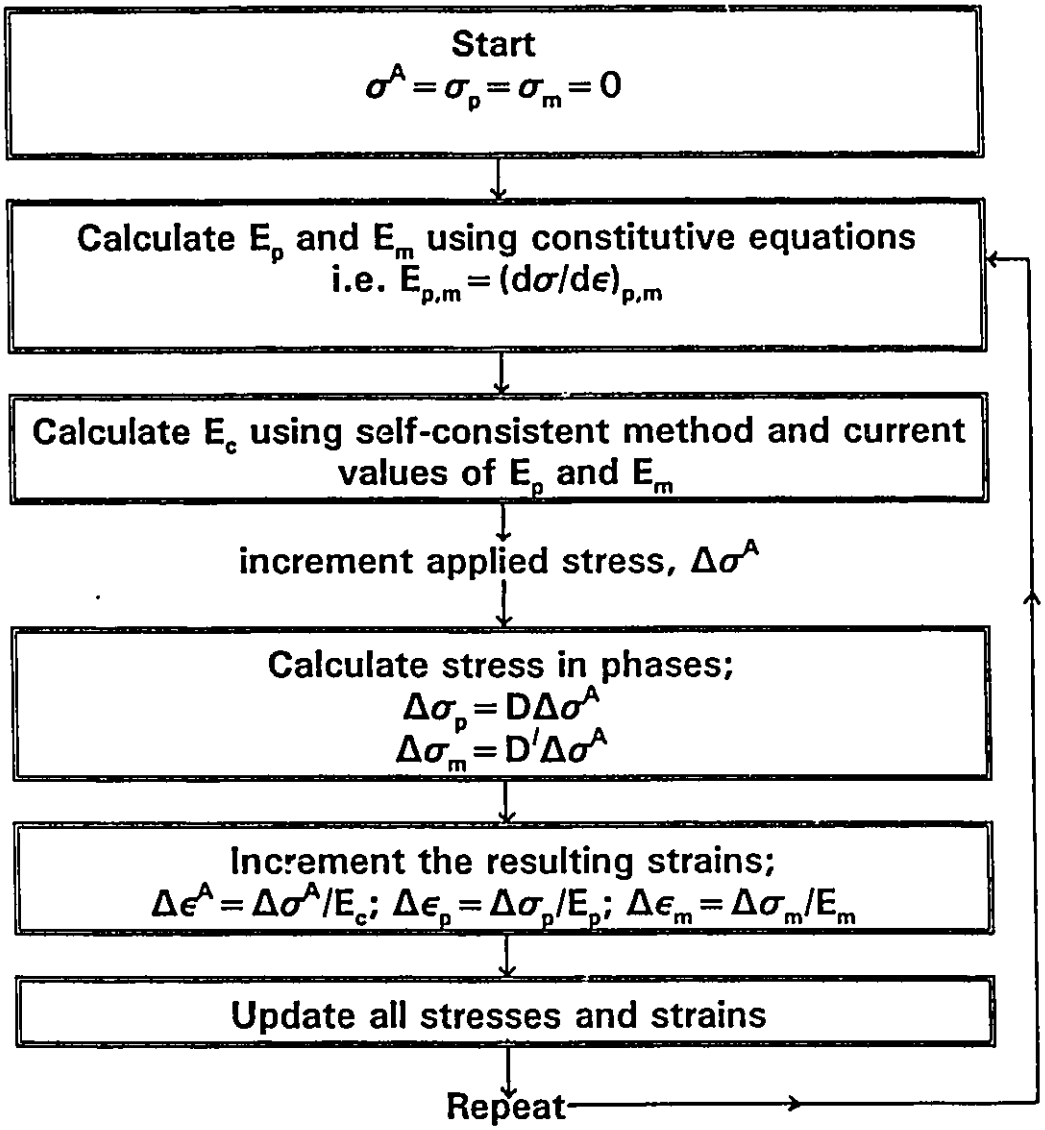

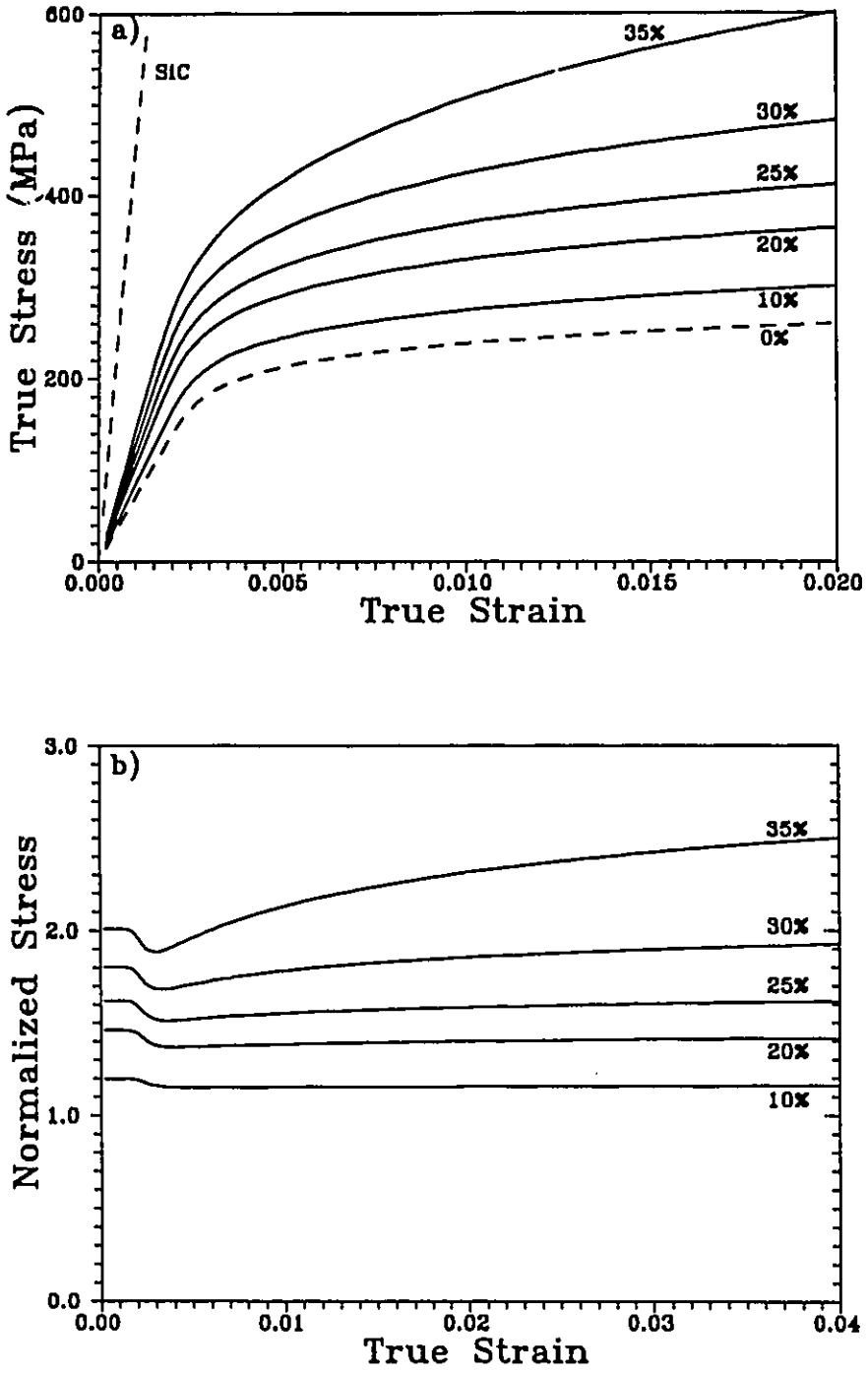

Figure 4.6: a) Predictions of composite σ-ϵ behaviour with various volume fractions of SiC particles. b) Composite flow strength normalized by alloy flow strength at the same strain (σ_c/σ_m).

is plotted as a function of total strain. These predictions illustrate that the strengthening ratio, (σ_c/σ_m) remains approximately constant after about 2% strain for all the cases except the 35 volume percent composite. This saturation effect was also observed in the experimental data (Figure 3.27). As a point of reference, the model predicts a strengthening ratio at saturation of 1.15 and 1.42 for the 10 and 20 vol% composites respectively. This is below the ratios measured experimentally which range from 1.25 to 1.30 for the 10 vol% and 1.5 to 1.6 for the 20 vol% composite, depending on ageing condition.

A physical interpretation of the drop in the strengthening ratio during the initial stages of plastic flow (Figure 4.6b) can be explained by referring back to the curves of Figure 4.6a. By inspection, it can be seen that the strain at which initial yielding occurs decreases as the SiC content increases. The incremental self-consistent solution can provide the overall composite strain at which the yield stress (σ_o) in the matrix is reached. This will be termed the composite yield strain and is plotted in Figure 4.7 versus the SiC content. As the SiC content increases the composite yields at a lower strain. Therefore there is a small region of strain where the composite begins to plastically flow, while the unreinforced alloy remains elastic. Consequently, in this region the strengthening ratio drops slightly. As would be expected this effect increases as the SiC content increases.

No provision for relaxation in the matrix was built into the model. In traditional Eshelby models, relaxation is an important aspect of the problem. As discussed in the introduction, this leads to the concept of unrelaxed and relaxed states. However, with the incremental linear elastic solution, relaxation is accounted for empirically through the use of the constitutive equation of the matrix. In this way, the stress transferred to the particle is determined by its sampling of the average behaviour of the material it is embedded in, which takes account of the current matrix behaviour using the instantaneous slope (or tangent modulus) of the matrix

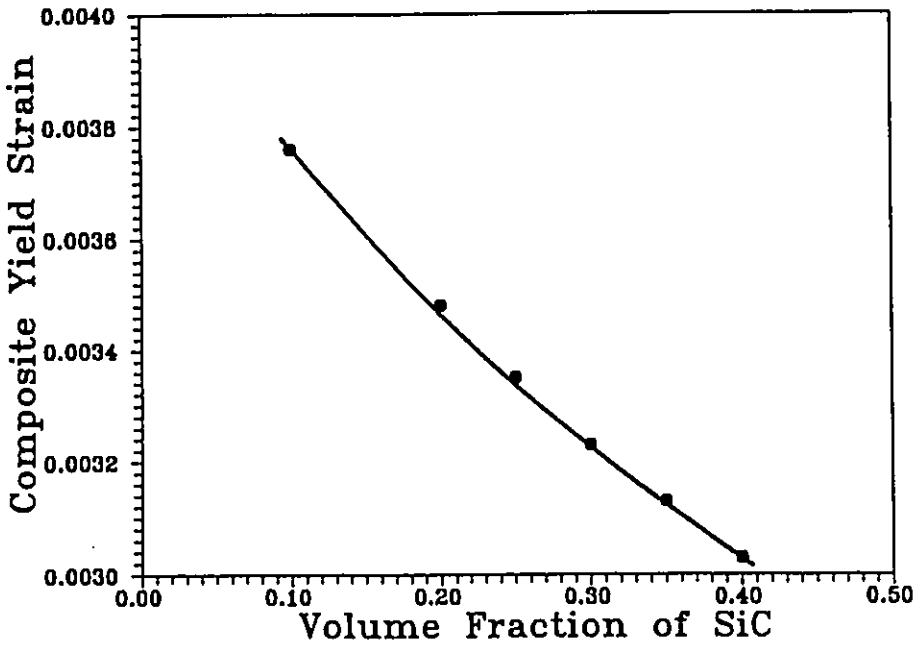

Figure 4.7: Composite yield strain (defined in text) versus the volume fraction of SiC particles.

stress-strain curve.

This method does not deal with the detailed plastic structure around the second phase particles. Consequently it does not lead to a particle size dependence of the relaxation process as described in section 1.4.2 (see Figure 1.10). In addition, as discussed in section 4.4.3 the averaging process used in the self-consistent model artificially inhibits local deformation that would occur to relieve local stress concentrations. Consequently, while the model does account for relaxation in an approximate way, it is not expected to be a rigorous treatment and should result in an overestimation of the flow strength of the composite.

Influence of Matrix Yield Strength and Strain Hardening Rate. To examine the influence of matrix strength and strain hardening rate, predictions from the model are plotted in Figure 4.8 for a 20 vol% composite. Composite stress and strain have been normalized by the yield strength σ_o and yield strain ϵ_o which quantify matrix behaviour according to the Ramburg-Osgood equation. Obviously changing the matrix strength only, will not change the strengthening ratio resulting from the addition of particles. However, it can be seen that an increase in strain hardening rate in the matrix does increase the strengthening ratio imparted by the SiC particles. These results have been replotted in Figure 4.8b normalized by the current stress in the matrix rather than σ_o. Again it is clear that the overall strengthening effect of the SiC particles increases as the hardening rate in the matrix increases.

Comparison With Finite Element Models. Figure 4.8 can be directly compared with the results of Figure 10 of Bao et al. (1991) represented here as Figure 4.9. Bao et al. explore strengthening of a matrix which behaves according to the Ramburg-Osgood equation and which is reinforced by 20 vol% of cylindrical particles with an aspect ratio of unity. Quantitative agreement between the two models is good. The self-consistent theory results in predictions of strengthening that are only about 5 to 10% below those predicted by Bao et al.. This is somewhat

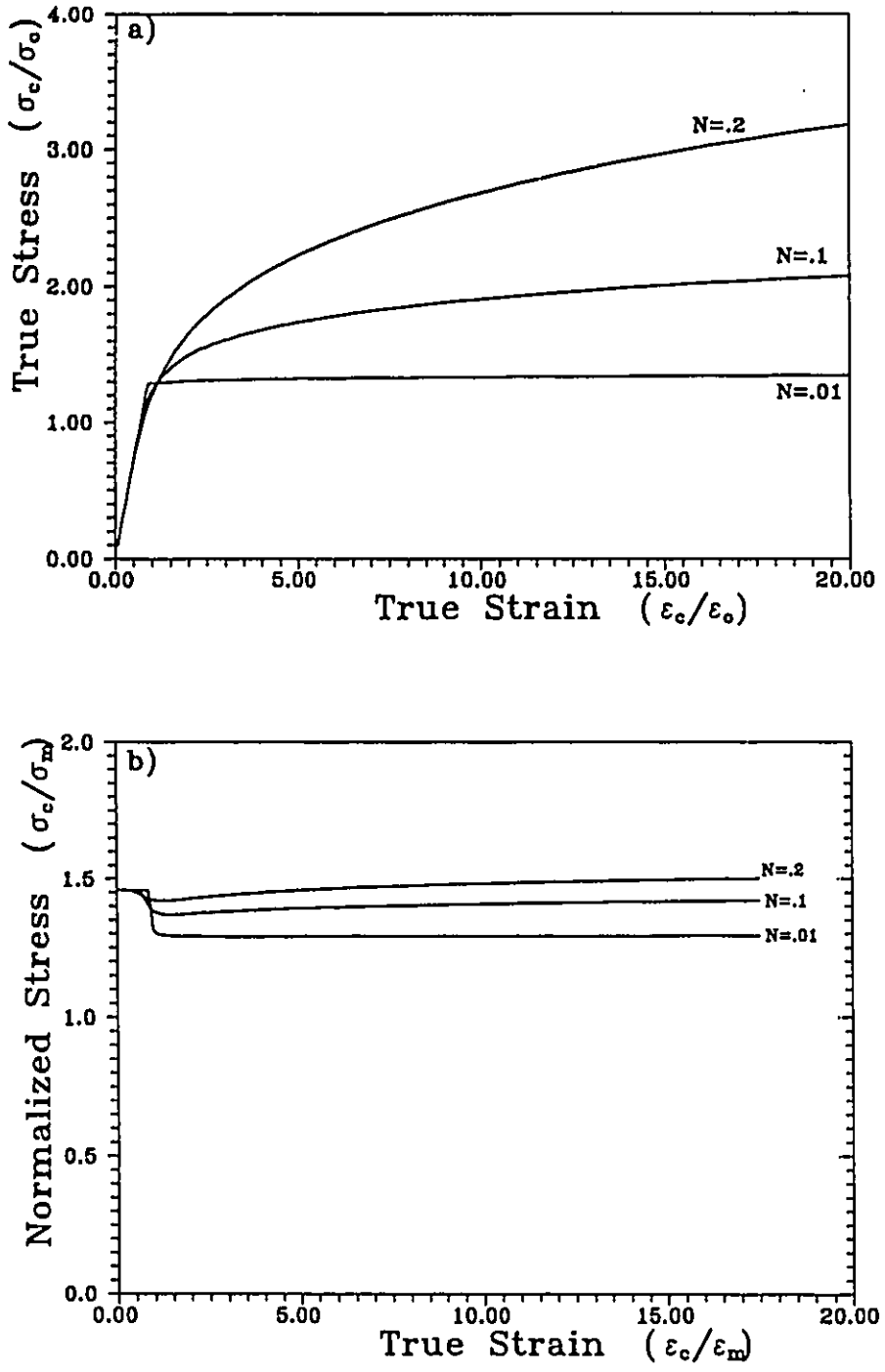

Figure 4.8: Composite strength as a function of matrix strain hardening rate N; a) normalized by σ_o; b) normalized by matrix strength σ_m. The strain is normalized by ϵ_o.

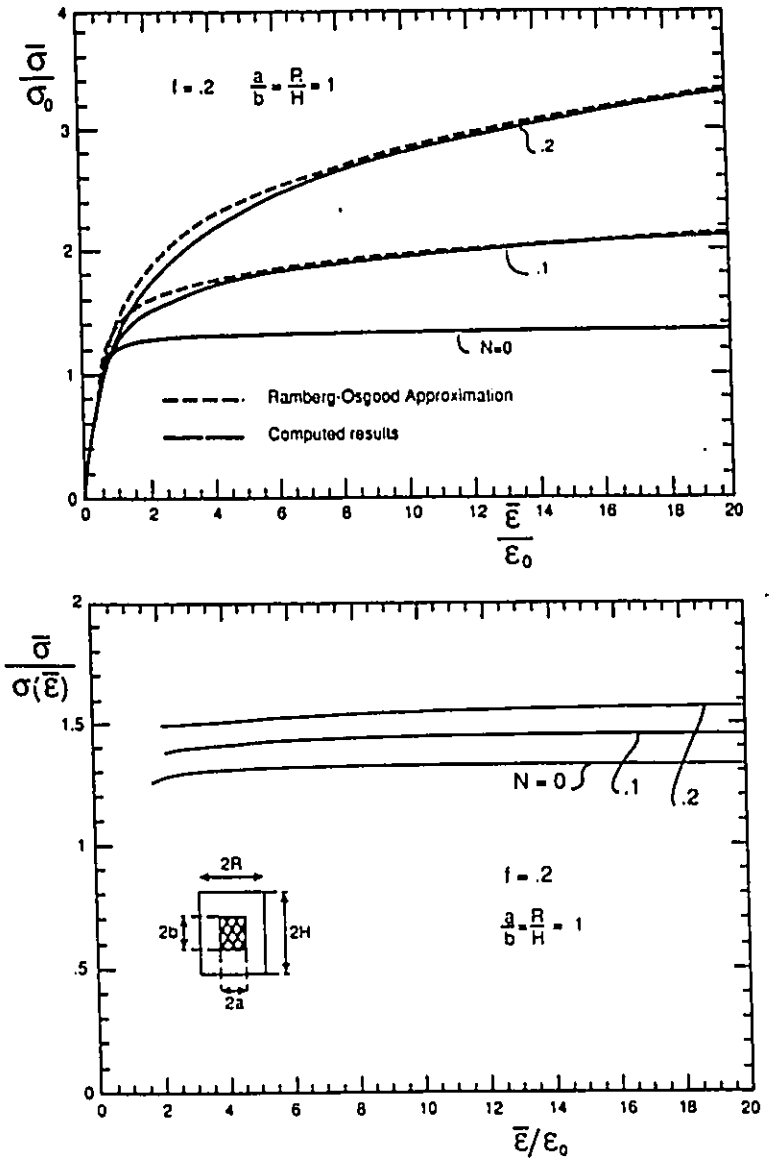

Figure 4.9: Results of Bao et al (1991) for composite strength (σ) versus N; a) normalized by σ_o; b) normalized by σ_m. Inset figure indicates the particle shape investigated.

surprising since their results consider cylindrical particles while the present model treats spheres. As discussed earlier, Bao et al.'s own calculations predict that reinforcement by spheres should result in strengthening which is 50% lower than that for cylinders. However, we have already noted that the self-consistent formulation is expected to overestimate composite properties. Thus agreement between the two models may be somewhat fortuitous. What is perhaps more significant than the quantitative agreement is the degree of similarity in the shape of the stress-strain curve predicted, and the trends concerning the effects of strain hardening rate. (Comparisons concerning trends in volume fraction also reveal good agreement with the finite element model.) Such agreement with alternative methods which can treat local stress states, supports the validity of the assumptions made in the present self-consistent theory concerning average stresses.

4.4.5 Influence of Particle Distribution

The experimental results for plastic flow on a polished surface, indicate the problem of interest. The distribution of particles in the composite is such that particle clusters and particle free regions are created on a macroscopic scale (of the order of 50 μm). This creates strain gradients in the material that are on a more macroscopic scale than those previously discussed due to, for example, sharp corners at particle ends. This inhomogeneous plastic flow may have an influence on the elastic/plastic transition and it is of interest to try a describe the nature of this effect.

In the previous section, the uniform case was defined by the average volume fraction of a distribution of particles. This description says nothing about the geometrical arrangement of the reinforcement. One way in which the effects of particle distribution can be studied is to define different periodic arrays such as the square and triangular arrays defined in Figure 4.10. This approach has been used by Brockenbrough et al. (1991) in their development of a finite element

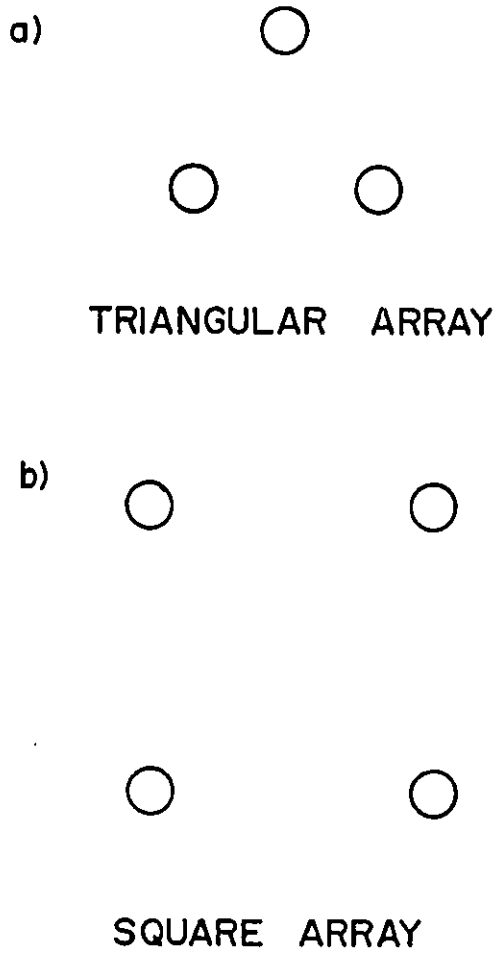

Figure 4.10: Various reinforcement array geometries as defined by Brockenbrough et al (1991).

model to describe the effects of fibre distribution on deformation. Although this study yields interesting results, it does not describe very well the particle distributions found in the composite materials studied here. In other approaches to clustering (e.g. Christman et al., 1989.) the shape of the unit cell has been changed such that the position of the particle in the cell is off centre. This can then be used to create vertical or horizontal clustering of the particles. This description of clustering still does not treat clustering on the more macroscopic scale in which it occurs in the composite studied here.

The approach taken in this study can be described by referring to Figure 4.11. We represent clustering in a more macroscopic way by considering that the composite is made up of a bi-modal distribution of particles. Consequently it can be represented by a region where the average volume fraction of particles is V_a and a second region where the volume fraction is V_b. In this case, we will always consider $V_b > V_a$. As an example, a composite with overall volume fraction $V_p = .2$ could be represented by a region of $V_b = 35\%$ and a region of $V_a = 0\%$ where each phase occupied 57% and 43% by volume of the entire composite respectively.

The overall composite properties can then be calculated using the same numerical procedure previously described but now considering that phase a is embedded in an infinite matrix of phase b or vice versa. The constitutive equations for these two phases are based on the calculations for the uniform case and are represented by the stress-strain curves of Figure 4.6.

The results of such a calculation using $V_b=35\%$ and $V_a=0\%$ and $V_b=40\%$ and $V_a=0\%$ are shown in Figure 4.12a and 4.12b respectively. These clustering conditions were chosen based on the particle distribution measurements made by Lloyd (1991) using image analysis techniques (see section 3.1.1). Included in the figure is the unreinforced data and the uniform 20% composite.

The model predicts that the initial strain hardening rate in the composite is higher in

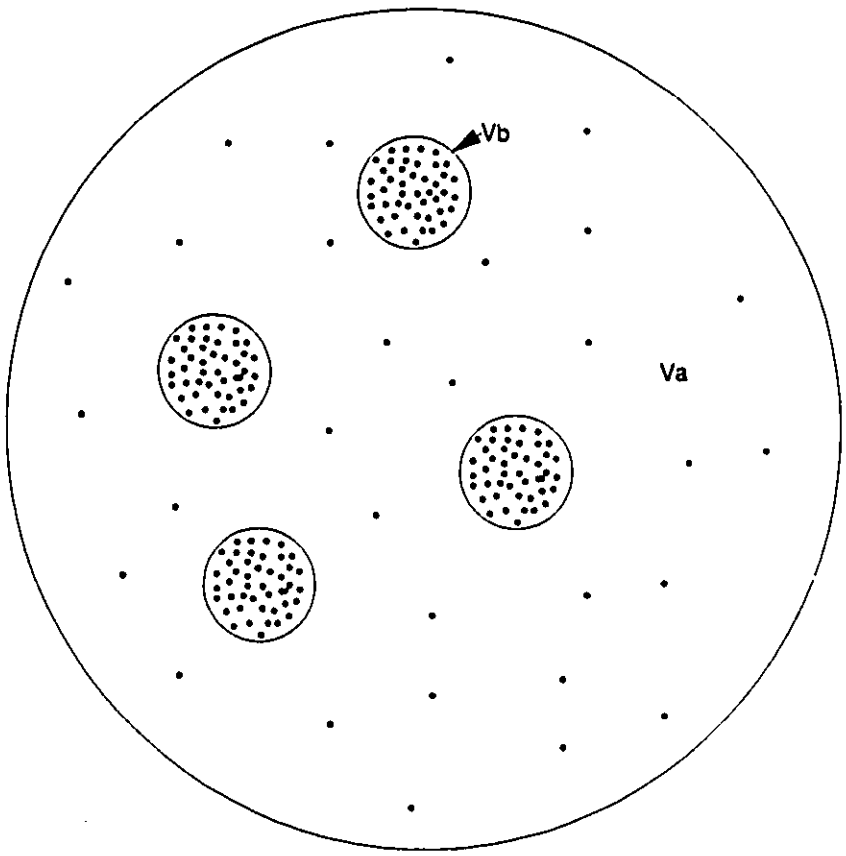

Figure 4.11: Schematic of a clustered structure represented by regions of high volume fraction (V_b) embedded in an infinite matrix of lower volume fraction (V_a).

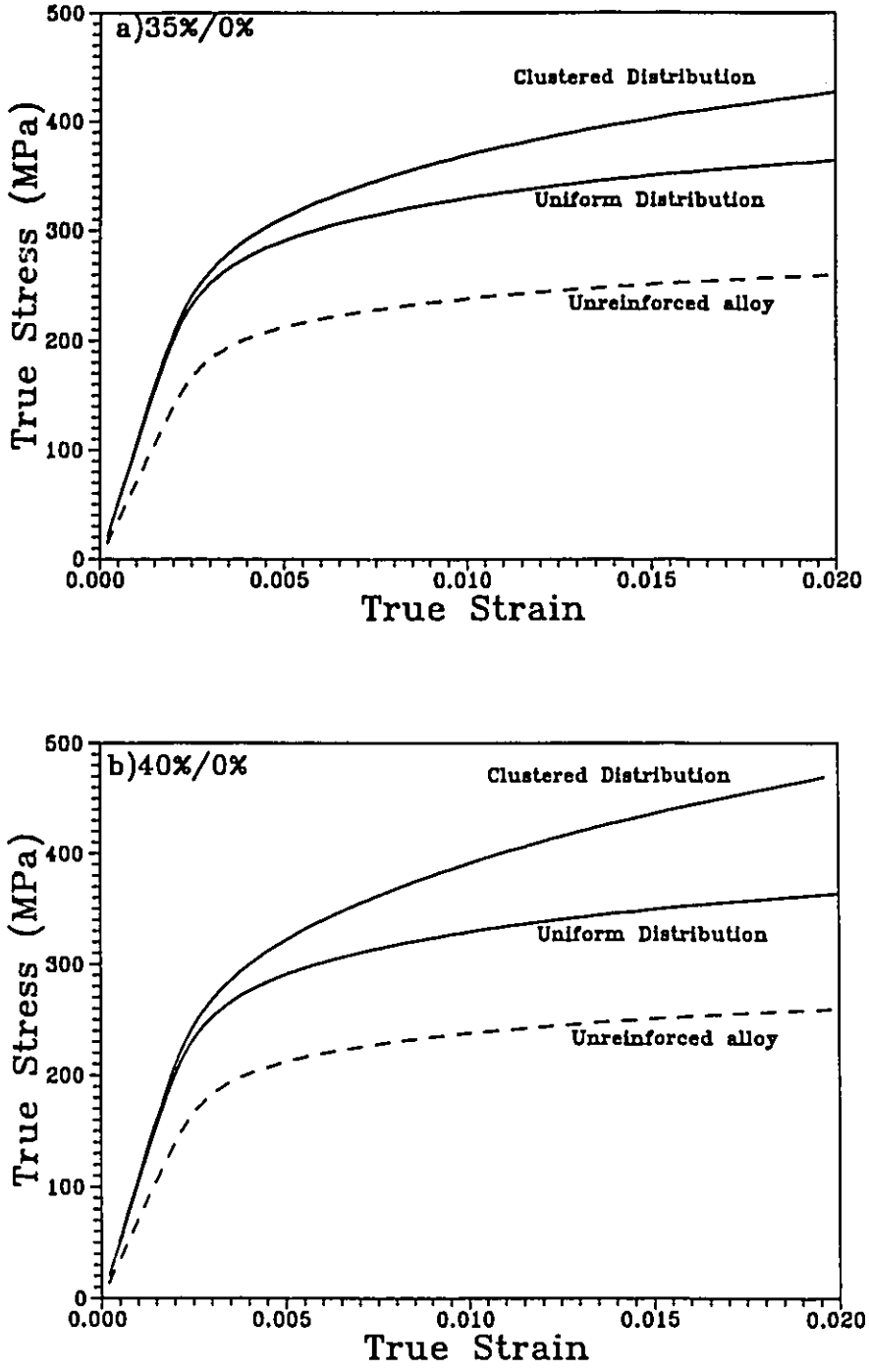

Figure 4.12: Effects of particle clustering on the stress-strain behaviour; a) using V_b=35%; V_a= 0% SiC; b) using V_b=40%; V_a= 0% SiC.

the clustered structures and the overall strengthening ratio increases. This degree of clustering represents a rather extreme case. Figure 4.13a shows the effects of varying the degree of clustering by changing the overall fraction that the 35% cluster occupies while maintaining an overall volume fraction of 20%. This requires that the matrix material change its SiC volume fraction from 0 to 5,10 and 15%. Figure 4.13b varies the degree of clustering by changing the SiC content of the cluster while maintaining the matrix rich phase at 0% and again the overall volume fraction at 20%. As the degree of clustering increases, the initial strain hardening rate and overall flow stress increases.

It is also useful to investigate how the strain hardening rate in the matrix influences the degree to which clustering effects the flow strength of the composite. This can be summarized by plotting the normalized stress (σ_c/σ_o), at a given normalized strain (ϵ_c/ϵ_o), versus the strain hardening exponent N (see Figure 4.14). A normalized strain of $\epsilon_c/\epsilon_o=5$ was chosen. Similar results are obtained at other values of normalized strain. These results indicate that the dependence of the strengthening ratio on the strain hardening rate in the matrix is approximately the same, regardless of the particle distribution chosen.

The results of Figure 4.12 and 4.13 are in qualitative agreement with the results of Bao et al. (1990). The approach of Bao et al. is similar to the present one in that the description of clustering is much like that of Figure 4.11. They also use a self-consistent approach, but the calculations of the stress in each phase is developed using a finite element technique. The constitutive equations used to describe the particle rich and matrix rich phases are assumed to be elastic/perfectly plastic. Therefore they have restricted themselves to evaluating the influence of particle distribution on the overall strengthening ratio of non-hardening solids and have not investigated the elastic/plastic transition. Nevertheless their results indicate the same trends as that described here. As the composite is clustered into particle rich and particle free regions, the

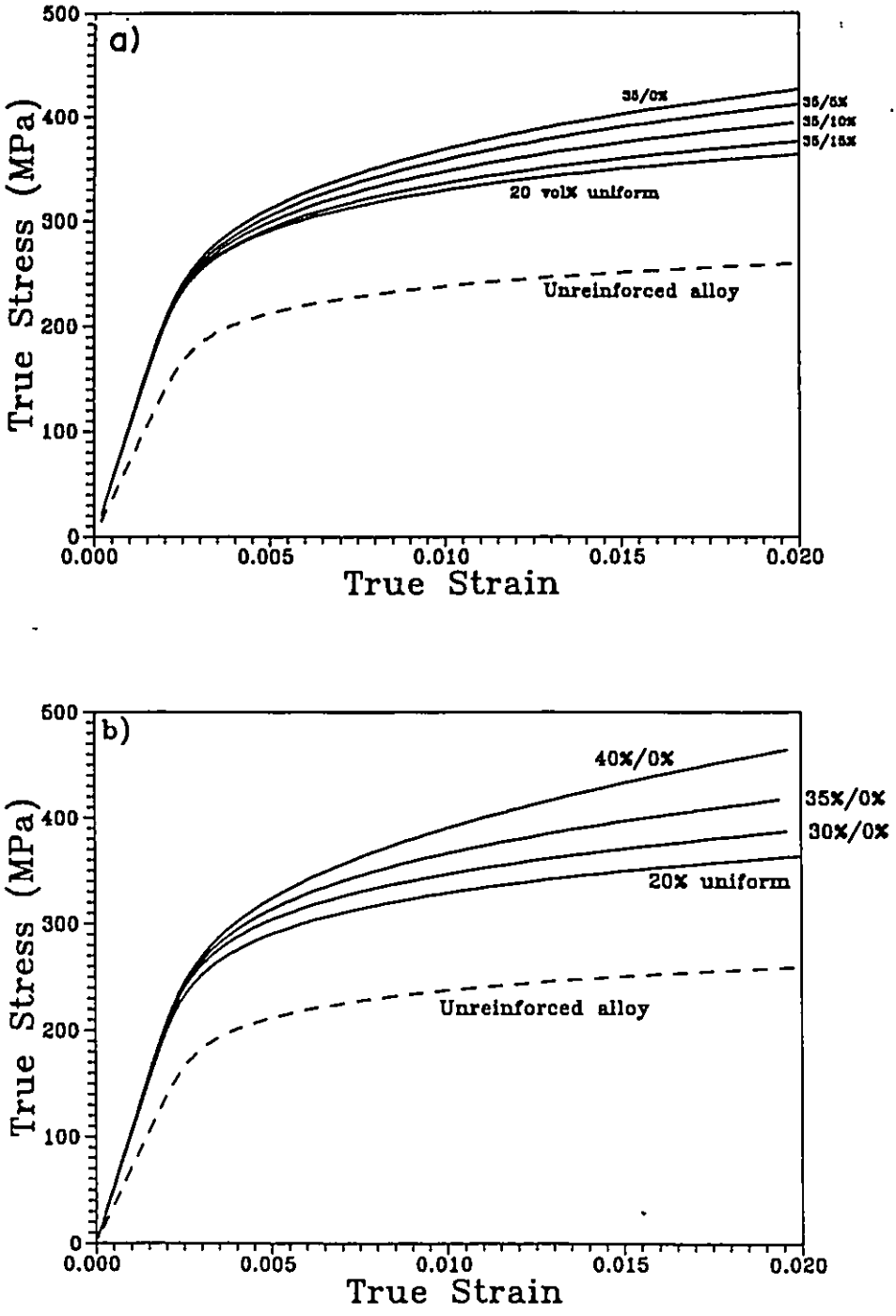

Figure 4.13: Variations in the degree of clustering; a) by changing the SiC content of the matrix rich phase V_a; b) by changing the SiC content of the clustered phase V_b.

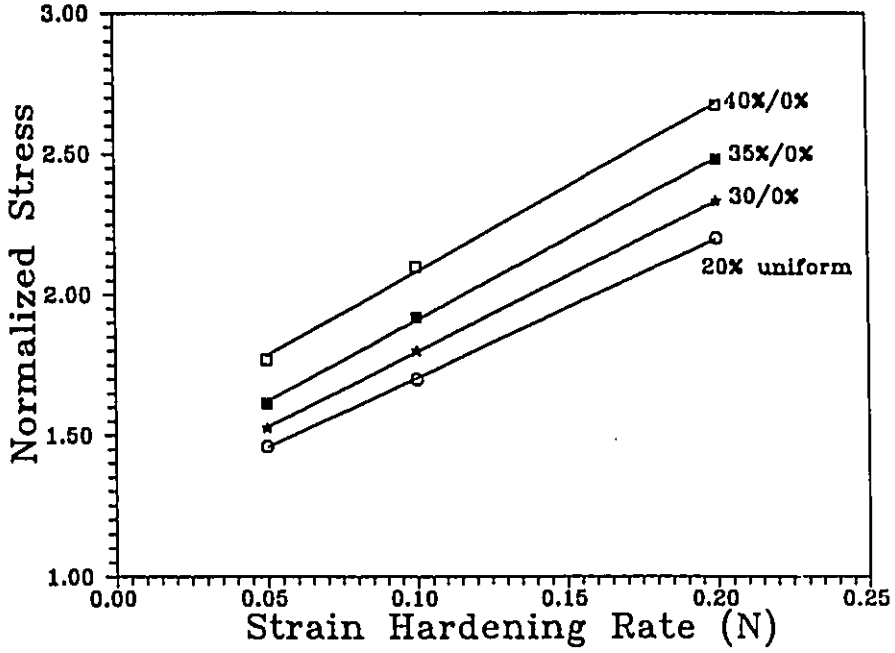

Figure 4.14: The normalized stress (σ_c/σ_o) as a function of matrix hardening rate N. The effects of clustering are also included. Values quoted are at a normalized strain of 5.

overall strengthening ratio increases compared to a uniform distribution.

4.5 Summary

A self-consistent analysis, based on Eshelby's equivalent inclusion method, has been developed to predict the stress partitioned between two phases under an applied stress. The model is successful in predicting the modulus of a composite material with a spherical reinforcement geometry which lies between the upper (Voigt) and lower (Reuss) bound predictions. In addition, it is successful in extending Eshelby's infinite solution to deal with composites containing a high volume fraction of second phase. In this regard it gives an excellent prediction of the experimentally measured elastic modulus of a number of SiC particle reinforced aluminum alloys up to volume fractions of 40%.

Extension of the model to investigate elastic/plastic deformation was accomplished by assuming incrementally linear elastic behaviour. Using this method the self-consistent model predicts that the addition of a uniform distribution of SiC particles increases the initial strain hardening rate in the material. The strain hardening rate increases as the SiC content increases. However, after strains of about 2% the unreinforced and composite curves become nominally parallel indicating that the SiC particles exert most of their influence in the very early stages of deformation. This is particularly the case for SiC contents below about 30 vol%. These predictions, based on a uniform distribution of second phase, agree well with predictions using FEM techniques using and a reinforcement geometry of a unit cylinder (aspect ratio of 1) (Bao et al., 1991). Both the self-consistent approach and the FEM method predicted that the overall strengthening effect of the SiC particles increases as the strain hardening rate of the matrix increases.

In most practical cases the distribution of reinforcement is not uniform, consequently

it is of use to examine the effects that a non-uniform distribution may have of composite properties. The particle distribution was varied by representing the global volume fraction of the uniform case by a bimodal distribution. This consisted of a phase with a SiC content above the global value (Cluster or particle rich region) and a phase whose SiC content was below the global value (particle free region). The self-consistent model was then used to predict the elastic/plastic stress-strain curve of a composite based on a two phase microstructure of this kind. The model predicts that the elastic modulus is relatively insensitive to the clustering of reinforcement into particle rich and particle free regions. However, the initial strain hardening rate in the composite increases (in comparison to the uniform prediction) as the degree of clustering increases. This then results in an overall increase in the flow strength of the composite.

CHAPTER 5:

DISCUSSION

5.1 Introduction

The order of discussion of the experimental results will begin with the low strain regime. In particular, the yield asymmetries observed between tension and compression will be discussed in terms of an internal stress of thermal origin. Other issues which influence the yield strength of the composite such as thermally induced dislocation substructure and stress partitioning to the SiC particles will also be considered. The role of stress partitioning to the SiC particles during the elastic/plastic transition will be discussed in more detail (section 5.3) by comparing the theoretical model developed in chapter 4 with the tensile results obtained experimentally. The role of particle distribution on the strain hardening rate of the composites will also be examined.

The influence of ageing condition, testing direction and plastic strain on the development of the Bauschinger effect will be discussed in section 5.4. The role of stress partitioning in the development of the Bauschinger effect will also be considered along with an examination of the relative importance of transient and permanent softening.

The influence of damage accumulation on strength as well as other alternative relaxation processes will be discussed (section 5.5), followed by a brief discussion of the influence of test temperature on the strengthening derived from the SiC particles (section 5.6).

5.2 Factors Influencing the Onset of Yielding

5.2.1 Internal Stress of a Thermal Origin

An explanation of the yield asymmetries observed between tension and compression in

section 3.2.2.3 can be described in terms of a thermal stress by referring to Figure 5.1. The simplest way in which to represent the internal stress distribution in a two phase system is illustrated in Figure 5.1a. If it is assumed that the internal stress in each phase is uniform then, since the stresses must balance;

$$(1-V_p)\sigma^{th}_m + V_p\sigma^{th}_p = 0 \qquad (5.1)$$

where V_p is the volume fraction of particles and σ^{th}_m and σ^{th}_p are the thermal internal stresses in the matrix and particle respectively. If the coefficient of thermal expansion (CTE) of the particle is less than that of the matrix, then the particle is in net compression and the matrix is in net tension. As discussed in the introduction, neutron diffraction results (Withers et al., 1987) confirm the sense of this stress balance.

When the material is deformed in tension, the matrix will yield when its stress reaches;

$$\sigma_{mt} = \sigma_y - \sigma^{th}_m \qquad (5.2)$$

where σ_{mt} is the tensile stress in the matrix and σ_y is the yield strength of the matrix. When tested in compression, the matrix will yield at a stress equal to;

$$\sigma_{mc} = \sigma_y + \sigma^{th}_m \qquad (5.3)$$

where σ_{mc} is the compressive stress in the matrix. The result is a strength differential between tension and compression of magnitude $2\sigma^{th}_m$ (Figure 5.1b).

Comparing this idealized picture with the experimental results for the unreinforced alloy (Figure 3.18) reveals good agreement. In this case the matrix can be considered to be an age hardenable Al alloy with a second phase of essentially pure Si. The volume fraction of Si is about 5% and the morphology is approximately equiaxed. The thermal expansion coefficients of the materials of interest in this study are listed in Table 5.1. Clearly the CTE mismatch for Al and Si is of the same sense and magnitude as that between A356 and SiC. The magnitude of the difference in the experimental flow curves in tension and compression is between 10 and 20 MPa

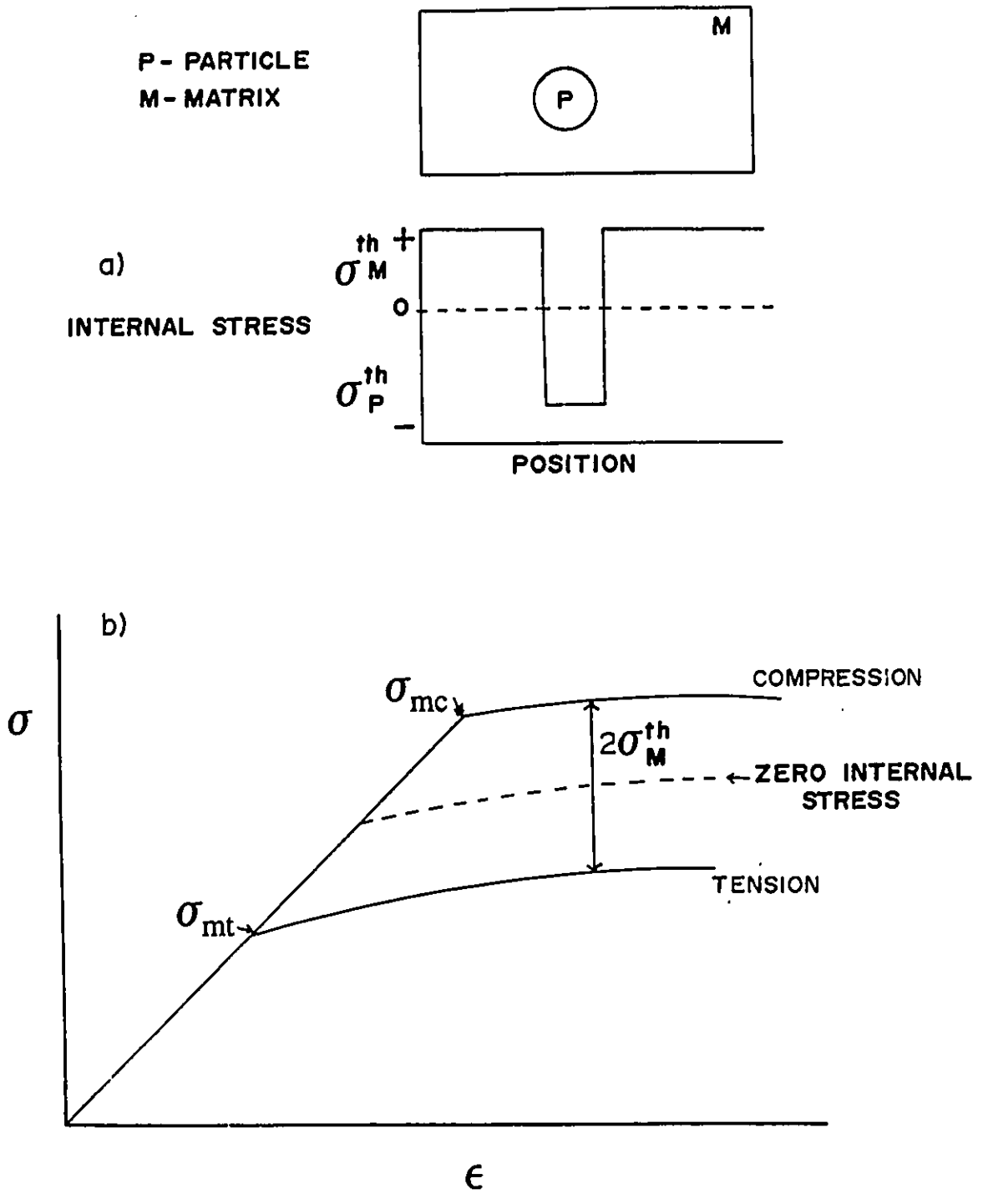

Figure 5.1: Influence of a thermal stress on deformation; a) a uniform distribution of internal stress; b) asymmetry between tensile and compressive flow curve.

Table 5.1 The coefficients of thermal expansion (CTE) for a variety material per degree celsius.

Material	Coefficient of Thermal Expansion (CTE) /C
SiC	3.8×10^{-6}
Si	3×10^{-6}
Pure Al	25×10^{-6}
A356	21.5×10^{-6}

depending on the heat treatment. Accordingly the magnitude of internal stress indicated by the experiments is about 5 to 10 MPa.

The problem of the shape misfit that results from a mismatch in CTE between the particle and matrix can be dealt with by the Eshelby equivalent inclusion method. Withers et al. (1989) have determined the residual stress and strain for a composite consisting of Al and SiC. Since the CTE mismatch is similar between Al and Si, these results can also be used for the unreinforced alloy. The predicted matrix residual stress for an aspect ratio of 1 and a volume fraction of 5% is about 25 MPa. This is roughly twice the value observed experimentally. This overestimation of the theory is likely to arise as a result of diffusional and plastic relaxation processes that occur during quenching, which are not accounted for in the model of Withers et al. (see chapter 1).

The tension and compression behaviour of the composites are quite different than that of the unreinforced alloy and not in agreement with the simple picture described in Figure 5.1. In this case the composite materials yield at a lower stress in compression. In addition, the two curves are not parallel, resulting in a cross over at higher strains. This effect varies in magnitude depending on the heat treatment and volume fraction of SiC.

One possible explanation for this discrepancy can be described on the basis of the detailed distribution of internal stress. Recent finite element studies on whisker reinforced composites have been initiated by a number of groups (Povirk et al., 1991; Levy and Papazian, 1991) to try and predict the distribution of internal stresses of a thermal origin and its influence on stress-strain behaviour. Upon quenching from high temperatures Levy and Papazian's results (Figure 5.2) indicate that large compressive stresses are developed in the matrix near the sharp corners of fibre ends. Conversely more moderate tensile stresses are developed in the matrix adjacent to the fibre length. This study offers a more detailed description of the internal stress distribution than the simple picture just developed (Figure 5.1). However, the distribution of stress in Figure 5.2 does

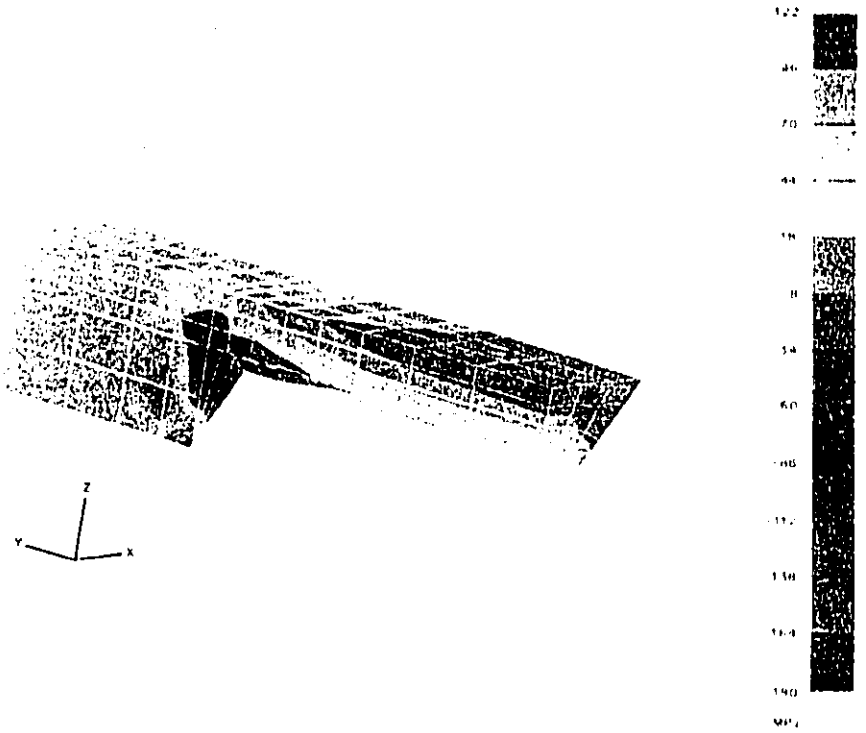

Figure 5.2: Predicted mean residual stress at room temperature after cooling a 20vol% SiC/5456 Al composite from 500°C. (Levy and Papazian (1991)).

indicate that, apart from the isolated regions of high compressive and tensile stresses, the majority of the matrix is under a net residual tension.

On the basis of the prediction of Levy and Papazian the expected behaviour in tension and compression can be described by referring to Figure 5.3. The local inhomogeneous distribution of internal stress leads to asymmetries in yielding. In particular, the matrix will yield at a lower applied stress in compression in the regions of large compressive internal stresses (i.e. near fibre ends). Conversely the matrix will yield at a higher applied stress in tension in the regions adjacent to the fibre. In this case, both the tensile and compressive curves lie below that expected when no internal stress is present. This differs from the description of Figure 5.1 where the situation of no internal stress lies between that of tension and compression. Once these local regions under high compressive/tensile internal stress have yielded, plasticity will begin to spread to the regions of the matrix in net residual tension. Therefore continued deformation should occur at a slightly lower stress in tension than in compression leading to a cross over in the stress-strain curves. (Although this appears to be a satisfactory description of the cross over effect, there may be other explanations. One possibility is that the rate of damage accumulation may differ in tension and compression. This could lead, for example, to a lower work hardening rate in tension, leading to a cross over condition. The question of damage will be discussed in a later section).

Predictions of stress-strain behaviour based on the distribution of internal stress shown in Figure 5.2 have been completed by Levy and Papazian (Figure 5.4). Very similar predictions were obtained by Povirk et al. (1991). Both these studies predict the cross over behaviour that was observed experimentally and reveal good qualitative agreement with the schematic description of Figure 5.3.

The finite element models just described deal with whisker reinforcements with an aspect ratio of 4. Finite element studies that deal with particle geometries closer to that used in the

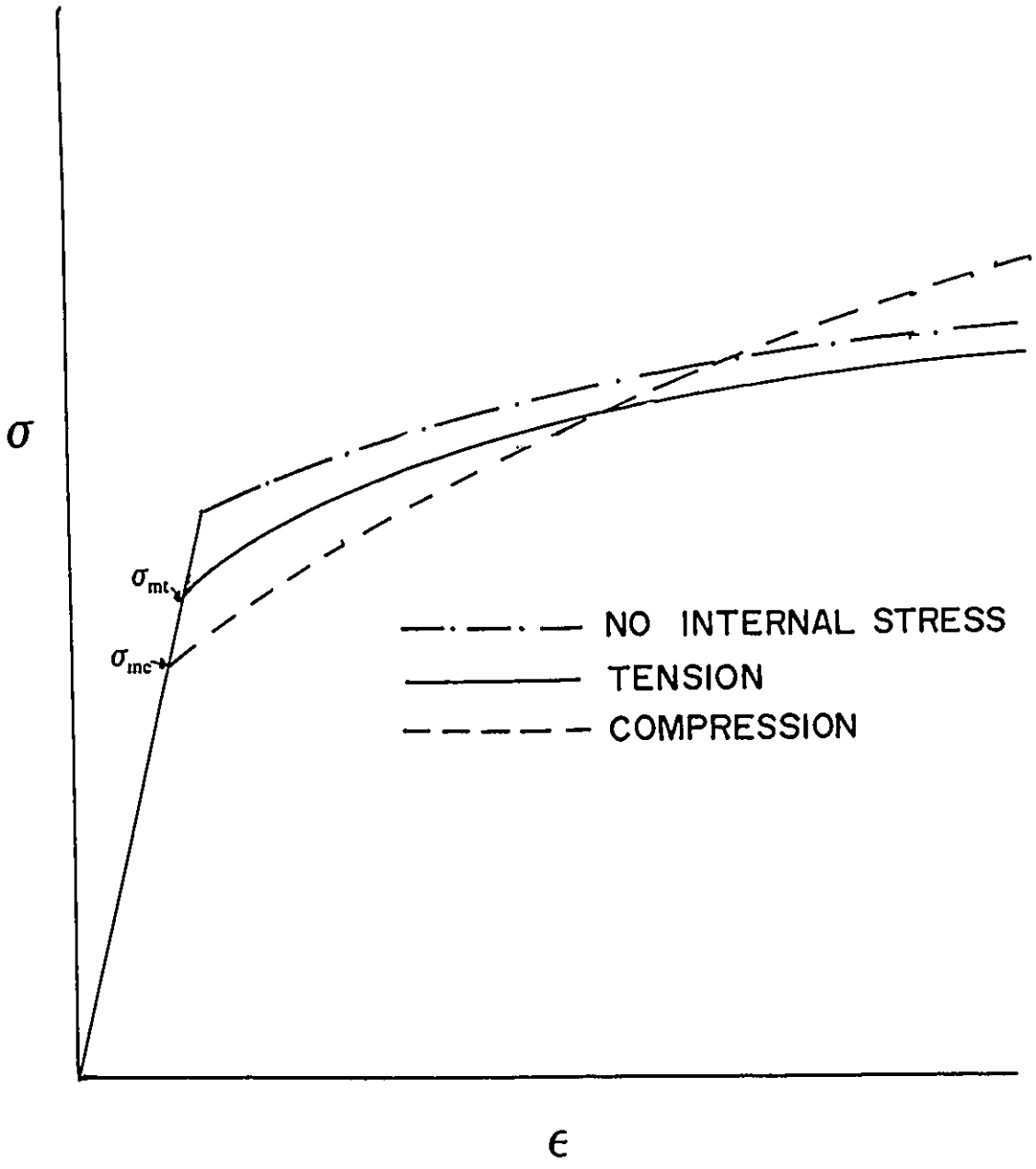

Figure 5.3: Idealized representation of the stress-strain response of a composite in tension and compression with a residual thermal stress state of the type described by Levy and Papazian (1991) in Figure 5.2

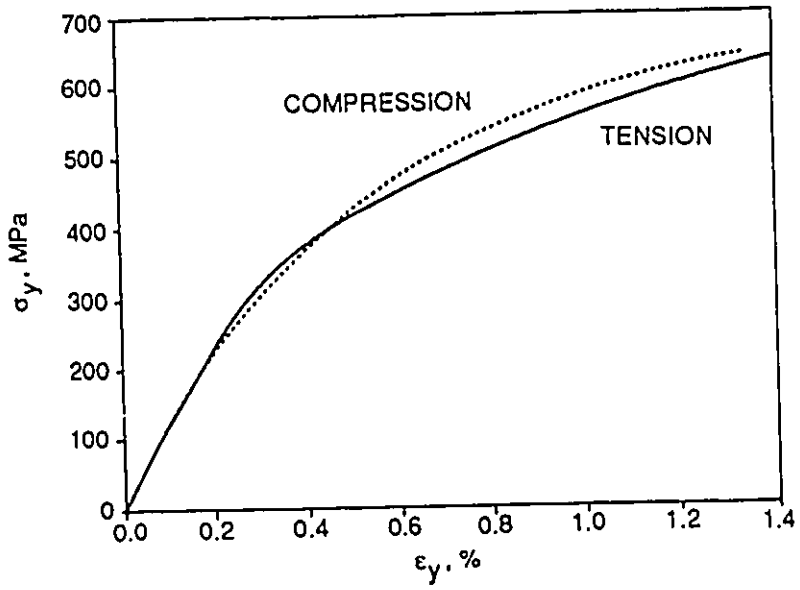

Figure 5.4: Predicted tensile and compressive stress-strain curves for a 20 vol% SiC/5456 Al composite with a residual thermal stress described by Figure 5.2. (Levy and Papazian (1991)).

composites of the present study have been completed by Zahl and McMeeking (1991). They have modelled the influence of thermal residual stress on the compressive/tensile behaviour of an elastic/perfectly plastic matrix reinforced with spherical and unit cylindrical particles. Although their results differ somewhat in magnitude, in all cases considered, the composites yield at a lower stress in compression than in tension. In addition both the tensile and compressive yield strength are below the value expected in a material with no internal stress present. There is some evidence of a prediction of a cross over effect however, since this model is based on perfectly plastic behaviour this effect is not large.

Similarities Between the Eshelby Method and FEM Techniques. We can now consider the differences in approach between the Eshelby formulation and finite element models. Both methods show that most of the matrix volume experiences a uniform tensile residual stress. (The relative magnitude of the uniform stress predicted will likely differ to some degree based on the contribution of relaxation that each model considers). With the Eshelby method it is assumed that this average stress is completely uniform. Conversely the finite element models are capable of calculating the local deviations in the internal stress distribution. The ability of each method to predict experimental results will depend on the magnitude to which the "real" local stresses in the material deviate from the overall average stress.

In the case of the composite material, the reinforcement is angular in shape and the volume fraction is high enough that particle-particle interactions and clustering can be significant. The finite element studies indicate that these factors lead to stress concentrations which can lead to local stresses that deviate significantly from the average. Consequently the behaviour of these materials follows that described by the finite element models. For the A356 alloy, the volume fraction is much lower and consequently the complicating effects of particle-particle interaction is reduced. This likely leads to stress concentrations that are smaller with less severe deviations

from the average. Consequently its behaviour is closer to that based on a uniform internal stress (Figure 5.1a). In this context even the finite element work of Levy and Papazian predicts that when the volume fraction of whiskers is reduced from 20% to 8%, behaviour in tension and compression agree qualitatively with the description of Figure 5.1b.

5.2.1.1 Influence of Matrix Strength on the Level of Internal Stress Developed

From the results of Figures 3.19 b and c, it is clear that the differences between tension and compression are dependent on the heat treatment. In particular, as the overall flow strength is reduced the cross over effect diminishes. This suggests that the level of internal stress that exists in the composite decreases as the overall flow strength of the matrix is reduced. An explanation for this can be offered based on the predictions of Levy and Papazian (1991) (Figure 5.5). In this case the plastic strain gradients that arise in the matrix as a result of cooling from 500°C in a 20 vol% SiC whisker reinforced 5456 Al alloy were predicted. Plastic deformation was considered to occur in the mesh elements where the von Mises stress (resulting from thermal internal stress) exceeded the yield strength of the matrix. (The temperature dependence of the yield strength was taken into account). Large plastic strains are associated with the regions in which large stress concentrations were predicted to occur (see Figure 5.2). However a large portion of the matrix has very little plastic strain associated with it (black regions).

From this description, it is evident that the magnitude of the local internal stress developed at room temperature depends on the yield strength in the matrix. Consequently the cross over effect that results from these internal stresses should be reduced as the matrix strength is reduced. The experimental results are consistent with this result. In the T61 condition the cross over effect is largest but diminishes in the OA200 case and nearly vanishes in the OA300 state. (The T4 condition can not be considered since the microstructure that develops in this case occurs after

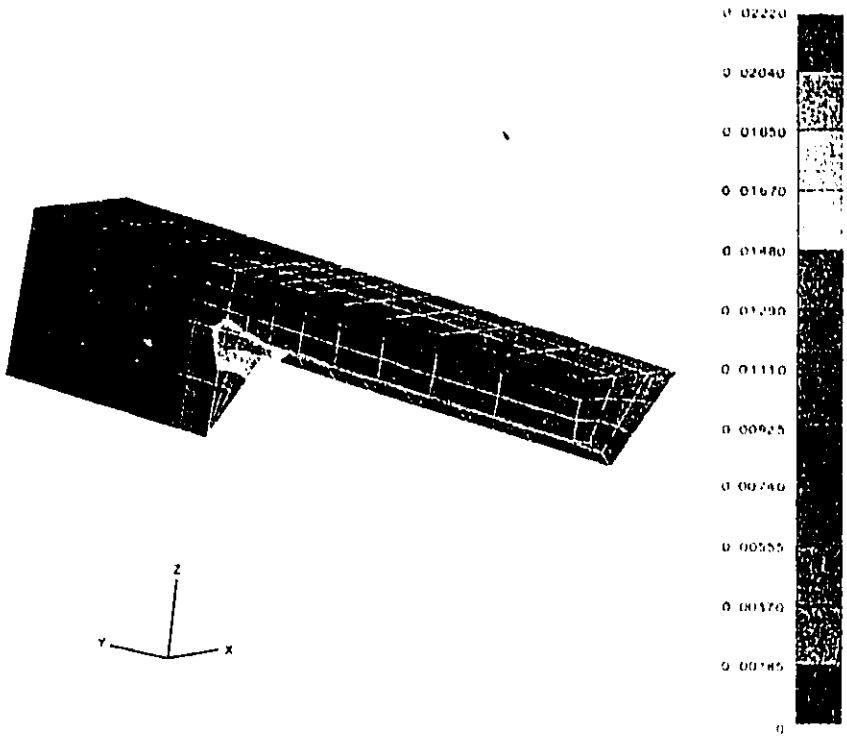

Figure 5.5: Predicted effective plastic strain at room temperature after cooling a 20 vol% SiC/5456 Al composite from 500°C. (Levy and Papazian (1991)).

the quenching step.)

In summary, the presence of an internal stress of thermal origin will influence the detailed shape of the stress-strain curve of the composite in the initial stages of deformation. However, the overall degree of strengthening achieved by the reinforcement is relatively unaffected by the presence of an internal stress. Consequently it cannot be considered as a strengthening mechanism. However, one possible source of strengthening is the dislocation substructure that is produced upon relaxation of the thermal stress.

5.2.2 Thermally Induced Dislocation Substructure.

As discussed in the introduction, the degree to which a thermally induced dislocation substructure should contribute to overall strength depends primarily on three factors;

1) the scale of the reinforcement ($\Delta\sigma \approx r/f$), where r and f are the particle radius and volume fraction respectively;

2) the degree to which the internal stress is relaxed by plastic flow;

3) the nature of the dislocation distribution throughout the matrix.

Recent work by Mummery et al. (1991) has systematically investigated the effects of reinforcement volume fraction and size, quenching rate (from 420°C to room temperature) and matrix strength on the yield strength (defined at .05% and .2% offset values) of Al/SiC_p composites . Their results are illustrated in Figure 5.6 for the .05% proof stress. A number of basic trends can be interpreted from the data.

1) An increase in volume fraction results in an increase in strength.

2) Quenching (Q) from 420°C to room temperature results in a higher strength than slowly cooling to room temperature (A), at least for the softer 1070 Al matrix.

3) There is some evidence that a decrease in particle size from 30 μm to 3μm increases strength.

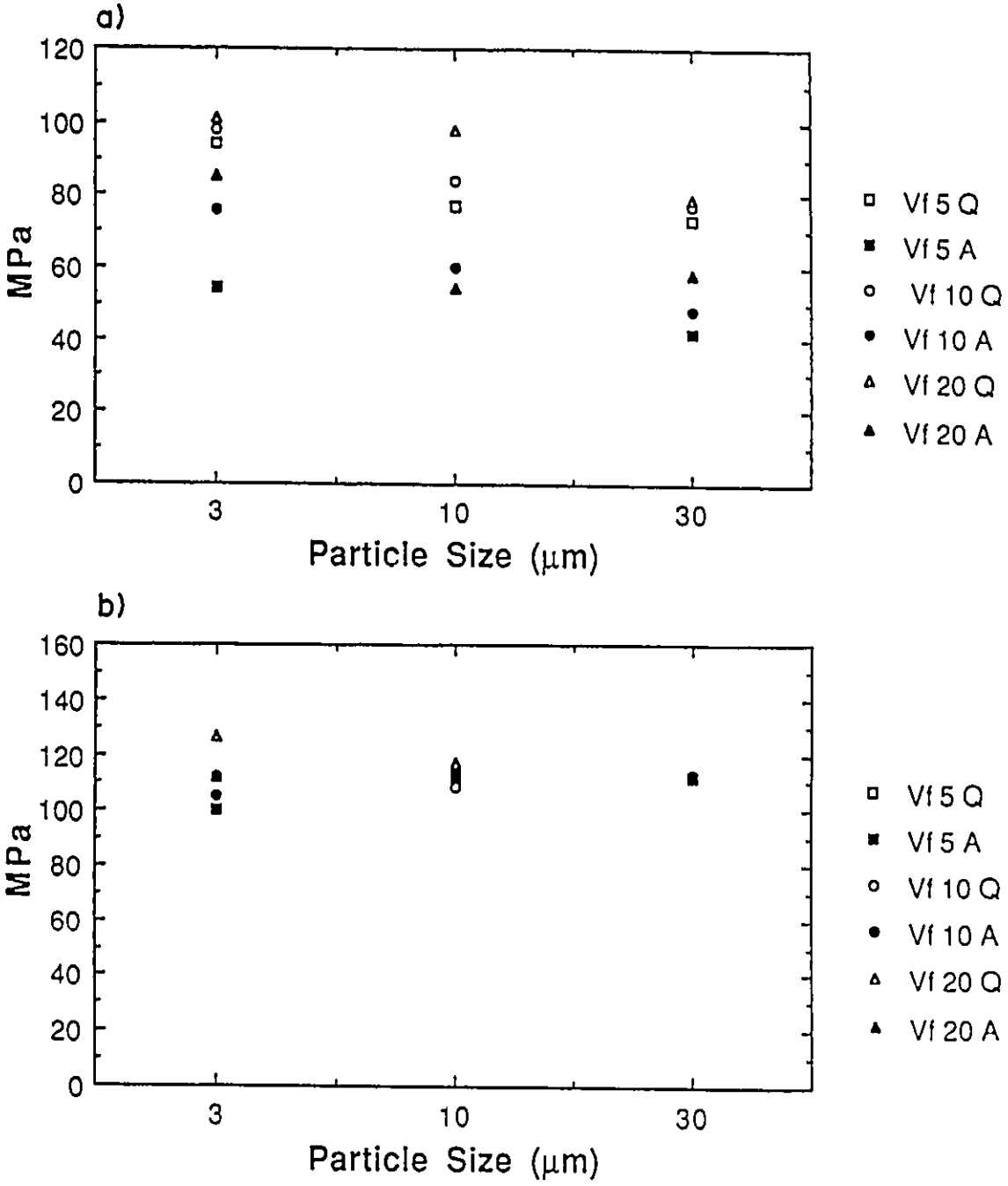

Figure 5.6: The .05% proof stress for Al/SiC composites versus particle size, quenching rate and volume fraction (V_f); a) 1070 Al; b) 5050 Al. Q and A indicate quenching and slow cooling respectively. (Mummery et al (1991))

In some cases however, no effects are seen in going from 30 to 10 μm or in going from 10 to 3μm.

4) The influence of cooling rate and particle size is greatly diminished in going from a composite based on commercially pure Aluminium (1070 Al) to an alloy of Al-1%Mg Alloy (5050 Al). In addition the authors state that for an age hardenable alloy matrix (6061 Al) (Mummery et al., 1991b) essentially no effect of particle size and cooling rate on strength is evident. Most other studies concerning quenching investigate only the degree of quenching and volume fraction on strengthening (Arsenault and Shi, 1986; Derby and Walker, 1988; Taya et al., 1991;). In general these results agree with that of Mummery et al. who report the most detailed work to date.

The degree too which quenching influences strength clearly depends on a number of factors and it is important to evaluate it for a given alloy/particle system. However it would appear, from the above evidence, that for more complex systems such as age hardenable alloys, the influence of thermally induced dislocation substructure may be quite small. This may be due to the fact that plastic relaxation is more difficult in these systems and that the dislocation substructure that is produced may be localized around the particles.

To confirm this statement, it was decided to investigate the influence of quenching on the stress strain behaviour for the composites under study here. The OA300 condition was chosen for this work for two reasons; 1) the matrix is in the softest condition and plastic relaxation should occur relatively easily; 2) the material could be quenched from 300 degrees with no microstructural change expected afterwards (such as that observed after a solution treatment step-T4). In order to change the degree of quenching, one sample was quenched to room temperature, the other quenched into liquid nitrogen. Both samples were then tested at room temperature. The results of these experiments are illustrated in Figure 5.7. In agreement with Mummery et al.'s results, the effects of quench magnitude appear to be rather small. Increasing the quench

magnitude by 200°C only increases the flow stress by 5 or 10 MPa for both the 10 and 20 vol% material. In the case of the 10 vol% composite this difference is only evident at low strains.

5.2.3 The Dependence of the Yield Strength on Particle Size

In addition to the work of Mummery et al., a number of other investigations also show a dependence of the yield strength on particle size (Humphreys et al., 1991; Kamat et al., 1991 Arsenault et al., 1991; Aikin and Christodoulou, 1991). The majority of these studies indicate that the particle size dependence is greatest when reinforcing matrices based on pure aluminium. Kamat et al. (1991) and Aikin and Christodoulou (1991) further illustrate that the yield strength of the composite can be correlated with a description based on some form of interparticle separation. (The particle size of the reinforcement in the work of Aikin and Christodoulou is between .3 and 1.3 μm which is considerably smaller than that typically found in MMC's). This apparent scale dependence would appear to support a description based on micromechanics and be in conflict with continuum mechanical models. However, there may be other sources responsible for the particle size dependence which are not based on dislocation/particle interactions.

One possible explanation is based on damage accumulation. The work of Brechet et al. (1991) indicates that the probability of a particle cracking increases as the particle size increases. Consequently, if damage accumulation does play a role in deformation at low strains, varying particle size could influence strength by varying the degree of damage accumulation. Hu (1991) has studied the tensile and compressive behaviour of an Al-Mg alloy reinforced with 13 μm and 165 μm SiC particles. In both tension and compression, the flow strength of the 13 μm SiC composite, even at very low strains, was significantly higher than that of the large particle material. In addition, particle cracking was much more extensive in the 165 μm SiC composite.

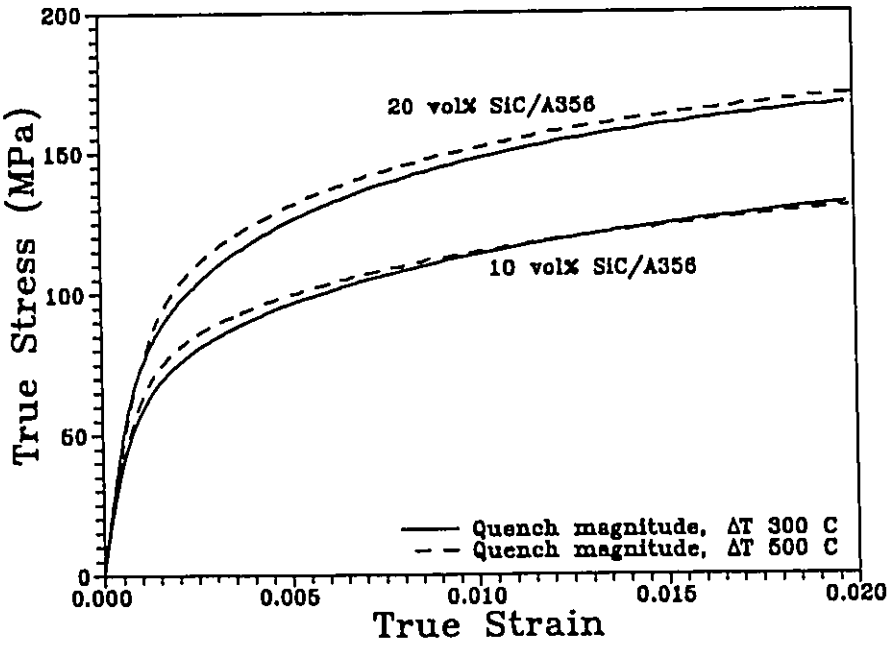

Figure 5.7: Influence of the degree of quenching on the strength of the 10 and 20 vol% composites in the OA300 ageing condition.

These experiments represent a rather extreme case, especially because the volume fraction was very high (i.e. about 50%). However, it does illustrate that damage accumulation may be partly responsible for the particle size dependence of strength that is observed. A second source of the particle size dependence is based on the relaxation of the back stress and will be discussed in the next section.

Some authors have suggested (Arsenault et al., 1991) that the .2% yield strength of metal matrix composites can be completely accounted for as a result of thermally induced substructure. Others agree that thermal substructure is important (Miller and Humphreys, 1991) but state that the "initial (before the proof stress) work hardening" is also a significant contributor to the .2% yield strength. While Miller and Humphreys do not derive a detailed expression for the initial hardening, they do suggest that the contributors to this are the development of a back stress and the dislocation substructure that relaxes it (see section 1.3.2.2)

A number of criticisms can be made of an interpretation based solely on thermal substructure.

1) It ignores the presence of a thermal internal stress. Our own experiments suggest that a thermal stress is present in the composite material and that it can influence the flow strength, especially at low strains.

2) The magnitude of the effect is dependent on the metal matrix type. While thermal substructure may be important for composites based on pure Al, the above discussion suggests that it may be very small for composites based on age hardenable alloys.

3) It ignores any stress partitioning to the particles which may occur during the elastic/plastic transition.

5.2.4 The Role of Stress Partitioning.

The fact that stress is partitioned to the particles during elastic deformation is evident from the experimentally measured increase in the modulus when SiC particles are added to an Al matrix. The discussion of Chapter 4 suggests that this degree of stress partitioning can be accurately predicted using the self-consistent analysis.

Interpretation of stress partitioning during plastic flow has traditionally been done using a back stress model similar to that of Brown and Clarke (1977). However, as discussed in Chapter 1, this is most applicable when the unreinforced alloy exhibits approximately linear hardening (stage II). Figures 3.23 and 3.24 indicate that, in most of the heat treatment cases, this does not occur in the present alloy until a strain of about .015 or .020 is reached. The difference between the flow curves (Figure 3.26) indicates that once this level of strain is reached, the strengthening effects of the particles are negligible, presumably due to alternative processes. This problem is emphasized by Withers et al. (1989), when applying their model based on Eshelby's inclusion method to the experimental results of Arsenault and Wu (1987) (Figure 5.8). The dashed line indicates the predicted linear hardening rate based on an unrelaxed back stress developed as a result of plastic flow around the elastic particles. The model gives very poor predictions of the dependence of hardening rate on strain. In particular, the composites exhibit very high hardening rates at low strains followed by rates that fall below that predicted for an unrelaxed state. (The results of Arsenault and Wu indicate a significant strength differential between tension and compression. These materials are powder metallurgy produced. As Withers et al. point out, some of this differential may be a result of decohesion between the particle/matrix interface.)

These results indicate that the majority of strengthening arises during the elastic/plastic transition, where the strain hardening rate in the composite is large. During this transition, stress

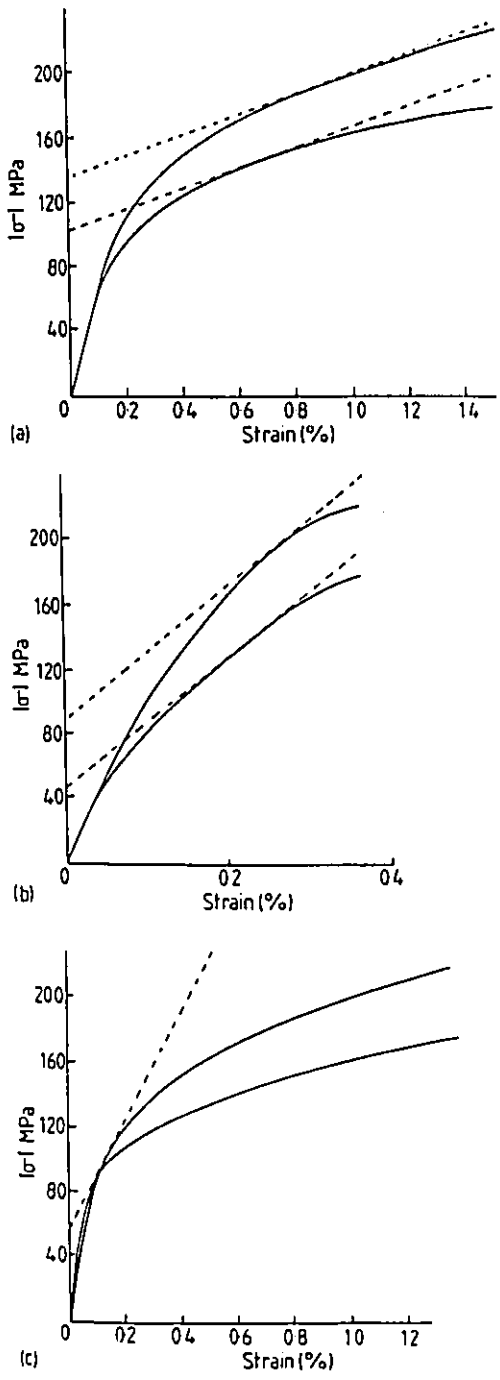

Figure 5.8: Plots of the predicted unrelaxed mean stress components of the hardening (dashed line) compared to the compressive (upper) and tensile (lower) loading curves of Arsenault and Wu (1987); a) 5% SiC and; b) 20% SiC whiskers; c) 20% SiC discs

is partitioned to the particles due to both elastic and plastic deformation in the matrix. The degree to which stress is partitioned is difficult to predict due to the complex nature of the deformation in this region. It is proposed that it is this stress partitioning which is the major source of the initial apparent hardening rate described by Miller and Humphreys (1991).

Influence of Particle Size. As mentioned in the last section, the observed particle size dependence of strength would appear to contradict a continuum mechanical model, such as the development of a back stress or stress partitioning, which is dependent only on volume fraction. However, a particle size dependence could be explained on the basis of a back stress mechanism as well.

As discussed in the introduction, the back stress that develops in a two phase material depends on the degree of plastic relaxation that occurs to relieve it. This relaxation is itself particle size dependent (Figure 1.9). As the particle size becomes smaller, relaxation becomes more difficult and more back stress will be developed. Consequently, even if the range of reinforcement scale investigated was such that the contribution of thermal and secondary dislocation substructure was insignificant, a particle size dependence of the yield strength might be expected due to the degree of back stress that can be developed at low strains.

Brown and Stobbs (1971b) have illustrated this point by obtaining an expression for the back stress in terms of the total strain, assuming that the unrelaxed state is not maintained. Their expression for the back stress becomes;

$$<\sigma>_m = \alpha \mu_m f \left(\frac{2b}{d}\right)^{1/2} \epsilon_T^{1/2} \qquad (5.4)$$

where d is the particle size and ϵ_T is the total strain.

5.2.5 Summary.

The discussion of this section points out the complexity of deformation in PMMC materials. There can be a number of competitive processes including thermal internal stress, enhanced dislocation substructure, back stress development and damage accumulation, all of which could influence composite strength in varying degrees. It is likely that the scale of reinforcement used in PMMC's is such that both scale dependent (e.g. thermal substructure) and scale independent (e.g. stress partitioning) processes contribute to strength. Scale dependent processes likely dominate when the particle size of the second phase is below 1 μm whereas scale independent processes dominate at particles sizes above 100 μm. A description of what happens between these limits is suggested by the work of Arsenault et al. (1991) for 20 vol% particle reinforced commercially pure Al (Figure 5.9). It is clear that the dependence of strength on particle size is much more sensitive at low particles sizes than at high particle sizes. Similar work which explores this very wide range of particle size with composites based on age hardenable matrices has not been reported. However it would be expected that the particle size dependence in this case would be much weaker. The situation is sufficiently complex that interpreting strength on the basis of a single point on the stress-strain curve (e.g. .2% proof stress), may be misleading. It is more appropriate to interpret behaviour based on the entire elastic\plastic portion of the stress-strain curve.

5.3 Elastic/Plastic Deformation in the Low Strain Regime

In this section the model for elastic/plastic deformation developed in chapter 4 will be applied to a prediction of the stress-strain behaviour obtained experimentally. One important result of both the self-consistent analysis and the FEM model of Bao et al. (1991) is that the strengthening effect of the SiC particles (as measured by σ_c/σ_o or σ_c/σ_m) depends on the strain

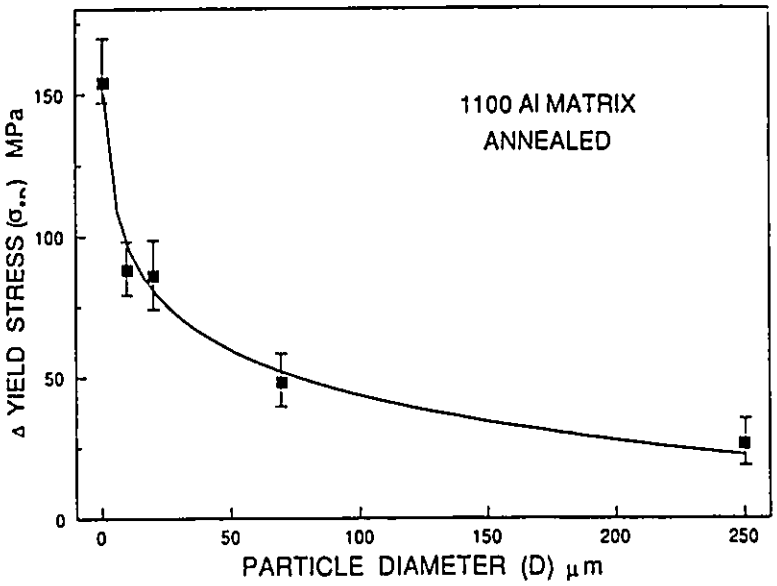

Figure 5.9: The increase in the yield stress ($\Delta\sigma$ at a .2% offset) of a commercially pure Al/SiC composite as a function of SiC particle size. (Arsenault et al (1991)).

Table 5.2: The values of σ_o and N for the unreinforced alloy.

Ageing condition	σ_o (MPa)	N
T4	95	.15
T61	200	.1
OA200	80	.15
OA300	40	.2

hardening rate in the unreinforced alloy. The Ramburg-Osgood equation was fitted to the experimentally determined stress-strain curves of the unreinforced alloy in the various ageing conditions. The values of σ_0 and N determined by this method are listed in Table 5.2. It was not possible to fit the entire stress-strain curve using a single value of N. However, an excellent fit was obtained over the strain regime of interest here (up to .02 strain). The results of the theoretical curves using the values of σ_0 and N in Table 5.2 are compared to the experimental curves in Figure 5.10.

Calculations using the technique described in Chapter 4 were performed using both the Ramburg-Osgood equation and the actual experimental data for the unreinforced alloy. The predictions of composite behaviour were essentially identical for both cases. Determining a value of σ_0 and N for the unreinforced data, allows a more direct comparison between the experimental curves and the predictions of the self-consistent method and the work of Bao et al. (1991).

The results of the theoretical prediction for the 10 and 20 vol% composites are shown in Figure 5.11 for the four heat treatments investigated. In this case the calculation was based on a uniform distribution of particles. The figures indicate that the elastic moduli of the composites are predicted very well. However, with the exception of the OA200 state, predictions based on a uniform distribution of particles underestimate the initial strain hardening rate in both the 10 and 20 vol% composites, resulting in a lower prediction of the flow stress than that experimentally measured.

Both the experimental data and theoretical predictions can be normalized by the values of σ_0 and ϵ_0 determined for the alloy for each ageing condition (Figure 5.12). To summarize this data, the strengthening ratio (normalized stress) at a normalized strain of ϵ/ϵ_0 of 5 is plotted as a function of the strain hardening rate of the matrix in Figure 5.13. (The trends are similar if other values of ϵ/ϵ_0 are chosen). Both the theoretical predictions and the experimental results are

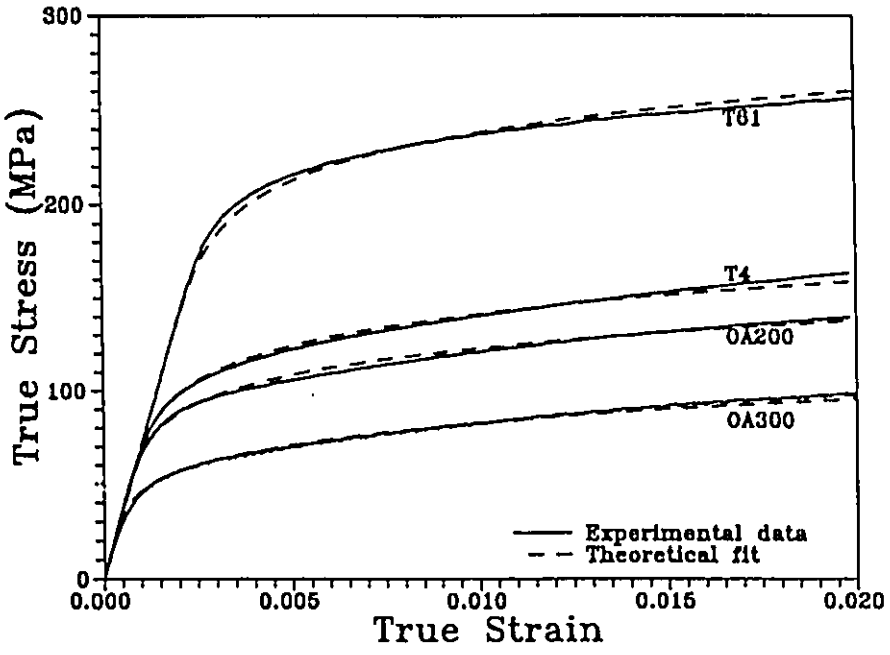

Figure 5.10: Comparison of theoretical and experimental stress-strain curves for the unreinforced A356 alloy in various ageing conditions.

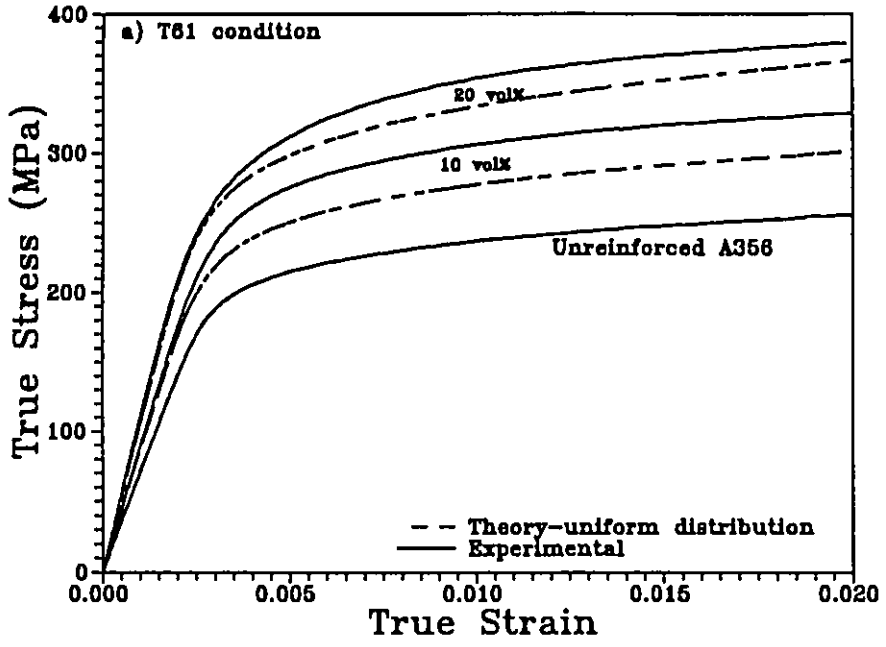
a) T61 condition
20 vol%
10 vol%
Unreinforced A356
Theory-uniform distribution
Experimental
True Stress (MPa)
True Strain
0
100
200
300
400
0.000
0.005
0.010
0.015
0.020

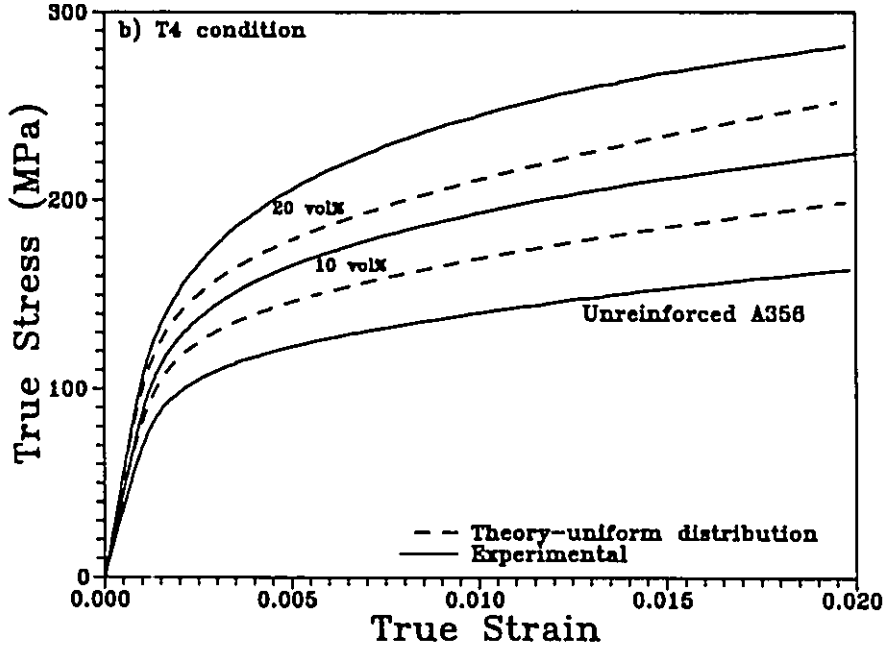
b) T4 condition
20 vol%
10 vol%
Unreinforced A356
Theory-uniform distribution
Experimental
True Stress (MPa)
True Strain
0
100
200
300
0.000
0.005
0.010
0.015
0.020

FIG. 5.11 a, b

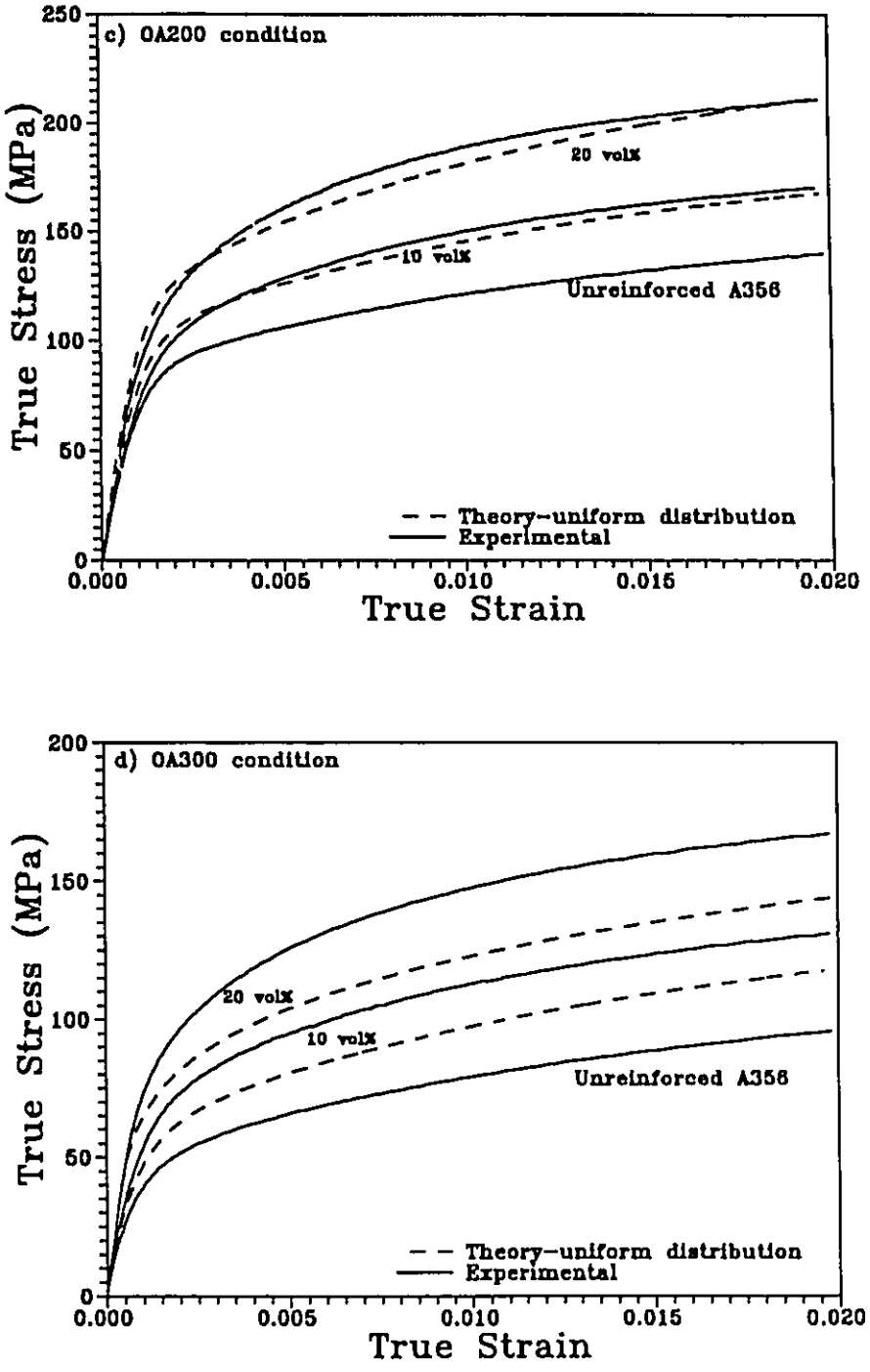

Figure 5.11: Comparison of the theoretical prediction, based on a uniform distribution of SiC particles, with experimental results for the 10 and 20 vol% SiC composites in the; a) T61; b) T4; c) OA200; d) OA300.

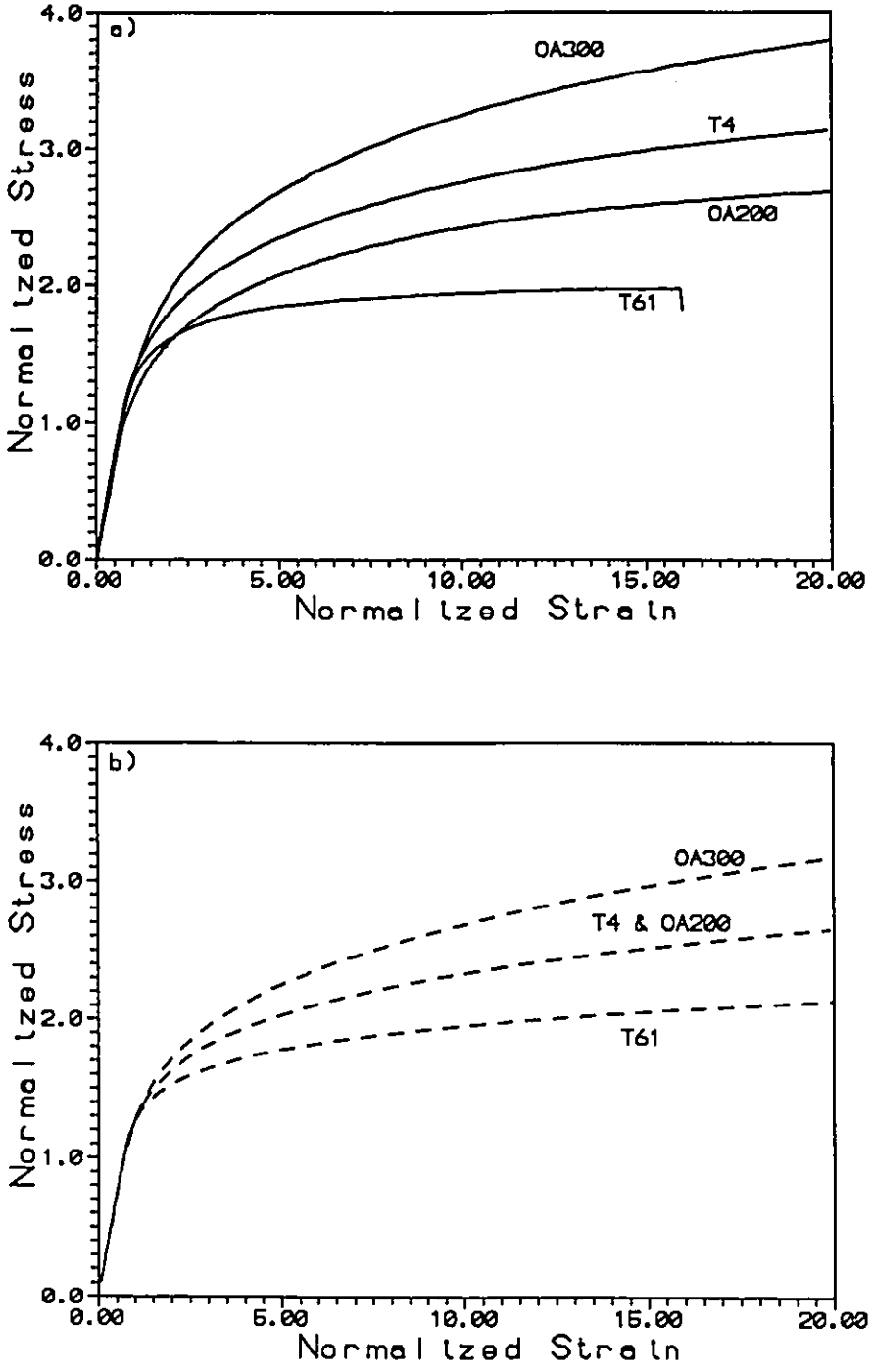

Figure 5.12: a) Experimental and b) theoretical stress-strain curves normalized by the values σ_o and ϵ_o determined for the unreinforced alloy in the various ageing conditions.

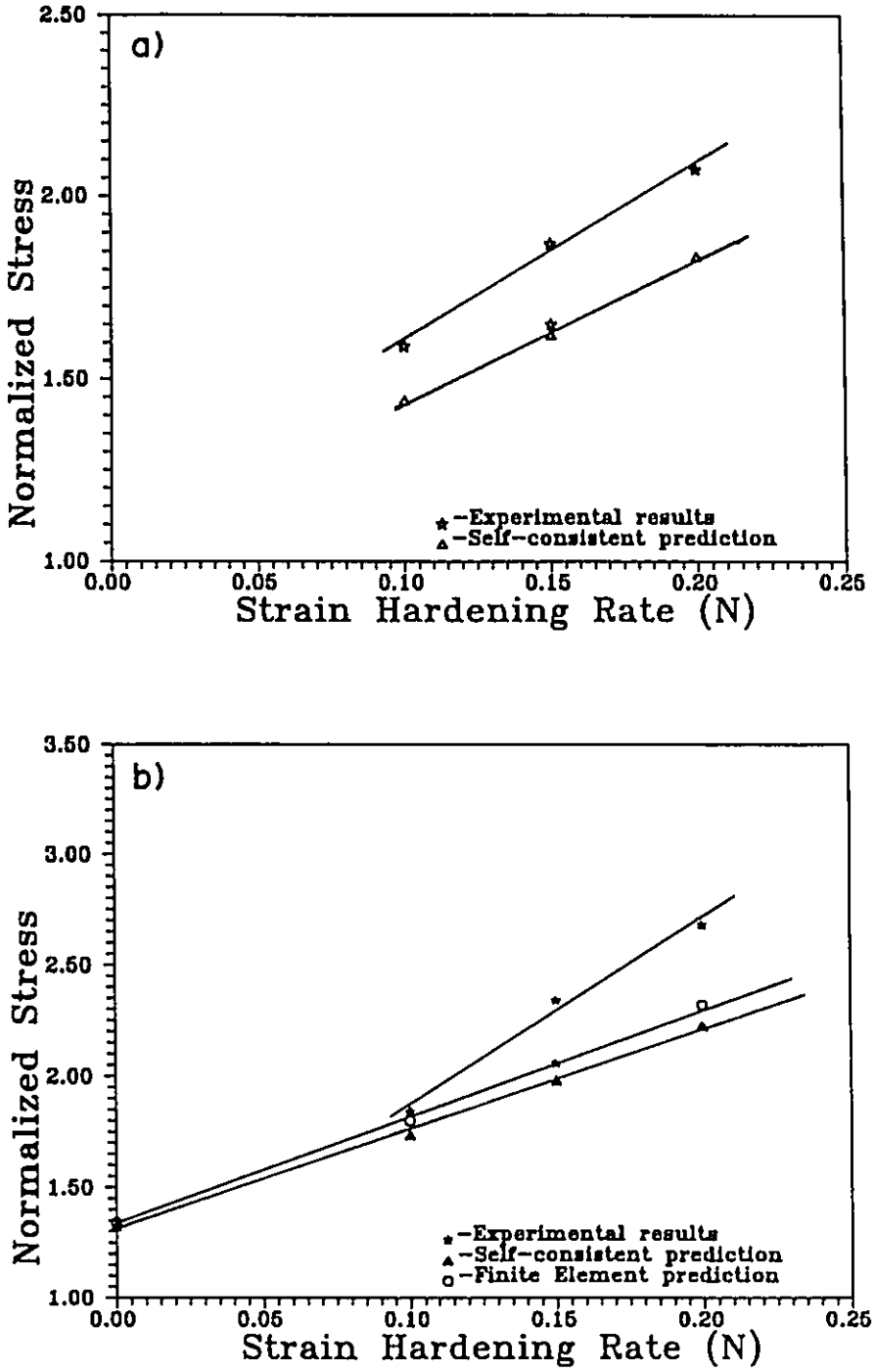

Figure 5.13: Normalized stress (σ_c/σ_o) as a function of the strain hardening rate in the matrix (N) for the; a) 10 vol% SiC and; b) 20 vol% SiC composites.

plotted. For the 20 vol% composite the results of the finite element predictions of Bao et al. are included as determined from Figure 4.8.

The self-consistent and finite element results both underestimate the measured strengthening ratio for all heat treatments except the OA200 state. The trends are similar for both the 10 and 20 vol% composites. Both theory and experiment indicate that the strengthening effect of the SiC particles increases as the strain hardening rate in the unreinforced alloy increases. However the experimental data exhibits a more rapid rise in σ_c/σ_m with an increase in N. Again the exception to this is the material aged to the OA200 state.

The anomalous behaviour exhibited by the material in the OA200 condition is perhaps related to the precipitate structure that is present in ageing state. The work of Dutta and Bourell (1990) and Appendino et al. (1991) (see section 3.1.2.2) indicate that accelerated ageing in the matrix as a result of the presence of SiC particles is most significant during the formation of the β' phase. The TEM results of section 3.1.2.3 indicate that the only ageing condition which contains β' precipitates is the OA200 state. The work performed was unable to confirm that the precipitate structure in this state was different in the composite and alloy as a result of an accelerated ageing effect. Nevertheless, this is one possible explanation for why the strengthening measured in the OA200 ageing condition is lower than that expected from the trends exhibited by the other ageing conditions.

In order to explain the discrepancy between the experimental and theoretical results, it is first important to review the assumptions made in the original formulation. There were three important assumptions made by the model of chapter 4.

1) The microstructure of the matrix in the composite is similar to that of the unreinforced alloy (i.e. any dislocation substructure created by plastic relaxation of the thermal stresses is assumed to be negligible).

2) The composite is initially stress free (i.e. no internal stress of thermal origin is present).

3) The original model assumed that the particles were not clustered into particle rich and particle free regions.

It is important to evaluate how the inclusion of these effects would alter the theoretical predictions.

The quenching experiments of Figure 5.7 suggest that the effects of quenching on the flow stress of the composite are small. This together with the results of Mummery et al. (1991) on commercial alloys indicates that the thermal substructure that may be created, is unlikely to account for the magnitude to which the theory underestimates the experimental results.

The experiments of Figures 3.19 indicate that a rather complex internal stress may exist in the composite materials, at least in the harder matrix conditions. As it has been developed, the self-consistent model represents a situation of no internal stress. Referring to Figure 5.3 it would be expected that the inclusion of an internal stress would result in the desired increase in strain hardening rate but the initial flow stress would be reduced rather than increased. Therefore inclusion of an internal stress of the nature described in section 5.2 would result in an even larger underestimation of the flow stress, at least at low strains. In addition it was observed in the experimental results section that composites tested in the OA300 state showed little anisotropy in tension/compression behaviour, indicating little internal stress. Therefore, if the presence of an internal stress was the only explanation for the higher strain hardening rate, a better predictions of behaviour based on a uniform distribution of SiC would be expected in this case.

5.3.1 Influence of Particle Distribution.

The experimental observations of plastic flow on a polished surface (section 3.2.4), suggest that initial plasticity in the composite material is very inhomogeneous. As a result of the

non-uniform distribution of the SiC particles, the matrix material in particle rich areas will be constrained and remain elastic while the matrix in particle free regions begins to deform plastically. It would be of value to estimate how this non-uniform particle distribution may effect the degree of strengthening developed during the elastic/plastic transition.

As described in Chapter 4, the theoretical calculations predict that the clustering of particles results in both an increase in the yield strength and initial strain hardening rate, resulting in an overall increase in flow strength. This suggests that such an effect may account for the discrepancy between the experimental and theoretical predictions described above. Application of the model of Chapter 4 to the experimental results requires an assumption of how the particles are distributed in the material under study here.

On the basis of the particle distribution studies of Lloyd (1991) using image analysis (see section 3.1.1) it was decided to represent the cluster with a constant volume fraction of either 40 or 35 vol% and to vary its volume fraction within the composite by changing the volume fraction of SiC particles in the particle free regions from 0 to 15%. In each case, the overall composite volume fraction was maintained at either 10 or 20 vol%.

An example of this calculation is shown in Figure 5.14 for the 20 vol% composite in the T4 condition. The main focus of the clustering model was to describe the high initial strain hardening rate in the composite. Therefore, the cluster description which best describes the initial strain hardening rate up to .005 strain is that based on a 35 vol% SiC cluster and a 0 vol% or particle free matrix. A similar procedure was used for the other conditions tested and the results are summarized in Figure 5.15. The best fit to the experimental results for the 20 vol% composite in all three ageing conditions shown was found to be based on a clustering distribution of a 35 vol% phase embedded in a 0% particle free phase. In this case the 35 vol% phase represents 60% of the total volume. In the 10 vol% composite the best fit was obtained using a

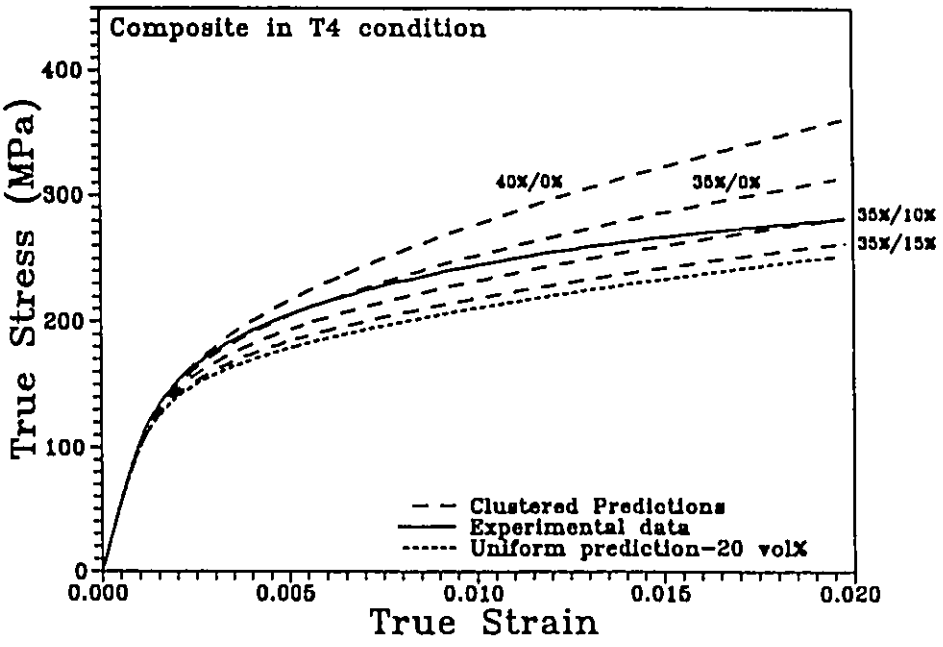

Figure 5.14: Comparison of experimental results with theoretical calculations which investigate a variety of clustering conditions. Included is the prediction for the uniform case. Calculation is based on the 20 vol% composite in the T4 condition.

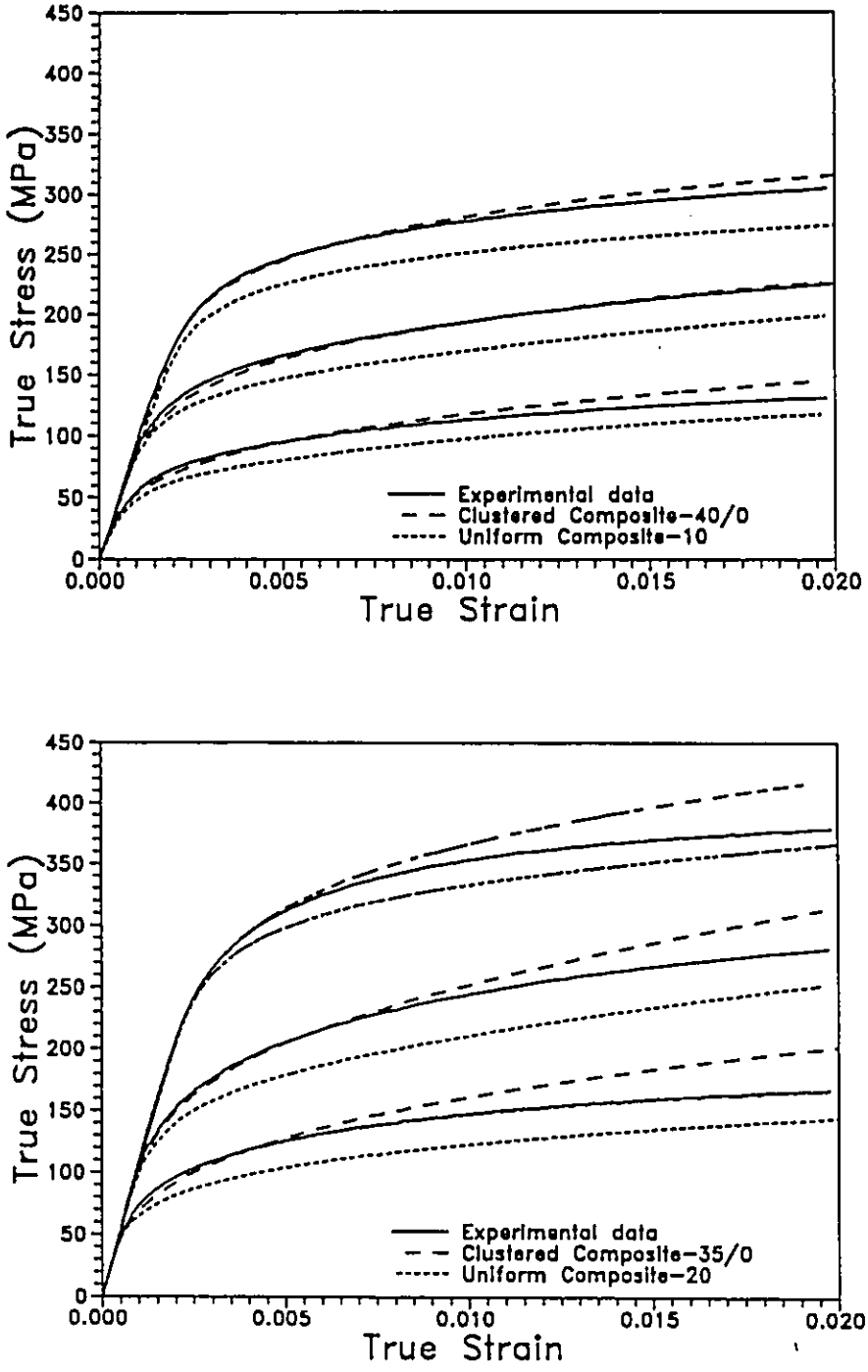

Figure 5.15: Comparison of the cluster description which best fit the initial experimental strain hardening rate in various ageing conditions; a) 10 vol%; b) 20 vol% SiC composites. Also included is the uniform prediction.

clustered distribution of 40%/0%. In this case the SiC rich phase occupies 27.5% of the total volume.

Although the inclusion of clustering is successful in predicting the initial portions of the stress-strain curve, it begins to overestimate flow behaviour at higher strains. One possible explanation for this is the onset of damage accumulation in the composite material. This will be discussed in more detail in a later section.

It is important to remain cautious when directly comparing the theoretical predictions of the clustering model with experimental results. Using the results of Lloyd (1991) as a guide, the degree of clustering chosen does give a better description of the experimental data. However, the bi-modal distribution used in the model is clearly a significant simplification of the real distribution in the composite. This is much more complicated and would perhaps best described by a number of clusters ranging in SiC content.

The other complication arises due to the assumption that no internal stress is initially present. The experimental results and the discussion of section 5.2 suggests that this is not the case. In particular, the detailed shape of the stress strain curve is influenced by the presence of a thermal stress. Figure 5.16 gives an example of how the description of clustering predicts the stress-strain curve in tension and compression. It is clear that the clustered predictions still give a better overall prediction of the flow strength than the uniform case. However its success in predicting the detailed shape of the stress-strain curve depends on the direction of testing. A model which can incorporate both the clustering effect and the complex thermal residual stress state will likely give a more realistic description of overall stress-strain behaviour.

In summary, it is proposed that the stress-strain behaviour of the composite material at low strains can be qualitatively described based on a clustered distribution of SiC particles. However, the degree of clustering which best fits the experimental data is a rather extreme case

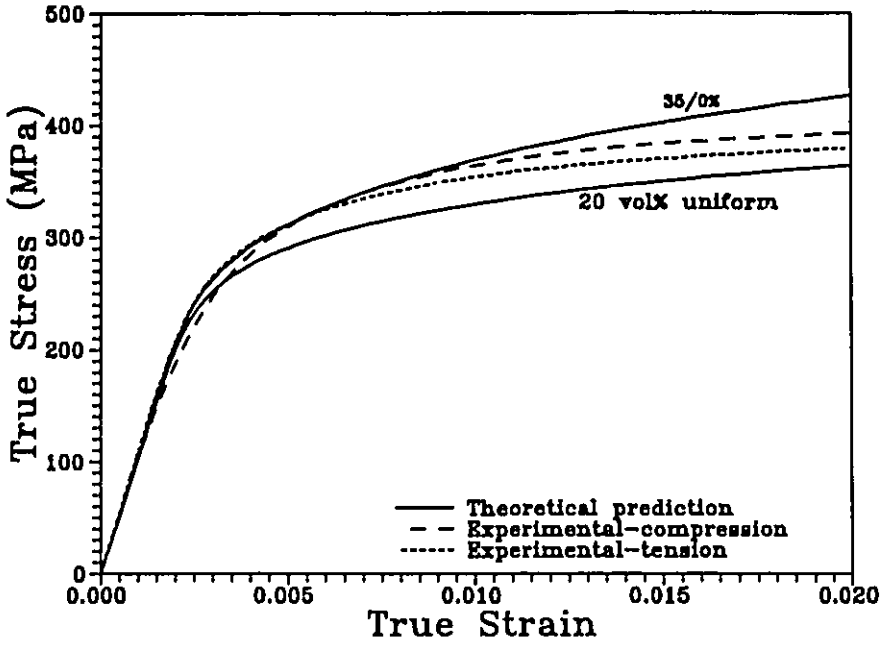

Figure 5.16: Illustration of the degree to which a clustering description (i.e. 35%/0%) can predict the initial strain hardening rate measured experimentally in tension and compression.

(i.e. 35 vol% SiC cluster; 0vol% matrix). Consequently, because of the complexity of the problem, a quantitative determination of the degree of clustering that results in the stress-strain behaviour observed, is beyond the scope of the model presented here. A more realistic description of clustering (i.e. a series of clusters with varying SiC content) and the inclusion of a thermal residual internal stress would likely lead to a more complete description of stress-strain behaviour.

5.4 The Bauschinger Effect

5.4.1 Influence of Ageing Condition

Section 3.1 has established the sequence of precipitation events in the A356 alloy as;

$$supersaturated\ solid\ solution \rightarrow G.P.zones \rightarrow \beta' \rightarrow \beta (Mg_2Si)$$

where the G.P.zones are coherent with the matrix, β' is a semi-coherent Mg_2Si precipitate and β is an incoherent Mg_2Si phase (Thomas, 1961; Lutts, 1961; Jacobs, 1972). Studies of the effects of ageing sequence on the Bauschinger effect have been most extensively performed on the Al-Cu system (Abel and Ham, 1966; Stoltz and Pelloux, 1976; Moan and Embury, 1979; Bate et al., 1982). This system has a similar precipitation sequence to Al-Mg-Si systems (Embury et al., 1989) involving;

$$supersaturated\ solid\ solution \rightarrow G.P.zones \rightarrow \theta'' \rightarrow \theta' \rightarrow \theta$$

where the G.P. zones and θ'' are coherent, θ' is semi-coherent $CuAl_2$ and θ is incoherent $CuAl_2$. In this system, the Bauschinger effect is largest in the alloy when aged to form the θ' and θ precipitates. The Bauschinger effect in the underaged structures (G.P.Z. and θ'') is quite low and comparable to that measured in pure Al (Abel and Ham, 1966). The evidence indicates (Moan

and Embury, 1979; Bate et al., 1982) that the θ' and θ precipitates are non-shearable and therefore support long range internal stresses of the type described by Brown and Clarke (1975). (The work by Moan and Embury indicates that the θ' particles eventually shear at large strains). This is the origin of the large Bauschinger effect observable in these ageing conditions.

Studies on other alloy systems (Gupta and Kodali, 1976 (Cu-Ni-Si); Stoltz and Pelloux, 1976 (Al-Cu-Mg and Al-Zn-Mg)) confirm that ageing to form shearable precipitates (i.e. G.P. zones) results in a small Bauschinger effect, while ageing to form non-shearable semi-coherent or incoherent particles increases the effect.

These results agree with the present study (see single loop Bauschinger experiments, Figure 3.35) in which the Bauschinger effect is smallest in the T4 and T61 condition which are characterized by the presence of G.P. zones. However the Bauschinger effect is largest in the OA200 condition where a combination of semi-coherent β' and coherent β precipitates exist. The decrease in the Bauschinger effect which was observed in the OA300 state, likely results from the dissolution of the β' precipitates that occurs during ageing at 300°C. These particles have a rather large aspect ratio and likely contribute significantly to the Bauschinger effect measured in the OA200 state.

Figures 3.40 b and c indicate that, in the case of the composite materials, the difference between the overaged and underaged materials depends on the level of plastic strain. At strains below about .01 the three ageing conditions studied indicate essentially the same Bauschinger loop width. This is in agreement with that observed for the unreinforced alloy which exhibits the same behaviour over the entire strain range studied. However at strains above .01 the loop width in the OA300 condition becomes larger. These observation may be related to damage accumulation.

Section 3.5 indicates that damage accumulation in the composite is measurably lower in the OA300 condition when compared to the T61 state. The level of damage develops with strain

and therefore may begin to influence properties to a significant degree at larger strains. This may contribute to the "saturation" effect seen in the T61 condition and the larger Bauschinger effect in the composite for the OA300 state. This argument could be confirmed by measurements of the Bauschinger effect in compression first conditions where the rate of damage is expected to be lower. Unfortunately, during this study, compression first tests were limited to prestrains below 1% (see section 2.2.1).

5.4.2 Influence of Initial Testing Direction

Figure 3.18 illustrates that a strength differential exists between tension and compression in the unreinforced alloy which suggests the presence of an internal stress of thermal origin (see section 5.2.1 for more details). Withers et al. (1989) point out that, when a material is deformed in tension, this thermal internal stress aids forward flow, but when the flow is reversed, it should hinder the resultant compressive flow. Alternately, when tested initially in compression, this thermal stress resists forward flow but aids reverse flow. Consequently, providing this thermal internal stress is not removed by forward plastic flow, the strength differential observed in the forward direction should also be present in the reverse portion of the curve.

The results of Figure 3.34a indicates that this is not the case. The reverse portion of the curves are identical regardless of the initial testing direction. This suggests that the internal stress that is initially present, is removed by the forward plastic deformation and therefore does not influence flow in the subsequent reverse direction. Although the interpretation of thermal stress is more complex in the SiC composite material, Figure 3.34b also suggests that the reverse portions of the flow curve are independent of the direction of initial testing.

5.4.3 The Bauschinger Effect and Stress Partitioning

From the discussion of Chapter 1, it is evident that in two phase materials the principle source of the Bauschinger effect is due to elastic loading of the particles during plastic flow. Consequently, a measure of the Bauschinger effect should indicate, in a qualitative way, the role that stress partitioning to the particle plays in strengthening. This is an important determination because of the controversy that exists in the literature (Arsenault, 1991; Miller and Humphreys, 1991b) concerning the importance of the particles as load bearing elements, particularly at strains below 0.2% plastic strain.

The experiments of section 3.3 (Figures 3.39 and 3.40), indicate that the Bauschinger effect develops rapidly as soon as plastic flow begins. By 0.2% plastic strain significant hysteresis forms in the reverse/forward cycle. The Bauschinger effect continues to develop with further deformation but rises much less rapidly at plastic strains above 1%. These experiments suggest that internal stress (and therefore stress partitioning to the particles) plays an important role in the development of strength at low strains.

In evaluating a model which describes monotonic stress-strain behaviour, it is important to determine whether it can also account for the Bauschinger effect or the development of internal stress development. The concept of stress partitioning during plastic flow which can cause an internal stress and lead to a Bauschinger effect can be described by referring to Figure 5.17. An element of the composite is isolated which contains a particle and matrix. A stress is applied so as to cause simple shear in the element. Initially both the particle and matrix deform elastically. If $E_p > E_m$ then stress partitioning will occur such that $\sigma_p > \sigma_m$. With continued straining the matrix becomes plastic and stress partitioning to the particles occurs also as a result of plastic flow. Since the matrix exhibits work hardening the elastic strain γ_{me}' after a plastic strain of γ_{mp} is larger than the elastic strain at the onset of yielding γ_{me}.

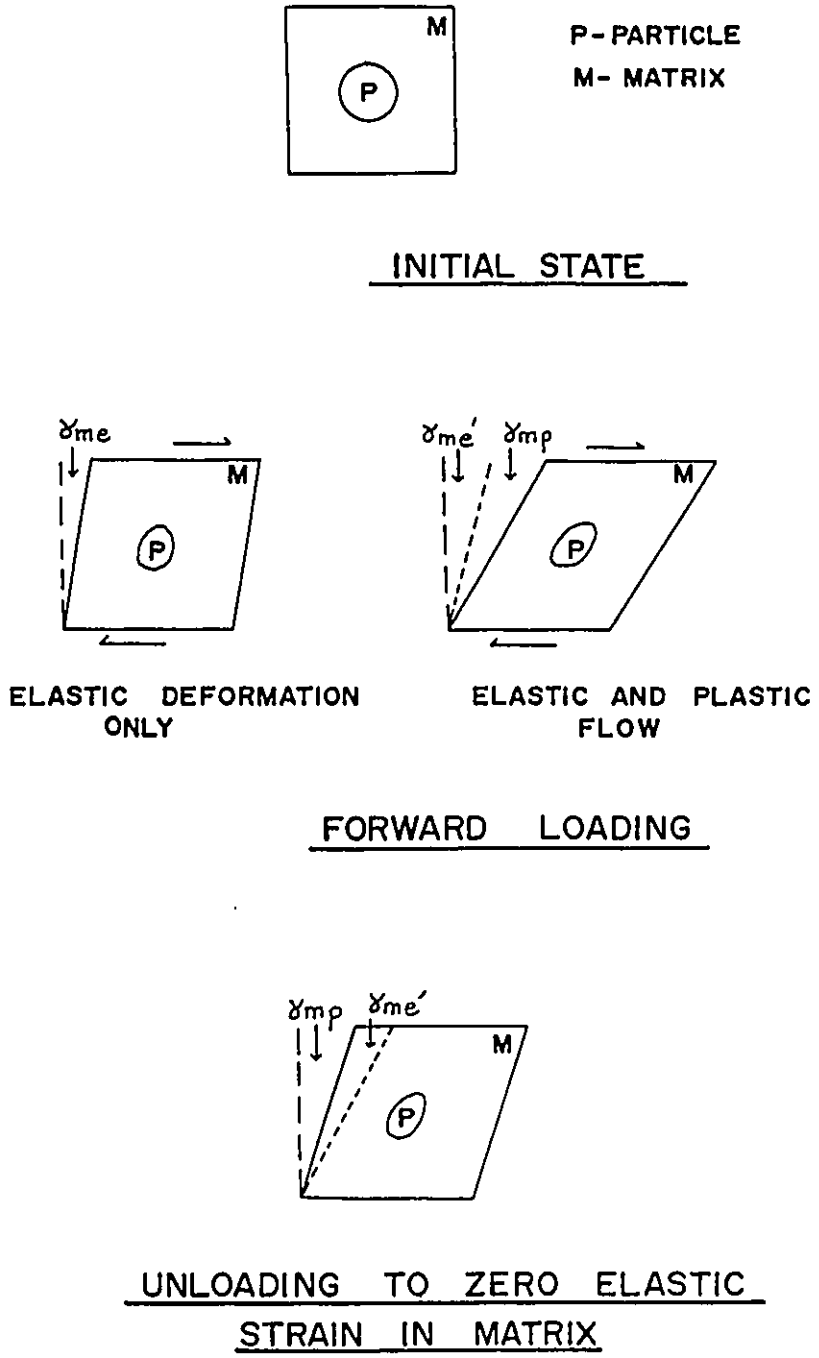

Figure 5.17: Schematic description of the shape change in an element of the composite when deformed in simple shear in the forward direction and then unloaded to a point of zero elastic strain in the matrix.

After a certain amount of plastic strain the element can be unloaded such that the elastic strain in the matrix is recovered and it is at a stress of zero (note that the particle will also be partly unloaded elastically). However the element still has a permanent shape change as a result of the plastic flow in the matrix. If it is assumed that the particle has remained elastic and no relaxation of the plastic shape misfit occurs, then the particle also experiences this permanent shape change. It is therefore still stressed in the forward direction. If it is assumed that the forward direction was tensile, further reverse strain would load the matrix elastically in compression while the particle will continue to unload in tension elastically. Therefore this represents an internal stress.

This process of stress partitioning is relatively easy to follow for the case of continuous fibres imbedded in an elastic/perfectly plastic metal. This case is well represented by Cu-W composites studied by Brown and Clarke (1977) and Lilholt (1977). This is primarily because the strains in the two phases are assumed to be equal to the applied strain. For the case of PMMC's the situation is more complex for a number of reasons.

1) The unreinforced alloy exhibits a significant Bauschinger effect without the addition of SiC particles. Consequently during unloading, it may not remain ideally elastic.

2) Because of the work hardening in the matrix, stress partitioning to the particles will continue to occur as a result of an increase in the elastic deformation in the matrix. This stress partitioning will be removed upon unloading and therefore should not contribute to the Bauschinger effect.

3) In the case of equiaxed particles both stress and strain are partitioned (i.e. $\epsilon_p \neq \epsilon_m$) during forward loading and reverse loading.

4) The principal feature of the Bauschinger effect in the materials studied here is the very rounded nature of the reverse flow curve (i.e. Transient softening). The detailed shape of this curve is likely to depend on the local distribution of internal stress that develops as a result of

inhomogeneous plastic flow. This will create complications similar to those described for the thermal internal stress discussed in section 5.2 based on a non-uniform distribution of internal stress.

Despite these complications, it should be expected that the description of stress partitioning provided by the self-consistent formulation is capable of providing a qualitative picture of the development of internal stress with plastic flow.

Figure 5.18a illustrates the stress-strain curve of the composite (solid line) as predicted by the self-consistent analysis (for a uniform particle distribution). This example is based on a matrix in the T61 condition reinforced with 20 vol% SiC. Also plotted are the predicted stresses in both the SiC and Al phases at a given level of composite strain (dashed lines). Included is a prediction of the elastic unloading of the composite to zero applied stress. The stress in the two phases are plotted versus the composite stress in Figure 5.18b. In both cases, the particles and matrix are assumed to unload elastically in the same proportion as they elastically loaded initially in the forward direction. This assumes that the plastic structure developed around the particles is stable during unloading. If this structure begins to reverse or relax itself, the particles may be unloaded to a larger extent than that predicted in the figure.

The development of an internal stress during the process described in Figure 5.17 can be followed by referring to Figure 5.18b. While both phases deform elastically the degree of stress partitioning remains constant. This is exhibited by the linear relationship between the stress in each phase and the composite stress (line segment OP and OP'). The slope of these lines are determined by the stress connectors of equation (4.14). At point P, the Al begins to deform plastically. The stress that is then partitioned to the particles is modified by sampling the current strain hardening rate (or tangent modulus) of the Al matrix. In this way, the model simulates the additional stress partitioning that arises as a result of plastic flow. The dashed line indicates the

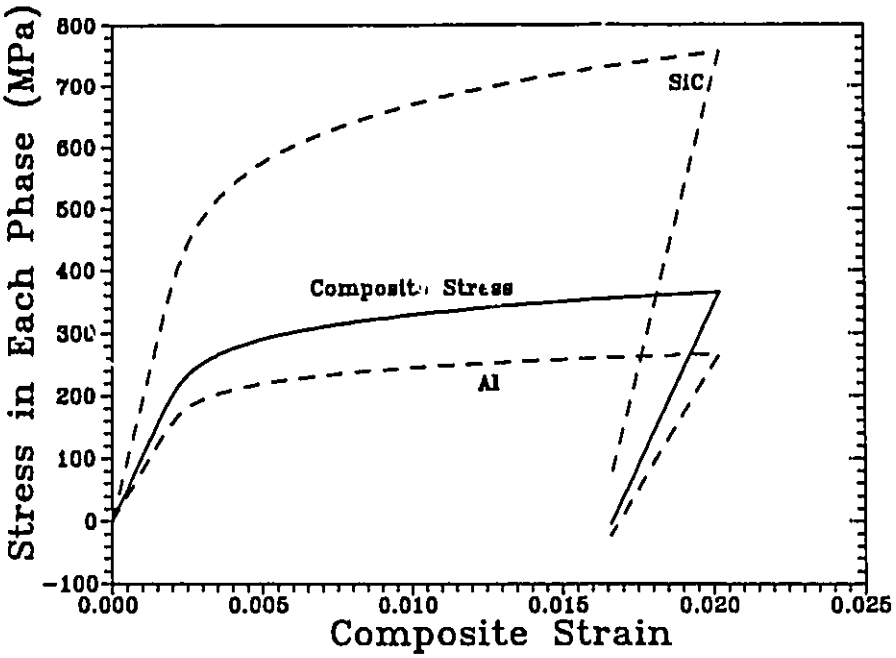

Figure 5.18a: The σ-ϵ curve of the composite (solid line) prestrained to 2% and unloaded to zero. Dashed line indicates stress in the Al and SiC phases at a given composite strain.

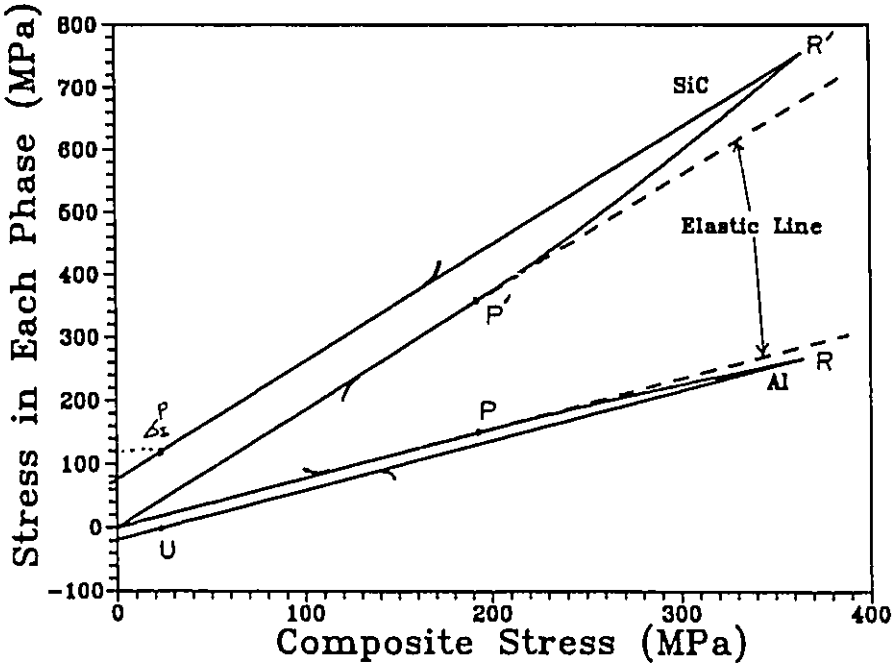

Figure 5.18: b) The stress predicted in the Al and SiC phases at a given composite stress during prestraining and unloading to zero.

stress that would have been partitioned to the particles if the matrix remained elastic. After a forward deformation of about 0.02 (see Figure 5.18a) the composite is completely unloaded. During this process both the matrix and the particles are unloaded elastically in the same proportion as they were originally loaded in the elastic regime. However, the amount of stress partitioning to the particles as a result of plastic flow cannot be removed as long as the matrix remains elastic and the plastic structure around the particle remains stable. The point U represents the point at which the matrix is unloaded to zero as described in Figure 5.17. It is clear that, at this point, the particles are still loaded in tension by σ^p_i. Unloading the composite to zero applied stress (point O) results in a situation of internal stress. In this case, the tensile stress in the particle is balanced by a compressive stress in the matrix such that equation (4.4b) is satisfied. The compressive stress in the matrix then aids reverse flow resulting in a Bauschinger effect.

The description of Figure 5.18 does illustrate that the relatively simple expression of stress partitioning that is developed in the self-consistent model does contain the essential features which can indicate the presence of an internal stress and consequently the Bauschinger effect. An estimate of this stress as a function of plastic strain can be constructed by determining the value of σ^p_i at various levels of plastic strain. Therefore the internal stress in this case will be defined as the stress in the particle at the point where the matrix is unloaded to zero. This value is plotted versus composite plastic strain in Figure 5.19. Comparisons of this description with the experimental results of Figure 3.39. reveals good agreement concerning the overall trends. In particular, internal stress develops rapidly at low strains but falls off at strain levels above 0.01.

An extension of the self-consistent analysis beyond the general description of Figure 5.18 to include a prediction of transient and permanent softening in the reverse flow curve is difficult. This is primarily the result of the complex reverse flow that can arise as a result of the instability of the plastic structure formed in the forward direction. However, some qualitative statements

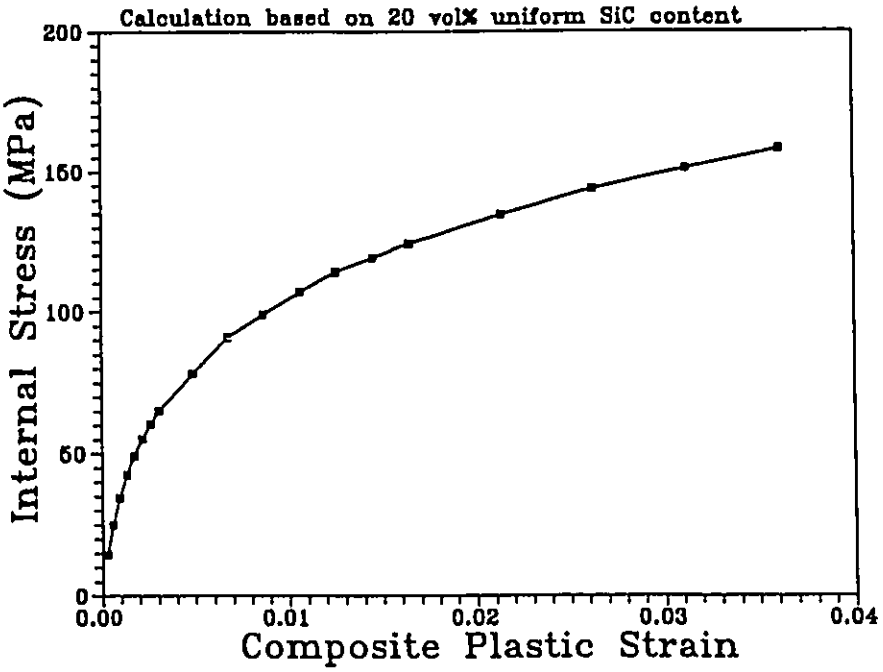

Figure 5.19: The predicted internal stress (defined in the text) developed during forward flow as a function of the level of plastic strain in the composite.

concerning the relative magnitudes of transient and permanent softening can be made by discussing the behaviour of particulate MMC materials in the context of the two simple models developed in sections 1.6.1 and 1.6.2.

5.4.4 Permanent and Transient Softening

As described in the introduction, the Bauschinger effect is often characterized by both transient and permanent softening. Because of the presence of a hard elastic phase, there is the possibility that the composite materials of interest here would exhibit a permanent softening effect. However, the experimental results of Figures 3.31 and 3.32 suggest that the magnitude of permanent softening is very small. These experiments were limited by the degree of compressive flow that could be performed. Work by Prangnell et al. (1992) investigated the Bauschinger effect in a 2618 Al reinforced with 12.5 vol% SiC particles of similar size and shape to the particles used in this investigation. Some of their results are shown in Figure 5.20. The dashed lines are the reverse compressive curves after prestrains in tension (solid line). The degree of prestrain is evident from the offset strains from the origin of the reverse curves and ranged from 1 to about 3.5%. In this case full reversal was possible. Essentially no permanent softening is evident from these experiments.

An explanation for the lack of permanent softening in these materials can be offered by considering the magnitude to which stress is partitioned to the particles during plastic flow. As discussed in section 1.5, the degree of stress partitioning depends strongly on the reinforcement geometry. For continuous fibres, stress partitioning is large and a significant permanent softening effect should be expected. For equiaxed particles, stress partitioning and the associated permanent softening effect should be much smaller. Nevertheless permanent softening has been measured in two phase materials such as single crystals of copper containing a fine dispersion of spherical

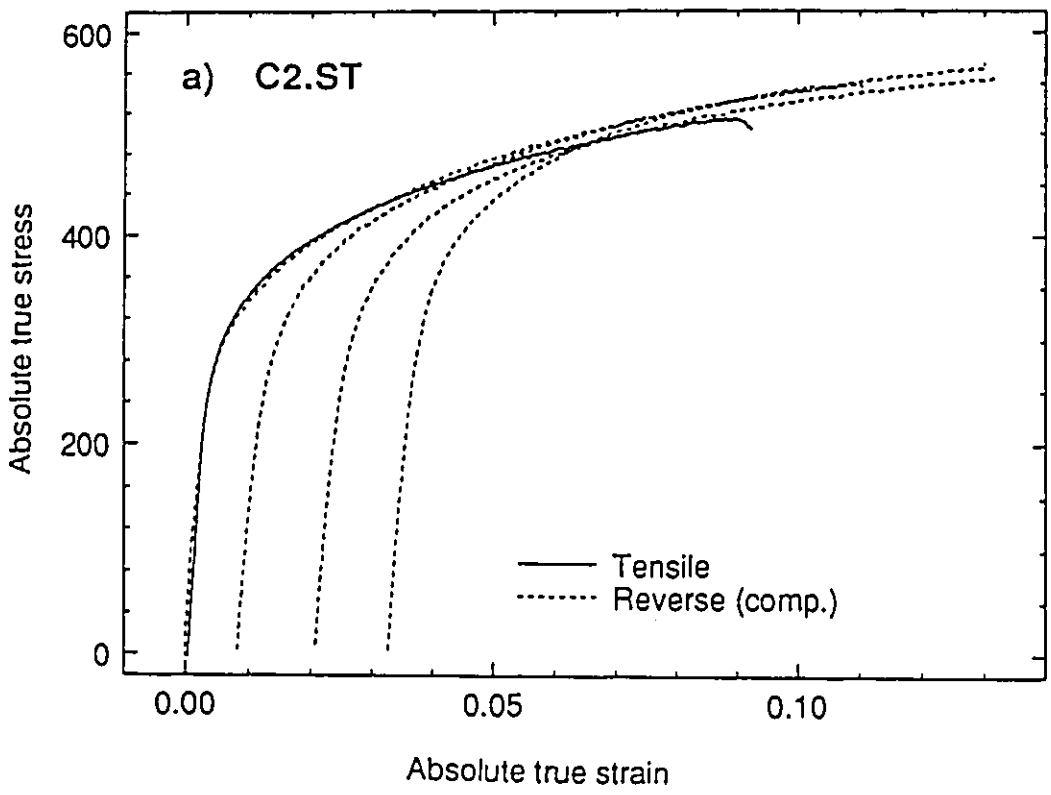

Figure 5.20: Forward (solid line) and reverse (dashed line) curves at various tensile prestrain for a 2618 Al alloy reinforced with 12.5 vol% SiC particles. (Prangnell et al (1992)).

SiO_2 particles (Atkinson et al., 1974). Therefore, the reinforcement geometry alone cannot rule out the possibility of permanent softening.

The calculations of Withers et al. (1989) illustrated in Figure 5.8 suggests a rather strong relaxation effect in the composite materials, which prevents the particles from being loaded to the degree that a model, based on an unrelaxed state, would predict. This limits the degree of internal stress and therefore permanent softening that would be measured in the materials studied here.

The magnitude of permanent softening measurable from a Bauschinger experiment also depends on the stability of the mean matrix stress developed during forward flow. This, in turn, depends on the stability of the plastic structure that develops around the particles. During a reversal in strain path the possibility exists for this plastic structure to relax and therefore reduce the amount of elastic load carried by the particle. In the case of materials like Cu-SiO_2, where the second phase is a fine dispersion, plastic flow produces a series of Orowan loops around the particles. This structure is relatively stable and considerable reverse straining may be required to remove the Orowan loops (Embury, 1987) leading to a measurable permanent softening effect. As mentioned in section 1.4.2, the plastic structure around a particle in a PMMC is likely more complex due to the multiplicity of slip in the polycrystalline matrix. Therefore the plastic structure may be inherently more unstable, leading to a reduction in the mean matrix stress during unloading and consequently a reduction in the amount of permanent softening that can be measured from a Bauschinger experiment.

This instability is emphasized by the extensive work of Wilson and Bate (1965, 1986, 1987) who analyzed the Bauschinger effect in spheroidised steels. These high carbon steels consisting of 17 volume percent of relatively coarse ($\approx$ 1-2 μm) cementite particles in a polycrystalline ferrite matrix are somewhat analogous to the composite materials of interest here.

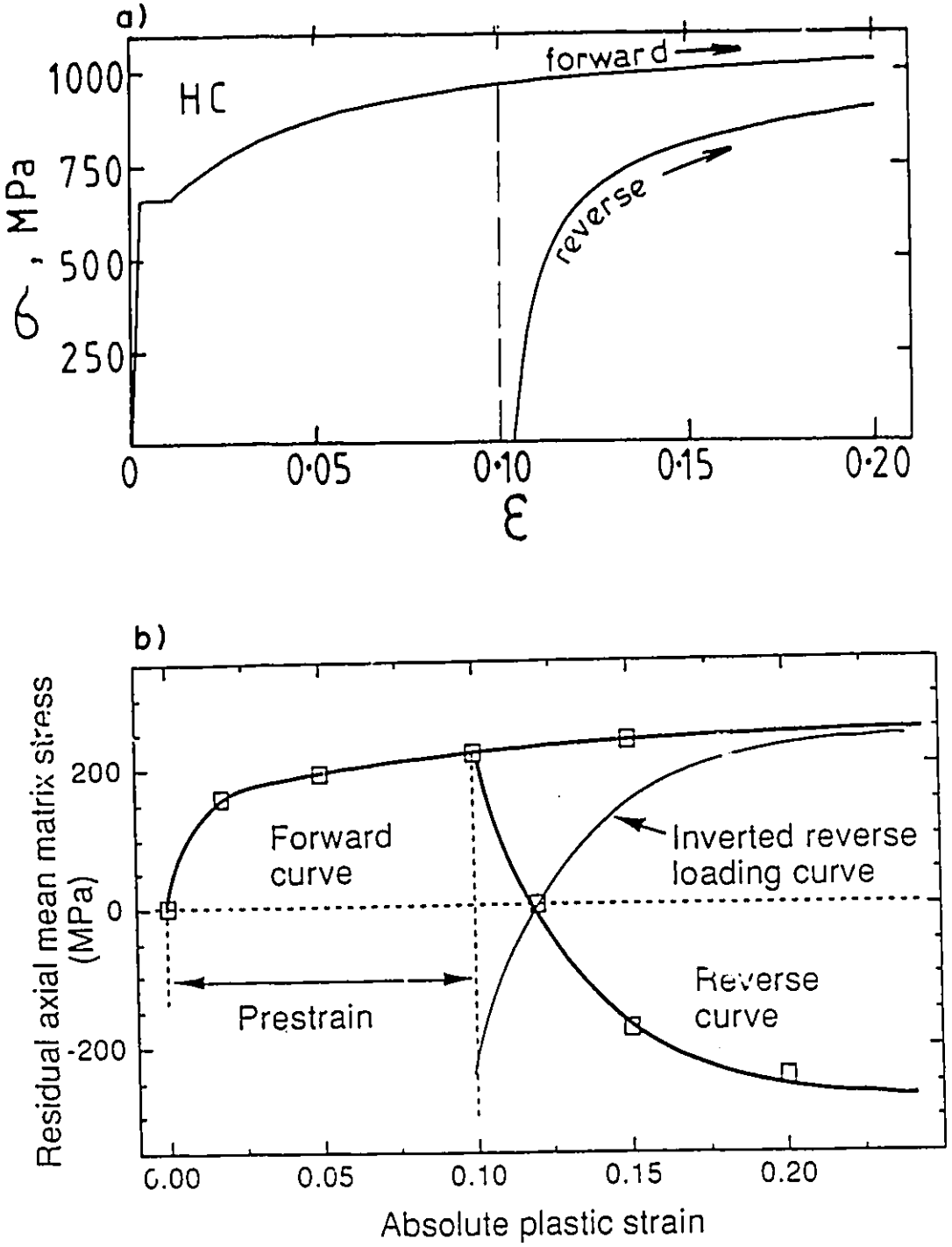

Figure 5.21: a) The forward and reverse curve for spheroidised steel (Wilson and Bate, 1986), b) x-ray diffraction measurements of the axial residual mean stresses made by Wilson and Bate (1986) (From Prangnell et al, 1992).

Wilson and Bate (1987) (Figure 5.21a) have shown that for spheroidised steels the reverse flow curve does not exhibit permanent softening even after reverse strains of up 10%. This behaviour is similar to that observed by Prangnell et al. (1992) in Figure 5.20. Consequently measuring a value for permanent softening and relating this to the mean matrix stress $<\sigma>_m$ is extremely difficult. Supporting evidence obtained by Wilson and Bate (1986) using x-ray diffraction measurements of the axial residual mean matrix strain during forward and reverse loading of spheroidised steels have been recently summarized by Prangnell et al. (1992) and are presented in Figure 5.21b. After a prestrain of 10% the load was reversed and the residual stress in the matrix was determined at various degrees of reverse straining. The mean matrix stress begins to reverse itself immediately upon load reversal and is removed much faster than it was originally developed in the forward direction. The results also suggest that the mean matrix stress developed in the forward direction is completely reversed, such that a reverse strain of equal magnitude (10%) results in the development of an equal but opposite mean stress in compression. These results agree with the lack of permanent softening observed in the Bauschinger experiments.

The Masing model described in section 1.6 indicates that inhomogeneous plastic flow will lead to a non-uniform distribution of internal stress. This leads to a prediction of a pronounced transient softening effect. The unreinforced alloy studied here exhibits a large transient softening effect which is a result of its polycrystalline nature and second phase microstructure. However the Bauschinger strain and loop width measurements (Figure 3.35 and 3.39) indicate that the transient softening effect increases as a result of the addition of SiC particles. This result suggests that the internal stress distribution in the composite is also inhomogeneous in nature. This fact is supported by the description of Levy and Papazian (1991) (see section 5.2.1) which predicts a non-uniform distribution of the thermal internal stress on the microscopic scale. As a result, the onset of yielding is very inhomogeneous. In addition, the results of plastic flow on a polished

surface and the self-consistent model of chapter 4 suggests that the non-uniform distribution of the SiC particles also leads to inhomogeneous plastic flow on a more macroscopic scale. These factors may combine to give the pronounced transient softening effect observed in the composites studied here.

5.5 Damage Accumulation

As described by Embury (1985) a number of alternative processes can occur during deformation which may alter the level of internal stress developed in a two phase material. Three primary processes of interest are; 1) diffusional relaxation; 2) plastic relaxation and 3) damage accumulation.

The experimental results discussed in chapter 3 indicate evidence of alternative processes. These include;

1) A rapid decrease in the strain hardening rate of the composite such that it becomes equal to or drops below that measured for the unreinforced alloy, depending on the ageing condition (Figure 3.25). This occurs at relatively low strains (e.g. 2 to 3%).

2) A saturation of the strengthening effect of the particles after 2% strain (Figure 3.26). In the hardened states (T4 and T61) a drop in the difference between the composite and alloy occurs at larger strains.

3) A rapid rise in the Bauschinger effect at very low strains is followed by a more modest rise after strains of .01 (Figure 3.39). In some cases (e.g. T61 ageing condition), a saturation of the Bauschinger effect is evident.

In this section, the objective is to estimate the degree to which damage accumulation may influence the flow strength of the composite.

5.5.1 The Influence of Damage Accumulation on the Flow Curve.

Evidence that damage accumulation occurs in MMC's prior to final fracture has been indicated by a number of studies (Vasudevan et al., 1989; Embury et al., 1991; Lloyd, 1991; Tao, 1991; Hunt, 1991). These studies also indicate that the primary damage mechanism is cracking of the hard second phase particle. In addition, the work of Lloyd (1991) and Hunt et al. (1991) indicate that this form of damage accumulation is accompanied by a decrease in modulus which is a function of the plastic strain level. The work of Tao (1991) and Lloyd (1991) also suggests that the damage accumulation, whether measured directly by observing the number of cracked particles or indirectly using modulus change measurements, increased approximately linearly with strain. Finally the work of Tao (1991) on the compression behaviour of the materials used in this study indicated that the level of damage accumulation in the T61 condition was higher than that in the OA300 condition, which is in agreement with results of section 3.5.

On the based of the above observations, the experimental results of section 3.5 can be used to estimate the degree to which damage accumulation lowers the flow strength of the composite. This was done by following the approach of Vasudevan et al. (1989) who suggest a simple model of damage accumulation by expressing the flow stress as;

$$\sigma = \sigma^{*}(1\text{-}D) \tag{5.5a}$$

where σ^{*} is the flow stress in the absence of damage and D is a damage parameter which varies from 0 at the onset of plastic flow to 1 at fracture. The apparent work hardening rate can then be expressed by differentiating the above expression to get;

$$\frac{d\sigma}{d\epsilon} = \frac{\partial\sigma^{*}}{\partial\epsilon}(1-D) - \sigma^{*}\frac{\partial D}{\partial\epsilon} \tag{5.5b}$$

where $\partial D/\partial\epsilon$ is the damage accumulation rate versus strain. The damage parameter was defined following the work of Lloyd (1991) as;

$$D=1-\frac{E_{pl}}{E_i} \qquad (5.6)$$

where E_{pl} is the modulus measured at a given level of plastic strain and E_i is the initial modulus. The relationship between D and ϵ_p was assumed to be linear and the slope was determined from the experimental results shown in Figure 5.22 using a linear regression technique. It was assumed that D had an initial value of zero at zero plastic strain. At a given value of strain, D was determined and substituted into equation (5.5) to determine the value of σ^*. The results of such a calculation on the unreinforced alloy and 20 vol% composite in the T61 condition are shown in Figure 5.23a.

Clearly the model predicts that the damage accumulation rate has the largest impact on flow strength at strains above .01. In addition, the flow strength in the composite is influenced to a larger degree than the alloy, reflecting the larger damage accumulation rate in that material. Figure 5.23b indicates how damage accumulation influences the strain hardening rate of the composite. While a rapid decrease in the hardening rate still occurs, the overall level of hardening is increased when compensating for damage accumulation. The degree to which the composite hardening rate drops below that of the alloy is also reduced when damage is accounted for.

An additional way in which damage may impact the observations made in Chapter 3 is in the "cross over" effect observed between tension and compression. In Figure 5.24, the tension and compression curves for the 20 vol% composite along with the tension curve corrected for damage are illustrated. The influence of damage at these low strains is small and would appear not to be a major contributor to the cross over effect. This comparison assumes that no damage accumulation occurs in compression. While this is not the case, observations have indicated (Tao, 1991; Zok, 1988) that, in PMMC's, the rate of damage accumulation in compression is lower than that in tension. This result would appear to indicate that issues related to thermal internal

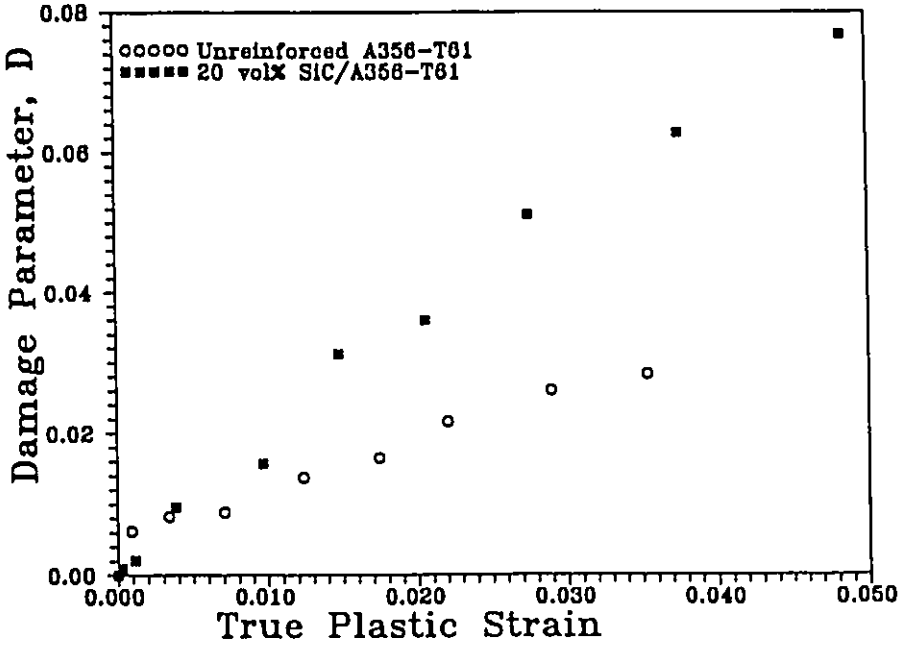

Figure 5.22: The damage parameter D, for the unreinforced alloy and 20 vol% composite in the T61 condition.

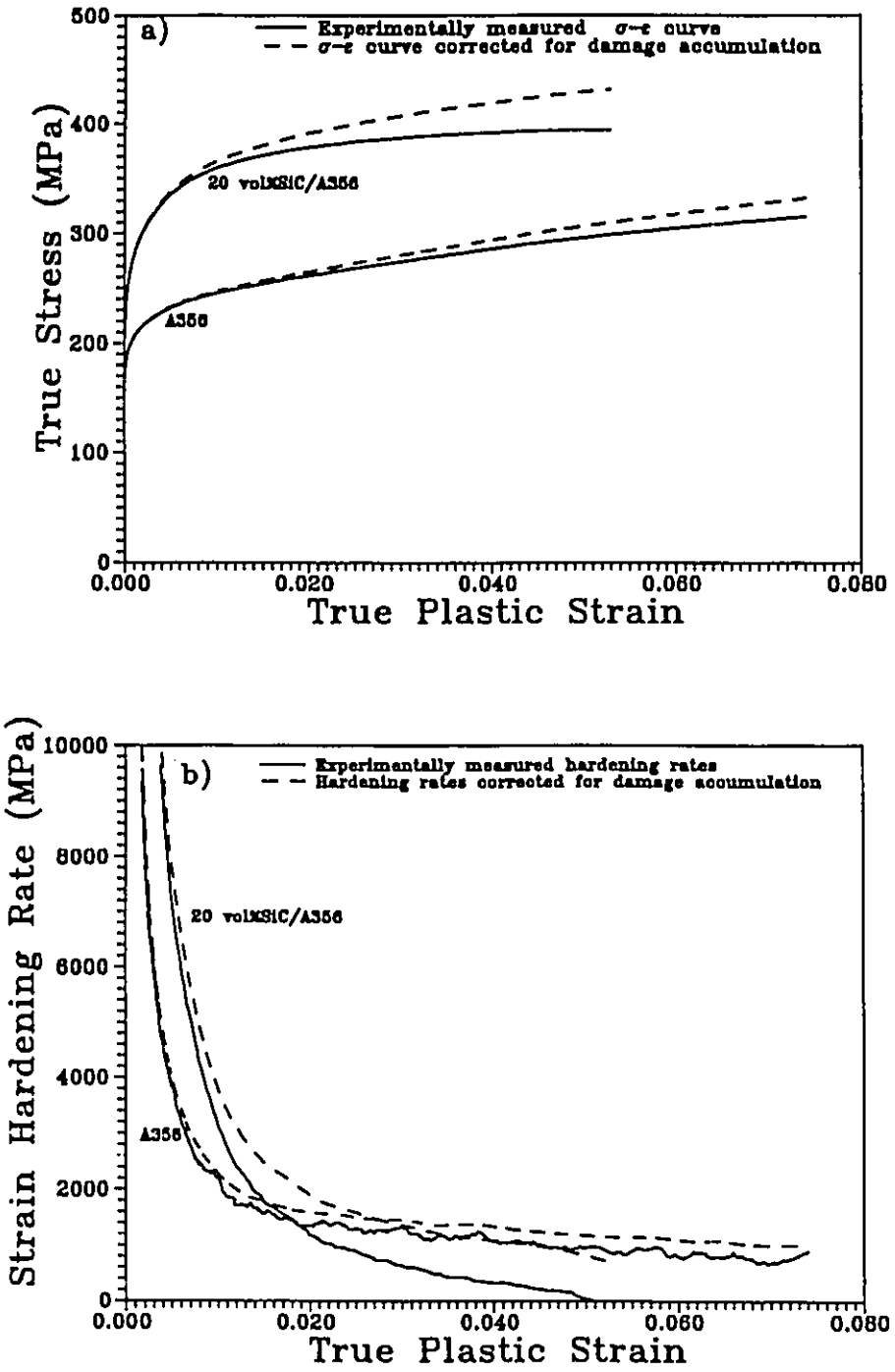

Figure 5.23: Experimentally measured properties and predictions of damage compensation for the alloy and 20% composite (T61 state). a) True plastic σ-ϵ curve b) strain hardening rate versus plastic strain (ϵ^c_p).

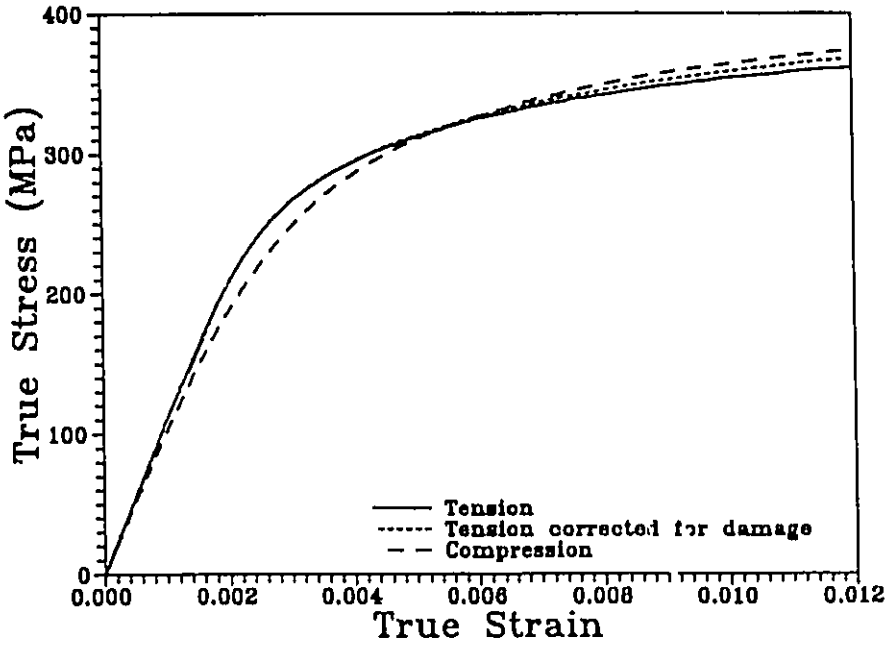

Figure 5.24: Comparison of tensile and compressive σ-ϵ curves when the tensile curve is corrected for damage. Results are for 20 vol% composite in T61 condition.

stresses discussed in section 5.2 are responsible for the cross over effect.

5.5.2 Alternate Relaxation Processes

The results of the last section do indicate that damage accumulation plays a role as a relaxation process. However, the rapid decrease in hardening rate that is still observed when compensating for damage indicates that other processes such as diffusion and plastic relaxation are also important. One way of assessing the importance of alternate relaxation processes is by comparing the experimental results with the self-consistent model at large strains. Figure 5.25 illustrates the experimental results for the 20 vol% composite in the T61 and OA300 states. Both the original data (lower) and data corrected for damage accumulation (upper) are shown. Included is the prediction for the uniform and clustered distribution.

Compensating for damage still results in an overestimation of the flow strength by the clustered distribution. It is also evident that even the prediction based on a uniform distribution begins to overestimate the strain hardening rate at higher strains. These observations point out both the inadequacy of how the model compensates for relaxation and the importance of relaxation processes other than damage in terms of the overall strength developed in the composite.

5.6 Influence of Test Temperature on Strengthening.

The discussion of section 1.4.2 indicates that relaxation, by plastic flow in the matrix, is relatively easy in PMMC's. The analysis of Levy and Papazian (1991) (see Figure 5.5) illustrates the approach of considering the plastic relaxation process on the continuum level. In this case, relaxation is predicted to take place whenever the internal stress reaches a value above the local yield strength of the metal matrix. The degree of strengthening (as expressed by the difference

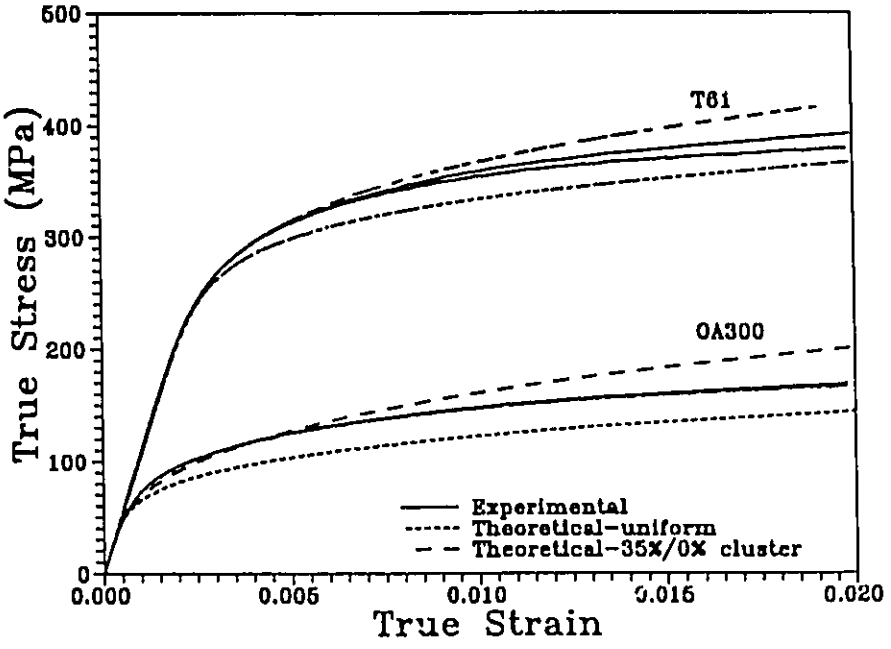

Figure 5.25: σ-ϵ curves for 20 vol% composite. Included are the experimental (solid lower) and damage corrected (solid upper) curves, and self-consistent predictions based on a uniform and clustered distribution (35%/0%)

between the flow stress of the composite and unreinforced alloy) derived from the SiC particles is therefore limited by the strength of the matrix which it reinforces. This is illustrated in Figure 3.26 which indicates that, as the matrix strength is reduced, the strengthening increment, $\Delta\sigma$, is also reduced. This trend is continued when testing the overaged materials at temperatures up to 300°C (Figure 3.45). This scaling of the composite strength with matrix strength can be expressed by plotting the ratio of the composite and alloy flow stress versus plastic strain (Figures 3.27 and 3.47). Both the self-consistent model and the FEM model of Bao et al (1991) predicts that the magnitude of this strengthening ratio is dependent only on the strain hardening rate of the matrix and not the matrix strength itself. This trend is indicated by the experimental results at low strains (Figure 5.13). Trends concerning the effects of strain hardening rate at higher strains, such as those plotted in Figure 3.27, are difficult to interpret because of the influence of damage accumulation.

For the materials tested at high temperatures, the possibility exists for additional relaxation processes to become dominant such as diffusional flow. If this were the case, the strengthening ratio at the higher temperatures should be lower than that measured at room temperature. However, the data in Figure 3.47 indicates that this does not occur. Rosler et al (1990) have derived an expression based on relaxation by diffusional assisted flow. This expression predicts a critical applied strain rate at which reinforcement strengthening will be eliminated. This strain rate depends on the aspect ratio and particle size of reinforcement as well as the test temperature. The best creep resistance would be offered by large ($\approx 100\ \mu m$) continuous fibres. While their calculations are based on an γTiAl matrix reinforced with Ti_2AlC particles, they do suggest that strain rates below $\approx 10^{-4}$ would be required to eliminate strengthening for the particle morphology used in this study. The strain rate used for the high temperature tests was $2x10^{-3}$. Consequently experiments which explore the effects of strain rate at high temperatures must be completed

before any conclusions can be made concerning the effectiveness of the SiC particles as a high temperature reinforcement.

CHAPTER 6:

SUMMARY AND CONCLUSIONS

The primary focus of this study was to investigate the strengthening mechanisms that arise when reinforcing an aluminum alloy with relatively coarse SiC particles of approximately equiaxed shape. In particular, the study was designed to determine the importance of the particles as load bearing elements. From the experimental results performed during this investigation a number of conclusions can be made. The presence of the SiC particles influences stress-strain behaviour most notably in the low strain regime. In particular, the elastic modulus and initial strain hardening rate are increased. The composite σ-ϵ curve (and to a similar extent the unreinforced alloy) is characterized by a rapid drop in the initial strain hardening rate with strain. Thus after extensive deformation the hardening rates in both the alloy and composite are similar and the σ-ϵ curves become nominally parallel. Consequently, for a variety of matrix ageing conditions and test temperatures which were explored, the maximum strengthening effect of the particles (as expressed by the difference between the composite and alloy flow stress) is reached by about 1% plastic strain. Nearly 80% of this is achieved by a plastic strain of .2%.

Some limited microstructural work designed to observe flow at low strains (i.e. below .2% plastic strain) reveals that deformation develops inhomogeneously. In particular, the onset of plastic flow appears to be associated with regions of the microstructure which are relatively particle free. This suggests that the nature of the SiC particle distribution in the composite materials may influence the initial strain hardening rate and therefore the strengthening developed at low strains.

The nature of the yield asymmetry in the composites studied suggests a residual stress state of thermal origin which has a very complex distribution. This internal stress influences the detailed shape of the stress-strain curve. The potential for this residual stress to relax by plastic flow in the matrix was investigated by varying the matrix strength through heat treatments. The magnitude of the internal stress, as suggested from the degree of yield asymmetry, decreases with a decrease in matrix strength.

An examination of the development of the Bauschinger effect in the composite indicates that an internal stress, as a result of inhomogeneous plastic flow, develops rapidly in the first .5% of plastic strain. Again the presence of a relaxation process which is initiated at relatively low strains is reflected in a "saturation" of the Bauschinger effect at strains above 1%.

Damage accumulation, primarily in the form of particle cracking, is among the possible alternative processes which limit the further development of internal stress. Estimates of the damage accumulation rate suggests that this process initiates immediately upon plastic flow, but does not significantly influence the development of strength until strains above 1%. The magnitude of damage accumulation was found to decrease as the matrix strength decreased.

This series of results indicate that stress partitioning to the SiC particles increases rapidly during the early stages of deformation and plays a important role in the development of the high strain hardening rates and consequently the level of strength observed in the composite. It also suggest that alternative processes such as plastic relaxation and, particularly at higher strains, damage accumulation, limit the strengthening process to the low strain regime.

The goal of the theoretical aspects of this work was to develop a model which could predict the degree of stress partitioned to second phase particles during the elastic/plastic transition and beyond. The model was also used to estimate the influence that the second phase particle distribution may have on the initial strain hardening rate in the composite. A self-

consistent analysis based on Eshelby's equivalent inclusion method has been developed for this purpose. The model is successful in describing the general characteristics of the composite stress-strain curve. It predicts an increase in elastic modulus and initial strain hardening rate, followed by a region in which the composite and alloy curve become nominally parallel. Excellent quantitative agreement between the experimentally measured elastic modulus and that predicted by the model was achieved.

In the case of a uniform distribution of SiC particles, the model underestimates the magnitude of the initial strain hardening rate. This may result from the fact that the particle distribution in the real material is somewhat inhomogeneous. The self-consistent analysis was therefore extended to investigate the effects of particle distribution on stress-strain behaviour. The distribution of particles was represented by a bimodal microstructure consisting of a particle rich and particle free phase. The results indicate that, as the degree of particle clustering increases, the initial strain hardening rate in the composite also increases compared to that predicted for the uniform case.

Direct applicability of this clustering model to the experimental results is difficult because of the complex nature of the particle distribution in the real materials. In addition, the model does not include a description of the non-uniform thermal stress present before testing. Nevertheless a description of the degree of clustering based on some experimental observations of particle distribution (Lloyd, 1991) results in an increase in strain hardening rate which is comparable to that measured experimentally.

APPENDIX A:

SOLUTIONS USING ESHELBY'S EQUIVALENT INCLUSION METHOD.

A.1 e^T in Terms of e^Λ for the Infinite Case.

The equation of interest for the equivalent homogeneous solution is;

$$C_p(e^C_{ij}+e^\Lambda_{ij}) = C_m(e^C_{ij}+e^\Lambda_{ij}-e^T_{ij}) \quad (A1)$$

The first step is to express e^C in terms of e^T using $\underline{S}$. This can be done by restating the fact that;

$$e^C_{ij}=S_{ijkl}e^T_{kl} \quad (A2)$$

Substituting this into equation (A1) and rearranging gives;

$$(C_p-C_m)S_{ijkl}e^T_{kl} + C_m e^T_{ij} = (C_m-C_p)e^\Lambda_{ij} \quad (A3)$$

Three equations can be created from equation (A3) by substituting values of ij= 11,22 and 33. For example e^C_{11} becomes;

$$e^C_{11} = S_{1111}e^T_{11} + S_{1122}e^T_{22} + S_{1133}e^T_{33} \quad (A4)$$

The symmetry of a sphere is such that (see Taya and Arsenault, 1989, pg.250);

$$S_{1111}=S_{2222}=S_{3333}=(7-5\nu)/15(1-\nu) \quad (A5)$$

and;

$$S_{1122}=S_{2233}=S_{3311}=S_{1133}=S_{2211}=S_{3322}=(5\nu-1)/15(1-\nu) \quad (A6)$$

Subtraction of one version of (A3) from another gives;

$$(C_p-C_m)[(S_{1111}-S_{1122})(e^T_{11}-e^T_{22})] + C_m(e^T_{11}-e^T_{22}) = (C_m-C_p)(e^\Lambda_{11}-e^\Lambda_{22}) \quad (A7)$$

Rearranging this equation gives;

$$e^T_{11}-e^T_{22}=\frac{(C_m-C_p)}{(C_p-C_m)\underline{S}-C_m}(e^\Lambda_{11}-e^\Lambda_{22}) \quad (A8)$$

where $\underline{S}=S_{1111}-S_{1122}$. From the symmetry of the problem it can then be stated that in general the transformation strain is related to the applied strain by;

$$e_{ij}^{T}=\left[\frac{(C_m-C_p)}{(C_p-C_m)\underline{S}-C_m}\right]e_{ij}^{A} \qquad (A9)$$

which is the value quoted for B in the main text.

A.2 e^T in Terms of e^A for the Finite Case.

In the finite case we must use the results of equation (4.10b) which expresses the fact that there is an internal stress which arises in a finite solid which must be balanced by the two phases;

$$V_m<\sigma>_m + V_p<\sigma>_p = 0 \qquad (4.10b)$$

This equation was originally stated for the finite case but is also valid for the infinite case. For the limit in which the volume fraction of particles approaches zero, the image or mean matrix stress must also vanish. This internal stress may arise from any shape misfit such as that which can result from a mismatch in CTE, elastic properties or plastic properties of the two phases. In this particular case we are interested in a mismatch is elastic properties. The shape misfit then arises only as a result of an applied stress. In the case where the elastic properties of the two phases are equal, no internal stress develops and the stress in the two phases is simply equal to the applied stress. When the elastic properties are different an internal stress results upon applying a load (i.e. there is stress partitioning), and the stress in the two phases can be expressed as;

$$V_m(<\sigma>_m + \sigma^A) + V_p(<\sigma>_p + \sigma^A)= \sigma^A \qquad (A10)$$

By inspection;

$$\sigma^p = <\sigma>_p + \sigma^A \; ; \quad \text{and} \quad \sigma_m=<\sigma>_m + \sigma^A \qquad (A11)$$

From equation (4.10b) it is clear that $<\sigma>_p$ and $<\sigma>_m$ must be of opposite sign;

$$<\sigma>_p = -(V_m/V_p)<\sigma>_m \qquad (A12)$$

Therefore, in the case of $E_p > E_m$ when a stress of $+\sigma^{\wedge}$ is applied $<\sigma>_p$ is positive and $<\sigma>_m$ is negative and $\sigma_p > \sigma_m$, expressing the concept of stress partitioning.

Using the method of the equivalent inclusion we can state;

$$\sigma^{I}_{ij(in)} = C_p(e^{C}_{ij} + e^{\wedge}_{ij} + <e>_{mij}) = C_m(e^{C}_{ij} + e^{\wedge}_{ij} + <e>_{mij} - e^{T}_{ij}) \qquad (A13)$$

or;

$$\sigma^{P}_{ij(in)} = <\sigma>_{pij} + \sigma^{\wedge}_{ij} = C_m(e^{C}_{ij} + e^{\wedge}_{ij} + <e>_{mij} - e^{T}_{ij}) \qquad (A14)$$

Since we are dealing with an equivalent homogeneous composite we can state that;

$$\sigma^{\wedge}_{ij} = C_m e^{\wedge}_{ij} \qquad (A15)$$

and equation (A13) simplifies to;

$$<\sigma>_{pij} = C_m(e^{C}_{ij} + <e>_{mij} - e^{T}_{ij}) \qquad (A16)$$

Using the fact that $<\sigma>_m = C_m <e>_m$ and substituting equation (A12) into (A16) gives;

$$-(1 - V_p/V_p)C_m <e>_{mij} = C_m(e^{C}_{ij} + <e>_{mij} - e^{T}_{ij}) \qquad (A17)$$

Rearranging equation (A17) gives;

$$<e>_{mij} = -V_p(e^{C}_{ij} - e^{T}_{ij}) \qquad (A18)$$

Recalling that $e^{C} = \underline{S}e^{T}$ equation (A18) can be simplified to give an expression for $<e>_m$ in terms of e^{T};

$$<e>_{mij} = -V_p(\underline{S} - I)e^{T}_{ij} \qquad (A19)$$

where I is the identity tensor.

Now that e^{C} and $<e>_m$ can both be expressed in terms of e^{T}, equation (A13) can be used to obtain an expression for e^{T} in terms of $e^{\wedge}$. This follows the same procedure as that described for the infinite case and gives;

$$e_{ij}^{T} = \left[\frac{(C_m - C_p)}{(C_p - C_m)\,[\underline{S} - V_p(\underline{S} - I)\,] - C_m} \right] e_{ij}^{\wedge} \qquad \text{(A20)}$$

which is the value quoted for B^f in chapter 4.

A.3 Elastic Modulus of the Composite.

The elastic modulus of the composite can be calculated in a simplified way by reviewing the details of the equivalent homogeneous composite (Withers et al, 1989). In this material the two phases have the same elastic modulus and therefore equation (4.10b) can be used in terms of the strain as;

$$V_m \langle e \rangle_m + V_p \langle e \rangle_p = 0 \qquad \text{(A21)}$$

The total strain in the composite e_c can then be calculated by summing all the strains in the two phases as;

$$e_c = (1-V_p)e_m + V_p e_p \qquad \text{(A22)}$$

or;

$$e_c = (1-V_p)(e^{\wedge} + \langle e \rangle_m) + V_p(e^{\wedge} + \langle e \rangle_p + e^{T}) \qquad \text{(A23)}$$

which simplifies to;

$$e_c = e^{\wedge} + V_p e^{T} \qquad \text{(A24)}$$

The modulus of the composite E_c can then be calculated as;

$$E_c = \sigma^{\wedge}/e_c = \sigma^{\wedge}/(e^{\wedge} + V_p e^{T}) \qquad \text{(A25)}$$

or;

$$1/E_c = e^{\wedge}/\sigma^{\wedge} + V_p e^{T}/\sigma^{\wedge} \qquad \text{(A26)}$$

In the homogeneous composite case $\sigma^{\wedge} = e^{\wedge} E_m$ and we get;

$$1/E_c = 1/E_m + V_p e^{T}/\sigma^{\wedge} \qquad \text{(A27)}$$

which is equivalent to the expression given by Zok (1988) using an argument based on elastic

energy. Using the results of (A20) this becomes;

$$\frac{1}{E_c}=\frac{1}{E_m}+\frac{V_p}{E_m}\left[\frac{E_m-E_p}{(E_p-E_m)\,[\underline{S}-V_p(\underline{S}-I)\,]+E_m}\right] \qquad (A28)$$

A similar approach applied to the infinite composite gives;

$$\frac{1}{E_c}=\frac{1}{E_m}+\frac{V_p}{E_m}\left[\frac{E_m-E_p}{(E_p-E_m)\,\underline{S}+E_m}\right] \qquad (A29)$$

These are equations (4.15) and (4.14) respectively as quoted in chapter 4.

A.4 The Stress in the Particle in Terms of an Applied Stress.

The stress in the particle can be calculated for the infinite case by recalling equation (A1);

$$\sigma^{P}_{ij(m)} = C_p(e^{C}_{ij}+e^{\wedge}_{ij}) = C_m(e^{C}_{ij}+e^{\wedge}_{ij}-e^{T}_{ij}) \quad (A1)$$

Using the equivalent homogenous expression, but now replacing C_m with C_c, the properties of the infinite composite, the stress in the particle becomes;

$$\sigma^{P}_{ij} = C_c(e^{C}_{ij}+e^{\wedge}_{ij}-e^{T}_{ij}) \qquad (A30)$$

If we consider an applied load in the ij=11 direction, then the stress in that direction is;

$$\sigma^{P}_{11} = E_c(e^{C}_{11}+e^{\wedge}_{11}-e^{T}_{11}) \qquad (A31)$$

Now $e_c=\underline{S}e^{T}$, and $e^{T}=Be^{\wedge}$ and the above equation simplifies to;

$$\sigma^{P}_{11} = E_c(\underline{S}B + 1 - B)e^{\wedge}_{11} \qquad (A32)$$

Substituting the value for B into this equation it can be shown that the expression simplifies to;

$$\sigma^{P}_{11}=E_c\left[\frac{E_p}{\underline{S}E_p+(1-\underline{S})E_c}\right]e^{\wedge}_{11} \qquad (A33)$$

Again in the homogeneous case $\langle\sigma\rangle_m = E_c\langle e\rangle_m$, therefore;

$$\sigma_{11}^{p} = \left(\frac{E_p}{\underline{S} E_p + (1 - \underline{S}) E_c} \right) \sigma_{11}^{A} \qquad \text{(A34)}$$

which is the result given in chapter 4.

REFERENCES

Abel,A., (1987), *Materials Forum*, **10**, pg. 11

Abel,A. and Ham,R.K., (1966), *Acta Metall.*, **14**, pg. 1489

Aikin,R.M. Jr. and Christodoulou,L., (1991), *Scripta metall. mater.*, **25**, pg. 9

Allen,A.J., Bourke,M., Hutchings,M.T., Krawitz,A.D. and Windsor,C.G., (1987), in *Res. Stresses in Sci. & Tech.*, ed. E.Macherauch and V.Hauk, **1**

Ansell,G.S., (1966), in *Oxide Dispersion Strengthening*, ed. G.S.Ansell, T.D.Cooper and F.V.Lenel, Gordon and Breach

Appendino,P., Badini,C., Marino,F. and Tomasi,A., (1991), *Mat. Sci.Eng.*, **A135**, pg. 275

Arsenault,R.J. and Shi,N., (1986), *Mat. Sci. Eng.*, **81**, pg. 175

Arsenault,R.J. and Taya, M., (1987), *Acta metall.*, **35**, pg. 651

Arsenault,R.J. and Wu,S.B., (1987), *Mat. Sci. Eng.*, **96**, pg. 77

Arsenault,R.J., (1991), *Scripta metall. mater.*, **25**, pg. 2617

Arsenault,R.J., Wang,L. and Feng,C.R., (1991), *Acta metall. mater.*, **39**, pg. 47

Asaro,R.J., (1975), *Acta metall.*, **23**, pg. 1255

Ashby,M.F., (1968), in *Oxide Dispersion Strengthening*, ed. G.S. Ansell, T.D. Cooper and F.V. Lenel, Gordon and Breach

Ashby,M.F., Tanner,L.E. and Gelles,S.H., (1969), *Phil. Mag.*, **19**, pg. 757

Ashby,M.F., (1971), in *Strengthening Methods in Crystals*, ed. A.Kelly and R.B.Nicholson, Applied Science Publishers Ltd.

Ashby,M.F. and Jones,D.R.H., (1980), *Engineering Materials 1*, Pergamon Press

Atkinson,J.D., Brown,L.M. and Stobbs,W.M., (1974), *Phil. Mag.*, **30**, pg. 1247

Bao,G., Hutchinson,J.W. and McMeeking,R.M., (1990), Report No. **MECH-163**, Harvard University

Bao,G., Hutchinson,J.W. and McMeeking,R.M., (1991), *Acta metall. mater.*, **39**, pg. 1871

Bardal,A. and Hϕier,R., (1991), in *12th Risϕ Inter. Sym.*, ed. N.Hansen, D.Juul Jensen, T.Leffers, H.Liliholt, T.Lorentzen, A.S.Pedersen, O.B.Pedersen and B. Ralph

Bate,P., Roberts,W.T. and Wilson,D.V., (1981), *Acta metall.*, **29**, pg. 1797

Bate,P., Roberts,W.T. and Wilson,D.V., (1982), *Acta metall.*, **30**, pg. 725

Beulieu,G., (1991), M.Sc. Thesis, McMaster University, Hamilton, Ontario

Brechet,Y., Embury,J.D., Tao,S. and Luo,L., (1991), *Acta metall. mater.*, **39**, pg. 1781

Brockenbrough,J.R., Suresh,S. and Wienecke,H.A., (1991), *Acta metall. mater.*, **39**, pg. 735

Brown,L.M., Woolhouse,G.R. and Valdre,U., (1968), *Phil. Mag.*, **17**, pg. 781

Brown,L.M. and Ham,R.K., (1971), in *Strengthening Methods in Crystals*, edited by A.Kelly and R.B.Nicholson, Applied Science Publishers Ltd.

Brown,L.M. and Stobbs,W.M., (1971a), *Phil. Mag.*, **23**, pg. 1185

Brown,L.M. and Stobbs,W.M., (1971b), *Phil. Mag.*, **23**, pg. 1201

Brown,L.M. and Clarke,D.R., (1975), *Acta metall.*, **23**, pg. 821

Brown,L.M., (1976), *Mat. Sci. Eng.*, **25**, pg. 181

Brown,L.M. and Clarke,D.R., (1977), *Acta metall.*, **25**, pg. 563

Buckley,S.N. and Entwistle,K.M., (1956), *Acta metall.*, **4**, pg. 352

Chen,I.W. and Argon,A.S., (1979), *Acta metall.*, **27**, pg. 785

Christman,T. and Suresh,S., (1988), *Acta metall.*, **36**, pg. 1691

Christman,T., Needleman,A., Suresh,S., (1989), *Acta metall.*, **37**, pg. 3029

Clyne,T.W., (1989), *Mat. Sci. Eng.*, **A122**, pg. 183

Cox,H.L., (1952), *Br.J.Appl. Phys.*, **3**, pg. 72

Derby,B. and Walker,J.R., (1988), *Scripta metall.*, **22**, pg. 529

Dieter,G.E., (1986), *Mechanical Metallurgy*, 3rd edition McGraw-Hill

Dutta,I., and Bourell,D.L., (1990), *Acta Metall.*, **38**, pg. 2041

Embury,J.D., (1985), *Met. Trans. A*, **16A**, pg. 2191

Embury,J.D., Lloyd,D.J. and Ramachandran,T.R., (1989), in *Aluminum Alloys - Contemporary Research and Applications*, ed. A.K.Vasudevan and R.D.Doherty, Academic Press

Embury,J.D., Newell,J., Tao,S., (1991), in *Proc. of the 12th Risφ Inter. Sym.*, ed. N.Hansen, D.Juul Jensen, T.Leffers, H.Lilholt, T.Lorentzen, A.S.Pedersen, O.B.Pedersen and B.Ralph

Eshelby,J.D., (1954), *J.Appl.Phys.*, **25**, pg. 255

Eshelby,J.D., (1957), *Proc. R. Soc.*, **A241**, pg. 376

Eshelby,J.D., (1961), *Progress in Solid Mechanics*, ed. I.N. Sneddon, and R. Hill, **2**, North Holland Pub. Co.

Goods,S.H. and Brown,L.M., (1979), *Acta metall.*, **27**, pg. 1

Gupta,S.P. and Kodali,S.P., (1976), *Trans JIM*, **17**, pg. 261

Hersey,A.V., (1954), *J.Appl.Mech.*, **21**, pg. 1

Hill,R., (1965), *J. Mech. Phys. Solids*, **13**, pg. 213

Hu,M.S., (1991), *Scripta metall. mater.*, **25**, pg. 695

Hull,D and Bacon,D.J., (1984), *Introduction to Dislocations*, 3rd edition, Pergamon Press

Humphreys,F.J., (1980), *Ann. Chim. Fr.*, **5**, pg. 25

Humphreys,F.J., (1988), in *Proc. of the 9th Risφ Inter. Sym.*, ed. S.I.Andersen, H.Lilholt and O.B.Pedersen

Humphreys,F.J., Basu,A. and Djazeb,M.R., (1991), in *Proc. of 12th Risφ Inter. Sym.*, ed. N.Hansen, D.Juul Jensen, T.Leffers, H.Lilholt, T.Lorentzen, A.S.Pedersen, O.B.Pedersen, and B.Ralph

Hunt W.H.Jr., Brockenbrough,J.R. and Magnusen,P.E., (1991), *Scripta metall. mat.*, **25**, pg. 15

Jacobs,M.H., (1972), *Phil. Mag.*, **26**, pg. 1

Kamat,S.V., Rollett,A.D. and Hirth,J.P., (1991), *Scripta metall. mater.*, **25**, pg. 27

Kelly,A., (1971),in *Strengthening Methods on Crystals*, ed. A.Kelly and R.B.Nicholson, Applied Science Pub. Ltd.

Kelly,A. and MacMillan,N.H., (1986), *Strong Solids*, Third Edition, Oxford Science Publications

Kocks,U.K., (1987), in *Unified Constitutive Equations for Creep and Plasticity*, ed. A.K. Miller, Elsevier

Kroner,E., (1958), *Z. Phys.*, **151**, pg. 504

Ledbetter,H.M. and Austin,M.W., (1987), *Mat. Sci. Eng.*, 89, pg. 53

Levy,A. and Papazian,J.M., (1991), *Acta metall. mater.*, 39, pg. 2255

Lilholt,H., (1977), *Acta metall.*, 25, pg. 571

Lloyd,D.J. and Dewing,E., (1988), in *Proc. Intern. Symp. on Advanced Structural Mater.*, ed. D.S. Wilkinson, Pergammon Press

Lloyd,D.J., Lagace,H., Mcleod,A. and Morris,P.L., (1989), *Mat.Sci.Eng.*, A107, pg. 73

Lloyd,D.J., (1990), Private Communication from Dr. D.J.Lloyd

Lloyd,D.J., (1991), in *Proc. of the 12th Risφ Inter. Sym.*, ed.N.Hansen, D.Juul Jensen, T.Leffers, H.Lilholt, T.Lorentzen, A.S.Pedersen, O.B.Pedersen, and B.Ralph

Lutts,A., (1961), *Acta metall.*, 9, pg. 577

Masing,G., (1927), *Wiss. Veroff Siemens-Konzern*, **III**, Band

Mecking,H., (1976), in *Work Hardening in Tension and Fatigue*, ed. A.W.Thompson, AIME

Miller,W.S. and Humphreys,F.J., (1991), *Scripta metall. mater.*, 25, pg. 33

Miller,W.S. and Humphreys,F.J., (1991b), *Scripta metall. mater.*, 25, pg. 2623

Moan,G.D. and Embury,J.D., (1979), *Acta metall.*, 27, pg. 903

Mummery,P.M., Derby,B., Cook,J., Tweed,J.H., (1991) presented at *"Euromat '91"*, Cambridge, U.K.

Nieh,T.G. and Karlak,R.F., (1984), *Scripta metall.*, 18, pg. 25

Orowan,E., (1959), in *Causes and effect of Internal Stresses and Fatigue in Metals*, Elsievier Sci. Pub.

Pedersen,O.B., (1983), *Acta metall.*, 31, pg. 1795

Povirk,G.L., Needleman,A. and Nutt,S.R., (1991), *Mat. Sci. Eng.* A132, pg. 31

Prangnell,P.B. and Stobbs,W.M., (1991) in *12th Risφ Inter. Sym.*, ed. S.I.Andersen, H. Lilholt and O.B.Pedersen

Prangnell,P.B., Stobbs,W.M. and Withers,P.J., (1992) submitted to *Mat.Sci. Eng.*

Rösler,.J, Bao,G. and Evans,A.G., (1990) *Internal Report, University of California at Santa Barbara*

Shigley,J.E., (1986), in *Mechanical Engineering Design*, 1st metric edition, McGraw-Hill

Smith,W.F., (1973), *Met. Trans.*, **4**, pg. 2435

Sowerby,R., Uko,D.K. and Tomita,Y., (1979), *Mat.Sci. Eng.*, **41**, pg. 43

Stoltz,R.E. and Pelloux,R.M., (1976), *Met. Trans. A*, **7A**, pg. 1295

Tanaka,K. and Mori,T., (1972), *J. Elasticity*, 2, pg 199

Tao, S., (1991), *M.Eng. Thesis*, McMaster University, Hamilton, Ontario

Taya,M. and Arsenault,R.J., (1989), *Metal Matrix Composites- Thermomechanical Behavior*, Pergamon Press

Taya,M., Lulay,K.E. and Lloyd,D.J., (1991), *Acta metall.*, **39**, pg. 73

Thomas,G., (1961), *Journal of the Inst. of Metals*, 90, pg. 57

Vasudevan,A.K., Richmond,O., Zok,F. and Embury,J.D., (1989), *Mat. Sci. Eng.*, **A107**, pg. 63

Vogelsang,M., Arsenault,R.J. and Fisher,R.M., (1986), *Met.Trans. A*, **17A**, pg. 379

Wang,N., Wang,Z., Weatherly, G., (1990), in *Fabrication of Particulates Reinforced Metal Composites*, ASM Int.

Weatherly,G.C, (1968), *Met. Sci.Jnl.*, **2**, pg. 237

Wilson,D.V. and Konnan,Y.A., (1964), *Acta metall.*, **12**, pg. 617

Wilson,D.V., (1965), *Acta Metall.*, **13**, pg. 807

Wilson,D.V. and Bate,P.S. (1986), *Acta metall.*, **34**, pg. 1107

Wilson,D.V. and Bate,P.S., (1987), *Mat. Forum*, **10**, pg. 33

Withers,P.J., Juul Jensen,D., Lilholt,H. and Stobbs,W.M., (1987), in *Proc. of ICCM-6/Eccm-2*, **2**, ed. by F.L.Matthews et al., Elsevier

Withers,P.J., Lilholt,H., Juul Jensen,D. and Stobbs,W.M., (1988), in *Proc. of the 9th Risφ Inter. Sym.*, ed. S.I. Andersen, H.Lilholt and O.B. Pedersen

Withers,P.J., Pedersen,O.B., Brown,L.M. and Stobbs,W.M., (1989), *Mat. Sci. Eng.*, **A108**, pg. 281

Withers,P.J., Stobbs,W.M. and Pedersen,O.B., (1989), *Acta metall.*, **37**, pg. 3061

Woolley,R.L., (1954), *Phil. Mag.*, **44** p.597

Zahl,D.B. and McMeeking,R.M., (1991), *Acta metall. mater.*, **39**, pg. 1117

Zok,F., (1988), *Ph.D. Thesis*, McMaster University, Hamilton, Ontario

Zok,F., Embury,J.D., Ashby,M.F. and Richmond,O., (1988), in *Proc. of the 9th Risφ Inter. Sym.*, ed. S.I.Andersen, H.Lilholt and O.B.Pedersen